

THESIS

CHARACTERIZING THE INFLUENCE OF ANTHROPOGENIC EMISSIONS AND
TRANSPORT VARIABILITY ON SULFATE AEROSOL CONCENTRATIONS AT MAUNA
LOA OBSERVATORY

Submitted by

Lauren E. Potter

Department of Atmospheric Science

In partial fulfillment of the requirements

For the Degree of Master of Science

Colorado State University

Fort Collins, Colorado

Spring 2013

Master's Committee:

Advisor: Sonia Kreidenweis

Eric Maloney
Delphine Farmer
Daniel Cooley

Copyright by Lauren E. Potter 2013

All Rights Reserved

ABSTRACT

CHARACTERIZING THE INFLUENCE OF ANTHROPOGENIC EMISSIONS AND TRANSPORT VARIABILITY ON SULFATE AEROSOL CONCENTRATIONS AT MAUNA LOA OBSERVATORY

Sulfate aerosol in the atmosphere has substantial impacts on human health and environmental quality. Most notably, atmospheric sulfate has the potential to modify the earth's climate system through both direct and indirect radiative forcing mechanisms (Meehl et al., 2007). Emissions of sulfur dioxide, the primary precursor of sulfate aerosol, are now globally dominated by anthropogenic sources as a result of widespread fossil fuel combustion. Economic development in Asian countries since 1990 has contributed considerably to atmospheric sulfur loading, particularly China, which currently emits approximately 1/3 of global anthropogenic SO₂ (Klimont et al., 2013). Observational and modeling studies have confirmed that anthropogenic pollutants from Asian sources can be transported long distances with important implications for future air quality and global climate change.

Located in the remote Pacific Ocean (19.54°N, 155.58°W) at an elevation of 3.4 kilometers above sea level, Mauna Loa Observatory (MLO) is an ideal measurement site for ground-based, free tropospheric observations and is well situated to experience influence from springtime Asian outflow. This study makes use of a 14-year data set of aerosol ionic composition, obtained at MLO by the University of Hawaii at Manoa. Daily filter samples of total aerosol concentrations were made during nighttime downslope (free-tropospheric) transport conditions, from 1995 to 2008, and were analyzed for aerosol-phase concentrations of the following species: nitrate (NO₃⁻), sulfate (SO₄²⁻), methanesulfonate (MSA), chloride (Cl⁻),

oxalate, sodium (Na^+), ammonium (NH_4^+), potassium (K^+), magnesium (Mg^{2+}), and calcium (Ca^{2+}).

An understanding of the factors controlling seasonal and interannual variations in aerosol speciation and concentrations at this site is complicated by the relatively short lifetimes of aerosols, compared with greenhouse gases which have also been sampled over long time periods at MLO. Aerosol filter data were supplemented with observations of gaseous radon (Rn^{222}) and carbon monoxide (CO), used as tracers of long distance continental influence. Our study applied trajectory analysis and multiple linear regression to interpret the relative roles of aerosol precursor emissions and large-scale transport characteristics on observed MLO sulfate aerosol variability.

We conclude that observed sulfate aerosol at MLO likely originated from a combination of anthropogenic, volcanic, and biogenic sources that varied seasonally and from year to year. Analysis of chemical continental tracer concentrations and HYSPLIT back trajectories suggests that non-negligible long distance influence from either the Asian or North American continents can be detected at MLO during all seasons although large interannual variability was observed. Possible influence of circulation changes in the Pacific Basin related to the El Niño-Southern Oscillation were found to be both species and seasonally dependent.

We further found an increasing trend in monthly mean sulfate aerosol concentrations at MLO of 4.8% (7.3 ng m^{-3}) per year during 1995-2008, significant at the 95% confidence level. Multiple linear regression results suggest that the observed trend in sulfate concentrations at MLO cannot reasonably be explained by variations in meteorology and transport efficiency alone. An increasing sulfate trend of 5.8 ng m^{-3} per year, statistically significant at the 90% confidence level, was found to be associated with the variable representing East Asian SO_2

emissions. The results of this study provide evidence that MLO sulfate aerosol observations during 1995-2008 reflect, in part, recent trends in anthropogenic SO₂ emissions which are superimposed onto the natural meteorological variability affecting transport efficiency.

ACKNOWLEDGEMENTS

I would first like to gratefully thank my advisor, Dr. Sonia Kreidenweis, for her guidance and encouragement during my time at Colorado State University and for her motivating enthusiasm regarding this project. I also thank my committee members, Dr. Eric Maloney, Dr. Dan Cooley, and Dr. Delphine Farmer, for generously contributing their own expertise to this work. I additionally acknowledge Dr. Colette Heald, Dr. Dave Thompson, and Dr. Jeff Pierce for many beneficial discussions.

I would like to acknowledge Dr. Barry Huebert, Dr. Steven Howell, and Dr. John Zhuang of the University of Hawaii at Manoa for supplying the Mauna Loa Observatory aerosol dataset and guiding the focus of this work. I thank Molly Morman for the contributions she made to this work during her internship at Colorado State University and Sam Atwood for the considerable amount of time he invested to teach me about the HYSPLIT model. Finally, I would like to sincerely thank my family for their unwavering support of my education and success.

This research was supported by the DoD Center for Geosciences/Atmospheric Research at Colorado State University under Cooperative Agreement W911NF-06-2-0015 with the Army Research Laboratory. I would also like to acknowledge support from the US National Park Service.

TABLE OF CONTENTS

ABSTRACT.....	ii
ACKNOWLEDGEMENTS.....	v
1. Introduction	1
1.1 Background	1
1.2 Anthropogenic Sources of Atmospheric Sulfur Dioxide	4
1.3 Trends in Anthropogenic Sulfur Dioxide Emissions	5
1.4 Asian Outflow and Long Range Transport	13
1.5 Mauna Loa Observatory.....	16
1.6 Natural Sources of Sulfate Aerosol at MLO	23
1.6.1 Sea Salt.....	23
1.6.2 Biogenic	26
1.6.3 Volcanic	31
1.7 Oxidation of Atmospheric Sulfur Dioxide to Sulfate Aerosol.....	35
1.8 Research Questions Addressed	39
1.8.1 What are the natural and anthropogenic components of sulfate aerosol at MLO?..	39
1.8.2 Can we identify long distance continental influence at MLO?.....	40
1.8.3 What are the meteorological controls on transport to MLO?	42
1.8.4 Can observed trends in MLO sulfate concentrations be attributed to anthropogenic sulfur dioxide emissions trends?.....	44
2. Data and Methodology	46
2.1 University of Hawaii Dataset	46
2.1.1 Measurement Details	46
2.1.2 Sea Salt and Biogenic Sulfate.....	47
2.1.3 Data Completion Analysis	48
2.2 Chemical Tracers for Continental Influence	52
2.2.1 Radon	52
2.2.2 Carbon Monoxide	54
2.3 SO ₂ Emissions	55
2.3.1 Anthropogenic East Asian SO ₂ Emissions.....	55
2.3.2 Kilauea, Hawaii Volcano SO ₂ Emissions	55
2.4 Multivariate ENSO Index.....	57
2.5 Long Range Transport Index.....	58
2.6 Hybrid Single Particle Lagrangian Integrated Trajectory Model.....	59

2.6.1	Model Details.....	59
2.6.2	Reanalysis Meteorological Fields.....	60
2.6.3	Trajectory Specifications to Match Observations.....	61
2.6.4	Residence Time Analysis of Trajectories.....	61
2.6.5	Concentration Weighted Trajectories.....	62
2.6.6	Meteorological Weighted Trajectories.....	63
2.7	Statistical Analysis.....	64
2.7.1	Monthly, Seasonal, Annual Averaging.....	64
2.7.2	Trend Calculation.....	65
2.7.3	Multiple Linear Regression.....	66
3.	MLO Sulfate Aerosol Observations.....	69
3.1	Influence of Natural Sulfate Sources.....	69
3.1.1	MLO Sea Salt Sulfate and Biogenic Sulfate.....	69
3.1.2	Volcanic Sulfate.....	76
3.2	MLO Anthropogenic NSS-Sulfate.....	80
3.2.1	Daily to Seasonal Variability.....	80
3.2.2	Interannual Variability and Trends.....	84
4.	Attribution of Sulfate Trends to Emissions and Transport Variability.....	91
4.1	Continental Influence at MLO.....	91
4.1.1	HYSPLIT Trajectory Analysis.....	91
4.1.2	Chemical Continental Tracers.....	100
4.2	Transport Controls on MLO Observations.....	113
4.2.1	Meteorology During Transport.....	113
4.2.2	Circulation Patterns.....	121
4.3	Multiple Linear Regression for Identifying Role of Transport.....	127
4.3.1	Regression Analysis of Continental Tracers.....	131
4.3.2	Regression Analysis of Anthropogenic NSS-Sulfate.....	136
5.	Conclusions and Suggestions for Future Work.....	141
5.1	What are the anthropogenic and natural components of MLO sulfate aerosol?.....	141
5.2	Can we identify long distance continental influence at MLO?.....	142
5.3	What are the meteorological controls on transport to MLO?.....	143
5.4	Can observed sulfate trends be attributed to anthropogenic emission trends?.....	145
	APPENDIX A.....	157
	APPENDIX B.....	160

LIST OF TABLES

Table 1.1: GOCART, GISS, and NCAR model specifications for atmospheric sulfur species from Chin et al. (2000).....	3
Table 1.2: Sources of non-sea-salt sulfate at MLO from Huebert et al. (2001).	23
Table 1.3: Sea water ionic composition and sodium mass ratios from University of Hawaii at Manoa School of Ocean and Earth Science and Technology (2012).	25
Table 1.4: Sources and Sinks of sulfur species using 1996 emission inventories (Berglen et al., 2004)	37
Table 2.1: Summary of months with data omitted from analysis based on low data completion or low temporal coverage.....	52
Table 3.1: Daily average concentration and contribution to total sulfate of sea-salt sulfate, biogenic NSS-sulfate, and anthropogenic NSS-sulfate	72
Table 4.1: Modeled sulfate budget for Mexico City and Southeast China with potential as defined in Equation (3.1) from Barth et al. (1999).	99
Table 4.2: Correlations of monthly independent variables during 1995-2008. Variables are defined by letter in Figure (4.34).	130
Table 4.3: Statistical significance and calculated β values with associated error for each independent variable used for regression of MLO radon.	134
Table 4.4: Statistical significance and calculated β values with associated error for each independent variable used for regression of MLO carbon monoxide.....	135
Table 4.5: Statistical significance and calculated β values with associated error for each independent variable used for regression of MLO radon.	140

LIST OF FIGURES

Figure 1.1: Annual sulfur (SO ₂ , DMS, and sulfate) emissions during 2001 used in the GOCART Model from Chin et al. (2007).	2
Figure 1.2: Gridded land based anthropogenic SO ₂ emissions in 2010 as calculated using the GAINS model by Klimont et al. (2013).	5
Figure 1.3: Historical anthropogenic SO ₂ emissions by region during 1850-2005 from Smith et al. (2011).	7
Figure 1.4: 1996-2010 SO ₂ emissions by sector and fuel type in (a) China and (b) India modified from Lu et al. (2011).	11
Figure 1.5: Annual average SO ₂ column satellite observations from SCHIAMACHY and OMI over eastern China compared with estimated SO ₂ emissions (Lu et al., 2011)	12
Figure 1.6: Annual trends based on deseasonalised monthly anomalies of 550nm SeaWiFS AOD during January 1998-December 2010. Red bars represent regions with statistically significant AOD (exceeding 90% confidence) from Hsu et al. (2012).	12
Figure 1.7: Mechanisms for long range transport of Asian pollutants across the Pacific Ocean from Liang et al. (2004). Export mechanisms include convective lifting (E1), warm conveyor belt lifting (E2), postfrontal boundary layer transport (E3), and low-level prefrontal jet transport (E4). Import mechanisms include advection into the mean free tropospheric westerly flow (I1), boundary layer transport (I2), large –scale subsidence in the Pacific High (I3), subsidence into the dry air stream of a cold front (I4), and subsidence induced by mountain waves (I5).	15
Figure 1.8: Seasonal cycle of contribution from different sources to Asian outflow during 1996. Asian outflow defined as Eastward CO flux (106 kg day ⁻¹) along 150°E between 10-60°N and integrated over the 1000-200 hPa column during 1996 from Liu et al. (2003).	16
Figure 1.9: Topographic map of the Island of Hawaii including Mauna Loa Observatory, Kilauea Volcano Crater (summit), Puu O’o (East Rift) from Luria et al. (1992).	20
Figure 1.10: Observed seasonal cycle of fine mode sulfate aerosol at MLO 1993-1996 from Perry et al. (1999).	21
Figure 1.11: Observed and GEOS-CHEM model predicted carbon monoxide concentrations at MLO during 2001 from Liang et al. (2004). Contributions to total CO from North America, Europe, Asia, and oxidation of CO and biogenic volatile organic compounds are also shown.	21
Figure 1.12: Cross-section of trade wind circulation from northeast (right) to southwest (left) from the COMET [®] Website at (http://meted.ucar.edu/) ©1997-2011, University Corporation for Atmospheric Research. All Rights Reserved.	22
Figure 1.13: April 2001 sea-salt emission used in the GOCART model from Chin et al. (2004).	25
Figure 1.14: Simulated monthly oceanic DMS emissions during January 2000 from Korhonen et al. (2008).	28
Figure 1.15: Simplified pathways of DMS oxidation and sulfate aerosol formation from Gondwe et al. (2003).	29
Figure 1.16: Important sources and production mechanisms for cloud condensation nuclei in the remote marine atmosphere from Quinn and Bates (2011).	29
Figure 1.17: Modeled percentage of the annual mean column burden of MSA (a), SO ₂ (b), and NSS-sulfate (c) that can be attributed to oceanic DMS emissions from Gondwe et al. (2003).	30
Figure 1.18: Global distribution of volcanoes from Siebert and Simkin (2002-).	33
Figure 1.19: : SO ₂ (A) and fine mode aerosol (B) concentrations associated with the Kilauea volcanic plume dispersion from Longo et al. (2005).	34

Figure 1.20: Global distribution of OH and H ₂ O ₂ from Chin et al. (2000).....	38
Figure 1.21: Seasonal cycle of natural and anthropogenic components of total NSS-sulfate at Midway Island (28°13'N, 177°22'W), nitrate, and mineral dust during 1981-1990 from Prospero et al. (2003).	39
Figure 1.22: Fractions of MLO Lagrangian back trajectory air parcels occurring over the Eurasian (squares) or American (triangles) continents 6-10 days prior to arrival at MLO from Lintner et al. (2007).	40
Figure 1.23: Clustered MLO HYSPLIT 5-day back trajectories by season during 1985-2001 from Earth System Research Laboratory (2012) (http://www.esrl.noaa.gov/gmd/dv/site/trajs/mlo_traj.jpg).....	41
Figure 1.24: NCEP/NCAR Reanalysis 700mb stream function (units 10 ⁷ m ² /s) contour composites for 1971-2002 during El Nino (red) and La Nina (blue) conditions during (a) January-February-March, (b) April-May-June, (c) July-August-September, and (d) October-November-December from Lintner et al. (2006).	44
Figure 1.25: Trends in springtime mean anthropogenic NSS-sulfate at Midway Island compared with SO ₂ emissions from China during 1980-2000 from Prospero et al. (2003).....	45
Figure 2.1: Timeline of monthly anthropogenic NSS-sulfate data completion and temporal spread. The threshold for including data points is indicated by the red lines.	51
Figure 2.2: Map of Kilauea Volcano Summit (left) and East Rift (right) plumes on the Island of Hawaii during trade wind conditions. Mobile sampling locations are indicated as regions where the Summit plume intersects Crater Rim Drive or the East Rift plume intersects Chain of Craters Road. Figure from Elias et al. (2002).	57
Figure 2.3: Correlation between sea level pressure anomalies and Asian outflow as defined by variations in simulated carbon monoxide along the cross-section represented by the red line (0-8 km, 30– 60°N, 150°E). Sea level pressure anomalies in the black box were used in the definition of the LRT1 index (Liang et al., 2005).	59
Figure 3.1: Mean seasonal cycle of sea salt, biogenic, and anthropogenic components of MLO total sulfate. Error bars represent the standard deviation of all available monthly mean total sulfate concentrations.....	72
Figure 3.2: Mean seasonal Cycle of MLO sea-salt sulfate and biogenic (DMS derived) sulfate concentrations. Error bars represent the standard deviation of all available monthly mean concentrations.	73
Figure 3.3: Percentage of NSS-sulfate attributed to oceanic DMS emissions in December-January-February (top), June-July-August (middle), and the annual average (bottom) Gondwe et al. (2003).	74
Figure 3.4: Concentration weighted trajectories of MLO methane sulfonic acid concentration from 1995-2008.	75
Figure 3.5: Percentage of annually averaged zonal mean vertical distribution of biogenic NSS-sulfate modified from Gondwe et al. (2003).	75
Figure 3.6: Timeline of mean monthly and annual SO ₂ emission rates from the Kilauea Volcano summit (blue) and east rift (red) and mean anthropogenic NSS-sulfate concentrations at MLO for each month during 1995-2008 data from Elias and Sutton (2012).	77
Figure 3.7: SO ₂ plume from Kilauea Volcano East Rift eruption during March 2008 from NASA Earth Observatory (2008).	78
Figure 3.8: Kilauea summit crater plume heights during March 2008-December 2010 from Elias and Sutton (2012).	79

Figure 3.9: Correlation of Kilauea summit SO ₂ emissions and MLO anthropogenic NSS-sulfate concentrations during 1995-2008 (a) and 2008 only (b). Data from Elias and Sutton (2012).	79
Figure 3.10: Annual total SO ₂ emission rates from Kilauea from Elias and Sutton (2012).	80
Figure 3.11: Daily, monthly mean, and monthly median anthropogenic NSS-sulfate concentrations at MLO.	82
Figure 3.12: Seasonal cycle in mean concentrations of anthropogenic NSS-sulfate at MLO 1995-2008 using mean day of year concentrations (a) and mean monthly concentrations (b).	83
Figure 3.13: MLO 10-day HYSPLIT back trajectories weighted with receptor anthropogenic NSS-sulfate concentrations.	84
Figure 3.14: Trend in MLO anthropogenic NSS-sulfate based on monthly (blue squares), March-April-May (green triangles), and annual (orange circles) mean concentrations.	87
Figure 3.15: Trend in MLO anthropogenic NSS-sulfate based on monthly (blue squares), March-April-May (green triangles), and annual (orange circles) median concentrations.	87
Figure 3.16: Annual trends in anthropogenic NSS-sulfate calculated separately for mean concentrations during each calendar month.	88
Figure 3.17: Annual trends in anthropogenic NSS-sulfate calculated separately for median concentrations during each calendar month.	89
Figure 3.18: Deseasonalized anthropogenic NSS-sulfate using mean and standard deviation of concentrations during each calendar month for all available data during 1995-2008.	90
Figure 4.1: 10-Day HYSPLIT back trajectories with MLO arrival times of 6Z, 12Z, and 18Z during each day of 2007.	96
Figure 4.2: Total residence time in hours calculated from all MLO HYSPLIT 10-day back trajectory endpoints during 1995-2008.	96
Figure 4.3: Total residence time in hours calculated from MLO HYSPLIT 10-day back trajectory endpoints during each calendar month combined over 1995-2008.	97
Figure 4.4: East Asian (orange) and American (purple) source regions defined by (70°E, 50°N, 150°E, 10°N) and (120°W, 50°N, 80°W, 10°N) respectively in relationship to the MLO source receptor site (red).	98
Figure 4.5: Seasonal cycle in continental contribution to MLO as determined by HYSPLIT back trajectory endpoints entering defined East Asian and American region boundaries.	98
Figure 4.6: Trends in monthly mean MLO 10-day HYSPLIT back trajectories originating from defined East Asian (orange) and American (purple) continental regions.	99
Figure 4.7: Seasonal cycle of chemical continental racers at MLO: gaseous radon (top), aerosol NSS-calcium (middle), and gaseous carbon monoxide (bottom).	106
Figure 4.8: Radon seasonal cycle at MLO 1991-2002 from Lintner et al. (2007).	107
Figure 4.9: MLO radon concentration weighted 10-day back trajectories for 1997-2010.	107
Figure 4.10: Modeled oceanic radon flux density for January (top) and July (bottom) modified from Schery and Huang (2004).	108
Figure 4.11: MLO NSS-calcium concentration weighted 10-day back trajectories for 1996-2008.	109
Figure 4.12: Annual dust emissions during 2001 used in the GOCART model from Chin et al. (2007).	109
Figure 4.13: MLO carbon monoxide concentration weighted 10-day back trajectories for 2005-2010.	110
Figure 4.14: Annual mean biomass burning emissions during 1997-2004 from van der Werf et al. (2006).	110

Figure 4.15: Trends in MLO chemical continental tracers: radon, NSS-calcium, and carbon monoxide. For radon a trend was calculated using all available data as well as two separate trends for the periods of 1997-2003 and 2004-2010 to determine whether the 1997-2010 patterns were likely a result of an instrumentation change in 2004.	111
Figure 4.16: Standardized anomaly in daily concentrations of MLO sulfate aerosol and chemical continental tracers: NSS-calcium aerosol, radon gas, and carbon monoxide gas during 2005-2008.....	112
Figure 4.17: Age weighted HYSPLIT back trajectories from the MLO receptor site. Color represents the gridded average transport time to MLO.	117
Figure 4.18: Pressure weighted HYSPLIT back trajectories from the MLO receptor site. Color represents the gridded average pressure level during transport to MLO.	118
Figure 4.19: Height (above sea level) weighted trajectories from the MLO receptor site. Color represents the gridded average height during transport to MLO.	118
Figure 4.20: Relative humidity (RH) weighted HYSPLIT back trajectories from the MLO receptor site. Color represents the gridded average RH during transport to MLO.	119
Figure 4.21: Precipitation weighted HYSPLIT back trajectories from the MLO receptor site. Color represents the gridded average surface precipitation beneath the air parcel position during transport to MLO.	119
Figure 4.22: Solar radiation weighted HYSPLIT back trajectories from the MLO receptor site. Color represents the gridded average solar radiation reaching the surface beneath the air parcel position during transport to MLO.	120
Figure 4.23: Seasonal cycle of NCEP/NCAR Reanalysis meteorological fields corresponding to HYSPLIT back trajectory locations. Each variable was normalized by the annual mean and standard deviation for intercomparison.	120
Figure 4.24: Multivariate ENSO Index (MEI) anomaly values for 1995-2008 (data from Wolter et al., 2012).	124
Figure 4.25: Autocorrelation of MLO chemical species and MEI beginning in January 1997..	124
Figure 4.26: Correlation between MEI and peak season monthly concentrations of radon (a) and carbon monoxide (b).	125
Figure 4.27: Correlation between MEI and peak season monthly concentrations of anthropogenic NSS-sulfate and NSS-calcium.	126
Figure 4.28: Timelines of all independent variables used for multiple linear regression.	129
Figure 4.29: Multiple linear regression results for MLO radon concentrations during 1997-2010.	134
Figure 4.30: Multiple linear regression results for carbon monoxide concentrations during 1995-2008.....	135
Figure 4.31: Multiple linear regression results for anthropogenic NSS-sulfate during 1995-2008 using selected meteorological regressors (d), (e), (i), and (j) as defined in Figure (4.28).	138
Figure 4.32: Multiple linear regression results for anthropogenic NSS-sulfate during 1995-2008 using selected meteorological regressors (d), (e), (i), (j), (g), and (h) as defined in Figure (4.28).	139
Figure 4.33: Annual combined SO ₂ emissions and average trend during 1995-2008 for China and India from Lu, Zhang, and Streets (2011).	139
Figure 4.34: Multiple linear regression of anthropogenic NSS-sulfate using all variables shown in Figure (4.28) as regressors. Their trends for observed monthly mean data and predicted monthly data are shown in blue and red respectively.	140

Figure 5.1: Time series of the Multivariate ENSO Index, Pacific Decadal Oscillation, and North Pacific Index.	144
Figure 5.2: Comparison between anthropogenic NSS-sulfate observations at MLO used in this study and NAAPS model total sulfate aerosol at the corresponding latitude and longitude of MLO.	146
Figure A.1: Daily MLO concentrations and trajectory origin during 2005.	157
Figure A.2: Daily MLO concentrations and trajectory origin during 2006.	158
Figure A.3: Daily MLO concentrations and trajectory origin during 2007.	158
Figure A.4: Daily MLO concentrations and trajectory origin during 2008.	159
Figure B.1: Normal probability plot to test for normality of radon residuals.	160
Figure B.2: Test for linearity of radon residuals.	161
Figure B.3: Test for independence of radon residuals.	161
Figure B.4: Test for homoscedasticity of radon residuals.	162
Figure B.5: Normal probability plot to test for normality of carbon monoxide residuals.	163
Figure B.6: Test for linearity of carbon monoxide residuals.	164
Figure B.7: Test for independence of carbon monoxide residuals.	164
Figure B.8: Test for homoscedasticity of carbon monoxide residuals.	165
Figure B.9: Normal probability plot to test for normality of anthropogenic NSS-sulfate residuals.	166
Figure B.10: Test for linearity of anthropogenic NSS-sulfate residuals.	167
Figure B.11: Test for independence of anthropogenic NSS-sulfate residuals.	167
Figure B.12: Test for homoscedasticity of anthropogenic NSS-sulfate residuals.	168

1. Introduction

1.1 Background

Atmospheric sulfur has important implications for both human health and the environment including local air quality, visibility, acid rain, and climate change (Stern et al., 2006). The widespread combustion of fossil fuels around the globe has resulted in an increase in anthropogenic sulfur emissions which are now much larger than natural sulfur emissions (Smith et al., 2001). Simulations performed using the Goddard Chemistry Aerosol Radiation and Transport (GOCART) model determined that during a year without significant volcanic activity, about 20% of sulfur precursor gases are from natural sources while 80% are anthropogenic, and estimated that about 40% of total precursor gases are effectively converted to sulfate aerosol (Chin et al., 2000). The distribution of sulfur emissions in the Northern Hemisphere is presented in Figure (1.1) and estimates of total global emissions, production, removal, and atmospheric lifetimes of important sulfur species are listed in Table (1.1), from Chin et al. (2000).

Although sulfate aerosol can be a primary pollutant emitted by anthropogenic fossil fuel consumption (Jacobson, 2002), direct sulfate emissions contribute only 2% of total sulfur emissions (Chin et al., 2000). The most abundant atmospherically relevant gaseous sulfur species include dimethyl sulfide (DMS) and sulfur dioxide (SO_2), both of which undergo oxidation to produce S(VI), generally present as sulfuric acid (H_2SO_4) or sulfate (SO_4^{2-}), by several oxidants and pathways in the gas phase, aqueous phase, and possibly via heterogeneous reactions on particle surfaces (Li et al., 2006).

Oxidation of DMS and SO_2 in the troposphere to produce sulfate aerosol has received a lot of attention in recent years due to the potential of the sulfate aerosol for impacting radiative forcing (Su et al., 2011). Sulfate particles in the atmosphere scatter incoming solar radiation

back to space, reducing the amount of radiation reaching the surface and therefore cooling the near-surface air. This mechanism is termed the aerosol “direct effect” on the radiative budget (Jacobson, 2002). Sulfate aerosols can also serve as cloud condensation nuclei, affecting radiative forcing of the atmosphere indirectly through modification of cloud lifetime and reflectivity (Benkovitz, 2006). Qualitatively the net direct and indirect forcing of all aerosol types is assigned a negative sign (cooling) and the forcing due to the direct effect of all aerosol types combined is estimated to be $-0.5 \pm 0.4 \text{ Wm}^{-2}$, which is thought to have counteracted some of the warming that would have otherwise been observed as a result of increasing greenhouse gases (Meehl et al., 2007).

Sulfate aerosols have lifetimes of approximately 4-5.8 days compared with 1.8-2.6 days for gaseous SO_2 (Chin et al., 2000). This increased lifetime allows for widespread transport of sulfate aerosols so that associated climate impacts can be observed on regional and global scales (Akimoto, 2003). Recent observations in the United States suggest that a linear relationship exists between SO_2 emissions and sulfate aerosol concentrations (Hand et al., 2012b) although this pattern is complicated by secondary sulfate production and transport efficiency over long distances which are both highly dependent on meteorological variability.

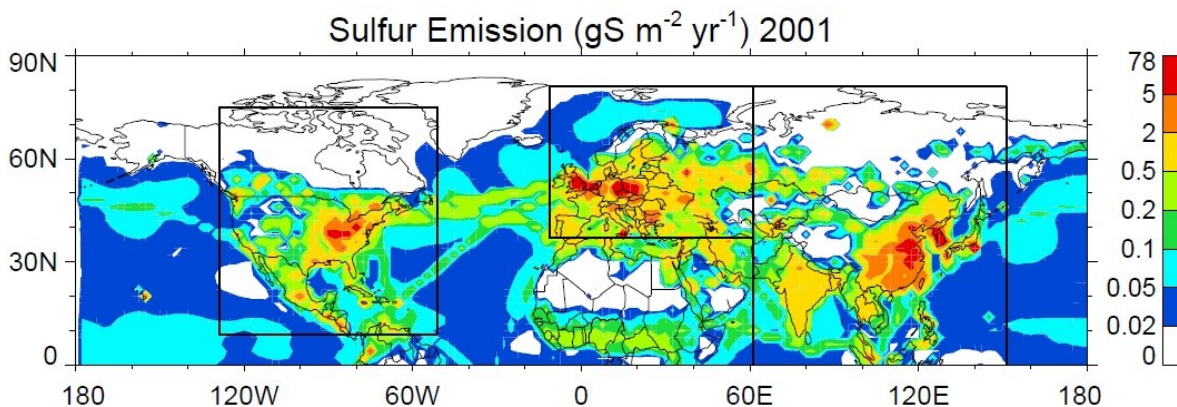


Figure 1.1: Annual sulfur (SO_2 , DMS, and sulfate) emissions during 2001 used in the GOCART Model from Chin et al. (2007).

Table 1.1: GOCART, GISS, and NCAR model specifications for atmospheric sulfur species from Chin et al. (2000).

Table 2. Comparison of Sulfur Budget From the GOCART Model With the GISS and NCAR Models

Budget Component	GOCART ^a		GISS ^b		NCAR ^c	
Total emission, Tg S yr ⁻¹	93.9		83.0		82.5	
SO ₂ anthropogenic	70.6	(75.2%)	64.6	(77.8%)	65.7	(79.6%)
SO ₂ biomass burning	2.3	(2.4%)	2.3	(2.8%)		
SO ₂ volcanic	5.5	(5.9%)	3.5	(4.2%)		
Sulfate anthropogenic	2.2	(2.3%)	1.9	(2.3%)		
DMS oceanic	13.3	(14.2%)	10.7	(12.9%)	15.5	(18.8%)
Total deposition, Tg S yr ⁻¹	93.0		83.4		81.0	
SO ₂ dry deposition ^d	41.2	(44.3%)	35.5	(42.6%)	24.5	(30.2%)
SO ₂ wet scavenging	10.6	(11.4%)	0.2	(0.2%)	1.6	(2.0%)
Sulfate dry deposition	5.1	(5.5%)	9.2	(11.0%)	3.7	(4.6%)
Sulfate wet scavenging ^d	34.7	(37.3%)	37.4	(44.8%)	51.2	(63.2%)
MSA dry deposition	0.1	(0.1%)	0.2	(0.2%)		
MSA wet scavenging	1.3	(1.4%)	0.9	(1.1%)		
SO ₂ production, Tg S yr ⁻¹	11.9		10.0		15.5	
From DMS+OH	10.4	(87.4%)				
From DMS+NO ₃	1.5	(12.6%)				
Sulfate production, Tg S yr ⁻¹	38.5		44.7		53.6	
In-air	14.0	(36.4%)	13.1	(29.3%)	9.2	(17.2%)
In-cloud ^d	24.5	(63.6%)	31.6	(70.7%)	44.4	(82.8%)
Burden, Tg S						
SO ₂	0.43		0.56		0.4	
Sulfate	0.63		0.73		0.57	
DMS	0.073		0.056		0.06	
MSA	0.028		0.023			
Lifetime, days						
SO ₂	1.8		2.6		1.9	
Sulfate ^e	5.8	(4.6)	5.7		4.0	
DMS	2.0		1.9		1.4	
MSA	7.1		7.6			
Loss frequency ^f , day ⁻¹						
SO ₂ dry deposition	0.26		0.17		0.17	
SO ₂ in-air oxidation	0.09		0.06		0.06	
SO ₂ wet processes ^g	0.22		0.15		0.31	
Sulfate dry deposition	0.02		0.03		0.02	
Sulfate wet scavenging	0.15	(0.2)	0.14		0.25	

^aThis work, 1990 simulation.

^bKoch et al. [1999].

^cBarth et al. [2000] and Rasch et al. [2000]

^dWet scavenging of SO₂ in the GISS and NCAR models was counted as a part of sulfate in-cloud production as well as sulfate wet scavenging budgets. See text for details.

^eThe numbers in parentheses for the GOCART model are the values that would be if SO₂ wet scavenging were considered as a part of sulfate wet deposition term, as treated by the GISS and NCAR models. See text for explanation.

^fLoss frequency is defined as the loss rate divided by the burden.

^gIncluding in-cloud oxidation and wet scavenging.

1.2 Anthropogenic Sources of Atmospheric Sulfur Dioxide

Anthropogenic emissions are estimated to contribute approximately 75-80% of global SO₂ emissions as summarized by Chin et al. (2000) in Table (1.1). The largest sources of anthropogenic SO₂ are coal and oil combustion in power plants (73%) and industrial processes (20%) although other important sources include shipping and vehicle exhaust (United States Environmental Protection Agency, 2012). The sulfur content of fuel largely determines the magnitude of SO₂ emissions from such combustion activities. Reliable emissions inventories exist for the U.S., Canada, and Europe, but detailed inventories for other regions are sparse and often less reliable, increasing the uncertainty of regional contributions to global atmospheric SO₂ emissions (Smith et al., 2001).

Anthropogenic SO₂ emission sources are particularly abundant in the Northern Hemisphere mid-latitudes although regions in the Southern Hemisphere with very little anthropogenic influence are typically dominated by natural sources of SO₂ (Gondwe et al., 2003). The geographic distribution of large SO₂ source regions over North America, Europe, and Asia can be seen in Figure (1.2). Over these Northern Hemisphere source regions, atmospheric SO₂ burden is typically greater during winter than during summer although anthropogenic sources contribute over 90% of column averaged SO₂ regardless of season (Gondwe et al., 2003). It is critical to fully understand the spatial and temporal variability of anthropogenic SO₂ emission sources because only this fraction of global atmospheric SO₂, potentially serving as a precursor for atmospheric sulfate aerosol, can potentially be reduced or managed for environmental mitigation purposes.

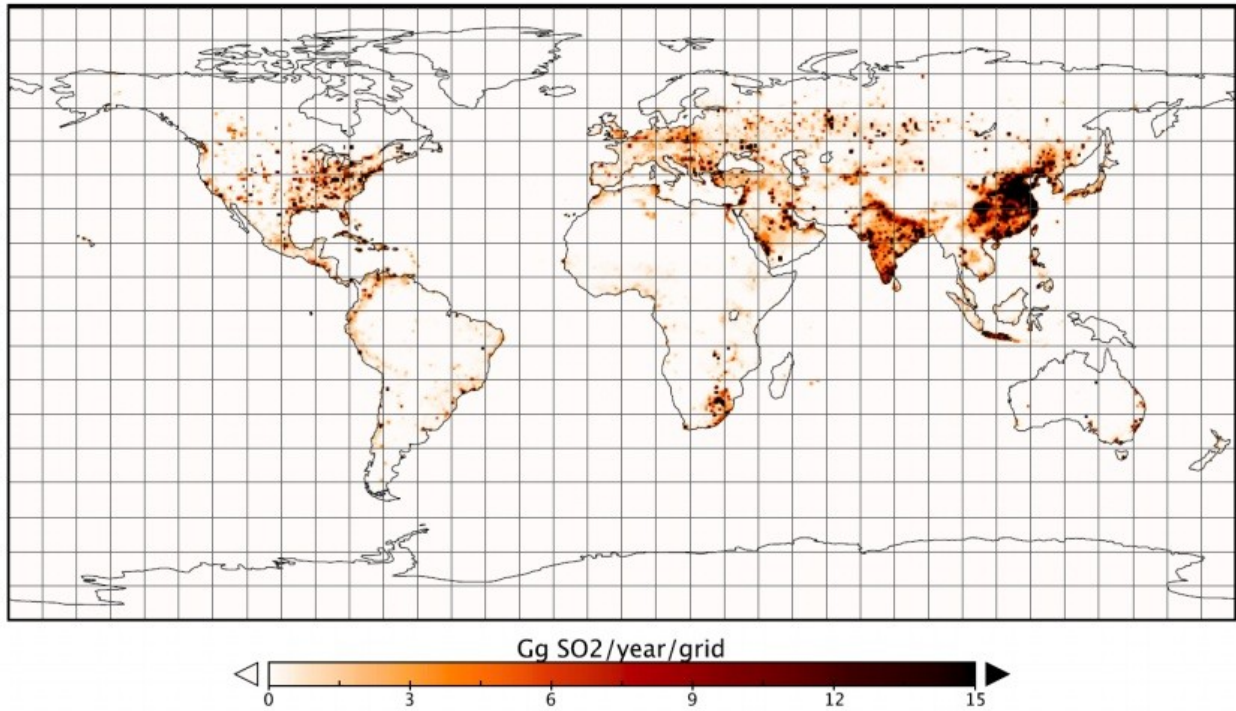


Figure 1.2: Gridded land based anthropogenic SO₂ emissions in 2010 as calculated using the GAINS model by Klimont et al. (2013).

1.3 Trends in Anthropogenic Sulfur Dioxide Emissions

Figure (1.3) from Smith et al. (2011) shows the trends in global SO₂ emissions by region from 1850-2005. North American anthropogenic SO₂ emissions during the first half of the 20th century were greater than for any other region, with emissions more than doubling from 1900-1950. North American SO₂ emissions reached a maximum during the 1970s and subsequently decreased, corresponding to an increasing environmental awareness in the United States and the timing of the US EPA Clean Air Act Amendments of 1970 which established National Ambient Air Quality Standards (NAAQs) for SO₂ (Jacobson, 2002). The Clean Air Act Amendments of 1990 additionally targeted sulfur species in an effort to reduce the harmful effects of acid rain throughout the country (Lynch et al., 2000). Following the widespread reductions on sulfur content of fuels and emissions controls such as scrubber technologies designed to reduce SO₂

emissions from coal fired power plants, declines in precipitation sulfate concentration were also observed across the United States (Smith et al., 2001; Likens et al., 2001). United States annual mean SO₂ emissions decreased a total of 55% during 2000-2010 and sulfate aerosol trends of similar magnitude were observed by the Interagency Monitoring of Protected Visual Environments (IMPROVE) Network at rural sites across the country (Hand et al., 2012b).

Decreasing SO₂ emissions in the United States and associated decreases in particulate sulfate concentrations have led to an increased proportion of particulate sulfate which is attributed to transboundary influence from outside sources (Hand et al., 2012b). Maximum monthly concentrations in sulfate have shifted from summer to spring at many Western US monitoring sites between 2000-2010 which may indicate decreasing contributions from local and regional sources and increasing contribution from East Asian sources (Hand et al., 2012a).

Quantifying the influence of international emissions on SO₂ and particulate sulfate concentrations in the United States has important implications for the attainment of regulatory standards.

During the second half of the 20th century, a shift in the geographic distribution of global anthropogenic SO₂ occurred with East Asian emissions surpassing both North American and European emissions for the first time (Smith et al., 2011). In 1980, SO₂ emissions from the North Atlantic Basin contributed about 60% of global emissions which decreased to 40% by 1995. Extremely rapid population growth and economic development resulted in a doubling of energy consumption in Asia between 1980 and 2003 which led to drastic increases in emissions of SO₂, NO_x, CO, black carbon aerosol (BC), and organic carbon aerosol (OC) (Ohara et al., 2007).

Global Anthropogenic SO₂ Emissions

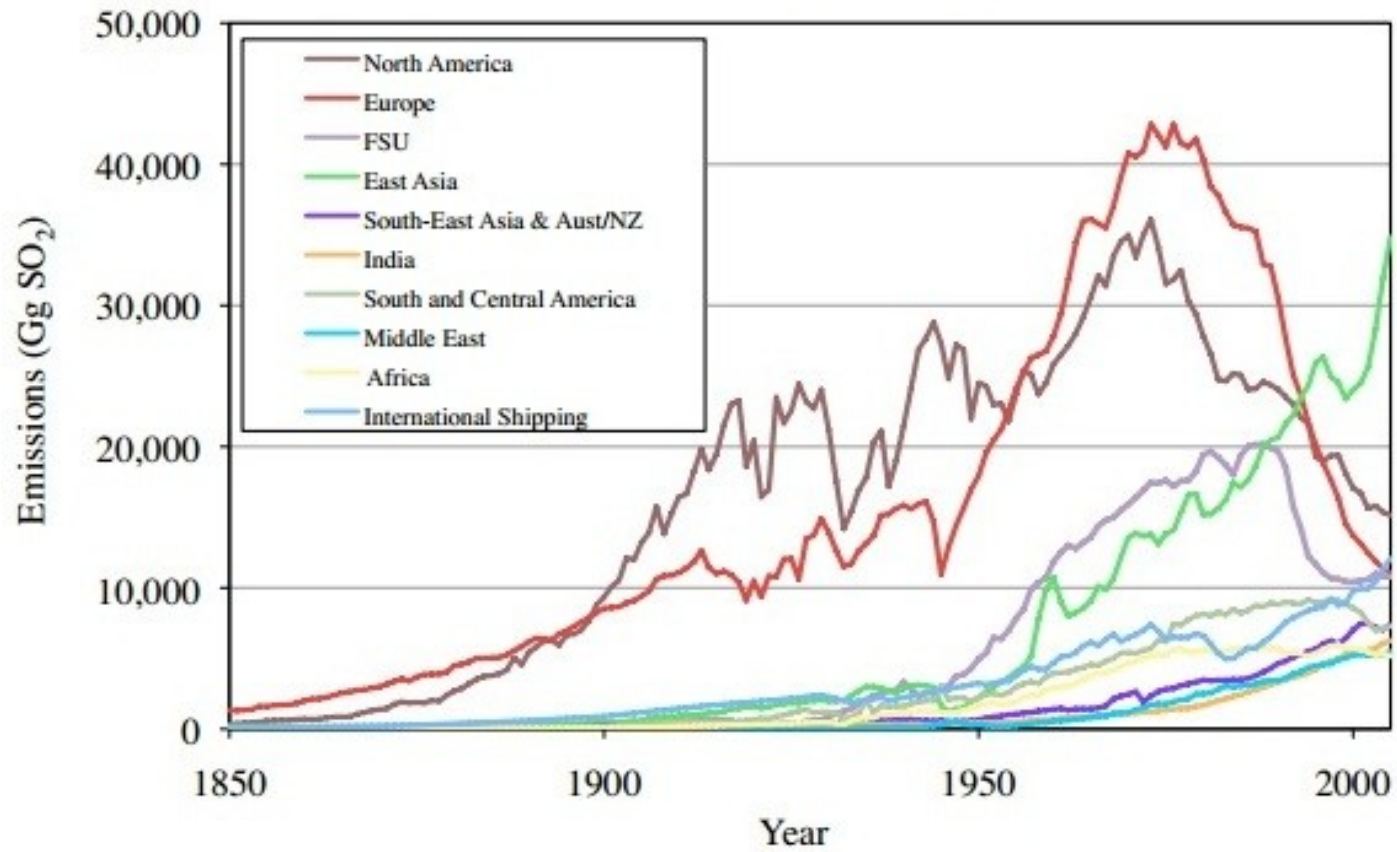


Figure 1.3: Historical anthropogenic SO₂ emissions by region during 1850-2005 from Smith et al. (2011).

SO₂ emissions from China now contribute more than 90% of the anthropogenic SO₂ emissions from East Asia and more than 25% of anthropogenic SO₂ emissions worldwide (Lu et al., 2010; Klimont et al., 2013). After an initial period of development during the late 20th century, Chinese SO₂ emissions peaked around 1996 and then subsequently decreased from 1996-2000 due to a slow-down of the country's economic growth and reduction of fuel consumption (Streets et al., 2000). Around the year 2000, the Chinese economy improved and emissions began increasing dramatically again (Lu et al., 2011). At the beginning of the 21st century, emissions of SO₂ were projected to increase 55% over 2000 emissions by 2020 when analyzed under the most pessimistic emissions scenario, comparable to the B1 scenario of the IPCC (Ohara et al., 2007). Pressure to protect environmental interests worldwide led The Ministry of Environmental Protection (MEP) to develop the Chinese 10th 5-Year Plan which established the goal of reducing SO₂ emissions in 2005 by 10% compared to 2000 emission levels (Su et al., 2011). However, this MEP goal was not met (Lu et al., 2010) and Chinese SO₂ emissions actually continued to increase 12.7% annually between 2000 and 2005 (Itahashi et al., 2012).

Figure (1.3) shows the recent and dramatic increase in emissions from East Asia and how significantly global emissions were impacted by developing nations. The global attention focused on continued rising anthropogenic emissions further motivated environmental policy measures in China which resulted in the widespread implementation of flue-gas desulfurization (FGD) in coal fired power plants between 2005 and 2007 (Lu et al., 2010). Although FGD devices to reduce SO₂ emissions were installed on a majority of power plants during 2006, the MEP admitted that the devices were less than 40% functional as of their implementation which generated concern about whether emissions reductions would indeed occur (Su et al., 2011).

However after 2007, operational problems with the FGD devices were under control and significant reductions were observed in SO₂ emissions (Itahashi et al., 2012). These new policies allowed for the Chinese 11th 5-Year Plan to be met successfully before the deadline of 2010 (Lu et al, 2010). After several years of dramatic increase, Chinese SO₂ emissions decreased by 3.9% annually between 2005 and 2009 (Itahashi et al. 2012). By the end of 2010, FGD devices were operating on 83% of power plants in China which contributed to the removal of an estimated 19.4 Tg SO₂ that would have otherwise been emitted during that year (Lu et al., 2011). The trend in SO₂ emissions from China and India during 1996-2010 is shown in Figure (1.4). Although SO₂ emissions from China are currently several times larger than from India, the consistent increase in emissions from India has offset a portion of the emissions decrease from China since 2006 and future emissions estimates in this region remain uncertain (Lu et al., 2011).

As additional long term satellite data have become available, emissions trends from East Asia can begin to be understood with greater confidence. Satellite instruments such as the Scanning Imaging Absorption Spectrometer (SCIAMACHY onboard the European Space Agency's ENVISAT satellite, launched in 2002) and the Ozone Monitoring Instrument (OMI, onboard NASA's EOS/Aura satellite, launched in 2004) are sensitive enough to detect large anthropogenic SO₂ sources for the first time (Lu et al., 2011). The reduction in emissions reported by the MEP was supported by OMI observations of decreasing total column SO₂ over the area during the same time period (Lu, et al. 2011). Figure (1.5) shows the relationship between estimated Chinese SO₂ emissions and recent satellite observations of SO₂ over Eastern Asia (Lu et al., 2011). There are a few key differences observed in this comparison of emissions based on technological emissions inventories and satellite retrievals. The timing of the emissions peak and peak in SO₂ observed by satellite differs by one year although the reasons for this

discrepancy are not obvious (Lu et al., 2011). Satellites also appear to observe an increase in emissions from 2009-2011 but emissions inventories suggest a further decrease during this time. Klimont et al. (2013) modeled anthropogenic SO₂ emissions between 2000 and 2010 and reported strong decreases in portions of China attributed to improved technologies although the country remained the largest single emitter of anthropogenic SO₂ in 2010.

Sulfate aerosol concentrations have been found to respond to gaseous SO₂ emissions trends with associated increases near regions with high emissions. Fine-mode aerosol optical depth (AOD) over China was observed by MODIS to peak around 2005-2006 and subsequently decrease by 2-7% annually (Itahashi et al., 2012). Hsu et al. (2012) reported statistically significant increasing trends in aerosol optical thickness observed by the SeaWiFS instrument during 1998-2010 over regions of Northern India as well as Eastern and Southern China as shown in Figure (1.6). In addition to the uncertainties of anthropogenic emission inventories, satellite observations of both SO₂ and AOD are still subject to many uncertainties which may explain some of the discrepancies between these developing datasets (Lu et al., 2011). The study of anthropogenic emissions from East Asia is an especially interesting topic of research because the variation and non-linearity of emissions trends over the study period (1995-2008) reflects the conflicting interests in economic development and environmental sustainability. This complicated interrelationship of priorities must be considered when analyzing the broader environmental impacts of such emissions variations (Lu et al., 2011).

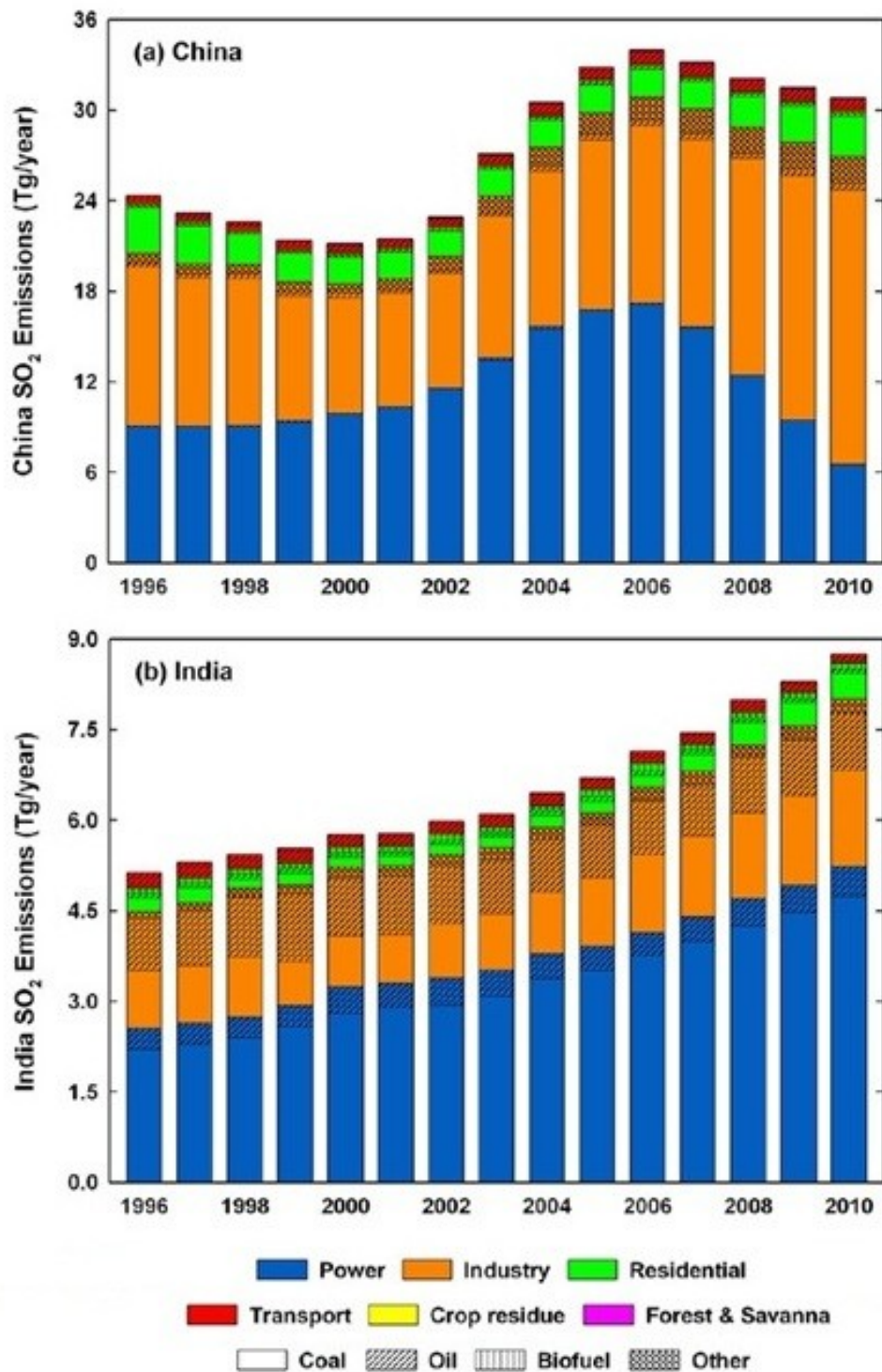


Figure 1.4: 1996-2010 SO₂ emissions by sector and fuel type in (a) China and (b) India modified from Lu et al. (2011).

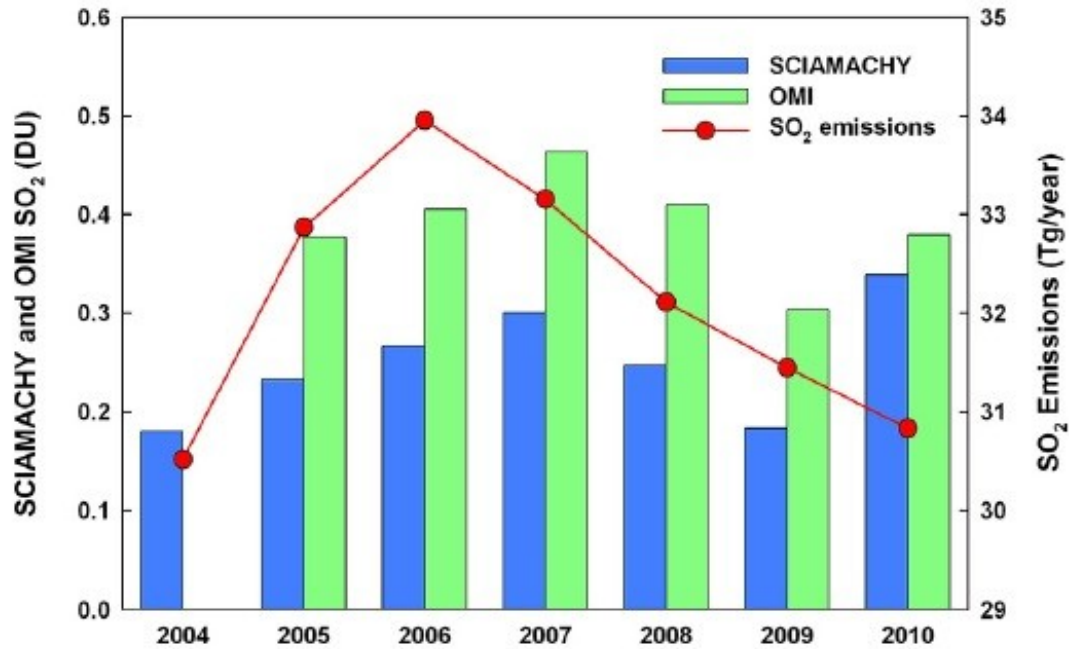


Figure 1.5: Annual average SO₂ column satellite observations from SCHIAMACHY and OMI over eastern China compared with estimated SO₂ emissions (Lu et al., 2011)

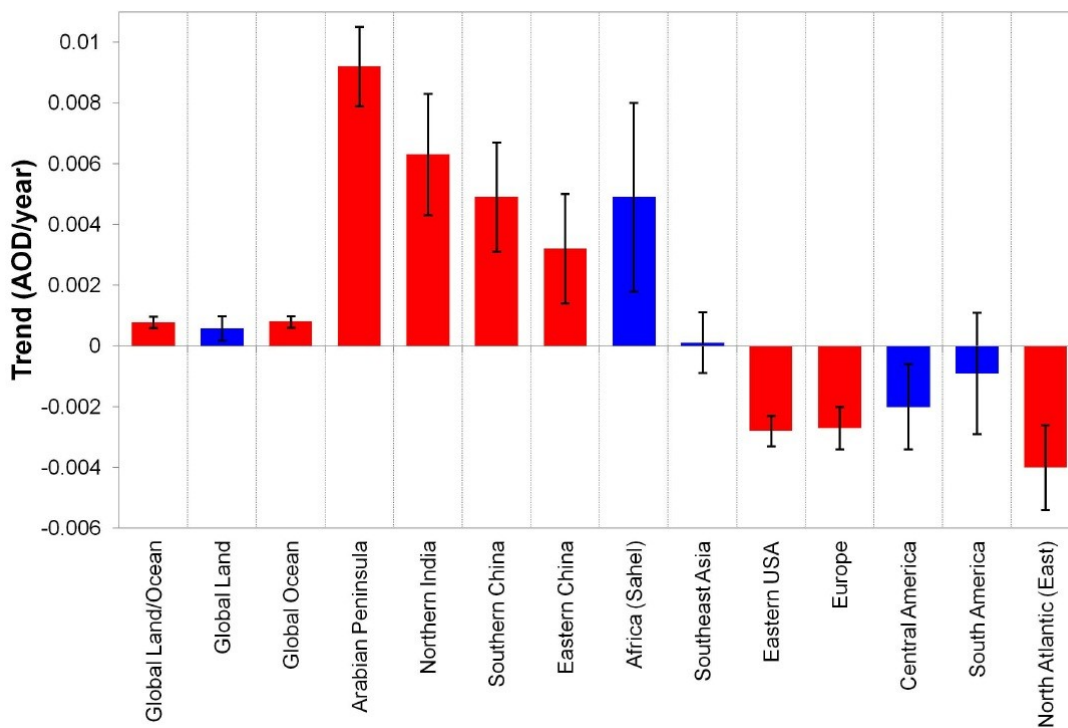


Figure 1.6: Annual trends based on deseasonalised monthly anomalies of 550nm SeaWiFS AOD during January 1998-December 2010. Red bars represent regions with statistically significant AOD (exceeding 90% confidence) from Hsu et al. (2012).

1.4 Asian Outflow and Long Range Transport

Dust and pollution outflow from Asia has been documented to have a pronounced impact on the atmospheric composition over the Pacific Ocean (Andreae et al., 1988; Perry et al., 1999). Asian outflow events occur in both the marine boundary layer and free troposphere via different meteorological mechanisms as summarized in Figure (1.7). In the marine boundary layer, outflow is related to the Asian monsoonal cycle, as an anticyclone develops over the continent and a cyclone develops over the northern Pacific Ocean after the summer monsoon season (Zahorowski, 2005). Boundary layer outflow events of this nature that affect the lower troposphere are typically associated with cold fronts in the source region (Liang et al., 2004) and most frequently occur in the mid-latitudes, between 30-45° N (Liu et al., 2003). Synoptic features associated with this seasonal change often result in an outflow of Asian gases and aerosols into the Pacific Basin, however, this process is relatively slow compared to free tropospheric outflow (Zahorowski, 2005).

Upper level outflow is facilitated by the jet stream associated with the Pacific storm track (Merrill et al., 1989). Throughout the year the position of the jet stream shifts such that the latitude band of efficient transport can vary anywhere from 20° N to 50° N (Talbot et al., 1997). During late winter and early spring, a combination of meteorological factors results in the most favorable environment for Asian pollution outflow in the free troposphere (Zahorowski, 2005). During this season, frontal activity over Asia are frequent and westerly winds are strongest, creating favorable conditions for transport into the Pacific (Balkanski et al., 1992). Free tropospheric outflow associated with cold frontal passage most frequently occurs between 20-35° N and an altitude of 2-6 km (Liu et al., 2003) although there is a northward shift in outflow during the summer (Liang et al., 2004). During the spring, lifting of air to the free troposphere

along the warm conveyor belt ahead of cold fronts accounts for 78% of long-range transport events that reach the middle and upper troposphere over the Northeastern Pacific, although during the summer, convective activity serves as an equally important export mechanism (Liang et al., 2004). Outflow events associated with cold fronts in the source region can occur every 5-8 days during the springtime (Heald et al., 2003)

Anthropogenic Asian outflow from 1000-200 hPa along the 150° E cross-section was shown by Liu et al. (2003) to be at a maximum during late winter and early spring, a minimum during summer, and increasing during autumn to repeat the seasonal cycle, as shown in Figure (1.8). Many studies have documented episodic transport events of dust aerosols (e.g. VanCuren and Cahill, 2002), gaseous carbon monoxide and ozone (e.g. Yienger et al., 2000), and anthropogenic aerosols (e.g. Jaffe et al., 1999) using observations at sites across the Pacific Ocean and along the western coast of the United States. Additional information gained from global chemical transport models and satellite observations have improved understanding of long range pollution transport from East Asian sources to North America. Heald et al. (2003) traced an Asian pollution outflow event during the spring of 2001 which split into a northern and southern branch, indicating two different pathways of pollution transport across the Pacific. Despite an identical source region, these two branches of outflow exhibited chemical differences partially due to the photochemistry enhanced by higher levels of solar radiation encountered along the southern transport branch (Heald et al., 2003). Such studies indicate that the occurrence of transpacific pollution transport is simultaneously dependent on meteorological conditions surrounding the Asian source region, across the Pacific transport corridor, and surrounding the receptor location of interest.

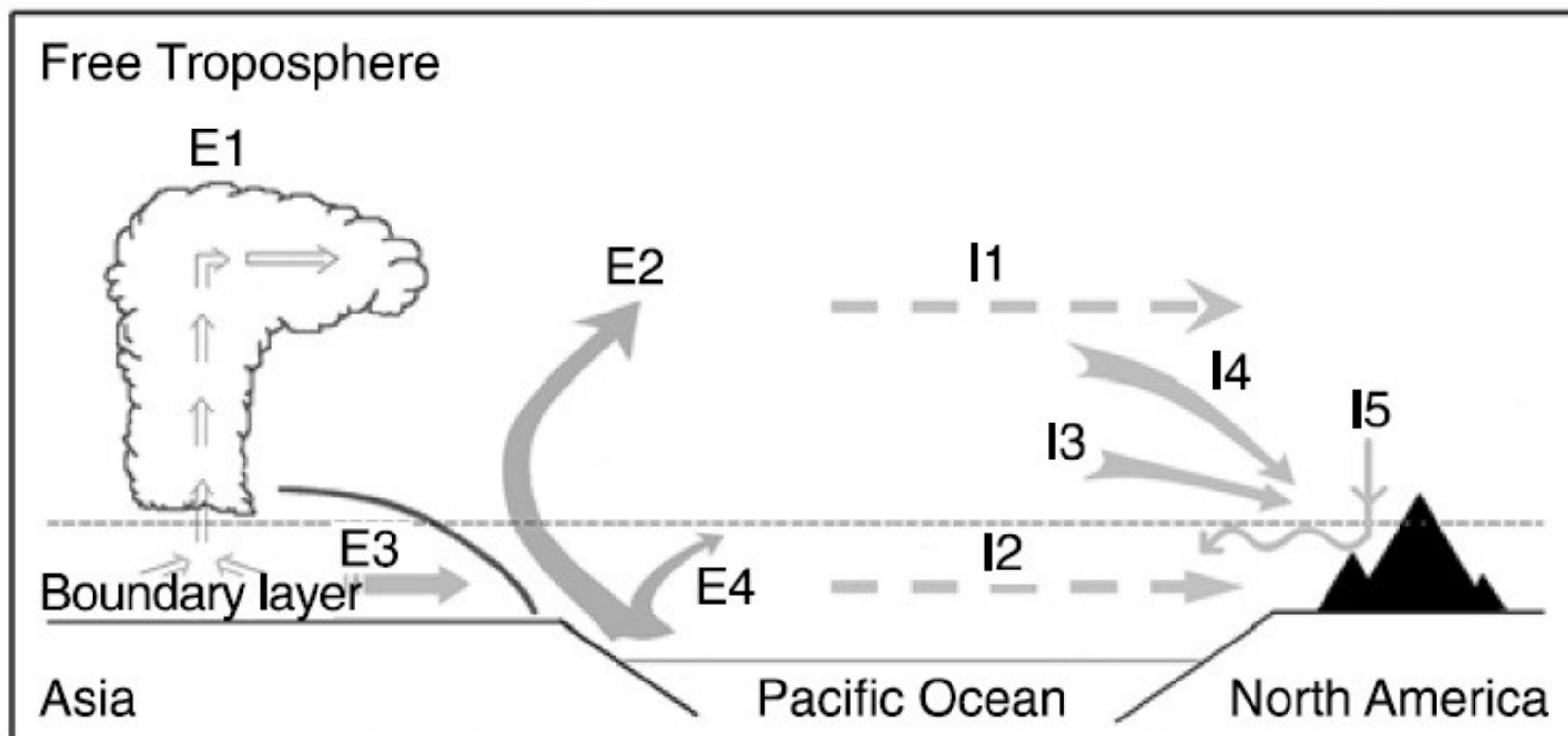


Figure 1.7: Mechanisms for long range transport of Asian pollutants across the Pacific Ocean from Liang et al. (2004). Export mechanisms include convective lifting (E1), warm conveyor belt lifting (E2), postfrontal boundary layer transport (E3), and low-level prefrontal jet transport (E4). Import mechanisms include advection into the mean free tropospheric westerly flow (I1), boundary layer transport (I2), large-scale subsidence in the Pacific High (I3), subsidence into the dry air stream of a cold front (I4), and subsidence induced by mountain waves (I5).

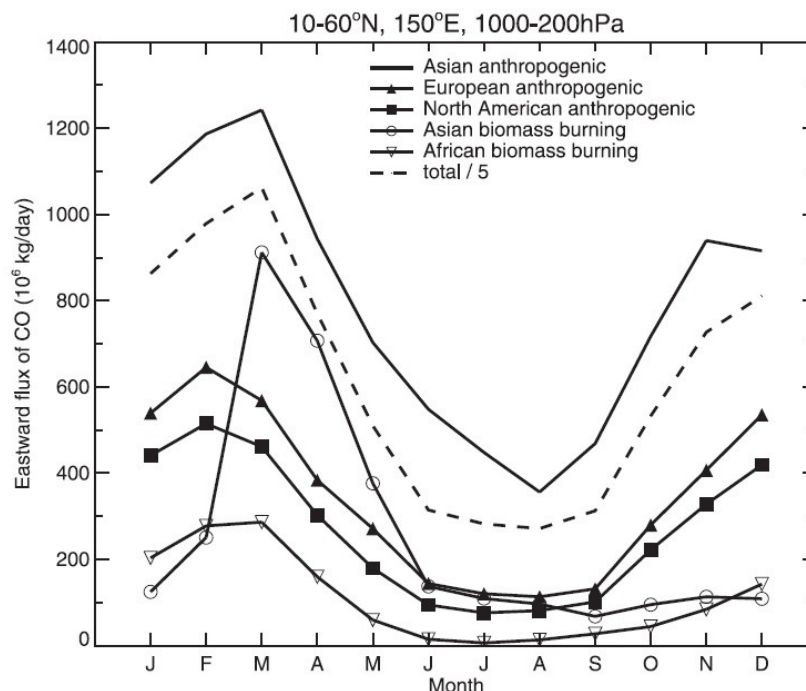


Figure 1.8: Seasonal cycle of contribution from different sources to Asian outflow during 1996. Asian outflow defined as Eastward CO flux (10^6 kg day^{-1}) along 150°E between $10\text{--}60^\circ\text{N}$ and integrated over the $1000\text{--}200 \text{ hPa}$ column during 1996 from Liu et al. (2003).

1.5 Mauna Loa Observatory

Located in the remote central Pacific Ocean, Mauna Loa Observatory (MLO) is an ideal and unique measurement site for ground-based, free tropospheric observations and is conveniently situated to observe the winter-spring outflow events from East Asia (Zahorowski, 2005). MLO is located on the Northern flank of Mauna Loa Volcano (19.54°N , 155.58°W , and 3397m ASL) as shown in Figure (1.9). The isolated island location was selected for this study in order to minimize local anthropogenic influences on observed sulfate concentrations and provides an excellent environment to study source-receptor relationships of pollutants in the free troposphere at long distances.

Trend analyses for determining changes in atmospheric composition are dependent on reliable observations acquired over a long time period (Hand et al., 2012b). The consistent

datasets available from MLO over the last 50 years have motivated many studies of long-term trends in atmospheric variables. The monitoring site has become an especially famous research station for its critical role in documenting the substantial increase in concentrations of carbon dioxide (CO₂) and other greenhouse gases over the last century (Keeling et al. 1976). However, in comparison to gas and dust transport, less work has been focused on understanding anthropogenic particulate matter (PM) transport to MLO. Understanding variations in PM concentrations that arrive at MLO after long range transport is more difficult than for greenhouse gases because PM is shorter lived, due to settling and washout during transport, and is thus less well mixed in the atmosphere. Further, aerosol-phase sulfate is a secondary pollutant, not directly emitted but rather formed in the atmosphere from a combination of sources and chemical transformation pathways.

Aerosol measurements from MLO contributed to the realization that soil dust originating in Asia could be transported extremely long distances downwind (Duce 1980, Parrington et al. 1983). Episodes of Asian dust transport to MLO have been well documented (e.g., Perry et al, 1999) and are found to occur most frequently during springtime due to the favorable meteorological conditions in the source region which allow for lofting out of the boundary layer, and dominant synoptic patterns which allow for fast transport in the free troposphere across the Pacific Ocean. Perry et al. (1999) pointed out that anthropogenic aerosol can also be transported to MLO, either with dust aerosol or in separate events. Figure (1.10) shows the observed seasonal cycle of fine sulfate at MLO during 1993-1996 from Perry et al. (1999). The peak in sulfate concentrations observed during March, April, and May suggests that anthropogenic influence alters the seasonal cycle at MLO from what would otherwise be expected from natural sources at a remote island location (Perry et al., 1999). Figure (1.11) from Liang et al. (2004)

shows the seasonal cycle of carbon monoxide concentrations at MLO during 2001 modeled using GEOS-CHEM and the associated contributions to total carbon monoxide from North America, Europe, Asia, and the oxidation of other species. The peak in Asian contribution to carbon monoxide at MLO also occurs during March, further suggesting that elevated springtime sulfate concentrations at MLO are a result of long range transport from the Asian continent.

Hawaii is located near the northern portion of the Hadley cell with warm air rising near the equator and subsiding near 30° N resulting in poleward motion of air aloft and equatorward motion of air in the boundary layer (Figure 1.12). This general circulation pattern results in northeasterly trade wind flow in the Northern Hemisphere tropics (Sanderson et al., 1993). Figure (1.12a) shows this circulation pattern in the central Atlantic Ocean which is analogous to the circulation in the central Pacific impacting Hawaii. Figure (1.12b) shows a cross-section of the resulting trade wind inversion feature which occurs as a result of northerly flow from cooler temperatures towards warmer temperatures. This cross-section shows boundary layer flow from northeast (right) towards southwest (left) with rising motion near the equator and subsiding motion at higher latitudes. As air near the northeast portion of this cross-section subsides, it warms via adiabatic compression and reaches a higher temperature than the cool air near the surface. This creates a very persistent inversion with dry stable conditions at higher altitudes. The mean height of the trade wind inversion above the island of Hawaii is approximately 2km, well below the height of MLO (Sanderson et al., 1993). The combination of downslope flow and elevation above the trade wind inversion typically result in very low aerosol concentrations at MLO during nighttime, ideal for minimizing local impacts and thus for detecting influence from long distance sources (Perry et al., 1999).

The unique combination of synoptic flow patterns surrounding MLO further motivated research on measurements taken at this location. MLO is located along the boundary of easterly trade winds in the tropics and westerly flow in the mid-latitudes. The latitude at which this flow reversal occurs varies, so that MLO has the potential to be impacted by Asian source regions during certain times of year and by North or Central American sources during other times of year (Huebert et al., 2001). MLO is largely influenced by transport from Eurasia during the Northern Hemisphere cold season and by transport from North America during the Northern Hemisphere warm season (Buermann et al., 2006). This seasonal shift is related to a deepening of the Aleutian Low located near Alaska which strengthens zonal flow across the Pacific along the midlatitudes during the cold season, and to the strong high-pressure system located to the northeast of MLO over the sub-tropical Pacific Ocean, which favors transport from the North American continent (Buermann et al., 2006). Understanding what factors control the characteristics of aerosols at MLO during times when each transport pathway is dominant, would provide valuable additional documentation of the evolution of aerosol characteristics during long-range transport, as well as providing insights into additional pathways for pollution impacts on the continental United States from distant sources.

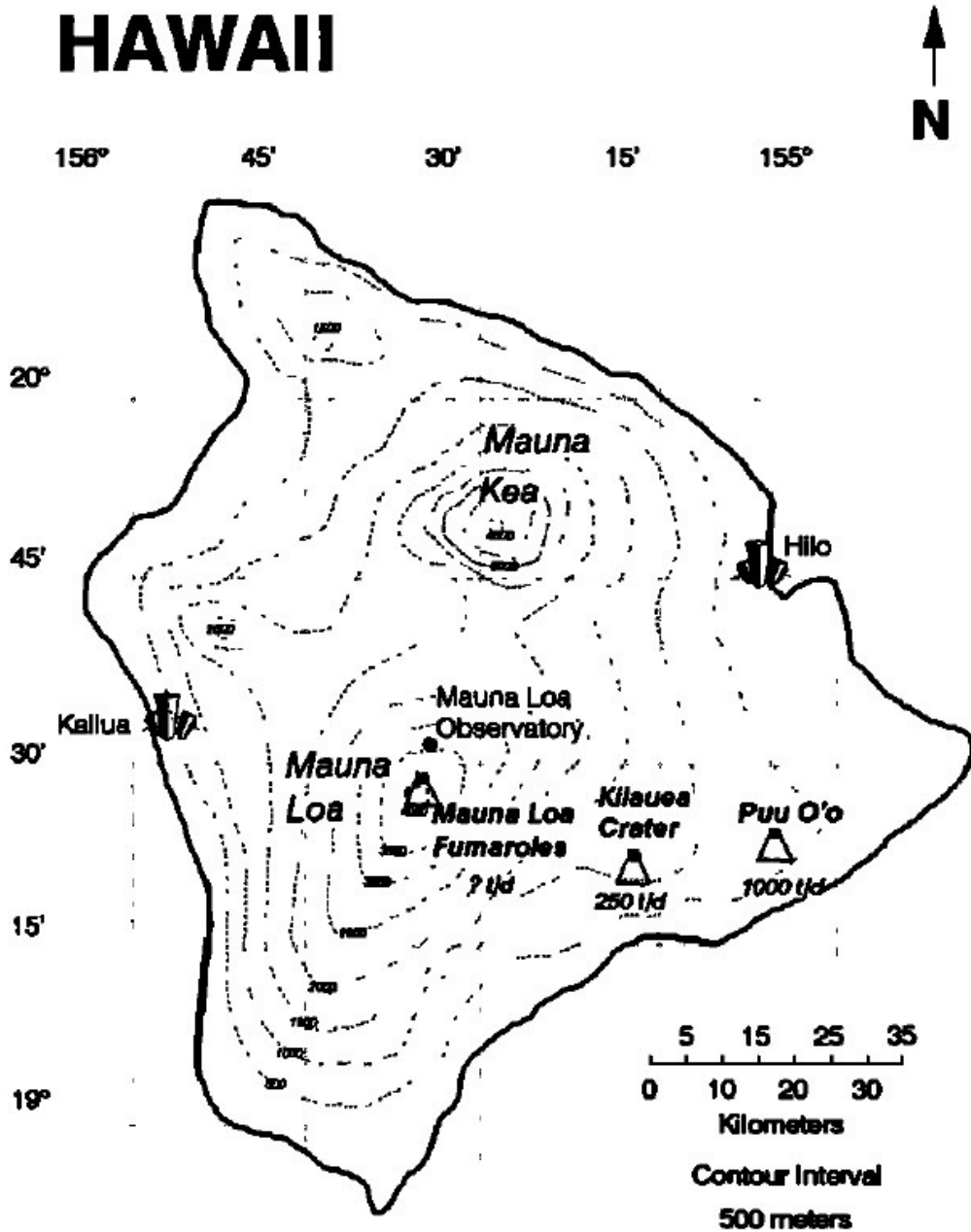


Figure 1.9: Topographic map of the Island of Hawaii including Mauna Loa Observatory, Kilauea Volcano Crater (summit), Puu O'o (East Rift) from Luria et al. (1992).

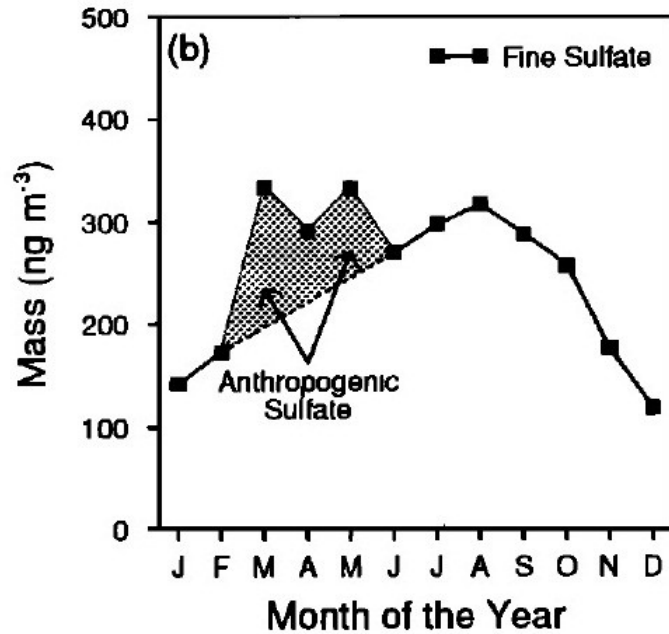


Figure 1.10: Observed seasonal cycle of fine mode sulfate aerosol at MLO 1993-1996 from Perry et al. (1999).

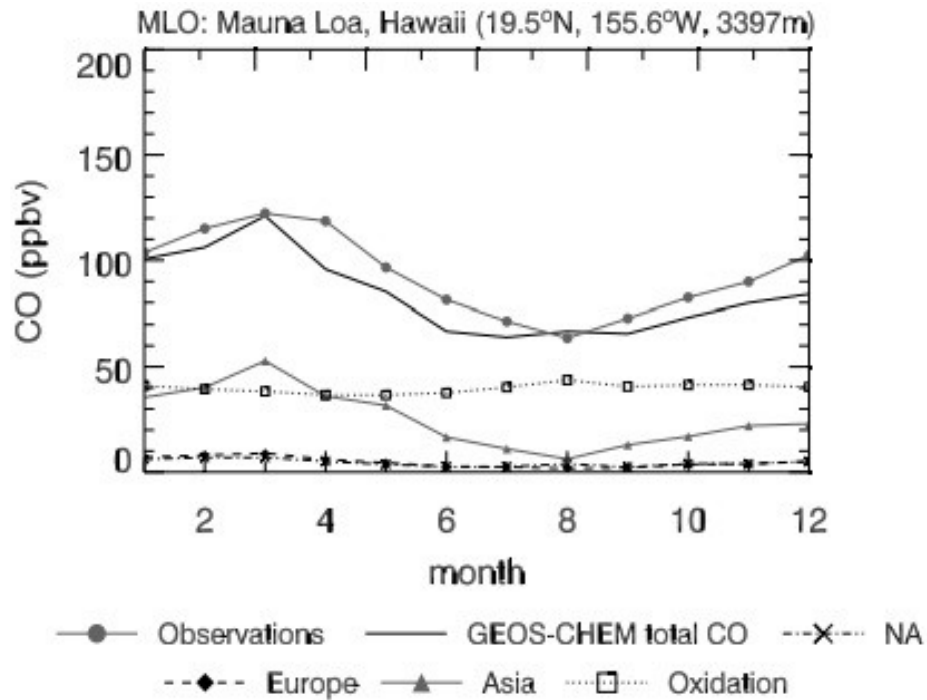


Figure 1.11: Observed and GEOS-CHEM model predicted carbon monoxide concentrations at MLO during 2001 from Liang et al. (2004). Contributions to total CO from North America, Europe, Asia, and oxidation of CO and biogenic volatile organic compounds are also shown.

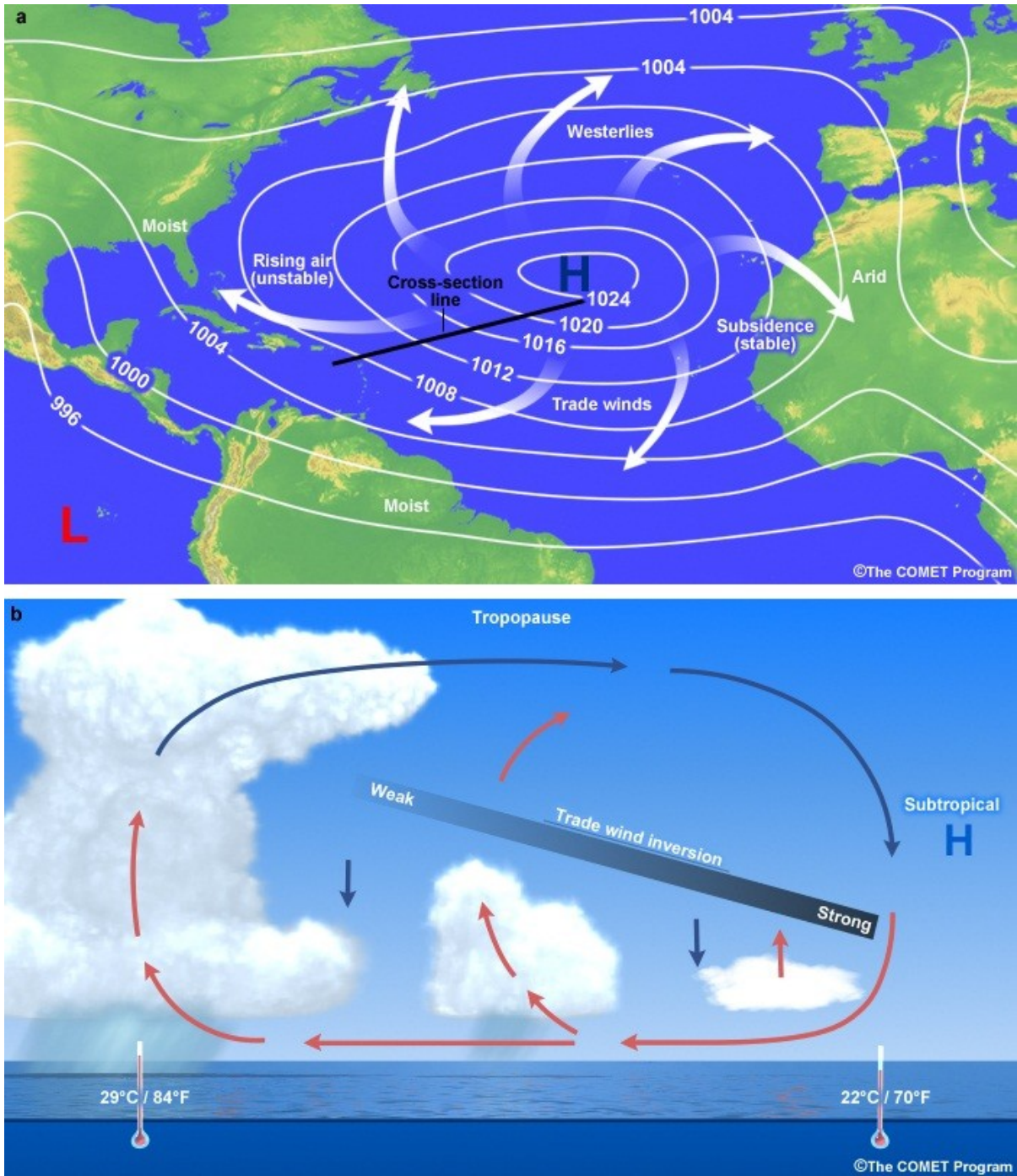


Figure 1.12: Cross-section of trade wind circulation from northeast (right) to southwest (left) from the COMET® Website at (<http://meted.ucar.edu/>) ©1997-2011, University Corporation for Atmospheric Research. All Rights Reserved.

1.6 Natural Sources of Sulfate Aerosol at MLO

The atmospheric SO₂ burden over Hawaii is influenced by both anthropogenic and natural sources although the relative source contributions vary significantly throughout time (Benkovitz et al., 2006). Table (1.2) summarizes the sources of non-sea-salt sulfate at MLO as simulated using the European Center/Hamburg Model (ECHAM4) (Huebert et al., 2001). To isolate the influence of rising anthropogenic emissions on sulfate aerosol concentrations at MLO, the natural contributions to atmospheric sulfate must be quantified and separated before making such comparisons.

Table 1.2: Sources of non-sea-salt sulfate at MLO from Huebert et al. (2001).

Sources	NSS, pmol mol ⁻¹
Natural	
Volcanoes	38
DMS	17
Anthropogenic	
Aircraft	0.48
United States and Canada	5.3
Europe	5.2
East Asia (90°–150°E, 10°–50°N)	43
Other	25
Total	134

1.6.1 Sea Salt

Although not included in Table (1.2), oceanic sea salt contributes 30-75% of total natural aerosol production (Ma et al., 2008). Sea salt aerosol emission rates are typically correlated with wind speeds along the ocean surface as sea spray drops are mechanically produced from the breaking of waves and are emitted directly to the atmosphere, primarily in the coarse mode of the

aerosol size distribution ($>2 \mu\text{m}$ in diameter) (Jacobson, 2002). About 96.8% of sea spray mass is water while 3.2% is salt (Jacobson, 2002). Six major ions typically compose over 99% of the dissolved salt mass in seawater as listed in Table (1.3) and mass ratios between these ions are usually assumed to be constant regardless of salinity (DOE, 1994). From these ratios, the mass of observed sulfate (and other species) attributed to sea salt aerosol can be calculated based on observed concentrations of other ions known to be dominated by oceanic sources. The remaining portion of a given species after subtracting the sea salt contribution is referred to as the non-sea-salt (NSS) portion.

Sea salt particles contribute a very small fraction of total particulate mass in highly polluted continental regions, but contribute a much larger mass fraction in remote regions, particularly in the Southern Hemisphere mid-latitudes (Ma et al., 2008). Typical sea-salt emission rates in the Northern Hemisphere are shown in Figure (1.13) from Chin et al. (2004). Northern Hemisphere emissions of sea-salt aerosols are largest from oceanic regions along the mid-latitudes (approximately 30°N - 60°N) although relatively high sea-salt emissions also occur in eastern portions of the tropical Pacific Ocean. Sea salt emissions are found to vary seasonally, with higher emissions in the Northern Hemisphere during winter and in the Southern Hemisphere during summer due to wind speed variations (Ma et al., 2008). Meteorological stability and convective activity can alter the vertical distribution of sea salt particles although aircraft observations have generally shown decreasing sea salt particle concentrations with altitude, as expected for a surface source (Reid et al. 2001).

Table 1.3: Sea water ionic composition and sodium mass ratios from University of Hawaii at Manoa School of Ocean and Earth Science and Technology (2012).

Mean Composition of Major Ions in Seawater		
Component	Mass Fraction	Mass Ratio to Na⁺
Chloride (Cl ⁻)	0.553	1.80
Sodium (Na ⁺)	0.307	1.00
Sulfate (SO ₄ ²⁻)	0.077	0.252
Magnesium (Mg ²⁺)	0.0369	0.120
Calcium (Ca ²⁺)	0.0117	0.0383
Potassium (K ⁺)	0.0113	0.0371

Data from University of Hawaii at Manoa (2012)

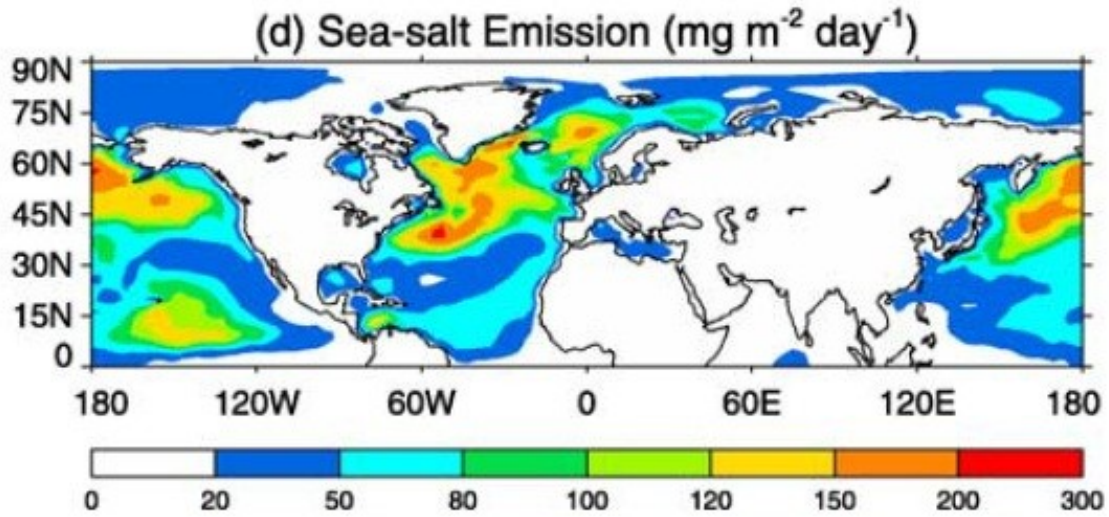


Figure 1.13: April 2001 sea-salt emission used in the GOCART model from Chin et al. (2004).

1.6.2 Biogenic

Marine phytoplankton are known to produce the compound dimethylsulphoniopropionate (DMSP) during biological activity which is subsequently processed by algae or bacteria to produce gaseous dimethylsulfide (DMS) (Gondwe et al., 2003). Dimethylsulfide (DMS) is believed to be the largest source of natural source of atmospheric sulfur although a robust understanding of the relationships between DMS and its oxidation products has yet to be fully established (Faloona et al., 2009). A majority of the DMS remains in the ocean where it is either consumed or oxidized. However, a small portion of the total oceanic DMS is released into the atmospheric marine boundary layer where its conversion to sulfur containing aerosol particles has important implications for air quality and global radiation balance (Gondwe et al., 2003). Model simulated DMS emissions are largest in the southern hemisphere as seen in Figure (1.14) from Korhonen et al. (2008) although large DMS fluxes are also predicted in portions of the equatorial Pacific Ocean and along certain coastal regions in the Northern Hemisphere. DMS emissions to the atmosphere cannot be precisely measured, but are derived from sea-surface DMS concentrations and approximations of the ocean-atmosphere exchange rate, for which the uncertainty is often as high as 50% (Kloster et al., 2006).

After DMS is emitted into the atmosphere, multiple possible oxidation pathways exist as summarized in Figure (1.15) from Gondwe et al (2003). Atmospheric DMS can undergo gas phase oxidation by either the hydroxyl radical (OH) during daytime or nitrogen dioxide (NO_3) during nighttime to produce SO_2 (and subsequently sulfate), or it can also be oxidized by OH to produce aerosol methanesulfonate (MSA), the anion of methanesulfonic acid (Gondwe et al., 2003). Because DMS is the only known source of MSA, the fraction of DMS which follows the oxidation pathway to form MSA as opposed to the pathway to form SO_2 can be utilized to

calculate the fraction of sulfate expected to originate from biogenic sources using observations of MSA. However this fraction is highly temperature dependent and therefore varies with both latitude and altitude (Saltzman et al., 1986).

Figure (1.16) shows the modeled percentage of annual mean global column MSA (a), SO₂ (b), and NSS-sulfate (c) atmospheric burdens which were attributed to oceanic DMS emissions, as opposed to any other natural or anthropogenic sources (Gondwe et al., 2003). Over the Northern Hemisphere Pacific Ocean, DMS emissions are estimated to contribute less than 20% of NSS-sulfate in this same region (Gondwe et al., 2003). Model results listed in Table (1.2) suggest that DMS contributes about 12% of total NSS-sulfate at MLO (Huebert et al., 2001). Globally, MSA peaks in the boreal winter months while NSS-sulfate peaks during the boreal summer months. Winter DMS emissions are largest in the tropics while summer DMS emissions are strongest in the southern hemisphere (Bates et al., 1992). A very strong north-south gradient is observed in DMS emissions and its total contribution to atmospheric concentrations of SO₂ and NSS-sulfate.

DMS emissions and the preferential oxidation mechanism to produce either MSA or SO₂ are of high importance to understanding the earth's radiation balance and implications for climate. The CLAW hypothesis, first introduced by Charlson et al. (1987), suggested that the biological activity responsible for DMS production plays a critical role in regulating the climate system through a negative feedback loop. The hypothesis asserts that warming of ocean surface temperature enhances phytoplankton activity and DMS production. The enhanced activity would in turn increase DMS-derived SO₂ and sulfate aerosol available to serve as cloud condensation nuclei (CCN). With increased CCN production, cloud albedo increases, decreasing the amount of incoming solar radiation to reach the surface, generating a cooling effect (Ayers and Cainey,

2007). Certain aspects of this proposed feedback loop have been supported by empirical evidence although more recently, Quinn and Bates (2011) suggested that the CLAW hypothesis is too simplistic to be fully representative of the real climate system and did not consider that DMS-derived sulfate aerosols serving as CCN are often transported long distances in the free troposphere, potentially separating regions of high DMS emissions and regions dominated by DMS-derived CCN. This study provided evidence that although DMS emissions can be an important source of sulfate aerosol, the relationship between oceanic emissions and climate is more complex than originally proposed by the CLAW hypothesis (Figure (1.16)).

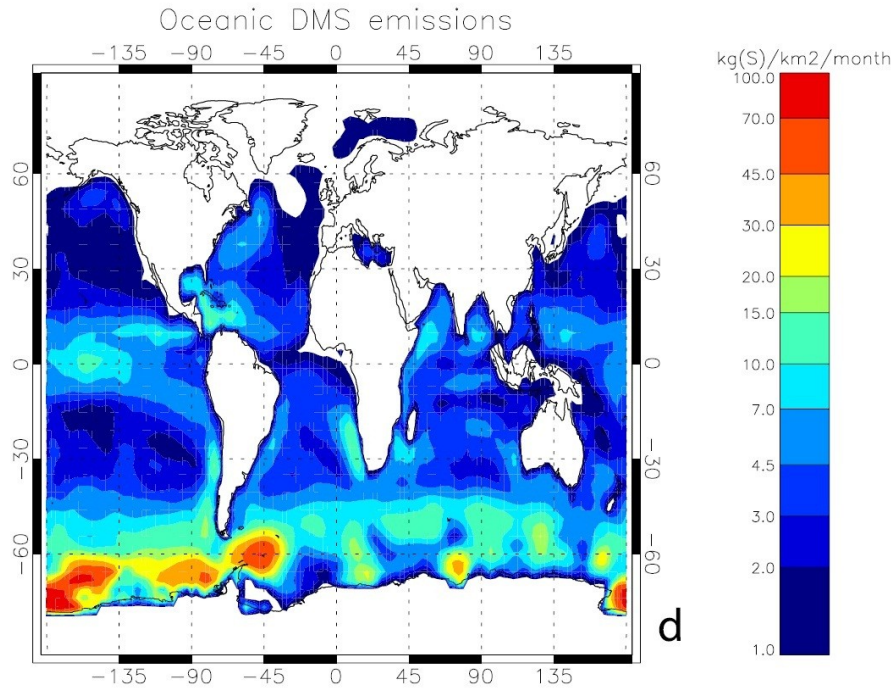


Figure 1.14: Simulated monthly oceanic DMS emissions during January 2000 from Korhonen et al. (2008).

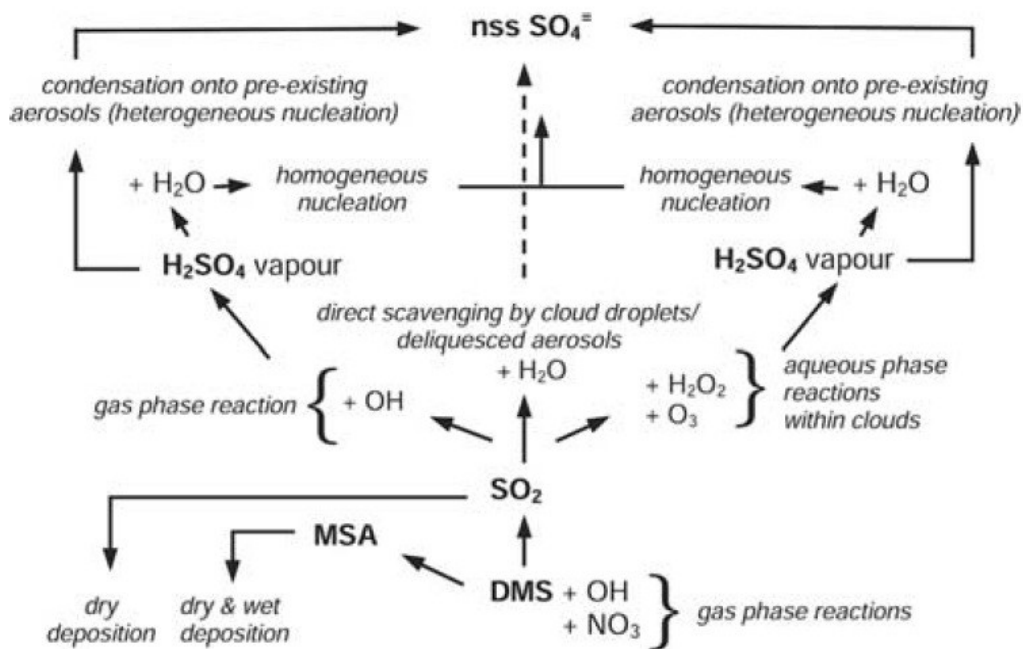


Figure 1.15: Simplified pathways of DMS oxidation and sulfate aerosol formation from Gondwe et al. (2003).

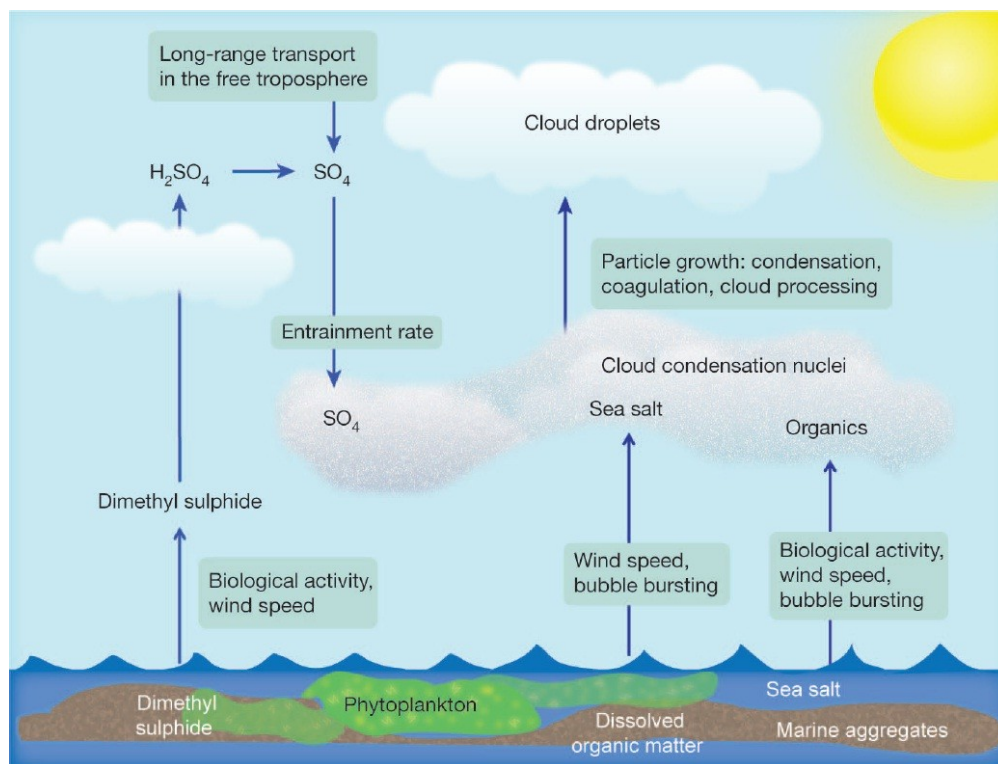


Figure 1.16: Important sources and production mechanisms for cloud condensation nuclei in the remote marine atmosphere from Quinn and Bates (2011).

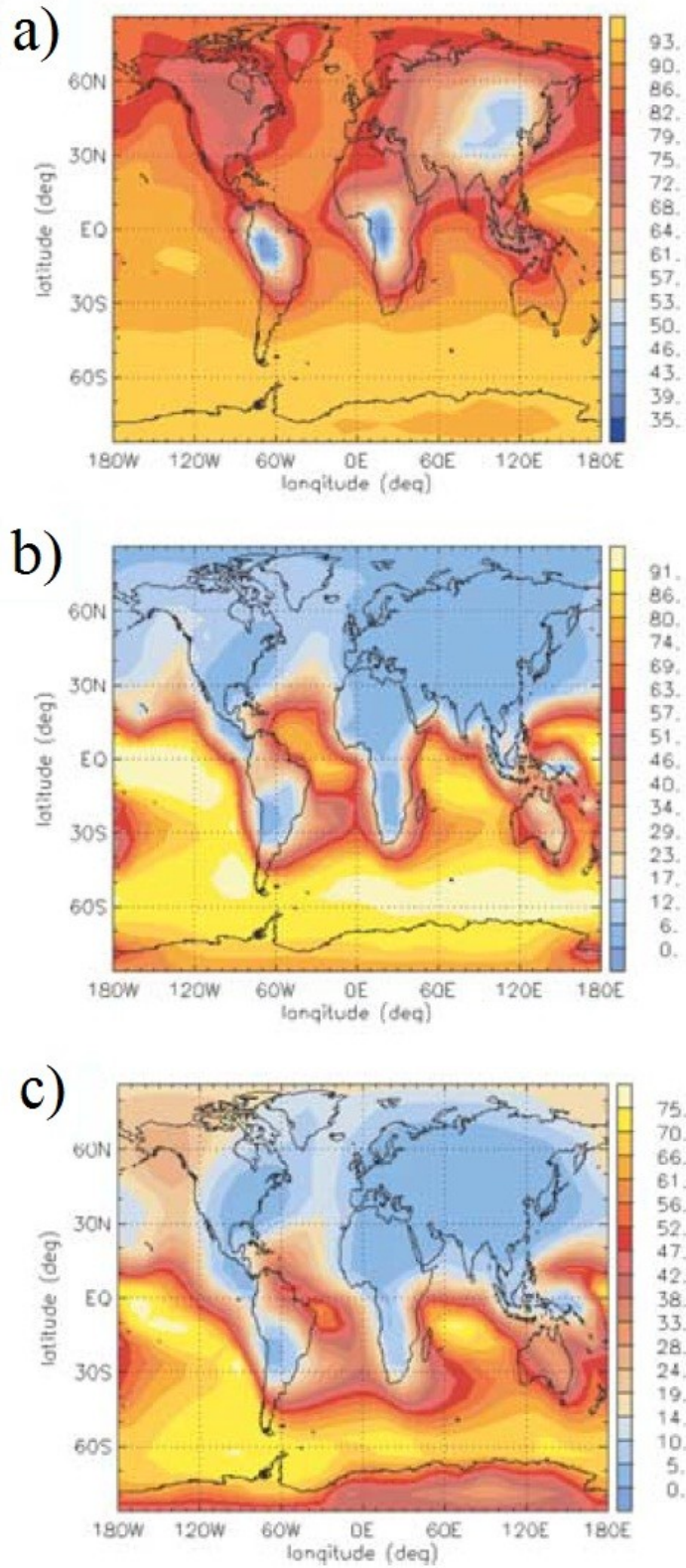


Figure 1.17: Modeled percentage of the annual mean column burden of MSA (a), SO₂ (b), and NSS-sulfate (c) that can be attributed to oceanic DMS emissions from Gondwe et al. (2003).

1.6.3 Volcanic

Unlike DMS, which is emitted in small amounts over widespread portions of the globe, volcanic emissions can be very large sulfur sources which are isolated to specific regions, primarily located along tectonic plate lines (Bates et al., 1992). The global distribution of volcanoes is shown in Figure (1.18). A majority of the planet's volcanoes (66%) are located in the Northern Hemisphere while less than 18% are located further south than 10°S (Bates et al., 1992). In general, sulfur emissions from volcanoes contribute a larger fraction of total emissions in the tropics and arctic regions where anthropogenic contributions are smaller, although the contribution remains non-negligible in the Northern Hemisphere mid-latitudes (Bates et al., 1991). SO₂ is the most abundant sulfur species emitted by volcanoes; primary sulfate aerosol emissions account for less than 1% of volcanic sulfur emissions (Bates et al., 1992). Globally, volcanic emissions are estimated to account for 4-9% of total SO₂ emissions as estimated by Chin et al. (2000) and Berglen et al. (2004).

SO₂ can be emitted to the troposphere by active eruptions and degassing of volcanoes and directly to the stratosphere during very explosive eruptions (Bates et al., 1992). SO₂ emitted during volcanic eruptions often has an extended lifetime when injected into the upper troposphere or lower stratosphere as opposed to anthropogenic emissions which are typically released closer to the surface (Andres and Kasgnoc, 1998). Volcanic sulfur emissions from major eruptions such as El Chichón (March 1982) or Pinatubo (June 1991) can be so substantial that the increased aerosol loading, particularly when injected into the stratosphere, perturbs the entire Earth's radiative balance for approximately 2 years following the eruption (Stenchikov et al., 1998). Evidence of these climate perturbations can be observed in historical surface temperature and precipitation data records (Trenberth and Dai, 2007). The temporary cooling of

surface temperatures observed after volcanic eruptions has been used as motivation for climate geoengineering strategies that would mimic a natural volcanic eruption to counteract a portion of the warming associated with anthropogenic climate change as a result of increasing greenhouse gas concentrations (Trenberth and Dai, 2007). Quantifying the contribution of volcanic emissions to atmospheric sulfate aerosol concentrations and subsequent impacts on the climate system is an important research area although the sporadic nature of volcanic activity generates difficulties in quantifying emissions estimates associated with volcanic SO₂ (Bates et al., 1992).

As shown in Table (1.2), the contribution of volcanic emissions to total NSS-sulfate at MLO was estimated to be approximately 28% by Huebert et al. (2001) although this contribution is highly dependent on current volcanic activity. Mauna Loa remains an active volcano although the last eruptive activity occurred in 1984 (Sanderson et al., 1993). Kilauea Volcano (1222m ASL) is located in Hawaii Volcanoes National Park to the southeast of Mauna Loa. Figure (1.9) shows the location and elevation of Kilauea Volcano in relation to Mauna Loa Observatory. Kilauea Volcano has been continuously erupting along the East Rift Zone since 1983. In March 2008, a new summit vent opened along the wall of the Halema'uma'u crater near the Kilauea summit and the first explosive activity since 1924 occurred during which both East Rift and Summit emissions increased significantly (Elias and Sutton, 2012).

During prevailing trade wind conditions, the volcanic plume is transported from Kilauea towards the southwest and wrapping around the island, although its vertical extent is generally capped by the trade wind inversion below the elevation of MLO (Longo et al., 2005). Figure (1.19) shows SO₂ and fine aerosol (<0.3 um diameter) concentrations around the southern side of Mauna Loa observed during August and September 2003 (Longo et al., 2005). SO₂ from Kilauea decreased with height as it flowed around Mauna Loa but aerosol concentrations

exhibited the opposite effect as secondary formation occurred during transport (Longo et al., 2005). Although MLO is located at a much higher elevation than Kilauea, it can be influenced by these volcanic SO₂ emissions under certain conditions. Luria et al. (1992) reported that elevated SO₂ concentrations at MLO peaked during daytime upslope conditions, and most frequently between October and January. A total of 24 elevated SO₂ concentration events were observed at MLO during nighttime downslope conditions over the 12 month period although 18 of these events were also accompanied with elevated carbon dioxide concentrations (Luria et al., 1992).

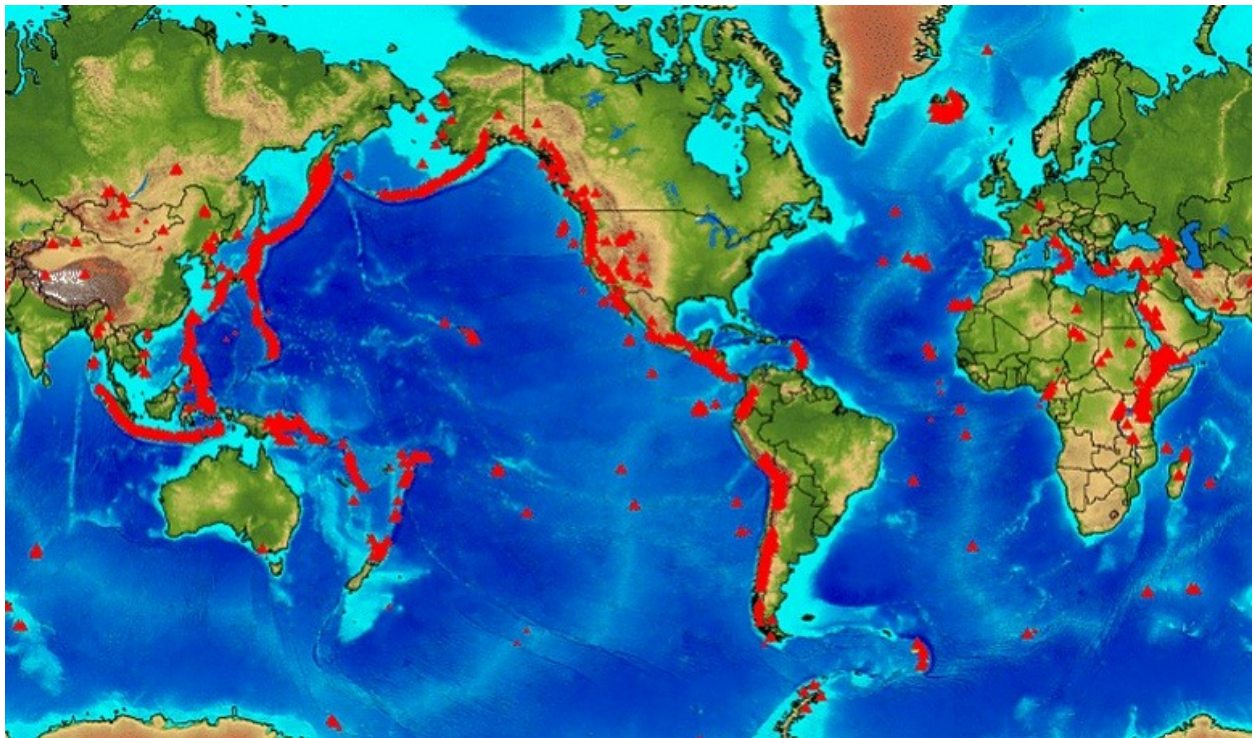


Figure 1.18: Global distribution of volcanoes from Siebert and Simkin (2002-)

1.7 Oxidation of Atmospheric Sulfur Dioxide to Sulfate Aerosol

Atmospheric SO₂ of anthropogenic, biogenic, and volcanic sources can follow a number of different oxidation pathways resulting in formation of sulfate aerosol, and it also can be removed from the atmosphere directly by wet and dry deposition. A detailed investigation into atmospheric oxidation of sulfur dioxide to sulfate is beyond the scope of this research although characteristics of the oxidation pathways to produce aerosol sulfate were considered when analyzing meteorological variables of interest. Table (1.4) provides additional information about the relative importance of different processes controlling SO₂ removal and sulfate formation, as deduced from global chemistry models. Approximately 49% of atmospheric SO₂ is removed via either gas phase or aqueous phase oxidation processes to produce other sulfur species (Berglen et al., 2004). Sulfate aerosols are produced primarily by either gas phase oxidation of SO₂ by OH radicals or aqueous phase oxidation of SO₂ in cloud droplets by H₂O₂ and O₃.

Gas-phase oxidation of SO₂ is typically the most dominant mechanism when relative humidity is below 70 percent (Jacobson et al., 2002). This gas-phase oxidation mechanism involves the following basic steps as summarized by Jacobson (2002):

- Oxidation of SO₂ (g) by OH to form sulfuric acid (H₂SO₄ (g))
- Condensation of H₂SO₄ (g) and water vapor onto aerosol particles or cloud droplets to form a H₂SO₄ (aq)-H₂O (aq) solution
- Dissociation of H₂ SO₄ (aq) in the solution to form SO₄²⁻

Aqueous phase oxidation of SO₂ to SO₄²⁻ in clouds is much more rapid than gas phase oxidation which has implications for the overall lifetime of the sulfur species during transport (Khoder, 2002). The rates of aqueous phase reactions to form sulfate are positively correlated with ambient water content because of the dependence on the amount of liquid water available

for reaction (Saxena and Seigneur, 1987). The favored oxidant for conversion of SO_2 to sulfate is H_2O_2 when pH levels are less than 6 and O_3 when pH levels are greater than 6 (Jacobson, 2002). The typical aqueous phase mechanism involves the following steps as summarized by Jacobson (2002):

- Dissolution of SO_2 (g) into liquid water to produce SO_2 (aq)
- Conversion of SO_2 (aq) to H_2SO_3 (aq) and dissociation of H_2SO_3 (aq) to HSO_3^- and SO_3^{2-}
- Oxidation of HSO_3^- and SO_3^{2-} to SO_4^{2-}

Both gas phase and aqueous phase reactions are highly dependent on the availability of atmospheric oxidants, particularly OH and H_2O_2 . The relationship between SO_2 emissions and sulfate particle concentrations becomes less linear near very large sources of SO_2 because oxidant concentrations can become a limiting factor (Liu et al., 2008). The primary source of OH in the free troposphere is photolysis of ozone to produce atomic oxygen in an excited state and subsequent reaction of the excited atomic oxygen with water vapor (Jacobson, 2002). Therefore, atmospheric OH concentrations are dependent on both solar radiation and humidity. Zonally averaged cross-sections of model derived OH and H_2O_2 concentrations during both January and July are shown in Figure (1.20). OH concentrations are typically largest near the equator with strong north-south gradients. In the tropics, OH concentrations are largest in the middle troposphere with lower concentrations near the surface and in the upper troposphere (Andreae and Crutzen, 1997). There is a very strong seasonal cycle in Northern Hemisphere OH concentrations with high concentrations during July and low concentrations during January. The seasonal variability in Northern Hemisphere H_2O_2 is less drastic although much higher concentrations are seen at midlatitudes during July than during January.

Table 1.4: Sources and Sinks of sulfur species using 1996 emission inventories (Berglen et al., 2004)

Table 7. Calculated Budget (Sources and Sinks) for the Sulfur Species Using 1996 Emission Inventory in the Model

	Absolute Number of Sources and Sinks, Tg(S)	Percentage
<i>DMS</i>		
Oceanic emissions	11.95	
<i>Sinks</i>		
NO ₃ oxidation	3.27	27.4
OH oxidation (abstraction)	4.41	36.9
OH oxidation (addition)	4.27	35.7
Total sinks	11.95	
<i>SO₂</i>		
Anthropogenic emissions <100 m	29.04	32.3
Anthropogenic emissions >100 m	35.34	39.4
Ship emissions	3.41	3.8
Volcanic emissions	8.00	8.9
Biomass burning emissions	2.25	2.5
DMS oxidation	10.88	12.1
H ₂ S oxidation	0.88	1.0
Total sources	89.80	
<i>Sinks</i>		
Wet deposition (large scale)	0.21	0.2
Convection	0.20	0.2
Subcloud scavenging	1.16	1.3
Dry deposition	41.49	46.2
Oxidation by OH (gas)	7.94	8.8
Oxidation by O ₃ (aqueous)	5.80	6.5
Oxidation by H ₂ O ₂ (aqueous)	28.90	32.2
Oxidation by HO ₂ NO ₂ (aqueous)	1.60	1.8
Catalytic (metals)	2.41	2.7
Stratosphere	0.09	0.1
Total sinks	89.80	
<i>SO₄²⁻</i>		
Anthropogenic emissions <100 m	1.53	3.1
Anthropogenic emissions >100 m	1.86	3.7
SO ₂ oxidation	46.65	93.2
Total sources	50.04	
<i>Sinks</i>		
Wet deposition (large scale)	39.40	78.7
Convection	3.22	6.4
Subcloud scavenging	0.03	0.1
Dry deposition	7.39	14.8
Total sinks	50.04	

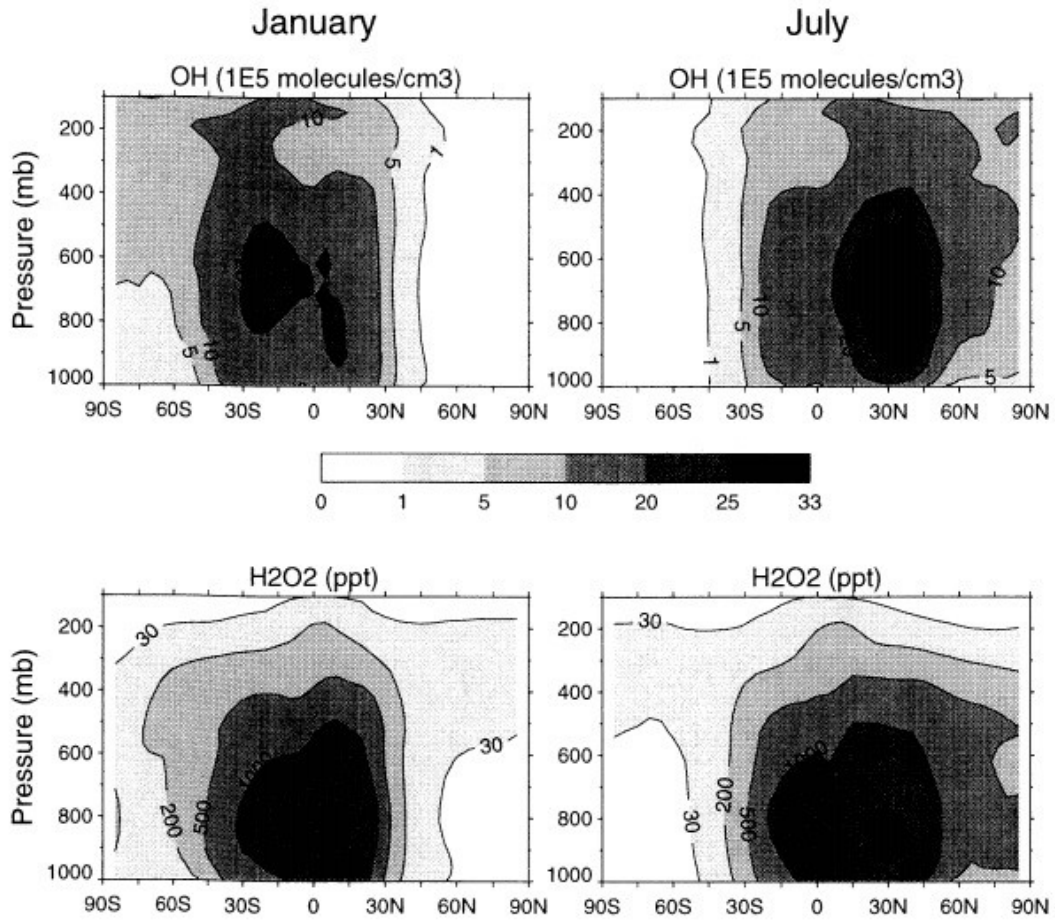


Figure 1.20: Global distribution of OH and H₂O₂ from Chin et al. (2000).

1.8 Research Questions Addressed

1.8.1 What are the natural and anthropogenic components of sulfate aerosol at MLO?

Prospero et al. (2003) examined aerosol concentrations of sulfate and nitrate at Midway Island (28°13'N, 177°22'W, sea-level) during 1981-2000. Anthropogenic sulfate concentrations were calculated using an assumed ratio of DMS oxidation products which is explained in more detail in Section (2.1.2). Figure (1.21) shows the seasonal cycle of natural, anthropogenic, and total sulfate at Midway Island during 1981-1990. Although Midway Island is located in the remote Pacific Ocean at approximately sea level while MLO is in the free troposphere, the work of Prospero et al. (2003) provided motivation for a similar analysis to estimate the relative contributions of anthropogenic and biogenic sources to observed sulfate aerosol at MLO. Separating these contributions allows for more appropriate comparisons with anthropogenic source region precursor emissions.

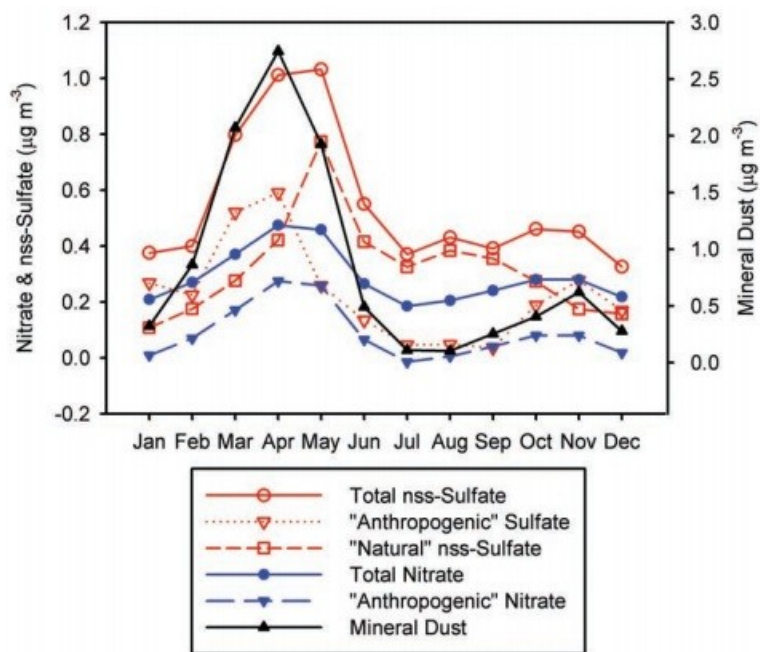


Figure 1.21: Seasonal cycle of natural and anthropogenic components of total NSS-sulfate at Midway Island (28°13'N, 177°22'W), nitrate, and mineral dust during 1981-1990 from Prospero et al. (2003).

1.8.2 Can we identify long distance continental influence at MLO?

In order to relate sulfate concentrations at MLO to SO₂ emission trends from continental sources, it is necessary to identify time periods when these regions are likely serving as a sources for observed sulfate at MLO. Figures (1.22) and (1.23) show examples of previous studies that have investigated the seasonal cycle of long distance continental influence at MLO using trajectory analysis, demonstrating frequent transport from the Asian continent during the winter and spring and from the American continent during the summer. This study applies HYSPLIT trajectory information as well as chemical tracer concentrations over a 14 year period in order to determine both the seasonal cycle and interannual variability of long distance continental influence on MLO and how this variability influences sulfate aerosol concentrations during the study period.

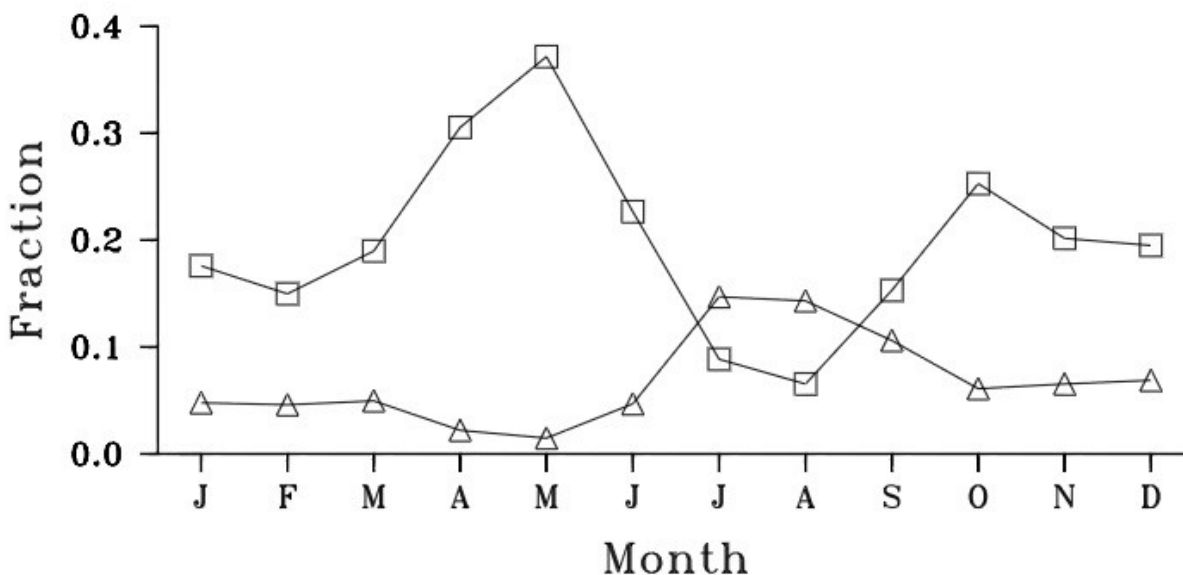
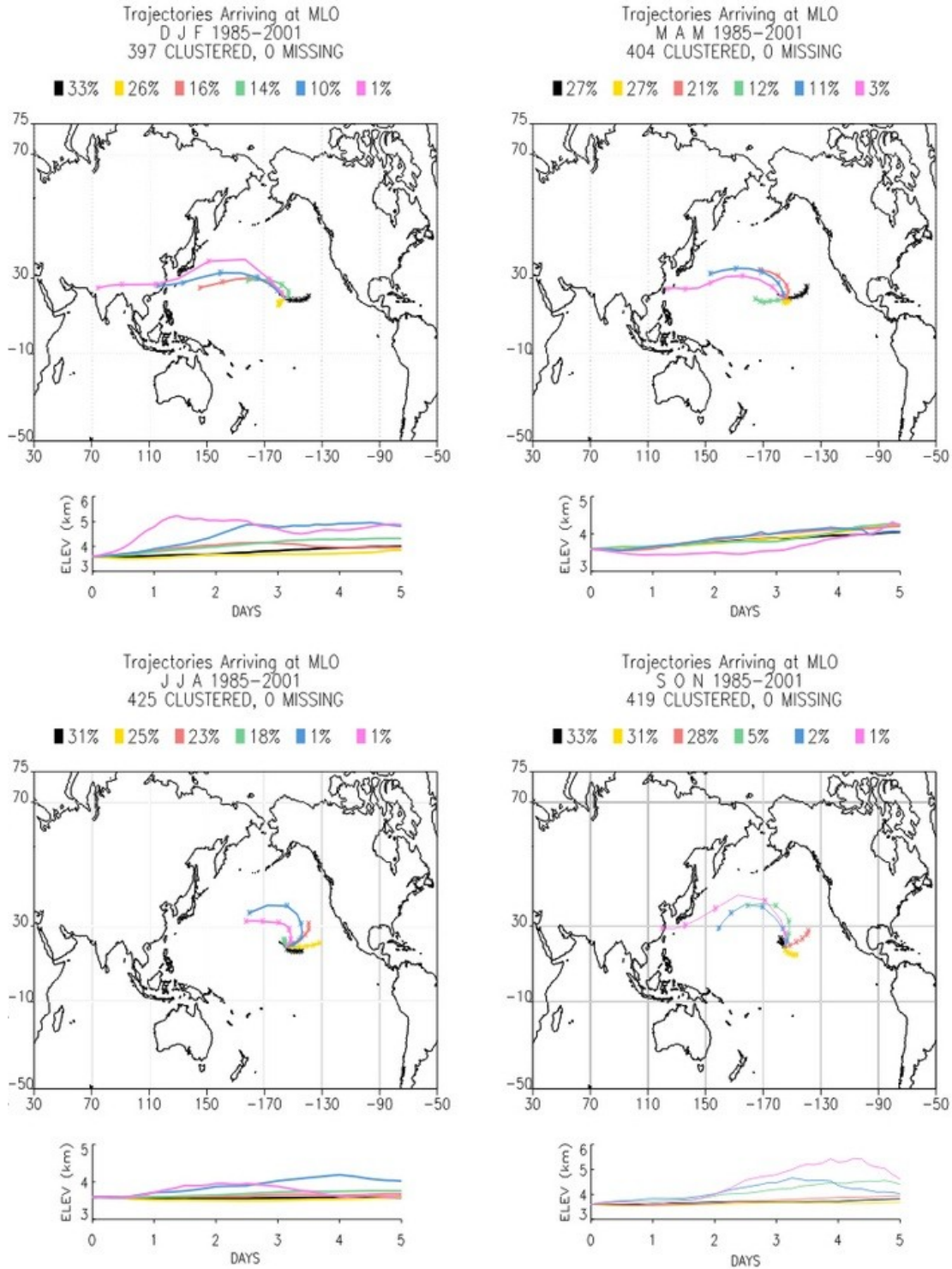


Figure 1.22: Fractions of MLO Lagrangian back trajectory air parcels occurring over the Eurasian (squares) or American (triangles) continents 6-10 days prior to arrival at MLO from Lintner et al. (2007).



Courtesy of Joyce Harris (NOAA CMDL)

Figure 1.23: Clustered MLO HYSPLIT 5-day back trajectories by season during 1985-2001 from Earth System Research Laboratory (2012)
(http://www.esrl.noaa.gov/gmd/dv/site/trajs/mlo_traj.jpg)

1.8.3 What are the meteorological controls on transport to MLO?

Sulfate concentrations at MLO are dependent on precursor emissions in source regions as well as variations in meteorological conditions which can impact production and transport of sulfate aerosol. Perry et al. (1999) noted that interannual variability of transport to MLO is linked to meteorology and not entirely dependent on source and sink characteristics and therefore any study examining anthropogenic aerosol trends at MLO must carefully account for meteorological variability. Meteorological conditions in the source region determine the likelihood that pollutants are lofted into the free troposphere while the height and speed of subsequent transport determines how quickly these lofted pollutants are transported.

Sulfate concentrations have been found to increase with increasing temperatures and increasing humidity which favors aqueous-phase sulfate oxidation (Tai et al., 2010). Meteorological or hydrological variability may influence production processes or background concentrations of natural sulfate precursors like DMS (Prospero et al., 2003). Precipitation during transport can increase wet deposition of sulfate aerosol which may reduce concentrations at MLO even during times of Asian continental origin. Tai et al. (2010) found that synoptic conditions control up to 40% of PM_{2.5} variability in portions of the United States. In the case of MLO, mid-latitude cyclone frequency in the East Asian source region determines how often pollutants are lofted into the free troposphere and characteristics of subsequent transport determine how efficiently these lofted pollutants are transported long distances.

The El Niño-Southern Oscillation (ENSO) is a phenomenon of coupled climate variability which involves interactions between the ocean and atmosphere (Wallace and Hobbs, 2006). Bjerknes (1969) first discovered the connection between El Niño and the Southern Oscillation, now commonly referred to as ENSO. ENSO can be detected from the interannual

variations in sea-surface temperature (SST) anomalies in the equatorial Pacific and the global pattern of sea level pressure around the globe (Bjerknes, 1969). SSTs vary in relationship to the strengthening and weakening of the equatorial trade winds, with a warm phase occurring in conjunction with weaker trade winds and a cold phase occurring at times of stronger trade winds (Wallace and Hobbs, 2006).

Shifts in global circulation patterns, as indicated by ENSO indices, have impacts on transport to MLO. These shifts have been found to contribute to the interannual and interdecadal carbon dioxide (CO₂) variability observed at MLO (Lintner et al., 2006) although little is known about the possible impacts on anthropogenic aerosol variability at MLO. Composite seasonal 700mb stream function patterns for 1971-2002 are shown in Figure (1.24) during both El Niño (red contours) and La Niña (blue contours) conditions. Linter et al. (2006) found that circulation patterns associated with anomalously high MLO CO₂ concentrations resembled these anomalous flow patterns known to be associated with El Niño and La Niña conditions. This relationship was found to be highly seasonally dependent, with positive MLO CO₂ anomalies associated with El Niño circulation patterns during winter, spring, and autumn and La Niña patterns during summer. Because anthropogenic aerosols likely originate from similar sources as CO₂, we expect that circulation changes as captured by ENSO indices might explain some of the seasonal and interannual variability of sulfate concentrations at MLO.

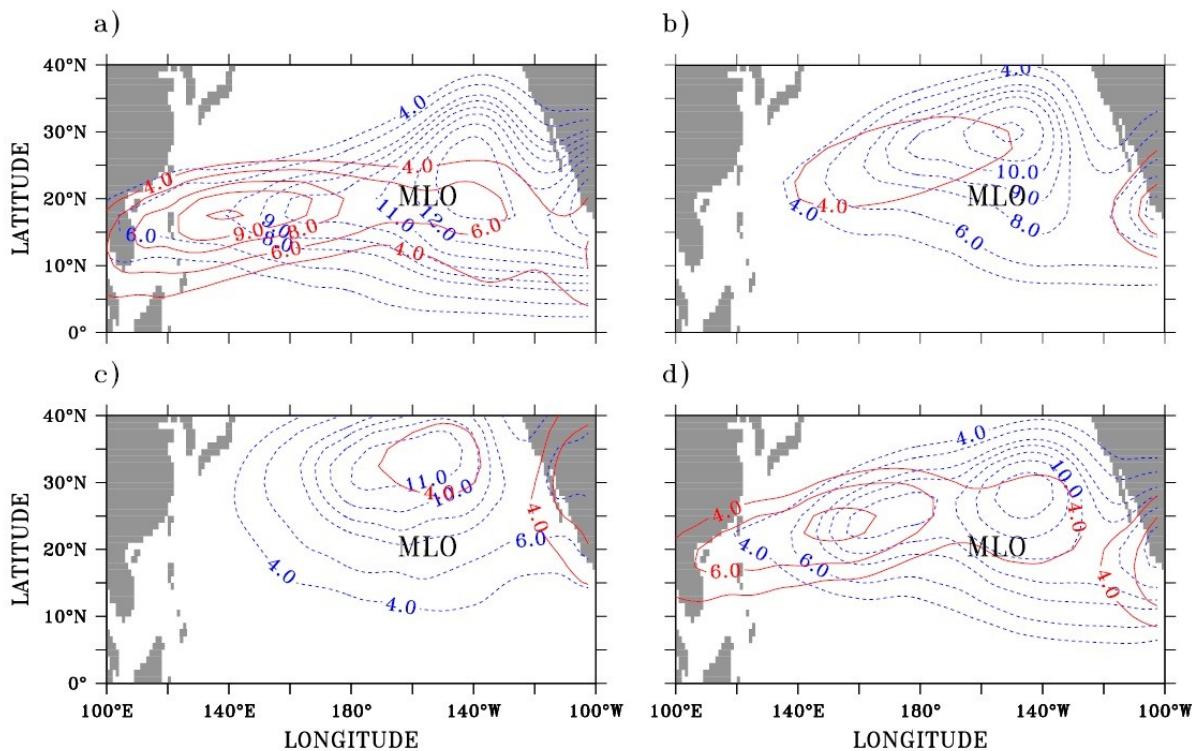


Figure 1.24: NCEP/NCAR Reanalysis 700mb stream function (units $10^7 \text{ m}^2/\text{s}$) contour composites for 1971-2002 during El Nino (red) and La Nina (blue) conditions during (a) January-February-March, (b) April-May-June, (c) July-August-September, and (d) October-November-December from Lintner et al. (2006).

1.8.4 Can observed trends in MLO sulfate concentrations be attributed to anthropogenic sulfur dioxide emissions trends?

Prospero et al. (2003) assert that consistent long-term observations at a remote location are needed for comparison with anthropogenic emissions in order to develop a more robust understanding of factors contributing to aerosol variability on multi-year timescales. Figure (1.25) shows the similarities that were observed between anthropogenic NSS-sulfate trends at Midway Island during 1980-2000 and emissions estimated and extrapolated by Streets et al. (2000).

The ultimate goal of this study is to perform an analysis of the factors that control transport of anthropogenic sulfate aerosol to MLO and subsequently to determine if a trend in

sulfate aerosol concentrations exists, after accounting for the influence of natural sulfate sources and transport variability. This study was able to utilize additional information available from updated anthropogenic emissions estimates and an extended MLO sulfate aerosol record since the work of Prospero et al. (2003) and Huebert et al. (2001). Anthropogenic sulfate observations were combined with information about long distance continental influence and meteorological controls on transport to determine whether the interannual variability in sulfate aerosol at MLO could be attributed to changes in meteorological conditions controlling transport favorability or whether the variability is more likely linked to changes in natural and anthropogenic precursor emissions.

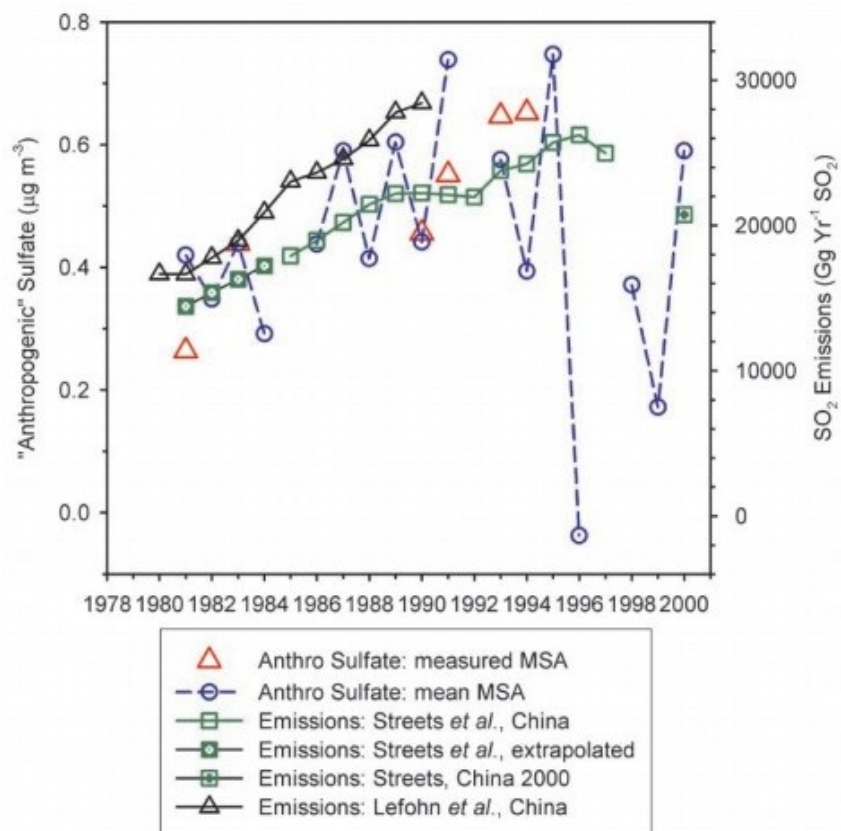


Figure 1.25: Trends in springtime mean anthropogenic NSS-sulfate at Midway Island compared with SO₂ emissions from China during 1980-2000 from Prospero et al. (2003).

2. Data and Methodology

2.1 University of Hawaii Dataset

2.1.1 Measurement Details

This study utilized a largely unpublished data set of aerosol ionic composition at Mauna Loa Observatory (MLO), obtained by the University of Hawaii at Manoa (PI, Prof. Barry Huebert). Daily integrated filter samples of total particulate matter were collected overnight (8pm-8am local time) during downslope conditions that brought free tropospheric air to the site. This measurement strategy minimized the effects of local emissions, including those of volcanic origin. Samples were collected from 1995 to 2008, and filters were analyzed for aerosol-phase concentrations of the following species: Nitric Acid ($\text{HNO}_3(\text{g})$), and aerosol-phase concentrations of nitrate (NO_3^-), sulfate (SO_4^{2-}), methanesulfonate (MSA), chloride (Cl^-), oxalate, sodium (Na^+), ammonium (NH_4^+), potassium (K^+), magnesium (Mg^{2+}), and calcium (Ca^{2+}). Valid free-tropospheric observations were selected based on the following criteria that made use of complementary observations that were taken at higher time resolution (Huebert et al., 2001):

- Southerly wind conditions (between 90° and 270°) during the duration of the nighttime measurement. Only southerly wind directions corresponded to downslope conditions as the observatory is located on the northern flank of Mauna Loa.
- Condensation nuclei concentrations less than 500 cm^{-3} . Higher number concentrations were likely to be strongly influenced by local combustion sources or volcanic activity.

- Dew point of less than 5° C. This criterion is based on the assumption that free tropospheric air masses were significantly drier than air masses of local origin that were recently in contact with the marine boundary layer.
- Carbon dioxide variation of less than 0.3 ppm. This criterion was included to remove possible influences from Mauna Loa volcanic emissions that were not filtered by the previous criteria.

For each overnight sample, a flag was assigned based on the number of hours that failed two or more of the above criteria. For this study, we used only data passing the strictest criteria requirements, excluding from further analysis all overnight samples containing more than one hour failing two or more of the above criteria. Data were converted from pptv units to mass units (either $\mu\text{g m}^{-3}$ or ng m^{-3}) using the molecular weight of each species, the average pressure of MLO (680 mb), and the average temperature of MLO (5° C).

2.1.2 Sea Salt and Biogenic Sulfate

Non-sea-salt (NSS) sulfate and calcium concentrations were calculated by using observed sodium (Na^+) concentrations to correct for the sea salt contributions using the mass ratios listed in Table (1.3). The anthropogenic fraction of NSS-sulfate was then computed using an assumption about the MSA/NSS-sulfate mass ratio expected from the oxidation of dimethylsulfide (DMS). As suggested by Prospero et al. (2003), based on sea-level data at Midway Island (28°13' N, 177°22' W), a ratio of MSA/ NSS-sulfate=0.07 was used in this study to determine the biogenic component of NSS-sulfate at MLO, although this ratio is temperature dependent and therefore may not accurately describe the DMS oxidation products expected at MLO (Section (1.6.2)). Each value of NSS-sulfate was partitioned into its biogenic (DMS-

derived) and anthropogenic components based on this ratio. When the observed MSA/NSS-sulfate ratio was greater than 0.07, all of the sulfate was assumed to be of biogenic origin. When the MSA/ NSS-sulfate ratio was less than 0.07, Equations (2.1) and (2.2) were used to calculate the biogenic and anthropogenic components.

$$[Biogenic\ NSS\ SO_4^{2-}](\mu g/m^3) = \frac{[MSA](\mu g/m^3)}{\frac{(\mu g/m^3\ MSA)}{0.07(\mu g/m^3\ NSS\ SO_4^{2-})}} \quad (2.1)$$

$$[Anthropogenic\ NSS\ SO_4^{2-}](\mu g/m^3) = [Total\ NSS\ SO_4^{2-}](\mu g/m^3) - [Biogenic\ NSS\ SO_4^{2-}](\mu g/m^3) \quad (2.2)$$

2.1.3 Data Completion Analysis

The strict quality control criteria imposed on the aerosol composition measurements substantially reduced the number of overnight observations available for analysis. The percentage of days with acceptable data quality was determined from the total number of overnight samples in each month which met quality control criteria and did not have missing data for any of the species required to calculate anthropogenic NSS-sulfate concentrations. Out of the 5,114 possible sample days during 1995-2008, only 2,901 were assigned a flag signifying that these measurements passed the strictest quality control criteria. Out of these observations, sulfate, sodium, or MSA concentration data were missing for 227 overnight samples. Therefore, 2,674 overnight anthropogenic NSS-sulfate concentrations were available for analysis representing approximately 52% of the maximum possible observations.

Additional steps were taken to reduce the error that may occur from omitting such a high percentage of data points. The trend and seasonal analyses applied in this study typically utilized monthly mean concentrations. These mean concentrations could be biased due to variability in

the number of daily data points included during each month: the observations that passed the quality control criteria were not evenly distributed in time and therefore certain months, seasons, or years contained considerably more usable data than others. The data coverage is summarized in Figure (2.1a). The 2,674 overnight samples were organized by month (blue squares) to determine how the percentage of usable data changed over time. Month-to-month variability in data completion was very high, ranging between 0% to greater than 90%. The 0% completion result for January of 1995 was due to the fact that consistent MSA observations did not begin until February of 1995 while many of the other low completion rates were primarily due to failed quality control criteria.

A threshold of 20% data completion (red line) was imposed to reduce the possible bias of months with very few (or zero) nightly observations while still maintaining a large enough dataset of monthly average values for robust trend and seasonal analysis. Months with data completion below this threshold (red circles) were eliminated from analyses comparing monthly mean anthropogenic NSS-sulfate concentrations with other monthly mean variables. Spring months (March, April, and May) are highlighted by green triangles in Figure (2.1a). Data completion during springtime months was higher than the threshold for all years, with the exception of April and May 1999. Therefore data during 1999 were omitted from analyses involving only springtime mean values. The annual average data completion for each year is indicated by the orange circle at the beginning of each year on the timeline. The completion percentages for annual mean data were always higher than the threshold, so all years were included in analyses involving annual mean values.

In addition to the data completion percentage during each month, the temporal spread (i.e. the range of dates with acceptable data quality during each month) was analyzed, to test the

hypothesis that patterns in the quality control flags during a month were likely to be associated with synoptic conditions. That is, during a given month, a short series of consecutive days under the influence of favorable synoptic conditions could result in enough observations to meet the data completion threshold of 20%, but not be representative of the concentration variability throughout the entire month. Consistent with the data completion calculation, temporal spread of nightly observations was determined after filtering for quality control criteria and missing data. The temporal spread was calculated by subtracting the smallest date with a valid observation from the largest date with a valid observation (Figure 2.1b). This metric provides an estimate for how evenly data points are spread throughout the month. A total of 7 observations during September 2000 met both quality control and missing data criteria. Therefore, 23.3% of the observations were acceptable and this month fell above the data completion threshold. However, the temporal coverage requirement showed that these 7 nightly observations occurred almost consecutively during a period of 9 days with no observations included during the rest of the month. Therefore, this month was also removed from the analyses. All other months that failed the temporal spread metric had already been removed by one of the other criteria.

A summary of months omitted from analysis is provided in Table (2.1) along with the reasons for omission. There was some overlap between months not meeting data completion requirements and months not meeting temporal coverage requirements with 8 of the 15 months failing both criteria. No distinct seasonal signal is evident in the omitted months, although slightly more omitted months fell during winter (DJF) and summer (JJA) than during spring (MAM) or autumn (SON).

Anthropogenic NSS-Sulfate Data Completeness and Temporal Spread 1995-2008

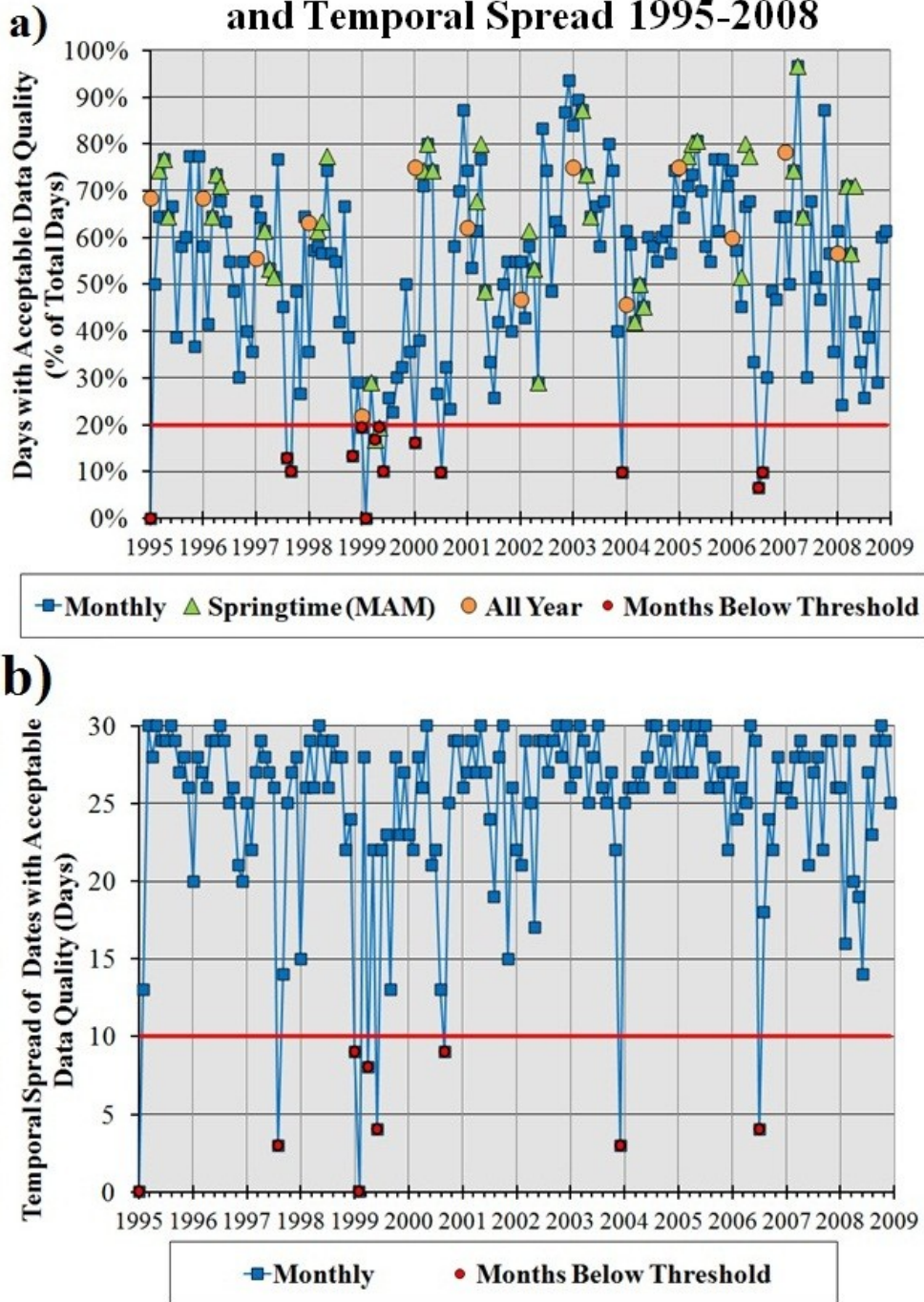


Figure 2.1: Timeline of monthly anthropogenic NSS-sulfate data completion and temporal spread. The threshold for including data points is indicated by the red lines.

Table 2.1: Summary of months with data omitted from analysis based on low data completion or low temporal coverage.

Data Deleted From Anthropogenic NSS Sulfate For Low Monthly Completeness or Temporal Coverage			
Year	Month	Completeness	Temporal Coverage
1995	1	✓	✓
1997	8	✓	✓
1997	9	✓	
1998	11	✓	
1999	1	✓	✓
1999	2	✓	✓
1999	4	✓	✓
1999	5	✓	
1999	6	✓	✓
2000	1	✓	
2000	7	✓	
2000	9		✓
2003	12	✓	✓
2006	7	✓	✓
2006	8	✓	

2.2 Chemical Tracers for Continental Influence

2.2.1 Radon

Radon (^{222}Rn) is often used as a tracer to identify continental influence on an air mass (Whittlestone et al, 1992). Radon gas is a decay produce of radium (^{226}Ra) which is present in many types of soils (Zahorowski, 2005). Radon fluxes from land are several orders of magnitude larger than fluxes from the ocean (Zahorowski, 2005). Therefore, radon concentrations in air masses that recently had contact with land are expected to be significantly higher than concentrations in air masses of oceanic origin. However, recent modeling studies have suggested that the relatively small oceanic radon fluxes are highly variable and may be relevant for certain coastal and marine locations, so oceanic sources of radon observed at MLO

should not necessarily be fully neglected (Schery and Huang, 2004). Radon is an inert gaseous species which is relatively unaffected by chemical reactions or wet deposition during transport (Whittlestone et al., 1992). The primary sink for radon in the atmosphere is radioactive decay with a half-life of 3.8 days, long enough that it can be used as a tracer for continental influence at remote locations several days downwind but also short enough that it does not substantially accumulate in the atmosphere (Zahorowski, 2005). Thus, high concentrations of radon at MLO were typically assumed to be representative of recent contact with continental land masses.

MLO hourly radon data for the time period January 1997-December 2008 were provided by Wlodek Zahorowski from the Institute for Environmental Research, Australian Nuclear Science and Technology Organisation. Details behind the instrumentation and operation of the radon detector at MLO are described in Whittlestone and Zahorowski (1998). Observations taken between 1997 and 2003 were made using a different detector than the observations taken from 2004-2010 so a shift in mean concentration was observed between the two time periods. Radon concentrations in this study are reported in units of milliBecquerels per cubic meter (mBqm^{-3}). The becquerel (Bq) is the standard unit for radioactivity which is equivalent to the disintegration of one atomic nucleus per second (Knoll, 2010). A strong diurnal signal was observed in radon concentrations at MLO due to local influences from the Hawaiian Islands during daytime upslope flow and free troposphere conditions during the nighttime downslope flow. Although radon was recorded hourly, for this study the data were averaged between 8pm and 8am local time to match the temporal pattern of the University of Hawaii aerosol observations. Daily observations that were removed from the aerosol data set due to local contamination flags were also removed from the radon dataset. Radon data were analyzed from

1997 to 2010 so that a majority of the data would overlap with anthropogenic NSS-sulfate observations.

2.2.2 Carbon Monoxide

Important direct anthropogenic sources of carbon monoxide (CO) include emissions from trucks and automobiles, non-transportation combustion, and certain industrial processes (Jacobson 2002). Biomass burning and secondary formation from the atmospheric oxidation of methane and non-methane hydrocarbons are also important sources of atmospheric carbon monoxide (Novelli, et al., 1992). The largest sink for CO is reaction with OH which also serves as a major control on global OH concentrations (Novelli et al., 1992). Novelli et al. (1992) determined that the lifetime of carbon monoxide against reaction with OH at MLO (estimated atmospheric pressure of 700mb) ranged between 0.7-1.3 months with the shortest lifetime during the summer and longest during the winter (Novelli, et al., 1992). In portions of the Northern Hemisphere, the seasonal cycles of CO and sulfate have been found to differ from each other despite the existence of many common emissions sources because oxidation of carbon monoxide with OH removes CO from the atmosphere while oxidation of sulfur dioxide with OH produces sulfate in the atmosphere (Bian et al., 2010). Carbon monoxide is well suited as another chemical tracer for continental transport to MLO because of its long atmospheric lifetime and insolubility, although like sulfate, interpretations of CO are complicated by a combination of sources and chemical processes.

Monthly concentrations of CO for the period of 1981-2010 and daily concentrations for the period of 2005-2010 were provided by Paul Novelli from the National Oceanic and Atmospheric Administration (NOAA) Earth System Research Laboratory (ESRL) as part of the CMDL/NOAA cooperative flask sampling program. The monthly mean concentrations

overlapping the anthropogenic NSS-sulfate dataset (1995-2008) as well as all available daily concentrations were used in this study to compare the influence of carbon monoxide sources with sulfate and other continental tracers.

2.3 SO₂ Emissions

2.3.1 Anthropogenic East Asian SO₂ Emissions

Annual SO₂ emissions were estimated by Lu, Zhang, and Streets (2011) for both China and India during 1996-2010 as shown in Figure (1.4). Emissions from these two countries were combined to create an annual estimate that was used to represent East Asian anthropogenic SO₂ emissions that had the potential to influence atmospheric composition at MLO. Combined emissions during 1995-2008 were used in this study to correspond with the time period of MLO anthropogenic NSS-sulfate concentrations.

2.3.2 Kilauea, Hawaii Volcano SO₂ Emissions

Kilauea Volcano (Section (1.6.3)) has an excellent data record with regular emissions observations since 1979 (Elias and Sutton, 2012). For this study, SO₂ emission rates were compiled for the period 1995-2008 from published estimates (Elias et al. 1998, Elias and Sutton, 2002, 2007, 2012). Emission rates were obtained separately for the summit and for the east rift of the volcano using vehicle-based spectrometer measurements (Elias et al., 2012). The summit and east rift emission zones are shown in Figure (2.2). Measurements of gas phase SO₂ were taken using a vehicle based spectrometer (FLYSPEC after 2004 and COSPEC prior to 2004) downwind of both locations along either Crater Rim Drive or Chain of Craters Road during periods of trade-wind conditions. SO₂ emission rates were calculated from these concentrations using the volcanic plume cross-sectional area and wind speed during the observation period.

Due to the necessary trade wind criterion, the number of valid daily observations varied considerably throughout the study periods and was typically very low. During 1995-2008, 55% of months had less than 5 days with summit emission observations while 70% of months had less than 5 days of East Rift emission observations. Because of the very low data completion, the 20% completion threshold used on the anthropogenic NSS-sulfate observations could not be applied to the volcanic emission rate data without omitting a majority of the monthly-mean data points.

We hypothesized that if Kilauea Volcano emissions influenced MLO aerosol observations on the regional scale, even after filtering the data for the direct plume influences, then periods with high SO₂ emissions would likely contribute to high monthly mean MLO anthropogenic NSS-sulfate concentrations. Monthly mean Kilauea summit and east rift volcanic SO₂ emissions were calculated separately from the respective irregular daily observations and compared with monthly mean MLO anthropogenic NSS-sulfate concentrations to determine whether relationships could be observed. Due to the irregular data observations and therefore missing values for monthly mean emissions, annual emissions estimates for the summit and east rift as calculated by Elias and Sutton (2012) were used for regression analysis which is discussed further in Section (2.7.3).

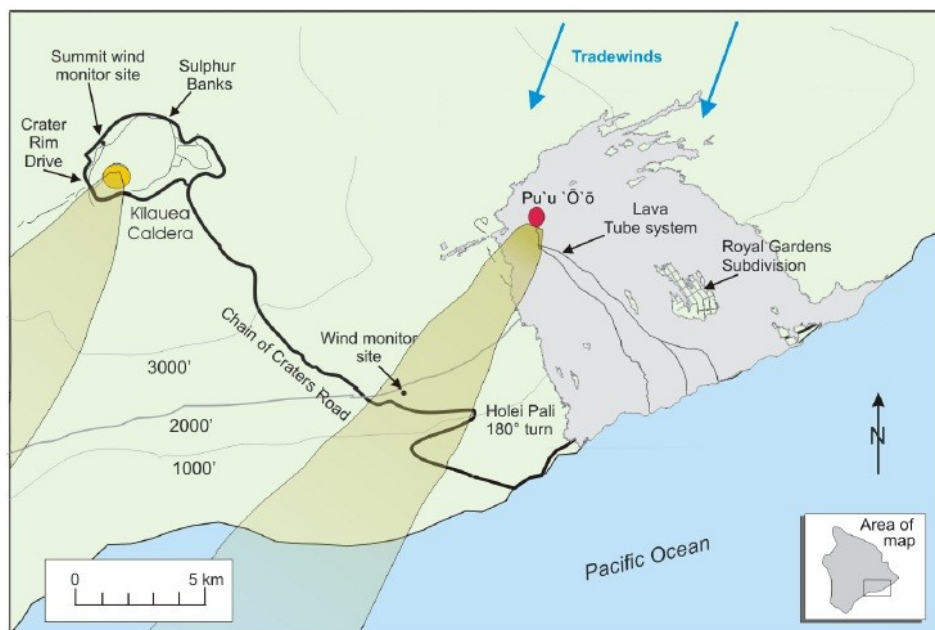


Figure 2.2: Map of Kilauea Volcano Summit (left) and East Rift (right) plumes on the Island of Hawaii during trade wind conditions. Mobile sampling locations are indicated as regions where the Summit plume intersects Crater Rim Drive or the East Rift plume intersects Chain of Craters Road. Figure from Elias et al. (2002).

2.4 Multivariate ENSO Index

The Multivariate ENSO Index (MEI) was used as an indicator of El Niño/La Niña phase for comparison with observational MLO chemical datasets. The index is calculated based on the following six observational variables over the tropical Pacific Ocean: sea-level pressure, zonal surface wind, meridional surface wind, sea surface temperature, surface air temperature, and total cloudiness sky fraction (Wolter, 2012). The MEI is then computed for each of twelve sliding bi-monthly time periods using principal component analysis of the six variables. These monthly values are then standardized by season and a reference period of 1950-1993 so that negative values of MEI represent the La Niña phase while positive values represent the El Niño phase (Wolter, 2012). The work of Lintner et al. (2006) motivated the application of an El Niño indicator to investigate the influence of transport variability on chemical concentrations at MLO.

2.5 Long Range Transport Index

Several meteorological indices of long range transport from East Asia to the Northeast Pacific were created by Liang et al. (2004) using GEOS-CHEM simulated CO concentrations as an indicator of long range transport. Long-Range Transport Index 1 (LRT1) was selected for use in this study, representing the efficiency of Asian outflow primarily related to mid-latitude cyclone activity in this source region of interest for MLO. Asian pollution outflow to the western Pacific was quantified using modeled column average (surface-8km) CO concentrations at 150°E across the 30-60° latitude range. A time series of this modeled CO was compared with observed NCEP/NCAR Reanalysis sea level pressure anomalies in the surrounding region and a significant negative correlation was found in Northeastern China as shown in Figure (2.3). Sea level pressure anomalies in the area of strongest negative correlation shown by the black box in Figure (2.3) were then used to generate a meteorological index that was found to explain 14-22% of the total variability in Asian outflow during 1992-2002 as further explained in Liang et al. (2005). Monthly LRT1 values from 1992-2012 were provided by Dr. Qing Liang (Atmospheric Chemistry and Dynamics Branch, NASA Goddard Space Flight Center) for comparison with MLO observational data. It was hypothesized that this index may explain a portion of the variability in transport of pollutants and continental tracers to MLO by indicating times of higher export efficiency and therefore a time series of LRT1 was compared with chemical data from MLO during regression analysis to determine if a significant relationship existed during the study period.

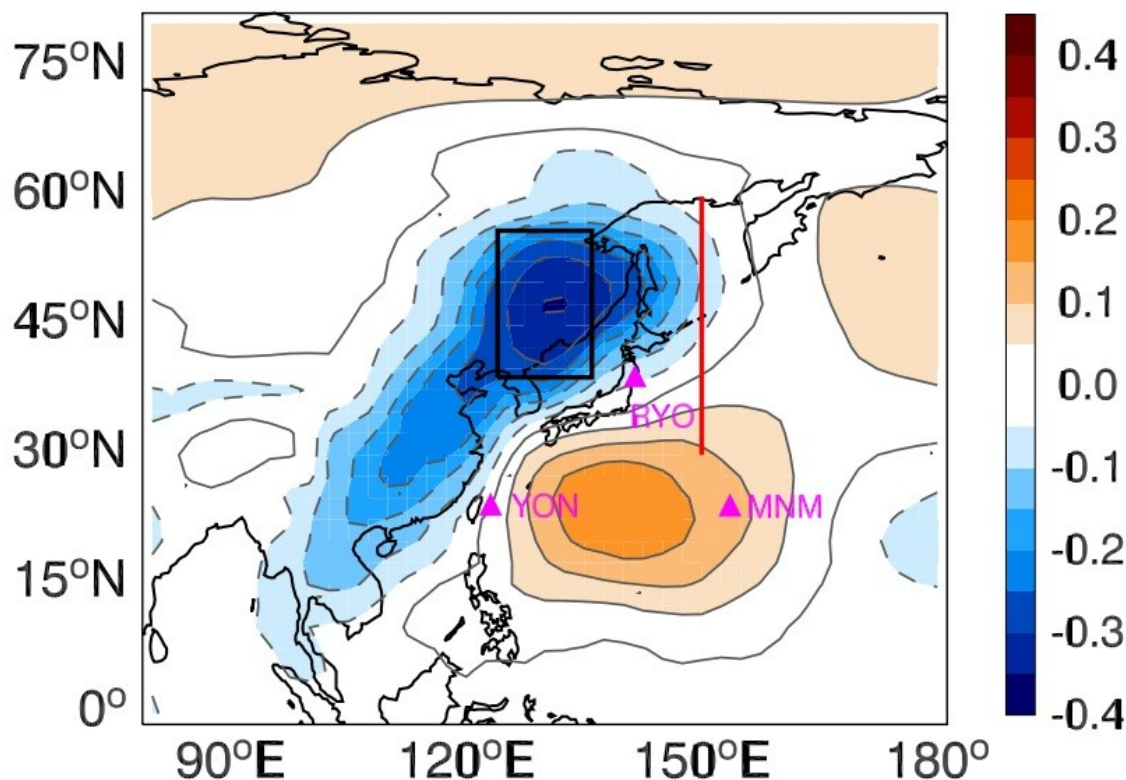


Figure 2.3: Correlation between sea level pressure anomalies and Asian outflow as defined by variations in simulated carbon monoxide along the cross-section represented by the red line (0-8 km, 30– 60°N, 150°E). Sea level pressure anomalies in the black box were used in the definition of the LRT1 index (Liang et al., 2005).

2.6 Hybrid Single Particle Lagrangian Integrated Trajectory Model

2.6.1 Model Details

The Hybrid Single Particle Lagrangian Integrated Trajectory (HYSPPLIT) Model is a trajectory modeling tool available through NOAA Air Resources Laboratory (ARL; <http://ready.arl.noaa.gov/HYSPLIT.php>) that has been utilized in both operational and research applications to enhance understanding of atmospheric chemical transport, dispersion, and deposition. The HYSPPLIT dispersion model has been applied towards more accurate forecasting of dust, wild fire smoke, hazardous materials, and volcanic ash emissions and transport (NOAA ARL, 2012). Additionally, the HYSPPLIT trajectory model can be run both forward and backward in time, useful for source-receptor applications. Relevant to this work, HYSPPLIT has

been applied in studies of East Asian dust and pollution transport to both MLO (e.g. Rinsland et al., 1999) and the Western United States (e.g. Weiss-Penzias et al., 2006).

Calculations in HYSPLIT are based on a hybrid combination of Eulerian and Lagrangian frameworks (Draxler et al., 1998). Eulerian models focus on a specific location in space and calculate both advection and diffusion on a fixed spatial grid while Lagrangian models are applied to an air parcel moving through space, therefore calculating advection and diffusion separately (Draxler et al., 1998). HYSPLIT utilizes the Lagrangian method for calculating advection and diffusion while chemical concentrations are calculated using a Eulerian fixed grid (Draxler et al., 1998). For this study, HYSPLIT was used only for particle trajectory calculations without application of the dispersion or diffusion models.

The HYSPLIT model can be run using a variety of available model meteorology datasets that have been processed into the format required by the model. The most basic meteorological inputs required to operate HYSPLIT include U and V wind components, temperature, height or pressure, and surface pressure (Draxler et al., 1998). Vertical velocity in HYSPLIT can be assumed to be isobaric, isosigma, isopycnic, or isentropic (Draxler et al., 1998). Additionally, if the meteorological fields used as input contain a vertical velocity field, this field can be used to dictate vertical motion in the model. For this study, meteorological model vertical velocity was selected to calculate trajectory motion.

2.6.2 Reanalysis Meteorological Fields

Archived NCEP/NCAR Reanalysis model meteorology was used as input for the HYSPLIT trajectory model. The NCEP/NCAR Reanalysis project produces a globally gridded dataset through a combination of numerical weather prediction models and assimilation of observational data (Kalnay et al., 1996). Global Reanalysis data are available at 6 hourly (0Z,

6Z, 12Z, 18Z), daily, and monthly time resolution with continuous coverage from January 1948 through the present. Reanalysis was favored for this project over other readily-available model meteorological datasets because of the consistent historical temporal coverage. The 2.5 degree by 2.5 degree spatial scale at 18 pressure levels between 1000hPa and 10hPa was sufficient to resolve synoptic scale patterns of interest to long distance intercontinental transport. NCEP Reanalysis data were provided by the NOAA/OAR/ESRL PSD, Boulder, Colorado, USA, from their website (<http://www.esrl.noaa.gov/psd/>).

2.6.3 Trajectory Specifications to Match Observations

The Windows PC version of HYSPLIT was utilized to calculate 10-day (240 hour) back trajectories from the Mauna Loa Observatory receptor site (19.54° N, 155.57° W) with a single starting location height of 3400m above sea level. In order to most accurately align the trajectory information with the University of Hawaii aerosol dataset, only back trajectories which arrived at MLO during nighttime, 8pm-8am local time (6Z-18Z) were included in the analysis. Therefore, the 6 hourly Reanalysis model meteorology was used to generate three separate trajectories with arrival times of 6Z, 12Z, and 18Z at the MLO receptor to correspond with each overnight aerosol observation. These trajectory calculations were performed for the period of 1995-2010 to overlap with the full extent of MLO aerosol and chemical tracer data.

2.6.4 Residence Time Analysis of Trajectories

Residence time analysis (RTA) is a statistical technique first defined by Ashbaugh et al. (1985) that has been applied to determine the regional locations of likely sources for a specific receptor site. Residence times are calculated from trajectory information based on the amount of time that an air parcel spends in each two-dimensional grid box in a region around the receptor

site, before arriving at the receptor site of interest. Possible pollutant source regions are identified using residence time analysis because it represents the opportunity of a passing air parcel to interact with and accumulate local pollutants for transport (Ashbaugh et al., 1985).

HYSPLIT back trajectories consist of a series of trajectory segments with endpoints representing the location of an air parcel at each one hour interval backward in time. Therefore, the number of trajectory endpoints occurring in each grid cell can be used to represent the distribution of residence times of an air parcel passing through the grid (Hopke et al., 2003). For this study, two-dimensional residence time distributions were calculated using a global grid of 1° latitude by 1° longitude cells. MLO receptor site HYSPLIT back trajectory endpoints occurring in a vertical column located above any grid cell over the selected time period of interest were counted to determine the total number of trajectory endpoints occurring in a selected grid during the time period of interest. RTA is also related to the probability that a selected air parcel was previously located in a selected grid during the time period of interest although due to the long distance trajectories of interest, probabilities of an air parcel passing through a selected cell in a continental source region are very low. Therefore, total residence times in hours were calculated, assigning each grid cell a representative importance in terms of likely source contribution to the MLO receptor site.

2.6.5 Concentration Weighted Trajectories

HYSPLIT trajectories can be combined with aerosol composition observed at a receptor site by matching trajectory arrival time at the receptor with the sampling time (Hsu et al., 2003). Although one integrated aerosol observation was taken for each overnight period between 1995 and 2008, three separate HYSPLIT trajectories corresponded to the same time period. It is not necessarily more representative of real transport patterns to combine trajectories into one

overnight average. In this work, we assigned the same 12-hour integrated aerosol measurement to the end times of each of the three HYSPLIT trajectories spawned during each aerosol sampling period. The same approach was applied to align trajectories with overnight mean concentrations of chemical continental tracers.

The aerosol observations were combined with back trajectories using the method of concentration weighted trajectories (CWT) (Hsu et al., 2003). This technique is especially useful for identifying sources of varying magnitudes which contribute to an observed species at a receptor site because regions which likely served as sources during high concentration events are given more weight than those regions which likely served as sources during low concentration events (Hsu et al., 2003). Similarly to RTA calculations, a 1 degree by 1 degree global grid was used for CWT analysis and Equation (2.1) was used to calculate the average weighted species concentration, C , for each ij th grid cell:

$$C_{ij} = \frac{1}{\sum_{l=1}^N \tau_{ijl}} \sum_{l=1}^N C_l \tau_{ijl} \quad (2.1)$$

In this equation, τ represents the number of trajectory endpoints and N represents the total number of aerosol observations, l , with trajectory endpoints occurring in each ij th grid cell (Hsu et al., 2003). Grid cells with a high C value highlight regions through which air parcels commonly pass before a high concentration event occurs at the receptor site. The calculated C_{ij} for grid cells around the boundary of the domain that have very few trajectory endpoints can be skewed by one high concentration event and should be considered with caution. For this study, grid cells with less than 5 total trajectory endpoints were eliminated to reduce bias.

2.6.6 Meteorological Weighted Trajectories

The following Reanalysis model meteorological variables were output from HYSPLIT for each trajectory, interpolated at each 1 hourly endpoint defined by time and particle location

along the trajectory: terrain height (m), potential temperature (K), ambient temperature (K), rainfall (mm per hr), mixed layer depth (m), relative humidity (%), and downward solar radiation flux (W/m^2). Certain variables are defined for the surfaces only (terrain height, rainfall, mixed layer depth, and downward solar radiation) while others are interpolated vertically to match trajectory location (potential temperature, ambient temperature, relative humidity). Selected meteorological variables were used to create meteorology weighted trajectories (MWT) using a similar method as described for the concentration weighted trajectories. Instead of applying only one concentration value to each endpoint along the trajectory, the Reanalysis meteorological parameter of interest along the trajectory is assigned to each hourly endpoint. These values were then combined over each 1 degree by 1 degree grid box to create a field of meteorological parameters using Equation (2.2):

$$M_{ij} = \frac{1}{\sum_{l=1}^N \tau_{ijl}} \sum_{l=1}^N M_l \tau_{ijl} \quad (2.2)$$

As in the CWT equation, τ represents the number of trajectory endpoints and N represents the total number of meteorological observations, l , with trajectory endpoints occurring in each ij th grid cell. M represents the mean value of the selected meteorological parameter in the ij th grid cell over the selected time period.

2.7 Statistical Analysis

2.7.1 Monthly, Seasonal, Annual Averaging

For the datasets with daily time resolution, a monthly mean time series was created for comparison with other monthly datasets. The arithmetic average of all daily observations meeting any specified criteria requirements was calculated for each month during the study period. To calculate a mean seasonal cycle in a monthly dataset, the arithmetic average of all monthly means in each of the twelve calendar months was used. This averaging method was

also used to deseasonalize monthly data for anomaly comparisons. The seasonal cycle of a dataset was removed by subtracting the average concentration for a selected month from each individual monthly mean concentration, producing anomaly concentrations. Annual average concentrations were calculated from the arithmetic mean of all available calendar months in each selected year.

2.7.2 Trend Calculation

Trend analysis was performed using the Theil-Sen trend estimator (Sen, 1968; Theil, 1950). The Theil-Sen trend estimator is a method of non-parametric linear regression calculated from the median linear slope between all possible pairs of two data points. The slope of a line connecting each set of two data points (x_i, y_i) and (x_j, y_j) is calculated, and the Theil-Sen trend slope, m , is defined as the median of all calculated slopes (Sen, 1968):

$$m = \text{median}\left[\frac{(y_j - y_i)}{(x_j - x_i)}\right] \quad (2.3)$$

This regression method is favored for computation of long-term trends because it more resistant to outlier data points than simple least squares regression (Hirsch et al., 1982). From the Theil-Sen slopes, the Kendall rank correlation coefficient (τ) was calculated and used as a test statistic for the trend relationship. Pairs of data points were ranked based on the magnitude of each x_i (y_i) compared with x_j (y_j) and Kendall's tau was calculated using Equation (2.4):

$$\tau = \frac{N_C - N_D}{n(n-1)/2} \quad (2.4)$$

where n is the total number of data points, N_C is the number of concordant pairs ($x_i < x_j$ and $y_i < y_j$ or $x_i > x_j$ and $y_i > y_j$), and N_D is the number of discordant pairs ($x_i < x_j$ and $y_i > y_j$ or $x_i > x_j$ and $y_i < y_j$) (Wilks, 2006). The statistical probability that a Kendall's τ value is different than zero was determined by calculating the p -value associated with the identified Theil-Sen trend. P -values

were reported with each trend calculation and relationships were considered statistically significant if $p < 0.1$, corresponding to a 90% confidence limit.

2.7.3 Multiple Linear Regression

A multiple linear regression (MLR) technique was applied in this study to investigate the influence of natural and anthropogenic variables on chemical concentrations observed at MLO. Concentrations of anthropogenic NSS-sulfate as well as of selected continental tracers were used as independent variables while selected emissions and meteorological variables were used as dependent variables. This regression model was used to calculate predicted values of a single dependent variable array, \hat{y}_i , given multiple independent variable arrays, x_{ki} , each containing n data points using equation:

$$\hat{y}_i = \beta_{0i} + \beta_{1i}x_{1i} + \beta_{2i}x_{2i} + \dots + \beta_{ki}x_{ki}, \quad i = 0, 1, \dots, n \quad (2.5)$$

The residual error, ε , is the difference between the observed (y_i) and predicted (\hat{y}_i) dependent variables. Each β coefficient is calculated considering all dependent variables simultaneously and can be interpreted as the response of y to changes in each x . The β coefficients are determined by using ordinary least squares which minimizes the sum of the squared residuals (RSS):

$$RSS = \sum_{i=1}^n (y_i - \beta_{0i} - \beta_{1i}x_{1i} - \beta_{2i}x_{2i} - \dots - \beta_{ki}x_{ki})^2, \quad i = 0, 1, \dots, n \quad (2.6)$$

A student's t-test was performed separately on each independent variable to determine if the results were significant at the 90% confidence level. The Pearson correlation coefficient was calculated for the observed and modeled independent variables to determine the strengths and weaknesses of the regression model.

The application of MLR requires that a set of basic assumptions be made about both the independent and dependent variables. All MLR results were evaluated using graphical

techniques to determine the validity of four statistical assumptions that are made when MLR is applied to data: normality, linearity, independence, and homoscedasticity (Nau et al., 2013).

Normality of the data was tested with a normal probability plot of the model residual values to determine if the error value associated with the regression solution was normally distributed. Using this method, the residual distribution quantiles are compared with quantiles from a normal distribution with the same sample size, mean, and standard deviation. If the residual values are normally distributed, the normal probability plot should exhibit a linear pattern. Large deviations from a linear fit represent non-normality, and can be a clue to how best to handle the violation of the assumption (NIST/SEMATECH, 2013). Linearity between the independent and dependent variables was tested by plotting model residuals as a function of model predicted dependent values. This plot was examined for obvious signs of curvature which may indicate that a linear relationship does not exist between the dependent and independent variables. Independence of the data was tested by analyzing autocorrelation plots of the model residuals to check for serial correlation. This technique provided an indication as to whether the data were highly correlated when lagged by a certain time interval. The Durbin-Watson statistic was calculated as a quantitative significance test. This statistic analyzes the significance of the autocorrelation residual at lag 1 and should be approximately equal to 2, and the autocorrelation coefficients should fall within $\pm \frac{2}{\sqrt{n}}$ of zero, where n is the number of data points used in the regression analysis. The upper and lower bounds on this preferred interval are also included on the autocorrelation plot. Residuals were plotted against both time and model predicted concentration to test for violations of homoscedasticity, or consistent variance with time. These plots were used to determine whether the residuals consistently increased with time, indicative of an unexplained trend.

After preliminary evaluation of these graphical tests, it was determined that applying a logarithmic transformation to all chemical datasets would correct violations of normality and linearity which are common in chemical datasets. A natural logarithm transformation was therefore applied to all dependent datasets prior to regression while the data used as independent variables remained unaltered. Comparisons observed and predicted dependent variables utilize results which have been transformed back into concentration units by applying the exponential function to the model results. Complete statistical assumption test results for radon, carbon monoxide, and anthropogenic NSS-sulfate are included in Appendix (B).

3. MLO Sulfate Aerosol Observations

3.1 Influence of Natural Sulfate Sources

3.1.1 MLO Sea Salt Sulfate and Biogenic Sulfate

Average concentrations and contributions of natural and anthropogenic components towards total sulfate observed at MLO are summarized in Table (3.1). Sulfate at MLO is largely dominated by anthropogenic NSS-sulfate although both sea-salt and biogenic (DMS-derived) components contribute a non-negligible portion of total sulfate at certain times. The average seasonal cycle of total sulfate, with separated contributions from each component is shown in Figure (3.1).

Sea-salt sulfate is the smallest component at MLO, contributing approximately 1.8% of total observed sulfate mass on average during 1995-2008 although this minor contribution was expected at the altitude of MLO. Sea salt must be lofted very high into the atmosphere, typically as a result of very strong convection, to be observed at this receptor site. Sofiev et al. (2011) report that although sea-salt concentrations typically decrease with increasing altitude, they have been found to increase with altitude in certain tropical locations as a result of deep convection along the intertropical convergence zone which likely also contributes to the observed sea salt sulfate at MLO.

Biogenic sulfate contributed approximately 15% of total sulfate on average during 1995-2008. As discussed in previous sections, the estimated biogenic sulfate concentrations are based on an assumed ratio between DMS oxidation products (MSA and NSS-sulfate) although this ratio is highly temperature dependent, has generally been measured in the marine boundary layer, and has uncertain relevance at a high-altitude tropical location. Error in calculated biogenic NSS-sulfate concentrations likely results from the assumption that all DMS oxidation

occurred in approximately the same boundary layer relevant temperature range. It has been suggested that the fraction of DMS oxidized to MSA increases with decreasing temperature and therefore also with increasing latitude (Castebrunet et al, 2009). If DMS oxidation occurred in the boundary layer prior to transport to MLO, the ratio of 0.07 may be an underestimate when compared to the higher latitude (and therefore lower temperature) Midway Island location, resulting in an overestimate of biogenic contribution.

The average of all observed MSA concentrations was 1.39 ng/m^3 at MLO while MSA concentrations were found to range between 10 and 50 ng/m^3 at Midway Island (Prospero et al., 2003). Although biogenic NSS-sulfate comprised a much smaller fraction of total sulfate at MLO than at Midway Island, the observed seasonal cycle in biogenic NSS-sulfate was similar (Prospero et al., 2003). At Midway Island, biogenic sulfate was found to peak during spring (May) with a possible secondary peak during summer (August) and lowest concentrations during autumn and winter (Prospero et al., 2003). At MLO, a similar seasonal cycle is observed although the springtime and summertime peaks appear to have shifted one month earlier, with highest concentrations in March and April and the secondary peak in July, as shown in Figure (3.2).

15.3% of total sulfate and 15.7% of NSS-sulfate at MLO was attributed to biogenic DMS emissions. This result is in agreement with the average contribution of DMS emissions to column NSS-sulfate over the Hawaiian Islands modeled by Gondwe et al. (2003) and shown in Figure (3.3). Gondwe et al. (2003) reported that approximately 15-20% of column NSS-sulfate atmospheric burden could be attributed to DMS emissions over Hawaii. They also reported a lower percentage contribution from DMS during the winter (DJF) months at this location which is consistent with MLO observations.

Figure (3.4) shows concentration weighted HYSPLIT back trajectories using MSA concentrations at MLO during 1995-2008. The weighted trajectories illustrate the fact that MSA concentrations were often elevated at times when the air mass observed at MLO passed over the region south and southeast of MLO, between the 0-15°N latitude band. Transport through these high DMS regions prior to arrival at MLO was less common than from the North, however, a clear north-south gradient was detected in MSA concentration weighted trajectories approaching MLO.

This result is consistent with the current understanding of oceanic regions of high DMS emissions, which serves as the precursor of secondary MSA (Korhonen et al., 2008). Although the largest fluxes of DMS occur in the southern hemisphere, the largest DMS emissions within the domain of interest for this study occur along the equatorial region south of the Hawaiian Islands and across a zonal band extending eastward towards Southern Mexico and Central America (Chapter 1, Section (1.6.2), Figure (1.15)). The lifetime of DMS is dependent on ambient concentrations of oxidants (OH and nitrate) but has been found to be as short as 12 hours during the summer season when OH concentrations are generally high as a result of increased solar radiation (Gondwe et al., 2003). Transport through this tropical region is also most common in summer. A short DMS lifetime in this region suggests that oxidation to MSA would have occurred near the source of DMS emissions prior to transport to MLO so source regions for the two species should be collocated. Frequent convection in the warm equatorial intertropical convergence zone likely provided a mechanism for introduction of near surface DMS and MSA to higher altitudes before transport to the MLO site. This pattern is consistent with the zonally averaged vertical profile of NSS-sulfate attributed to DMS emissions, shown in Figure (3.5) (Gondwe et al., 2003). The approximate location of MLO (19.54° N and 680mb)

was added to the figure, symbolized with a black symbol. At this location, there was a similar meridional gradient in biogenic NSS-sulfate as observed using concentration weighted trajectories, with a larger biogenic component south of MLO and lower biogenic component north of MLO where anthropogenic pollution sources are much greater.

Table 3.1: Daily average concentration and contribution to total sulfate of sea-salt sulfate, biogenic NSS-sulfate, and anthropogenic NSS-sulfate

MLO Contributions to Total Sulfate 1995-2008		
Component	Mean Concentration	Mean Fraction of Total Sulfate
Sea-Salt Sulfate	3.016 (+/- 8.25) ng/m ³	1.79 (+/- 3.90)%
Biogenic NSS-Sulfate	18.6 (+/- 17.9) ng/m ³	15.3 (+/- 17.4)%
Anthropogenic NSS-Sulfate	0.175 (+/- 0.200) μg/m ³	83.2 (+/- 17.4)%

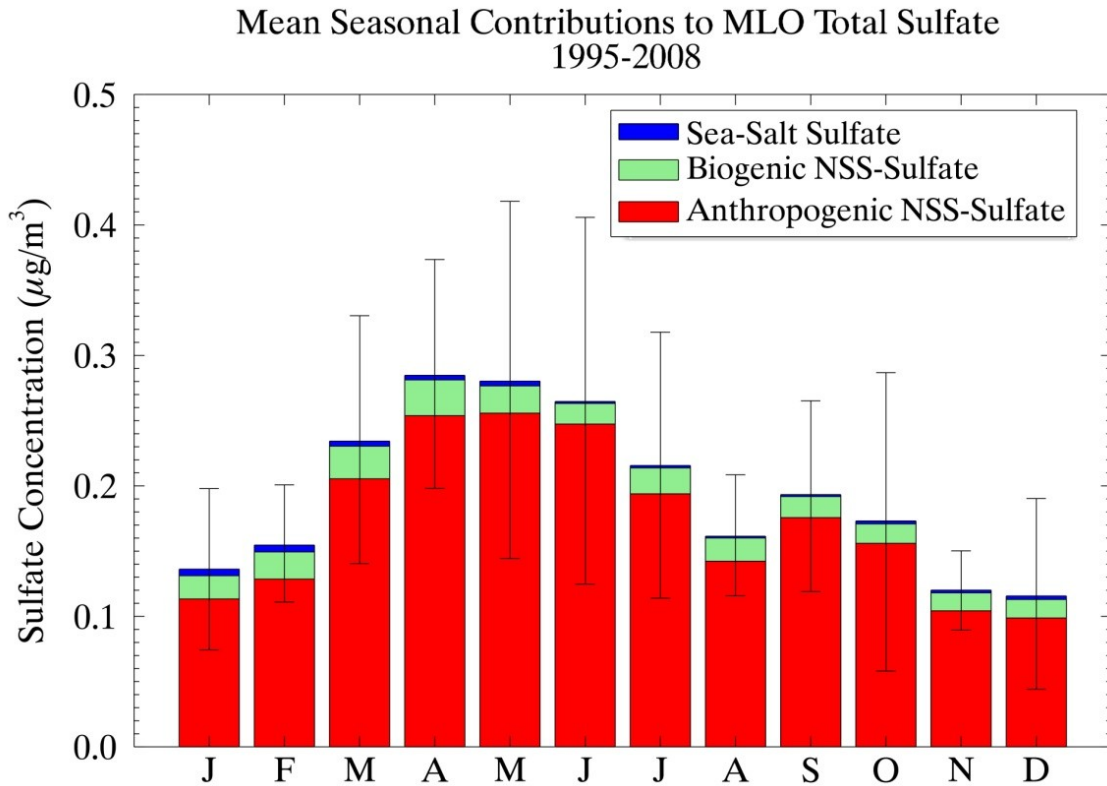


Figure 3.1: Mean seasonal cycle of sea salt, biogenic, and anthropogenic components of MLO total sulfate. Error bars represent the standard deviation of all available monthly mean total sulfate concentrations.

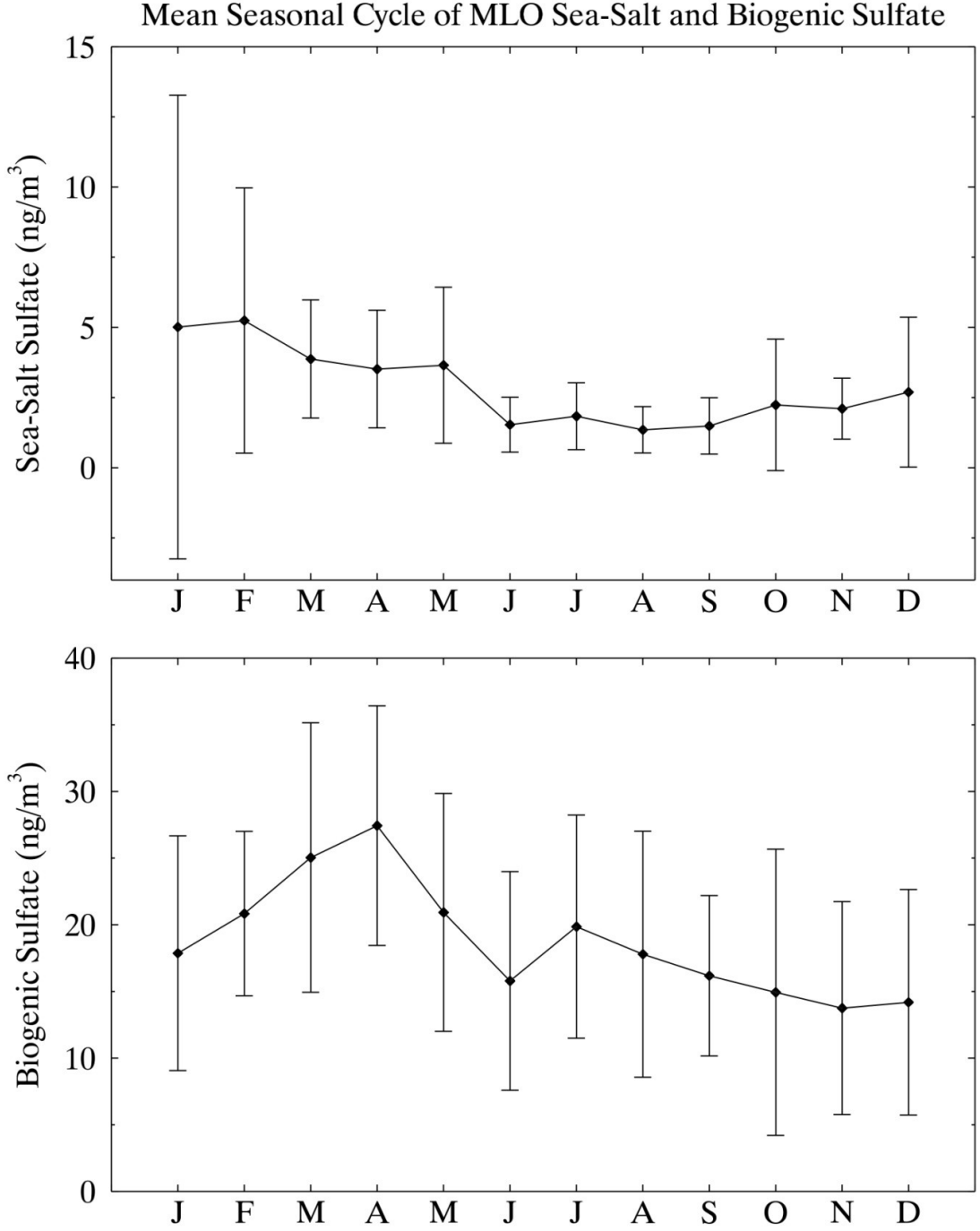


Figure 3.2: Mean seasonal Cycle of MLO sea-salt sulfate and biogenic (DMS derived) sulfate concentrations. Error bars represent the standard deviation of all available monthly mean concentrations.

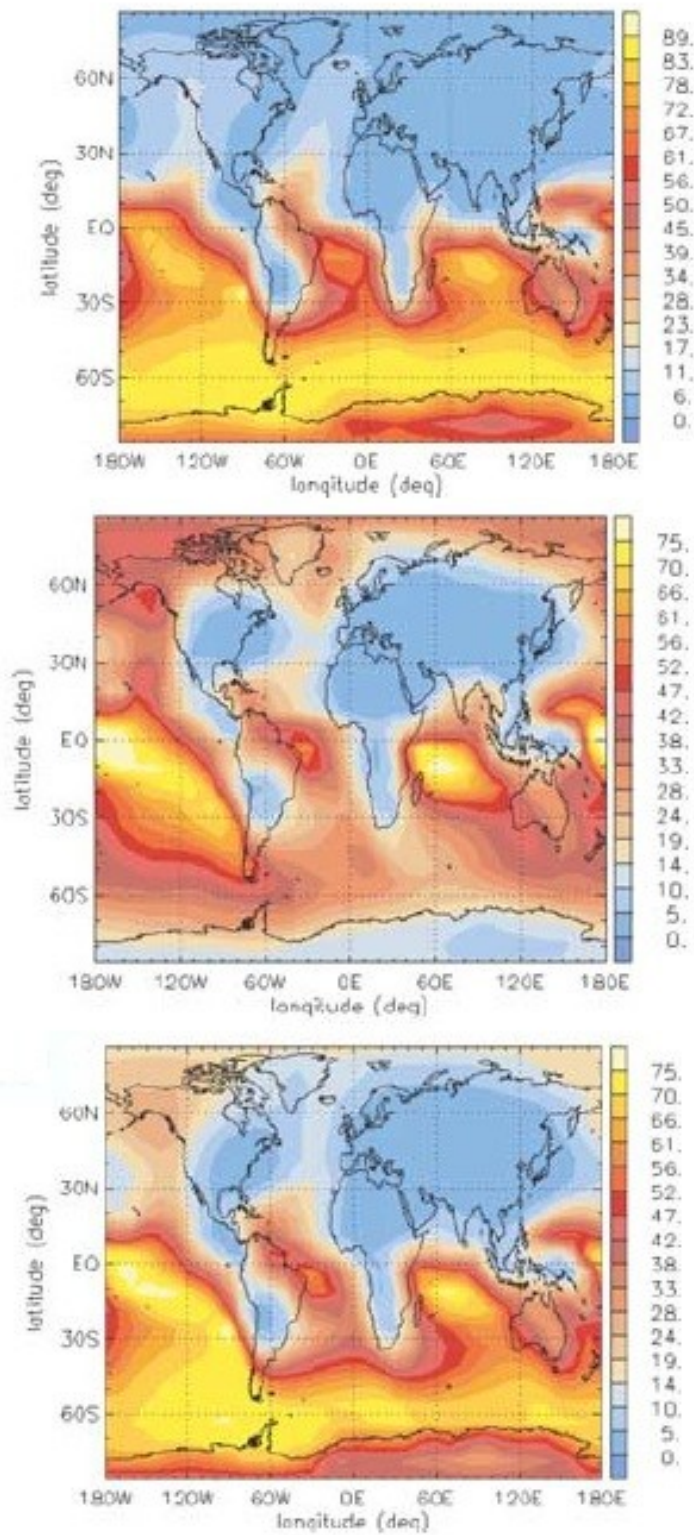


Figure 3.3: Percentage of NSS-sulfate attributed to oceanic DMS emissions in December-January-February (top), June-July-August (middle), and the annual average (bottom) Gondwe et al. (2003).

Methanesulfonate (MSA) Concentration Weighted Trajectories
1995-2008

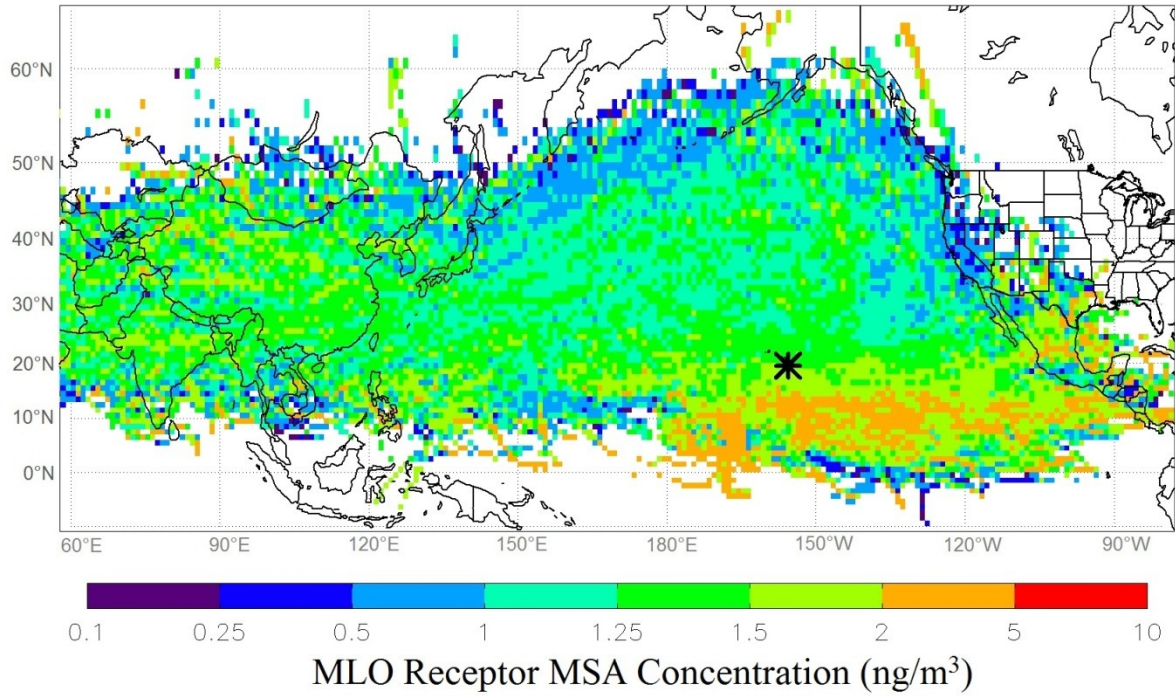


Figure 3.4: Concentration weighted trajectories of MLO methane sulfonic acid concentration from 1995-2008.

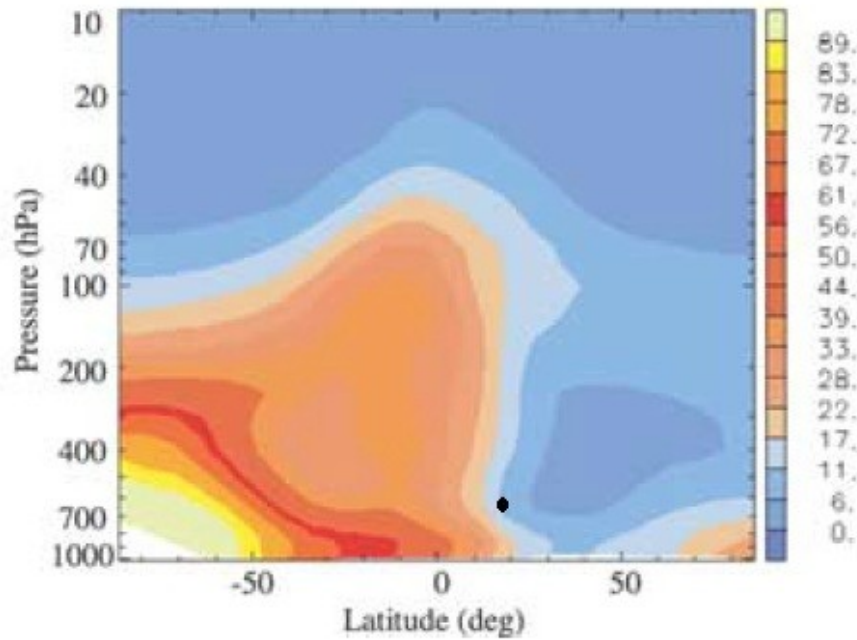


Figure 3.5: Percentage of annually averaged zonal mean vertical distribution of biogenic NSS-sulfate modified from Gondwe et al. (2003).

3.1.2 Volcanic Sulfate

Monthly and annual mean Kilauea Volcano emissions rates from the Summit (blue) and from the East Rift (red) as calculated from the limited available daily observations are displayed in Figure (3.6). Mean monthly anthropogenic NSS-sulfate concentrations which were screened to remove volcanic influence (Section (2.1.1)) are plotted in black. In general, there appeared to be little direct connection between Kilauea Volcano emission rates and MLO anthropogenic NSS-sulfate although there are slightly offset corresponding peaks in both Kilauea emissions and anthropogenic NSS-sulfate concentrations during select months. Both datasets exhibit large positive deviations during 2001, 2005, and 2008. East rift emissions were at least an order of magnitude greater than summit emission rates throughout the time period until after the spring of 2008 when a dramatic increase in summit emissions was observed after the documented eruption and anthropogenic NSS-sulfate concentrations spiked shortly after. The SO₂ plume observed by the Ozone Monitoring Instrument (OMI) onboard NASA's Aura satellite shortly following the eruption in March 2008 is shown in Figure (3.7). Although the plume appears to wrap around Mauna Loa Volcano, the plume height remained well below the height of MLO as shown by the frequency of plume height observations above sea level in Figure (3.8).

When the entire study time period (1995-2008) was considered, no statistically significant correlation was found between monthly mean anthropogenic NSS-sulfate concentrations and either summit SO₂ emission rates ($R^2=0.08$) or east rift SO₂ emission rates ($R^2=0.01$). The anomalously high peak in springtime anthropogenic NSS-sulfate at MLO during 2008 suggests that perhaps the region is being impacted by the higher summit emission rates which had not been observed during the previous years. The correlation between anthropogenic NSS-sulfate and summit emission remains weak ($R^2=0.09$) for the year of 2008 alone but

improves slightly ($R^2=0.17$) when a 1 month lag is applied so that anthropogenic NSS-sulfate concentrations are compared with summit emissions from the previous month (as shown in Figure (3.9)). Despite the screening process designed to remove volcanic influence from the MLO aerosol observations, certain similarities existed in the emissions and sulfate aerosol datasets which provided motivation to include the volcanic emissions to represent a possible source in additional analyses of anthropogenic NSS-sulfate aerosol. Due to the irregularly spaced Kilauea SO_2 observations, several monthly emissions estimates were missing data during 1995-2008 so annual emissions totals calculated by Elias and Sutton (2012), shown in Figure (3.10), were used for further analyses.

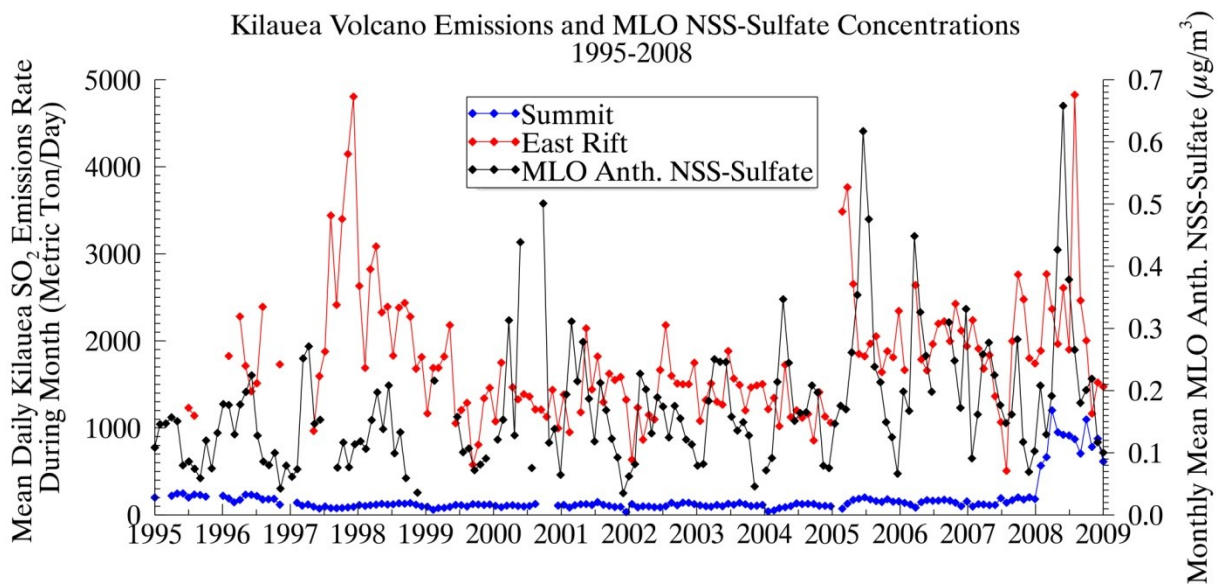


Figure 3.6: Timeline of mean monthly and annual SO_2 emission rates from the Kilauea Volcano summit (blue) and east rift (red) and mean anthropogenic NSS-sulfate concentrations at MLO for each month during 1995-2008 data from Elias and Sutton (2012).

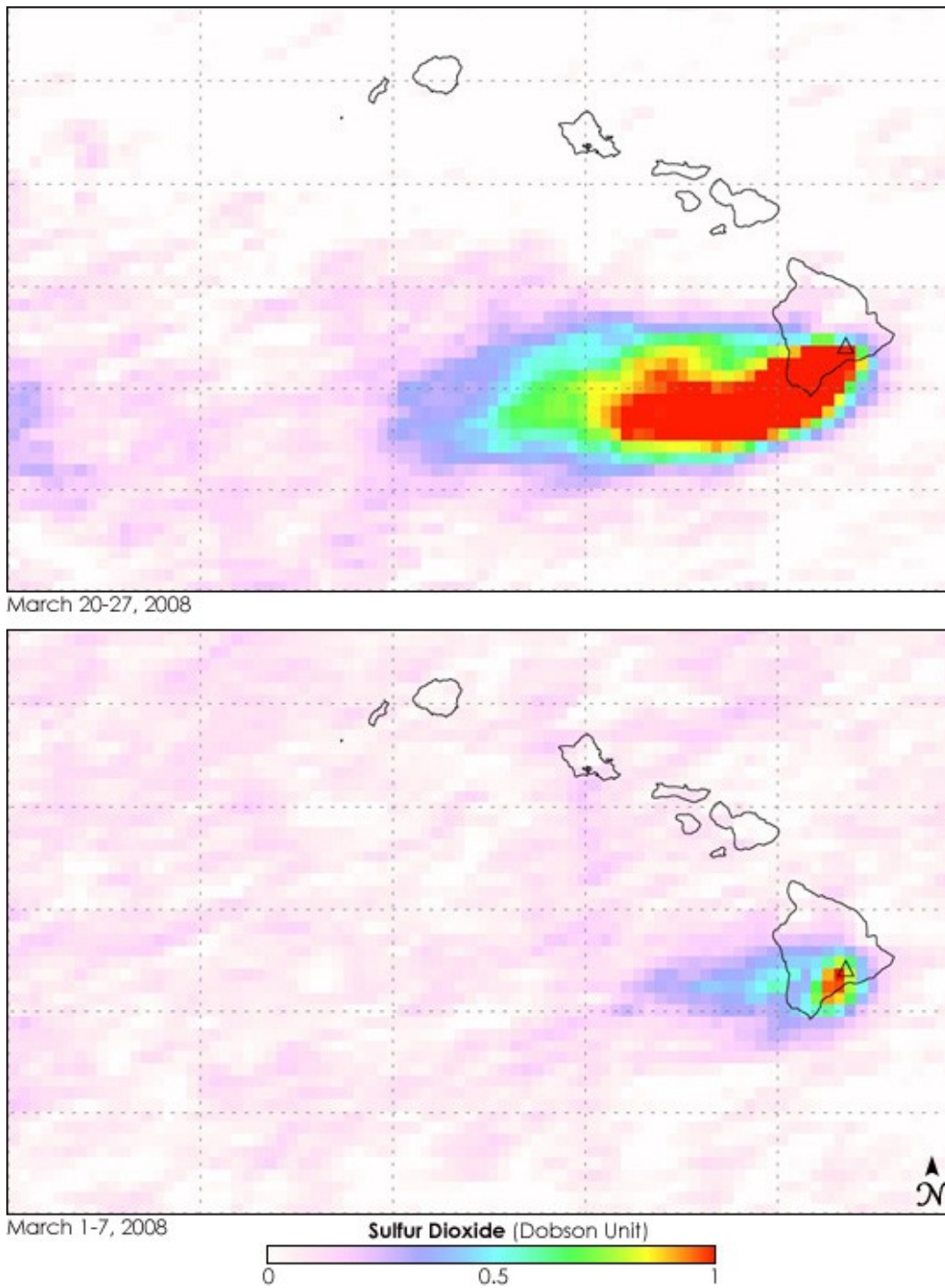


Figure 3.7: SO₂ plume from Kilauea Volcano East Rift eruption during March 2008 from NASA Earth Observatory (2008).

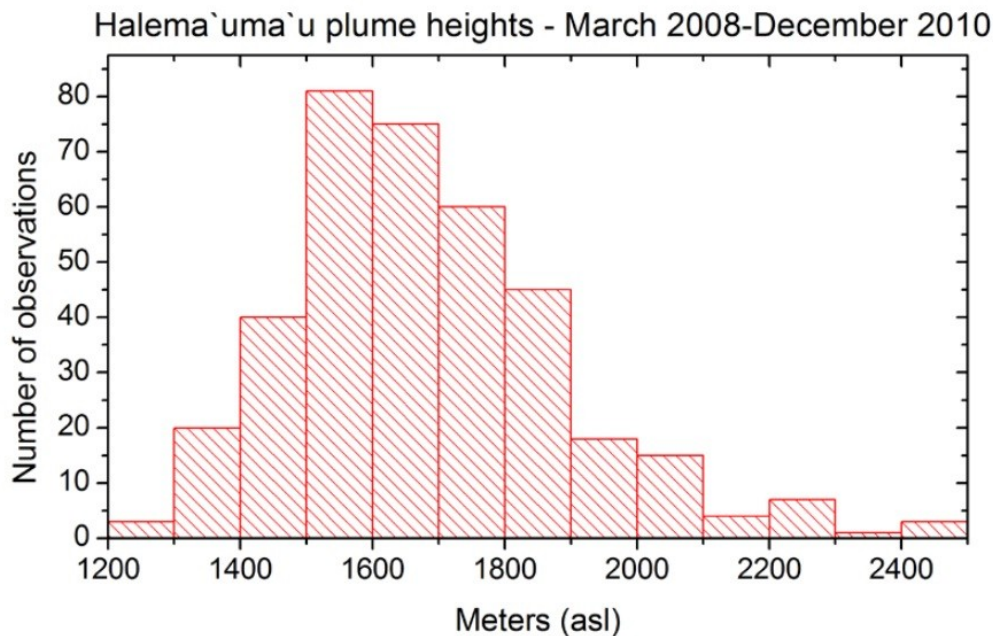


Figure 3.8: Kilauea summit crater plume heights during March 2008-December 2010 from Elias and Sutton (2012).

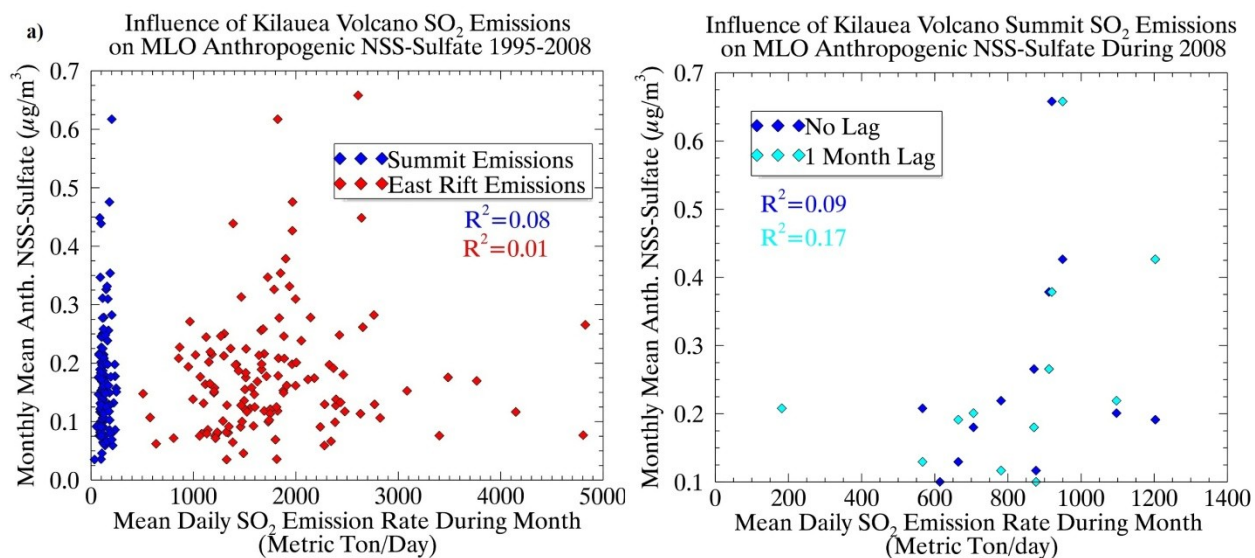


Figure 3.9: Correlation of Kilauea summit SO₂ emissions and MLO anthropogenic NSS-sulfate concentrations during 1995-2008 (a) and 2008 only (b). Data from Elias and Sutton (2012).

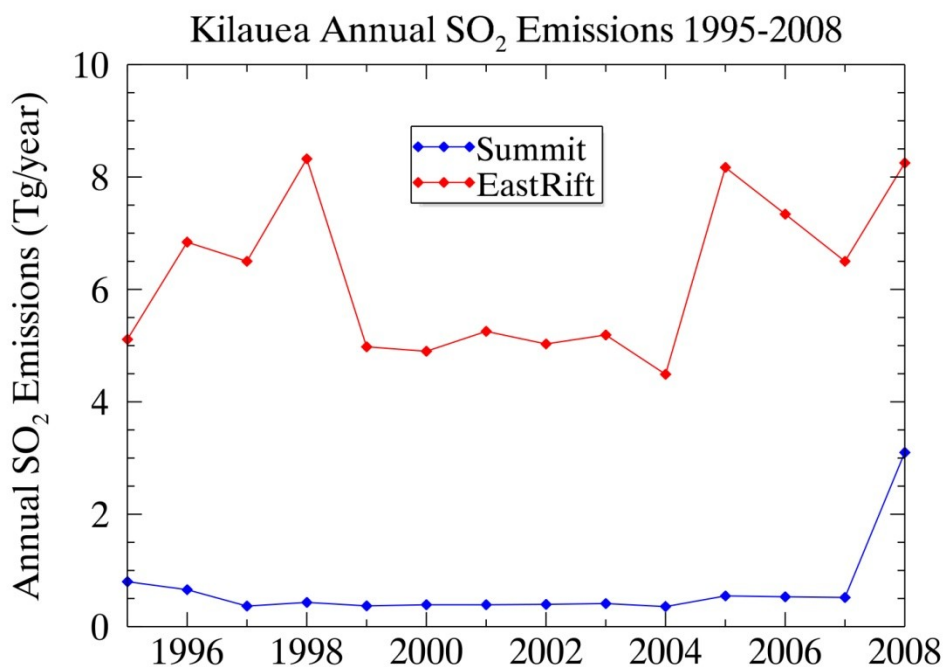


Figure 3.10: Annual total SO₂ emission rates from Kilauea from Elias and Sutton (2012).

3.2 MLO Anthropogenic NSS-Sulfate

3.2.1 Daily to Seasonal Variability

Daily, monthly mean, and monthly median concentrations of anthropogenic NSS-sulfate during 1995-2008 are shown in Figure (3.11). Daily concentrations (black) exhibited very high variability with concentrations spanning several orders of magnitude. Monthly mean concentrations (green) varied between 0.03 and 0.7 $\mu\text{g m}^{-3}$ during the study period. In general, overnight integrated anthropogenic-NSS sulfate concentrations were very low compared with typical urban concentrations and more representative of background levels although periods of relatively high concentrations typically occurred over multiple consecutive daily observations. The mean seasonal cycle of anthropogenic NSS-sulfate concentration during 1995-2008 is shown in Figure (3.12). Maximum concentrations occurred during the springtime although a secondary concentration peak occurred during autumn. Figure (3.12a) shows combined daily averages from 1995-2008 while Figure (3.12b) shows combined monthly averages during 1995-

2008. Although this seasonal cycle was fairly consistent during 1995-2008, interannual variability is high as indicated by the scatter in Figure (3.12a) and the large standard deviation error bars in Figure (3.12b). The largest amount of variability occurred during the same months that high concentrations occurred (April, May, June) while months with low concentrations (November, December, January) exhibited less variability from year to year.

Anthropogenic NSS-sulfate concentration weighted trajectories for 1995-2008 are shown in Figure (3.13). Possible anthropogenic contributions from both the American and Asian continent were detected from this method as indicated by the higher than average anthropogenic NSS-sulfate concentrations at MLO during periods of time when trajectories passed over these continental source regions. Then relationships are further analyzed in Section (4.1.1).

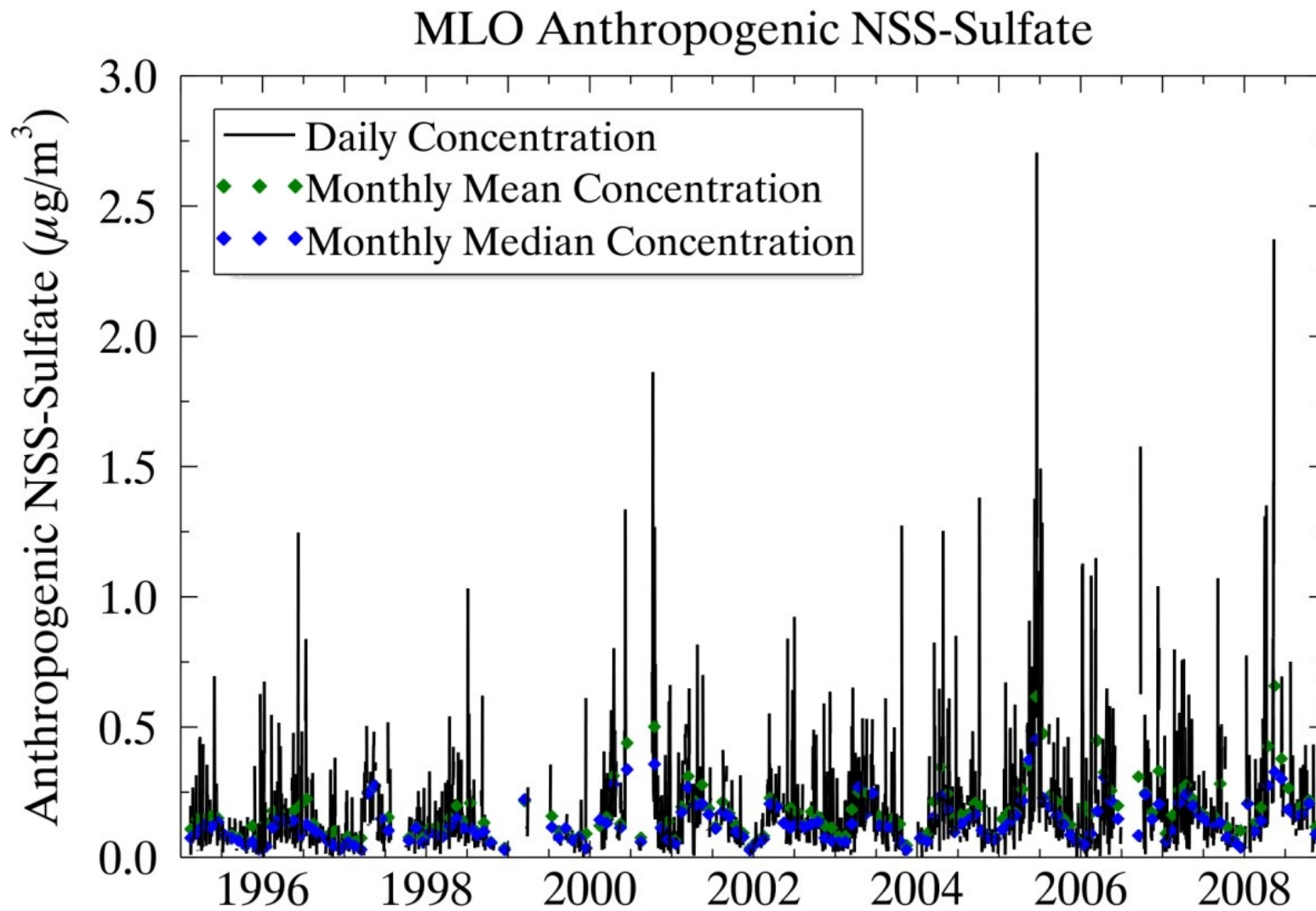


Figure 3.11: Daily, monthly mean, and monthly median anthropogenic NSS-sulfate concentrations at MLO.

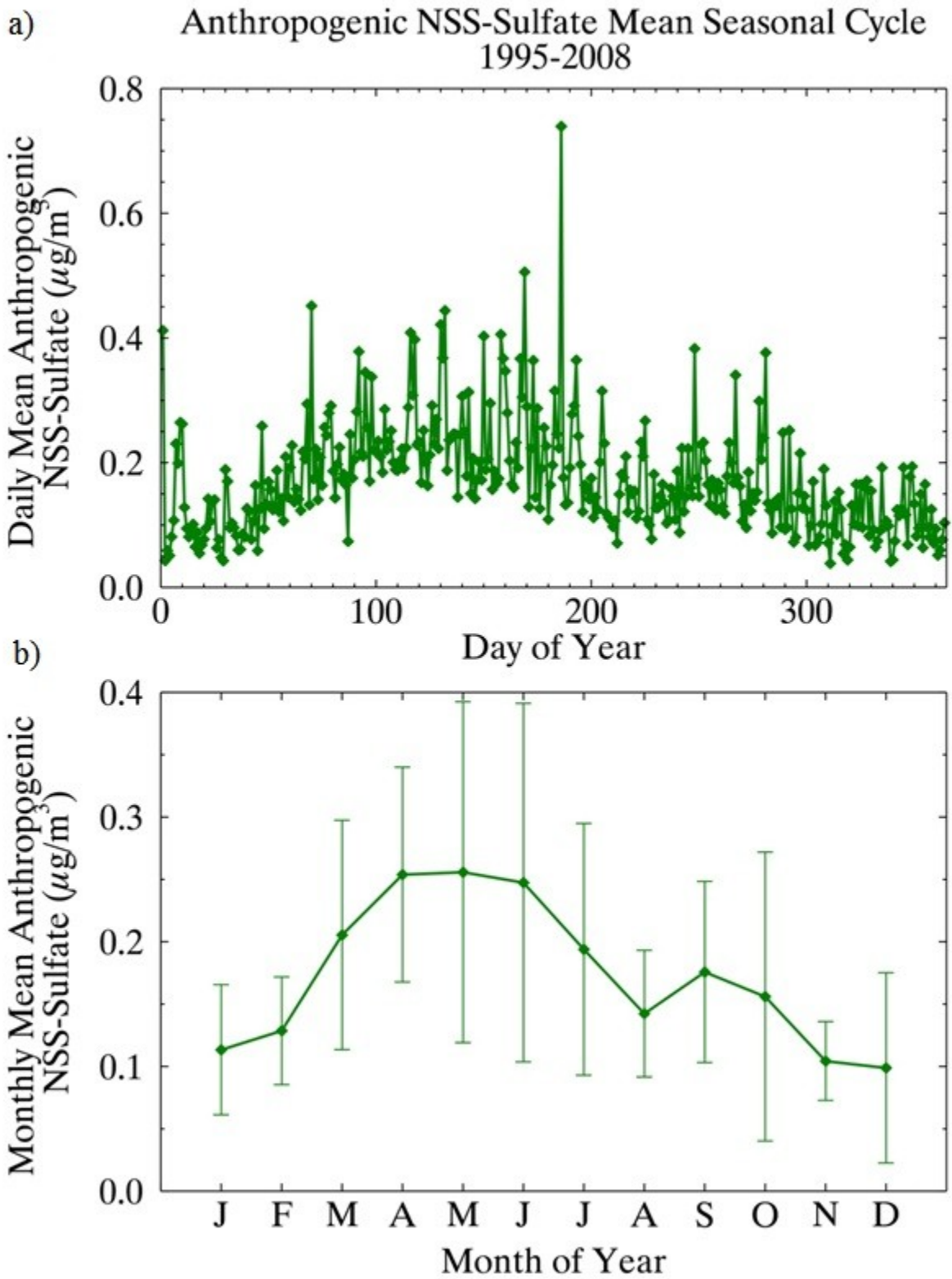


Figure 3.12: Seasonal cycle in mean concentrations of anthropogenic NSS-sulfate at MLO 1995-2008 using mean day of year concentrations (a) and mean monthly concentrations (b).

Anthropogenic NSS-Sulfate Concentration Weighted Trajectories 1995-2008

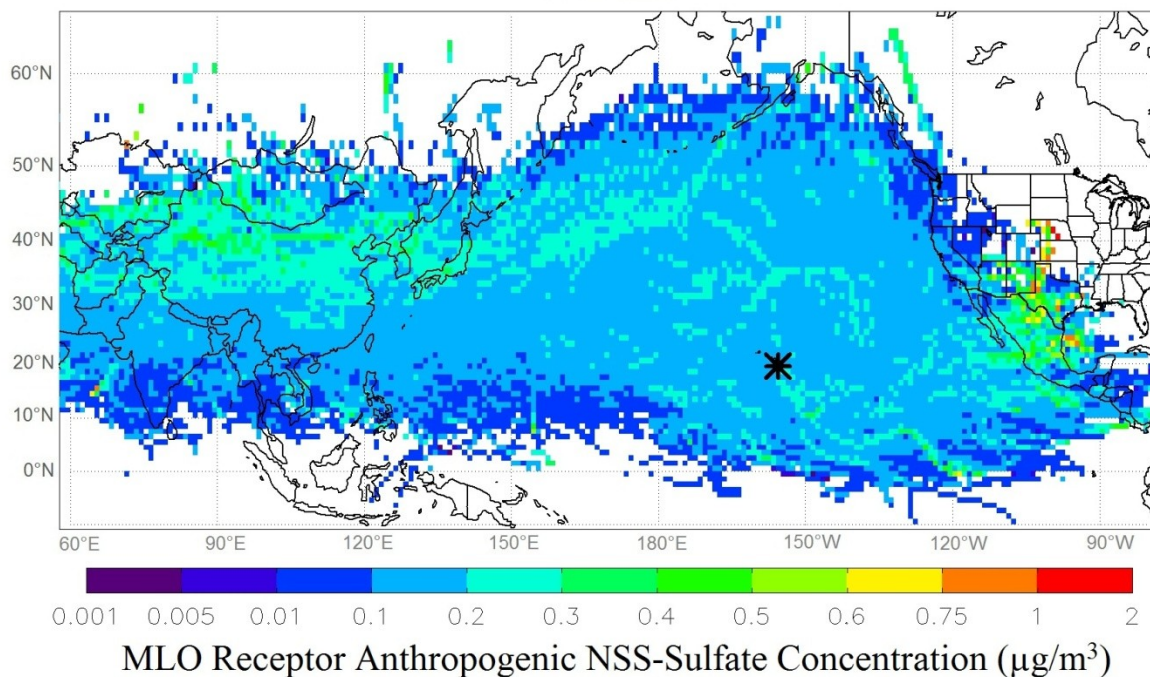


Figure 3.13: MLO 10-day HYSPLIT back trajectories weighted with receptor anthropogenic NSS-sulfate concentrations

3.2.2 Interannual Variability and Trends

A statistically significant (>90%) increasing trend in monthly anthropogenic NSS-sulfate concentrations at MLO was identified during the time period of 1995-2008 as shown in Figures (3.14) and (3.15). Trends were calculated for monthly mean and median concentrations as well as combinations of annual and seasonal concentrations. Mean (median) anthropogenic NSS-sulfate concentrations increased on average at a rate of 4.8% (4.4%) equivalent to $7.3 \text{ ng}/\text{m}^3$ ($5.0 \text{ ng}/\text{m}^3$) per year between 1995 and 2008. A trend of 6.2% (4.7%) or $14.2 \text{ ng}/\text{m}^3$ ($9 \text{ ng}/\text{m}^3$) was observed for mean (median) springtime (March-April-May) concentrations as shown in Figures (3.14) and (3.15). An increasing trend of approximately 5% per year representing $8.4 \text{ ng}/\text{m}^3$ ($6.7 \text{ ng}/\text{m}^3$) was observed for annual mean (median) concentrations between 1995 and 2008.

Hand et al. (2012b) reported that the IMPROVE monitoring site located in Hawaii Volcanoes National Park (19.43°N, 155.26°W, 1258.5m ASL) was one of only three sites in the country to experience increasing trends in annual mean sulfate during 2000-2010. Sulfate aerosol concentrations increased at a rate of 9.4% per year at this site during 2000-2010 although the location of this site relative to MLO makes it more likely to be influenced by the increase in Kilauea emissions during 2008. The statistical significance of the trend ($p < 0.01$) suggests that other factors besides an increase during a single year may have contributed to the increasing trend over a ten year period.

Figures (3.16) and (3.17) show the trends in MLO anthropogenic NSS-sulfate concentrations for the mean and median concentrations during each calendar month available for analysis. Calendar months with red text exhibited statistically significant (>90%) increasing trends during 1995-2008. Statistically significant trends were observed in both mean and median concentrations during the springtime months of April and May and the autumn months of August, September, and October. The largest annual percentage increase in anthropogenic NSS-sulfate was observed in August, September, and October because concentrations were typically lower during these months than during the springtime although the largest trend in terms of additional anthropogenic NSS-sulfate mass per year was observed during the spring. The timing of the springtime and early autumn increasing trends corresponded to the timing of both the primary and secondary peak concentrations observed in the anthropogenic NSS-sulfate seasonal cycle.

All available anthropogenic NSS-sulfate concentrations were also deseasonalized and standardized anomaly values were analyzed to evaluate the relative importance of months with and without statistically significant trends as shown in Figure (3.18). A highly significant

($p < 0.01$) positive trend of larger magnitude that observed for the seasonal monthly data was found for the deseasonalized data. This result indicates that the seasons with increasing anthropogenic NSS-sulfate trends were more important than the seasons without increasing trends at MLO and that, despite a few exceptions, anthropogenic NSS-sulfate concentration were generally higher towards the end of the study period (2005-2008) than towards the beginning of the study period (1995-1999) regardless of season.

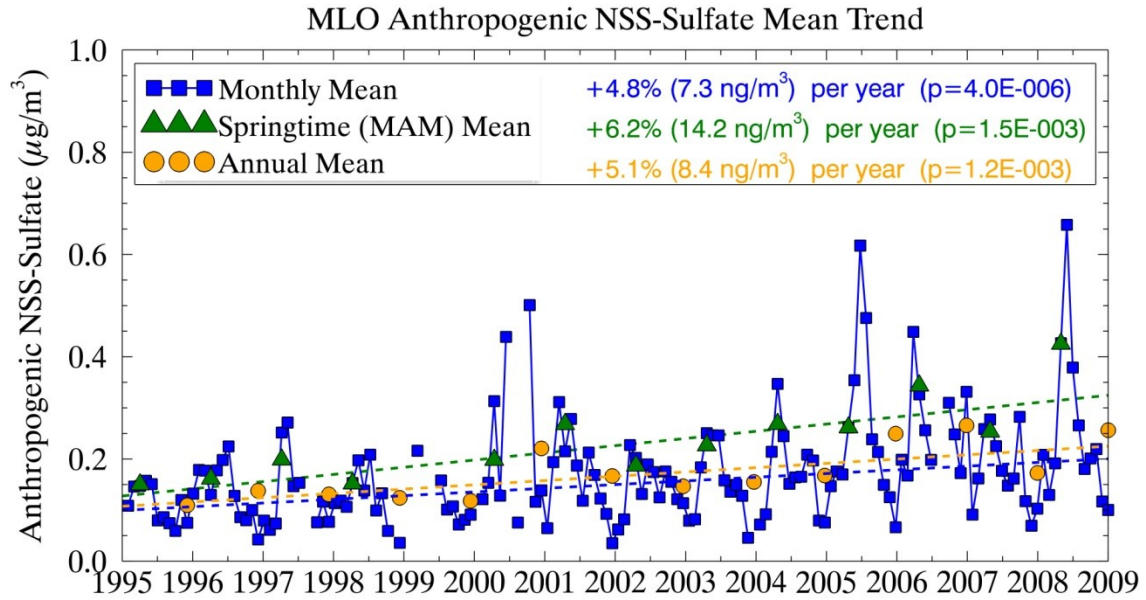


Figure 3.14: Trend in MLO anthropogenic NSS-sulfate based on monthly (blue squares), March-April-May (green triangles), and annual (orange circles) mean concentrations.

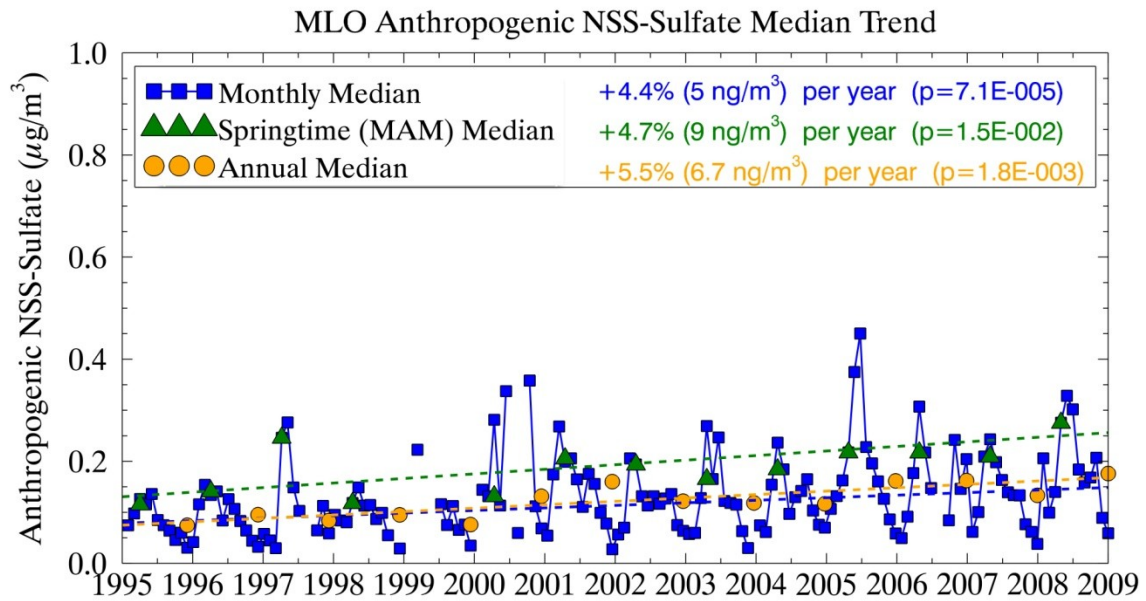


Figure 3.15: Trend in MLO anthropogenic NSS-sulfate based on monthly (blue squares), March-April-May (green triangles), and annual (orange circles) median concentrations.

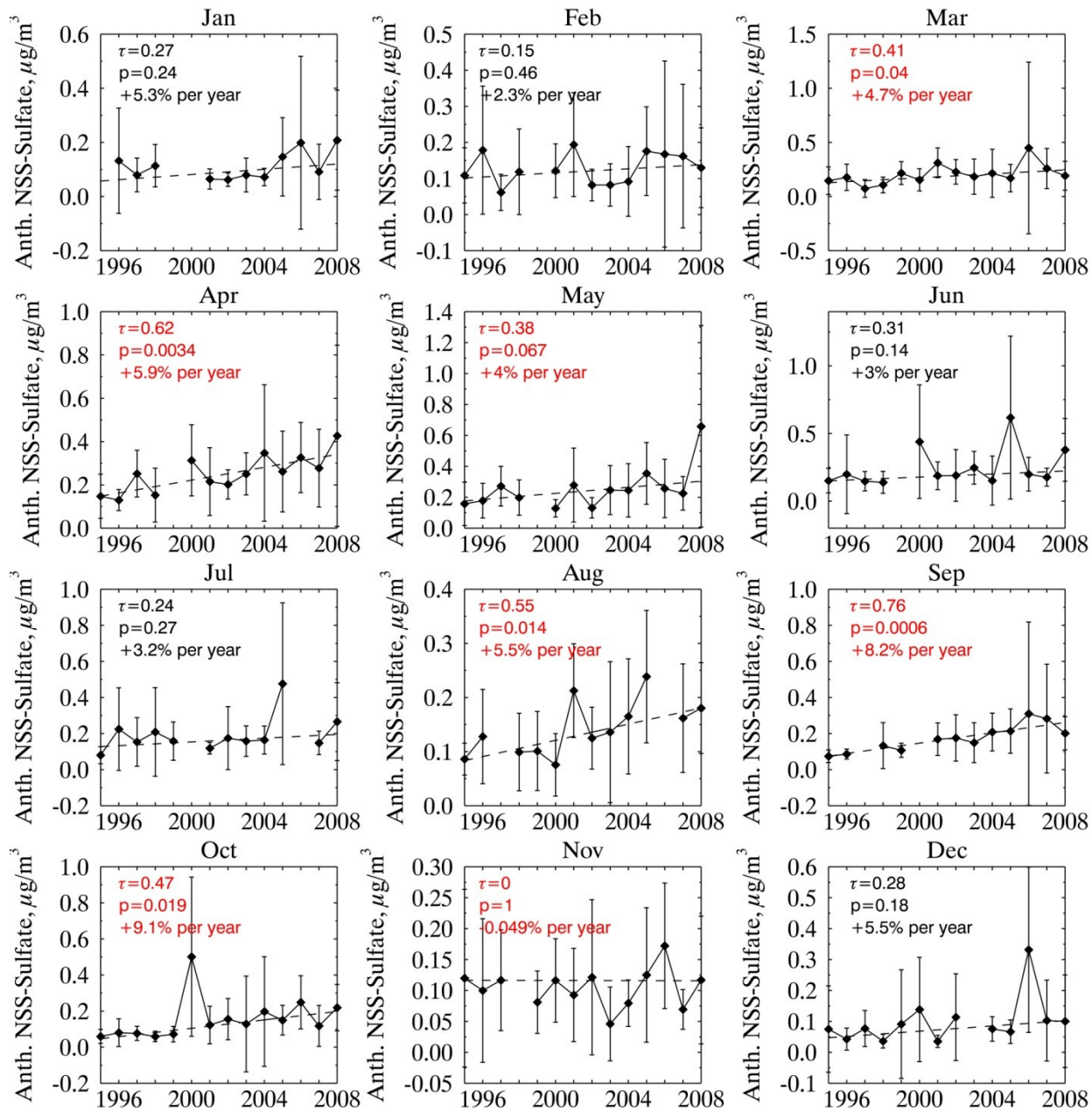


Figure 3.16: Annual trends in anthropogenic NSS-sulfate calculated separately for mean concentrations during each calendar month.

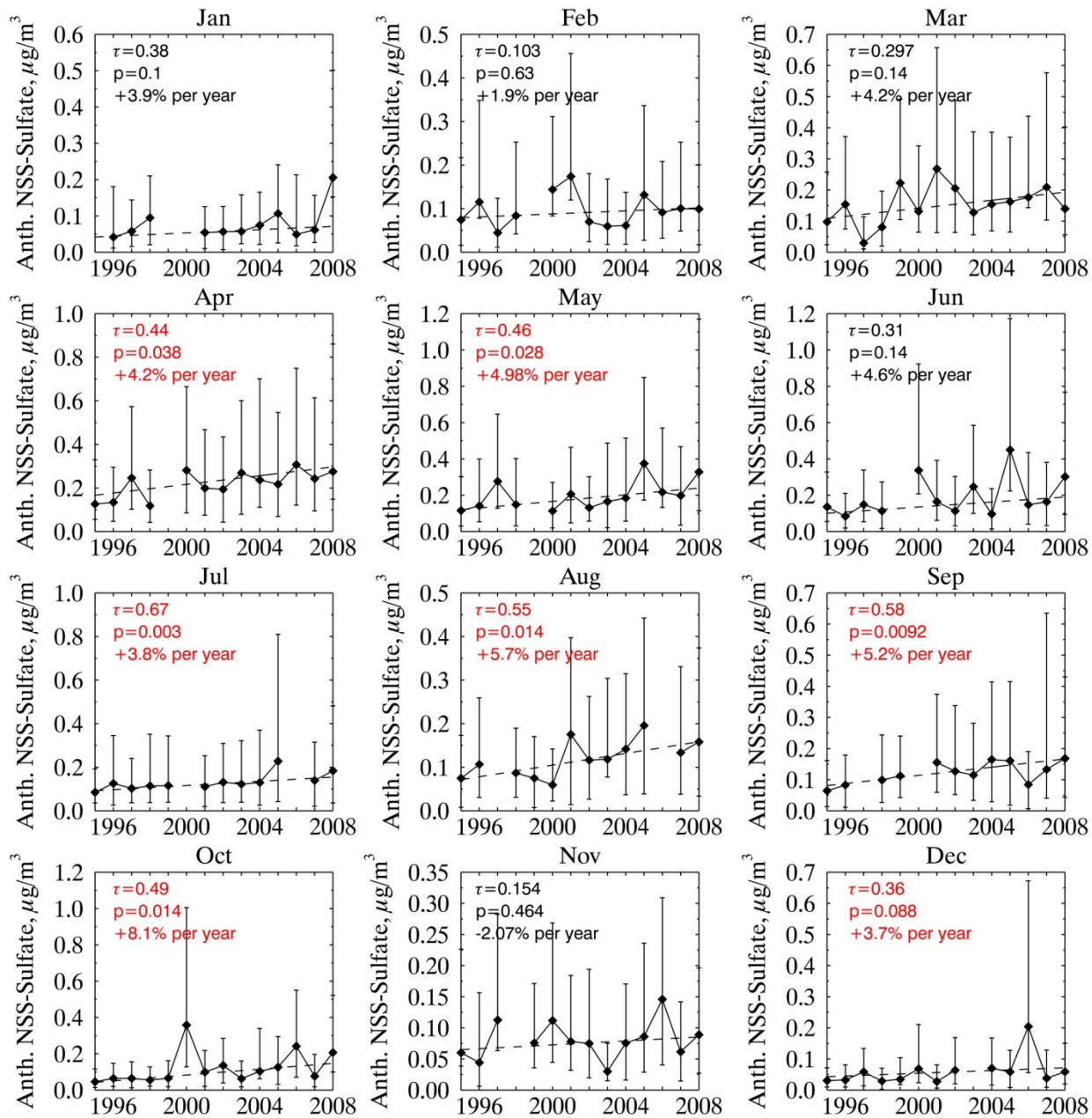


Figure 3.17: Annual trends in anthropogenic NSS-sulfate calculated separately for median concentrations during each calendar month.

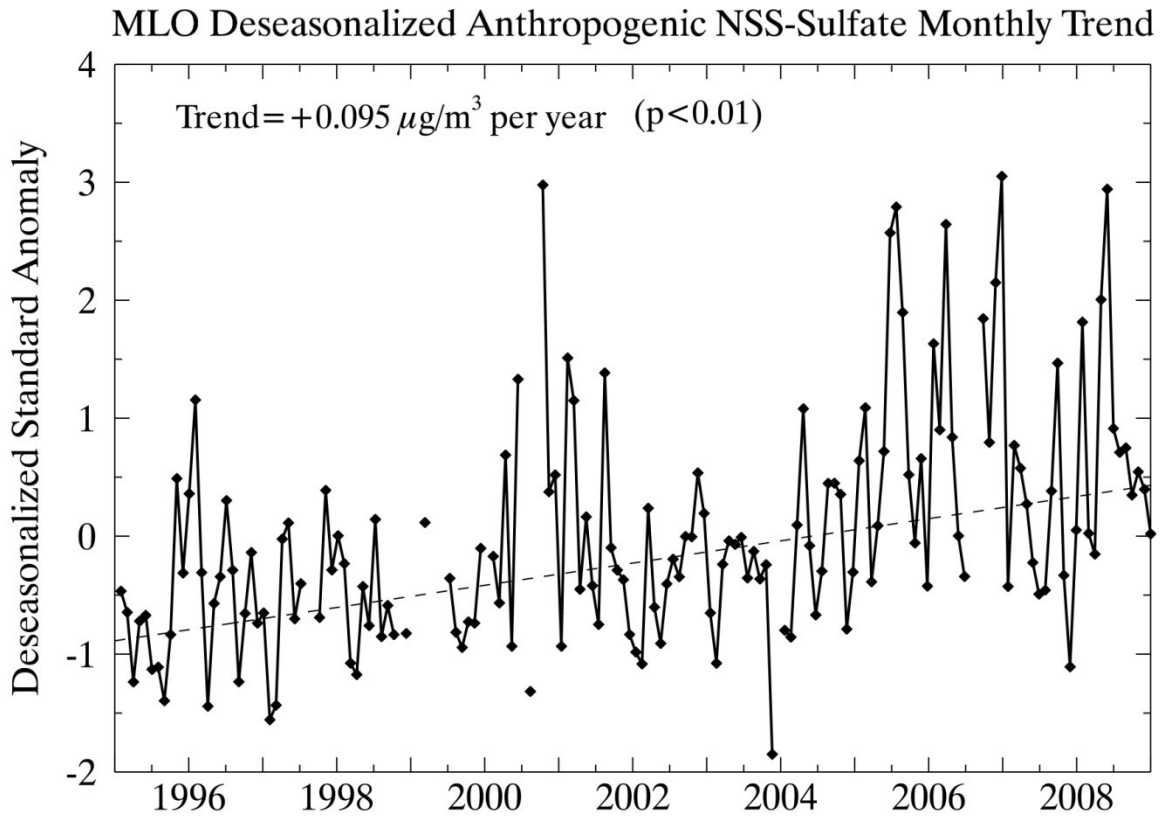


Figure 3.18: Deseasonalized anthropogenic NSS-sulfate using mean and standard deviation of concentrations during each calendar month for all available data during 1995-2008.

4. Attribution of Sulfate Trends to Emissions and Transport Variability

The fact that the statistically significant trends generally were observed during the same months that were found to have the highest average concentrations suggests that the same set of phenomena were likely controlling both the seasonal cycle and long term trends in anthropogenic NSS-sulfate concentrations at MLO. It was hypothesized that the secondary peak in anthropogenic NSS-sulfate concentrations was primarily controlled by transport from the American continent and possible influences from biomass burning emissions, as indicated by the elevated concentrations over the American continent in Figure (3.12), while the springtime peak was primarily controlled by anthropogenic emissions and meteorological patterns in East Asia. The observed patterns in anthropogenic NSS-sulfate were combined with information about meteorology, transport patterns, and anthropogenic precursor emissions to quantify the impact of recent increases in East Asian emissions on sulfate aerosol trends at MLO.

4.1 Continental Influence at MLO

4.1.1 HYSPLIT Trajectory Analysis

MLO 10-Day HYSPLIT back trajectories during 2007 are shown in Figure (4.1). Each day of the year contains three trajectories with MLO arrival times of 6Z, 12Z, and 18Z. Trajectory color represents the variations in modeled transport throughout time during the selected year with the arrival time of the trajectory at MLO indicated by the color scale. The seasonal pattern observed in daily trajectory pathway is present during all years included in the study although interannual variations in transport were observed in trajectory origin during the study period.

Residence time analysis results for the entire study period are shown in Figure (4.2). This method summarized daily trajectory information during 1995-2008 to identify regions

which were likely to serve as source regions to MLO. Grid boxes in the domain were colored based on the number of HYSPLIT endpoints which were recorded passing through the grid during 1995-2008. The lighter colored grids extending from East Asia into the Pacific indicated the most frequently observed long distance transport pathway to MLO. Over the entire study period, an air parcel observed at MLO had approximately the same likelihood of passing over any same-colored region before arriving at the receptor location.

The seasonal cycle of RTA results over the time period of 1995-2008 is shown in Figure (4.3). Transport from the East Asian region was most prevalent during winter and early spring with a transitional period during May/June, more prevalent influence from North America during July and August, and another transition period back towards strong wintertime East Asian influence in October/November. HYSPLIT trajectories were assigned to be of either East Asian or American origin when entering a region defined on the north, south, east, and west as (50°N, 10°N, 80°E, and 150°E) and (50°N, 10°N, 120°W, and 80°W) respectively as shown in Figure (4.4). Trajectory origin regions were not defined to be mutually exclusive so trajectories passing through both regions during the 10 days of transport prior to arrival at MLO were counted as both East Asian and American, although this rarely occurred. On average during 1995-2008, between 30 and 80% of HYSPLIT 10-day back trajectories passed through either the East Asian or American continental regions prior to arrival at MLO. The seasonal cycle of trajectory origin from each continental region is summarized in Figure (4.5). The combined continental trajectory fraction was largest during the winter and early spring and smallest during autumn (September-October). HYSPLIT trajectories were most likely to pass through the East Asian region during the winter months (December, January, and February) and were least likely to pass through this region during the summer months (July and August). Despite very little influence from the East

Asian region, a secondary peak in anthropogenic NSS-sulfate was observed in September. The large number of trajectories which passed through the American region during August and September may have contributed towards this observed secondary peak. This pattern was consistent with the findings of Buermann et al. (2007) who reported elevated North American influence at MLO during July and August. The trends in monthly HYSPLIT trajectory fraction which originated in the East Asian and American regions are shown in Figure (4.6). During 1995-2008, a decreasing trend was observed in East Asian trajectory origin and an increasing trend was observed in American trajectory origin, although only the trend in American trajectories was significant at a confidence level greater than 90%. The seasonal cycles were evident although the peaks in continental origin for each region were typically offset from each other. Continental trajectory origin during 2008 was particularly anomalous without clear peaks in winter/spring East Asian origin or summer American origin.

One limitation to the presented residence time analysis and continental trajectory analysis is that source regions were displayed in a two dimensional framework without regard for trajectory height as it crossed over a selected grid box boundary. Often trajectories which passed over the continental regions were very high above the boundary layer and likely only minimally influenced by surface pollutants. This was particularly true for the trajectories that passed over the East Asian region during the winter, when the boundary layer was typically very shallow and upper level wind speeds across this region were very high. The influence of trajectory height and meteorological variables during transport is discussed more in Section (4.2.1).

Average concentrations of anthropogenic NSS-sulfate were lower during times that trajectories passed over the Asian continent as opposed to the American continent, as shown in Figure (3.12). This finding likely arises because the American continent serves as a source

region much less frequently than the Asian continent, and thus means are influenced by many clean marine trajectories. During the winter, trajectories very frequently passed over the Asian continent, although synoptic conditions in Eastern Asia were not favorable for lofting pollutants into the free troposphere for long range transport until the spring, as discussed in Section (1.4). When concentration weighted trajectories over East Asia were combined over all seasons, the averaged values were slightly lower than the averaged values for North America, but are elevated above the averaged values observed over oceanic regions. Concentrations were frequently elevated during times when trajectories passed over Mexico and the United States, which served as source regions to MLO more frequently during the summer months. The higher anthropogenic NSS-sulfate concentrations on days when air masses passed over the American continent were likely a result of either anthropogenic industrial or biomass burning emissions across this region.

Interestingly, characteristics of two possible source locations for MLO anthropogenic sulfate located near the regions with elevated concentration weighted trajectories (Mexico City and China) were examined by Barth et al. (1999) using the NCAR Community Climate Model (CCM3) to determine how the Central American megacity and large industrial area in Asia contribute to global sulfate burden. Table (4.1) from Barth et al. (1999) shows the modeled sulfate budget for Mexico City, Southeast China, and the remainder of the world. These two MLO relevant source regions combined contributed approximately 10% of the total global sulfate burden (Barth et al., 1999). A slightly higher fraction of sulfate originating from southeast China was subject to wet deposition, as precipitation rates around southeast China were higher than surrounding Mexico City. The potential of sulfate, calculated using Equation (4.1),

is an estimate of how likely SO₂ emitted in a particular region will be converted to sulfate and remain SO₄²⁻ in the atmosphere (Rasch et al., 1999).

$$Potential (day) = \frac{SO_4^{2-} (kg S) derived from region}{Sulfur emitted in region (kg S/day)} \quad (4.1)$$

Sulfate tagged from Mexico City had a longer lifetime and larger potential on average than sulfate tagged from southeast China. These results suggested that although East Asia contributes more significantly to the global sulfate burden than Mexico City, SO₂ emitted from Mexico City has a shorter lifetime and is more likely to be converted to sulfate which then remains in the atmosphere longer than sulfate derived from southeastern China. Barth et al. (1999) explained that higher precipitation rates occur around southeastern China than in Mexico City which is expected to increase washout of East Asian sulfate near the sources. Additionally, they suggested that the differences in SO₂ lifetimes suggest that the region surrounding southeast China is oxidant limited, but the increased levels of H₂O₂ near the equator created an oxidant rich and SO₂ limited atmosphere around Mexico City. These results from Barth et al. (1999), summarized in Table (4.1), provide a possible explanation for the results of the anthropogenic NSS-sulfate concentration weighted trajectories are biased towards representing the contribution from the American continent when compared with the Asian continent. Although a higher burden of MLO anthropogenic NSS-sulfate likely originated in the East Asia region because this transport pathway is dominant, precursor emissions from the American continent contributed to the MLO sulfate burden more efficiently and were more likely to remain in the atmosphere long enough to be transported to MLO.

MLO Nightly (6Z, 12Z, 18Z) 10-Day HYSPLIT Back Trajectories (2007)

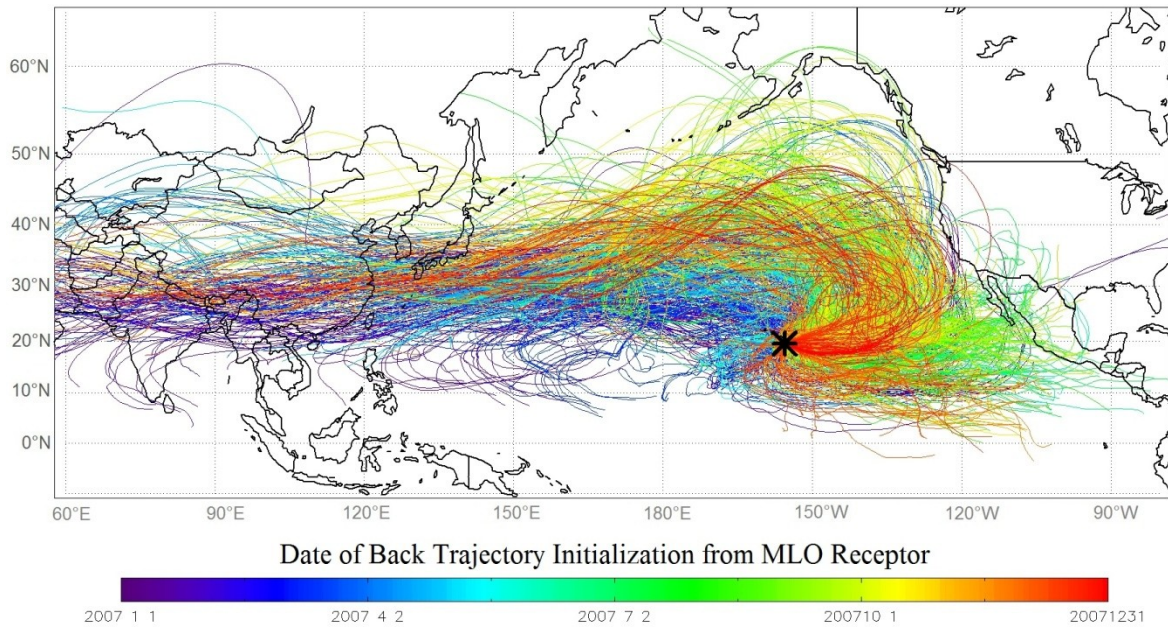


Figure 4.1: 10-Day HYSPLIT back trajectories with MLO arrival times of 6Z, 12Z, and 18Z during each day of 2007.

Residence Time Analysis
1995-2008

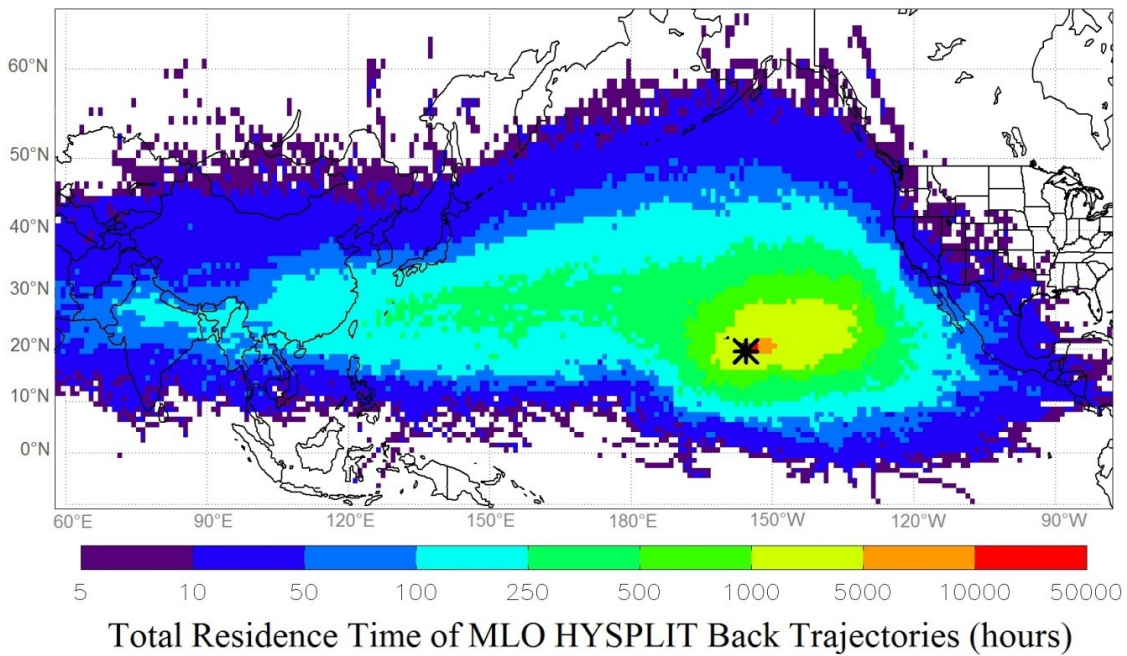


Figure 4.2: Total residence time in hours calculated from all MLO HYSPLIT 10-day back trajectory endpoints during 1995-2008.

Seasonal Cycle of Residence Time Analysis

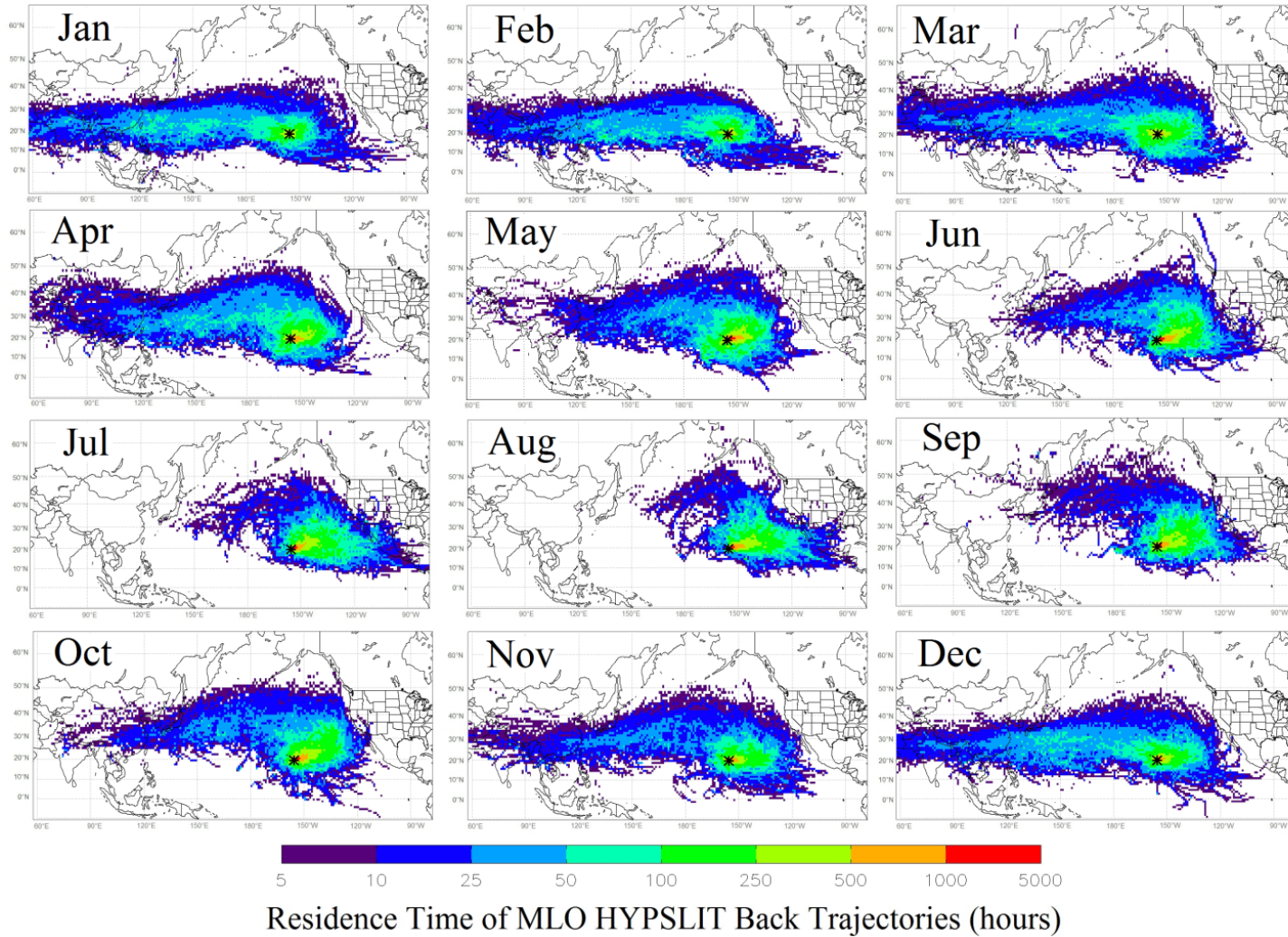


Figure 4.3: Total residence time in hours calculated from MLO HYSPLIT 10-day back trajectory endpoints during each calendar month combined over 1995-2008.

Regions of Continental Origin for MLO HYSPLIT Trajectories

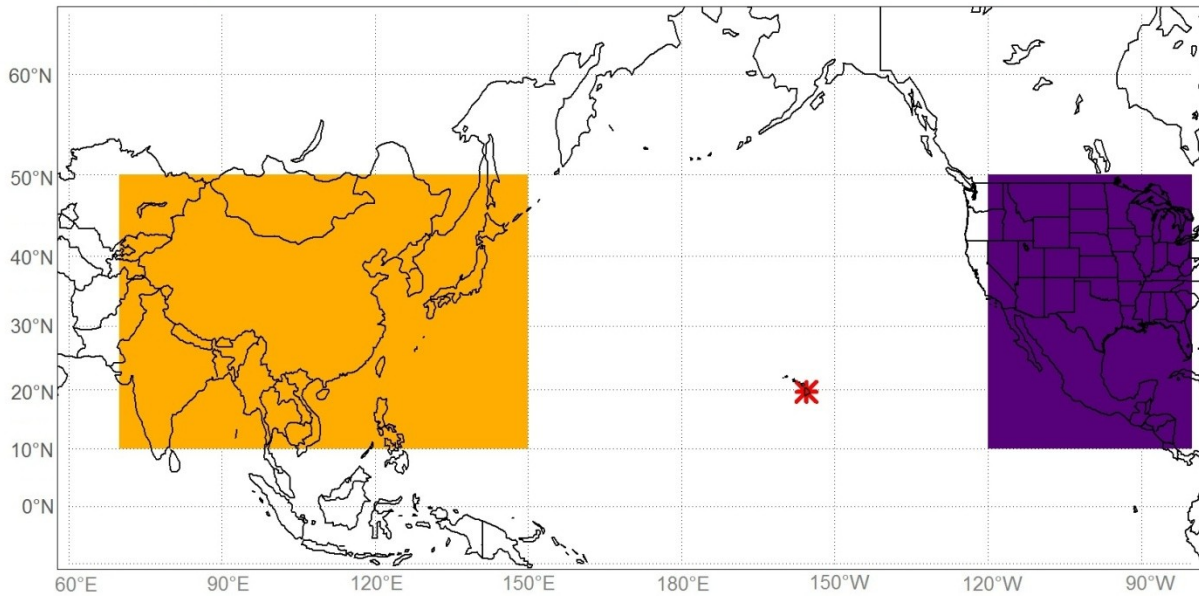


Figure 4.4: East Asian (orange) and American (purple) source regions defined by (70°E, 50°N, 150°E, 10°N) and (120°W, 50°N, 80°W, 10°N) respectively in relationship to the MLO source receptor site (red).

Seasonal Cycle of MLO 10-Day HYSPLIT Back Trajectories

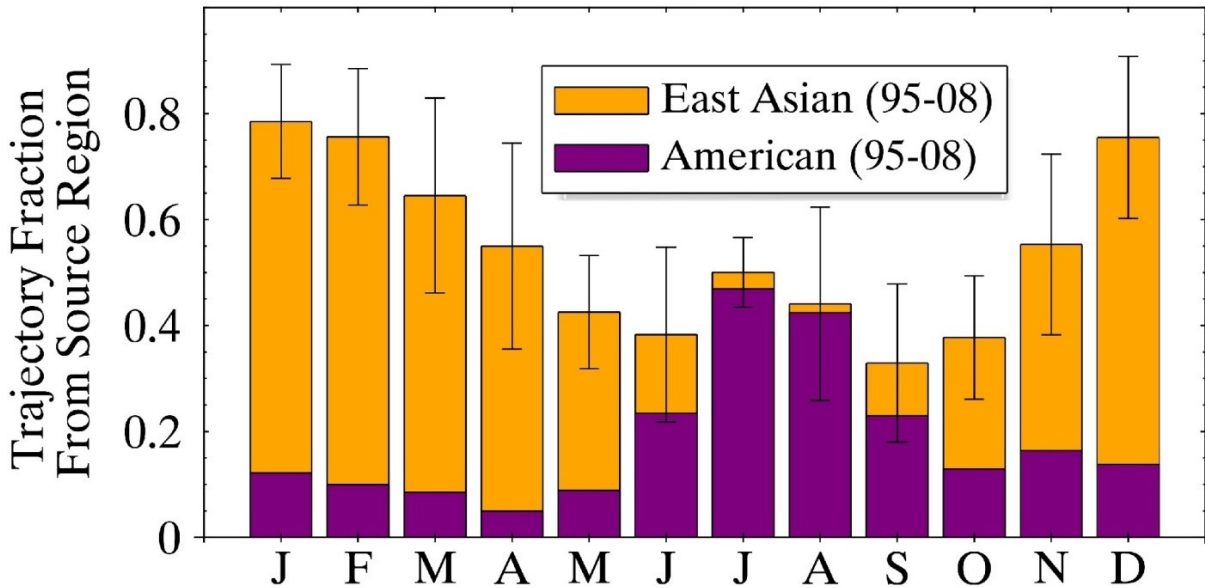


Figure 4.5: Seasonal cycle in continental contribution to MLO as determined by HYSPLIT back trajectory endpoints entering defined East Asian and American region boundaries.

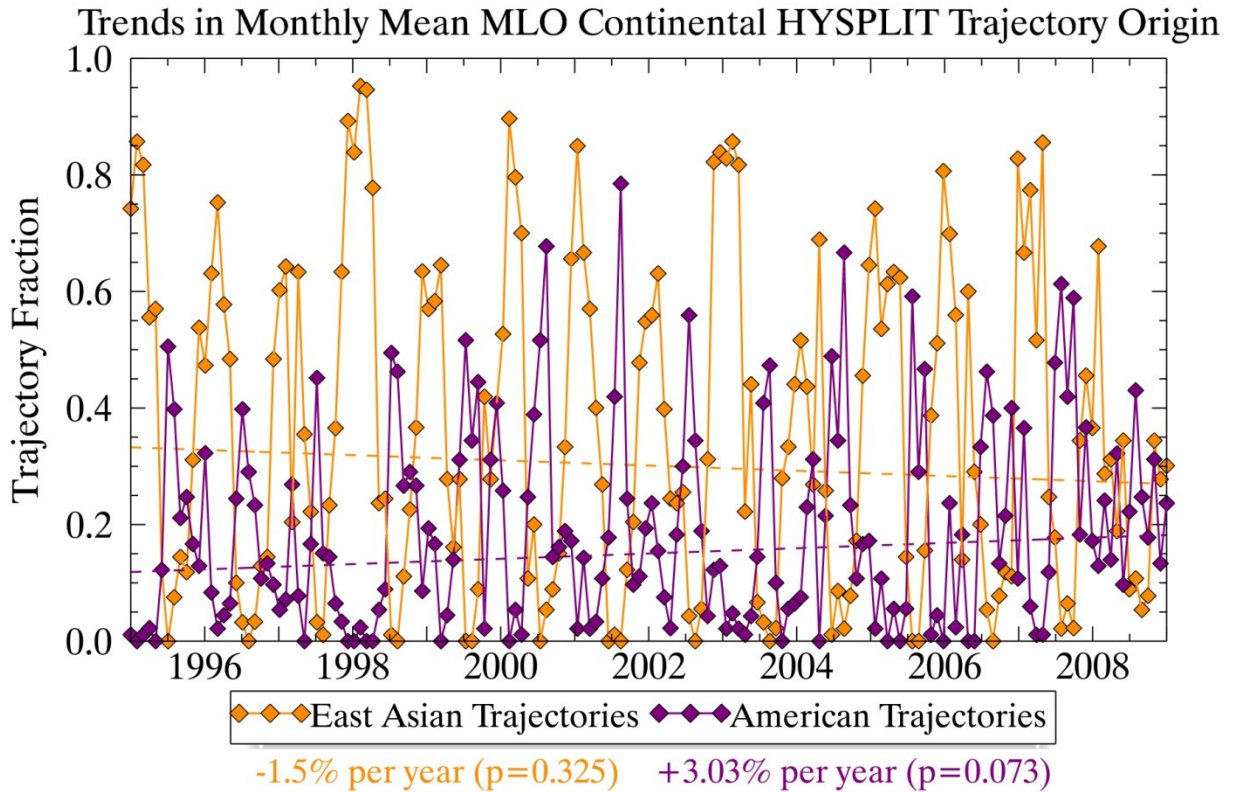


Figure 4.6: Trends in monthly mean MLO 10-day HYSPLIT back trajectories originating from defined East Asian (orange) and American (purple) continental regions.

Table 4.1: Modeled sulfate budget for Mexico City and Southeast China with potential as defined in Equation (3.1) from Barth et al. (1999).

Aerosol Sulfate Budget in the Simulation

	Mexico City	Southeast China	Rest of World
Source, Tg S yr⁻¹	0.392	5.17	49.29
Primary emissions	0.010 (3%)	0.154 (3%)	1.16 (3%)
SO ₂ + OH	0.064 (16%)	0.747 (14%)	8.48 (17%)
S(IV) + H ₂ O ₂	0.303 (77%)	3.860 (75%)	31.62 (64%)
S(IV) + O ₃	0.015 (4%)	0.411 (8%)	8.03 (16%)
Sink, Tg S yr⁻¹	0.411	5.24	49.20
Dry deposition	0.024 (6%)	0.25 (5%)	3.4 (7%)
Wet deposition	0.387 (94%)	4.99 (95%)	45.8 (93%)
Burden, Tg S	0.0062	0.052	0.52
Lifetime, days	5.5	3.6	3.9
Potential, days	4.6	2.5	2.4

4.1.2 Chemical Continental Tracers

Seasonal cycles of three continental tracers selected in this study, gaseous Radon (Rn^{222}), aerosol NSS-calcium (Ca^{2+}), and gaseous carbon monoxide (CO) are shown in Figure (4.7). The three chemical tracers are known to have different emissions sources and atmospheric behavior which are unique to the constituent. Combining the seasonal cycle, trends, and source characteristics of these three continental tracer species with the HYSPLIT trajectory modeling and anthropogenic NSS-sulfate results provided additional insight into how a combination of both meteorology and anthropogenic emissions impacted observed chemical concentrations at MLO.

As discussed in Section (2.2.1), radon is a simplified tracer, compared with anthropogenic NSS-sulfate, because it is naturally emitted from soil, is not dependent on variations in anthropogenic activities, has a known half-life, and is resistant to washout by precipitation. The seasonal cycle in radon was used as an indicator of the seasonal cycle in continental boundary layer influence at MLO. Although radon is not emitted from anthropogenic sources, it was assumed to provide an indication for which air masses observed at MLO recently came into contact with either the Asian or American continent, and therefore were likely also influenced by surface anthropogenic sources on the continent. Radon concentrations were highest during the late winter and early spring (February, March, April) and were lowest during the late summer (July, August, September). These observations follow a similar seasonal cycle as reported in previous radon modeling studies (Balkanski et al., 1992). The seasonal cycle in Figure (4.7) shows that radon concentrations are highest during early spring when contributions from the Asian continent dominate. However, radon from American sources was found to contribute up to 30% of radon at MLO and is most significant during the summer

months (Balkanski et al., 1992). In contrast to the peak in American continental origin for trajectories shown in Figure (4.5), a clear secondary peak in radon during the summer months was not observed in this study and radon variability remained very low between July and September. This pattern is consistent with the results of Lintner et al. (2007) using the same radon dataset over a subset over a different time interval as shown in Figure (4.8). Lintner et al. (2007) reported slightly higher peak concentrations during February-March-April which can likely be attributed to the fact that only nighttime downslope radon concentrations were included in this study, whereas Lintner et al. (2007) included all 24 hours of available data.

The contrast between continental and oceanic radon contribution to MLO can be easily observed in Figure (4.9), which shows radon concentration weighted trajectories over the period 1997-2010. We expected to see high radon contributions from both the Asian and American continents with very low contributions from the surrounding Pacific Ocean. On average, over a period of many years, it is clear that radon concentrations are significantly higher at MLO when the air mass passed over a continental land mass within the last 10 days. Radon concentrations were generally elevated when trajectories passed over any portion of the Asian continent. Elevated radon concentration weighted trajectories also occurred over the Pacific Ocean, between 20°N and 50°N, extending off the eastern coast of Asia. This pattern may be attributed to trajectory trailing effects along the most common transport pathway for air masses after contact with the Asian continent before reaching MLO. It has also been suggested by Schery and Huang (2004) that radon emissions from the tropical Pacific Ocean, although much smaller than emissions from land, may contribute a non-negligible fraction of total radon to a remote marine location such as MLO. Mean fluxes of oceanic radon modeled by Schery and Huang (2004) are shown in Figure (4.10). These oceanic sources likely contributed to the elevated

radon concentration weighted trajectories observed near the southern boundary of the transport domain, between the equator and 20°N, particularly in the region of relatively high surface winds to the southeast of MLO. Elevated radon concentrations were also seen when trajectories passed over the American continent but the effect was much less widespread. High concentrations only occurred when trajectories passed over the center of the continent, providing more time for interaction with radon emitted from the surface which was lifted into the transport pathway. Very low radon concentrations were observed during times of transport over the Eastern Pacific Ocean despite the fact that Schery and Huang (2004) predicted relatively high oceanic radon fluxes during the summer off the coast of the western United States which may be attributed to the higher trajectory altitude over this region as discussed in Section (4.2.1).

The second continental tracer, NSS-calcium, was used as a proxy for dust transport to MLO. NSS-calcium concentration weighted trajectories indicating possible sources of dust observed at MLO are shown in Figure (4.11). We expected to see high concentration weighted trajectory values over the arid regions of East Asia, particularly Northern China, and possibly portions of the Southwestern US and Mexico. On average, elevated levels of NSS-Calcium were observed during times that trajectories passed over central China, portions of Mongolia, and Northern India, corresponding with desert regions which are known to serve as major sources of atmospheric dust as shown by annual dust emissions from the GOCART model in Figure (4.12). To a lesser extent, higher concentrations were also observed on average when trajectories passed over the southwestern US and portions of Mexico when compared with the surrounding Pacific Ocean.

The observed seasonal cycles of radon and NSS-calcium were similar. However, radon concentrations peaked earlier in spring (February-March-April) than NSS-calcium

concentrations (April-May). The patterns in the NSS-calcium concentration weighted trajectories agreed well with radon concentration weighted trajectories in general, although the contrast between values over ocean regions and continental regions were slightly less noticeable for calcium. Different atmospheric lifting and removal processes can likely account for some of the seasonal and transport differences between these two continental tracers. NSS-calcium is a soluble aerosol species which is subject to atmospheric removal via both dry and wet deposition. Therefore, NSS-calcium concentrations were lower during the late winter and early spring months when convective activity increased and the most probable transport pathway passed through regions of high precipitation rates (Section (4.2.1)). The primary removal process for radon is radioactive decay so observed radon concentrations at MLO were expected to be dependent on speed of transport from the continental source region, which was highest during the winter (Section (4.1.1)).

The third chemical continental tracer used in this study was carbon monoxide (CO), a gas. Observations of CO transport served as a tracer of anthropogenic activity, but also was strongly dependent on emissions from biomass burning in source regions. It has been estimated that approximately 39% of carbon monoxide observed at MLO can be attributed to springtime transport from East Asian sources (Liang et al., 2004). Shown in Figure (4.7), carbon monoxide concentrations at MLO were highest during March and April, lowest during the summer months, and steadily increased during autumn and winter. The seasonal peak in carbon monoxide concentrations corresponded to the two-month overlapping time period when radon and NSS-calcium concentrations were also highest and also aligned with the Southeastern Asia biomass burning season which is typically most active during March-April (Liu et al., 2003). Figure (4.13) shows carbon monoxide weighted trajectories using the daily concentration data available

during 2005-2010. Interestingly, this figure contains both similarities and differences from the previous continental tracer trajectory patterns. Carbon monoxide concentrations were frequently elevated when air masses were transported across southeastern Asia and portions of the western Pacific Ocean extending from 10-20°N, which are known to be biomass burning source regions as shown in Figure (4.14). As shown in Figure (1.18), this region is also highly concentrated with volcanoes which may have contributed some of the carbon monoxide observed at MLO. Carbon monoxide concentrations were dependent on a combination of anthropogenic and biomass burning emissions, the transport and meteorological variables controlling radon and NSS-calcium, and the abundance of atmospheric OH which controls atmospheric photochemistry.

Interannual variability and trends in each of the three chemical continental tracers are shown in Figure (4.15). A statistically significant decreasing trend was observed in radon concentrations at MLO while trends in carbon monoxide ($p=0.112$) and NSS-calcium ($p=0.441$) were not significant at the 90% confidence level. The decreasing trend in radon, while statistically significant, may be influenced by the instrument change during 2003-2004 as discussed in Section (2.2.1). Trends were also calculated separately for the time periods of 1997-2003 and 2004-2010, partitioned into the two instrument periods. A decreasing trend was also found for the period of 2004-2010 although it was not significant at the 90% confidence level.

The interannual variability in each of the species was quite substantial. The relative magnitudes of the late winter/early spring peak concentrations of both radon and carbon monoxide generally exhibit similar patterns during 2005-2009 with anomalously high peak concentrations during 2005, 2007, and 2008 and anomalously low peak concentrations during 2006 and 2009. The variability of springtime NSS-calcium concentrations didn't follow the

patterns observed in radon and carbon monoxide as clearly, although the relative magnitude of peak concentrations in 1997-1998 and 2000-2001 were similar for both radon and carbon monoxide. During 2002, anomalously high late winter/early spring radon concentrations were observed while calcium and carbon monoxide concentrations were both anomalously low. Very high NSS-calcium concentrations were observed during the spring of 2008 which were not seen in either radon or carbon monoxide but were also observed in anthropogenic NSS-sulfate concentrations, as shown in Figure (3.14).

To demonstrate the relationships which existed between anthropogenic NSS-sulfate and the selected chemical continental tracer concentrations at MLO at a higher time resolution, Figure (4.16) shows daily concentrations during 2005-2008, the time period for which daily resolution data were available for all species. Additionally, information about trajectory source obtained using the defined East Asian and American source regions discussed in Section (4.1.1) were added, as lines indicating whether any trajectories originated from either source region on the selected day. Figure (4.16) demonstrated the offset seasonal cycles of radon and carbon monoxide, peak concentrations occurred 1-2 months prior to NSS-calcium and anthropogenic NSS-sulfate peak concentrations, particularly during 2005. Examples of consecutive days with anomalously high concentrations of all species occurring at the same time that trajectories originated from the East Asian region can be found (e.g. during January 2006, March 2007, and April 2008), although at times anthropogenic NSS-sulfate concentrations increased drastically for one or more days while concentrations of other continental tracers remained low, and trajectories were not consistently of continental origin (e.g. June 2005 and May 2008). Because of the discrepancy between aerosol and gaseous species during May 2008, it was hypothesized that a portion of this peak in anthropogenic NSS-sulfate may have been related to volcanic

emissions. A more detailed investigation of daily trajectory origin during times of high anthropogenic NSS-sulfate concentrations may provide help to identify additional anthropogenic or natural SO₂ sources occasionally impacting sulfate variability at MLO which were not considered in this study, particularly shipping emissions and additional volcanos. Timelines of daily concentrations for each of the species and associated continental trajectory origin shown in Figure (4.16) are included in Appendix (A), plotted separately for each year during 2005-2008.

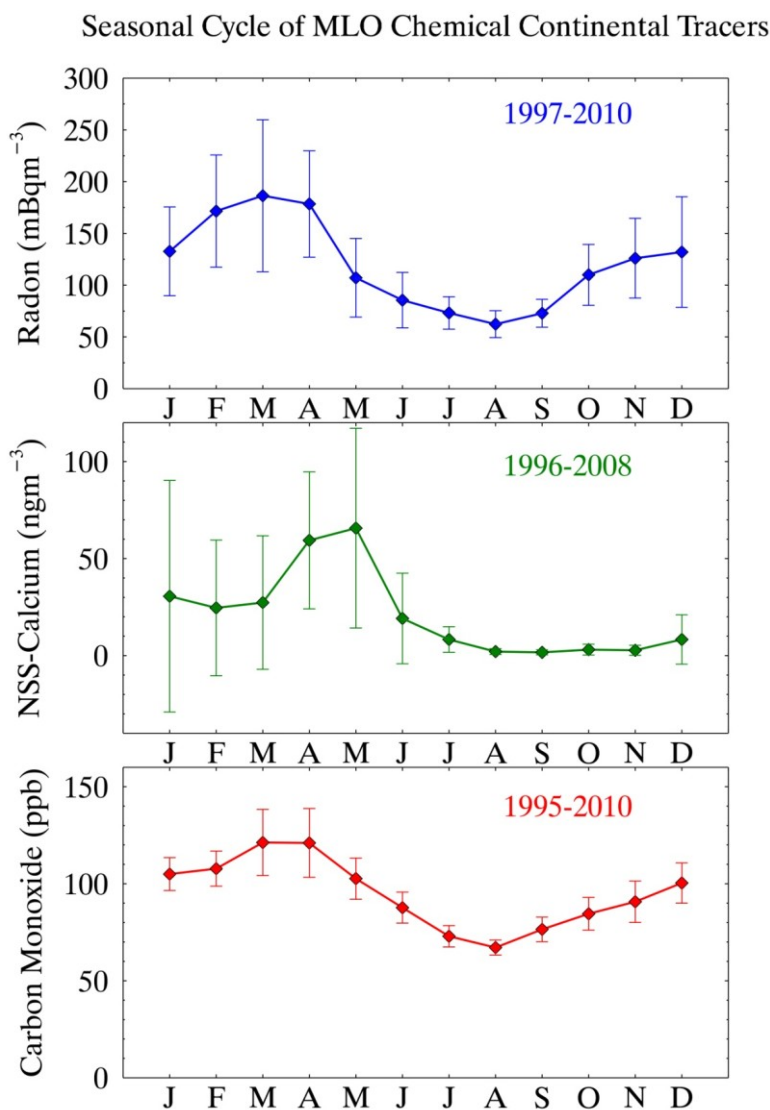


Figure 4.7: Seasonal cycle of chemical continental tracers at MLO: gaseous radon (top), aerosol NSS-calcium (middle), and gaseous carbon monoxide (bottom).

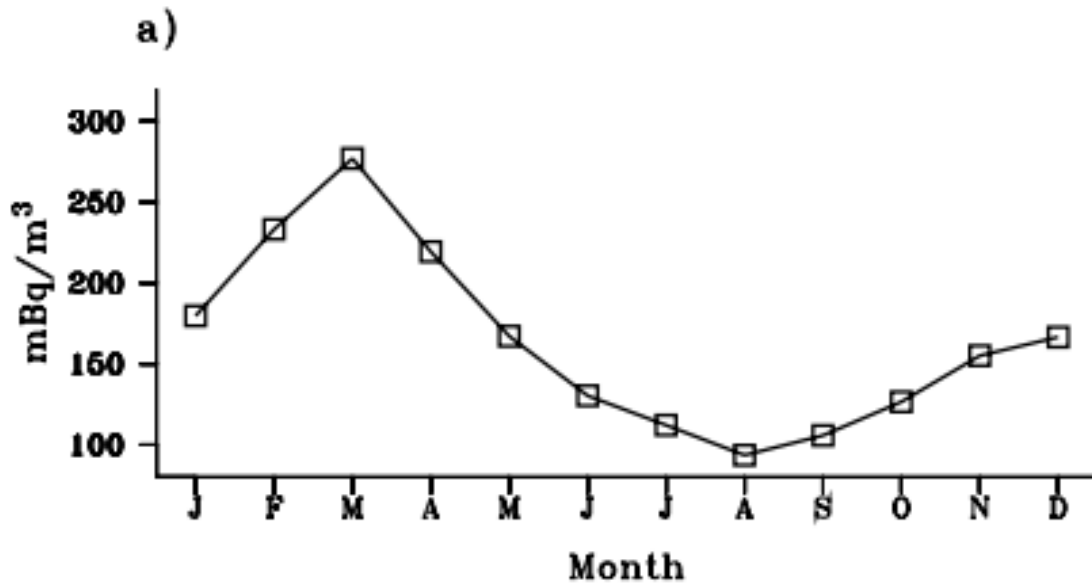


Figure 4.8: Radon seasonal cycle at MLO 1991-2002 from Lintner et al. (2007).

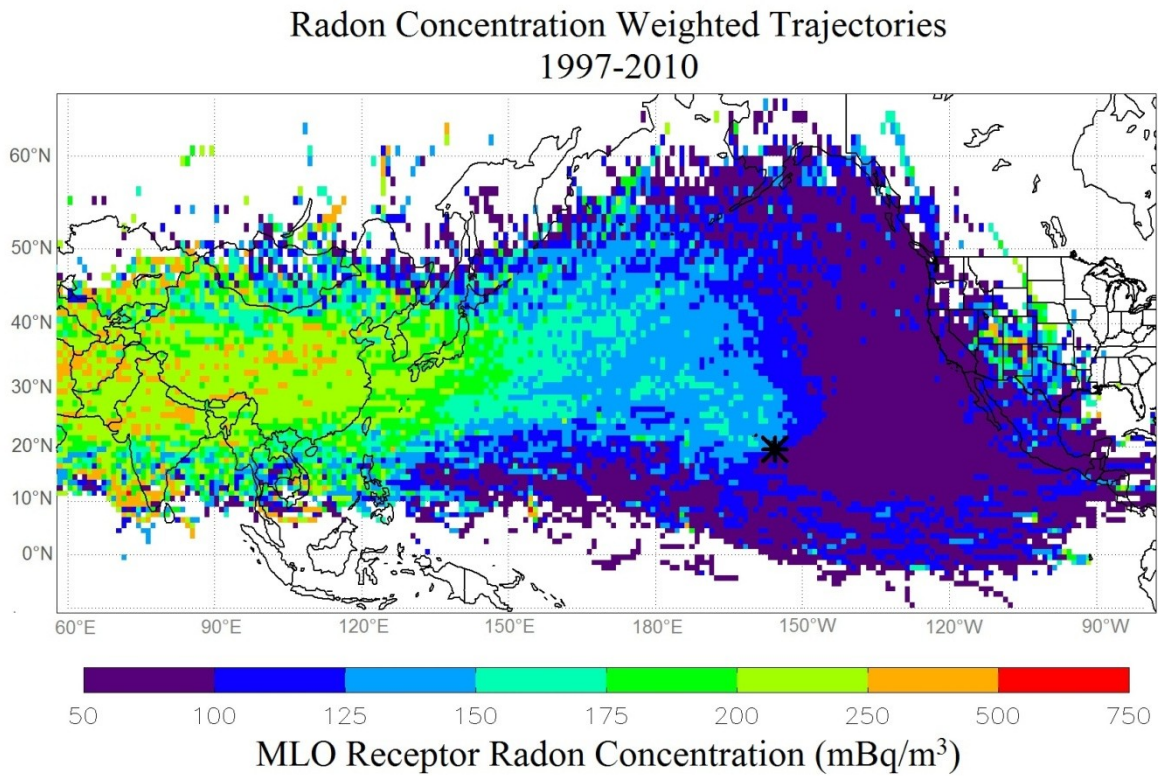


Figure 4.9: MLO radon concentration weighted 10-day back trajectories for 1997-2010.

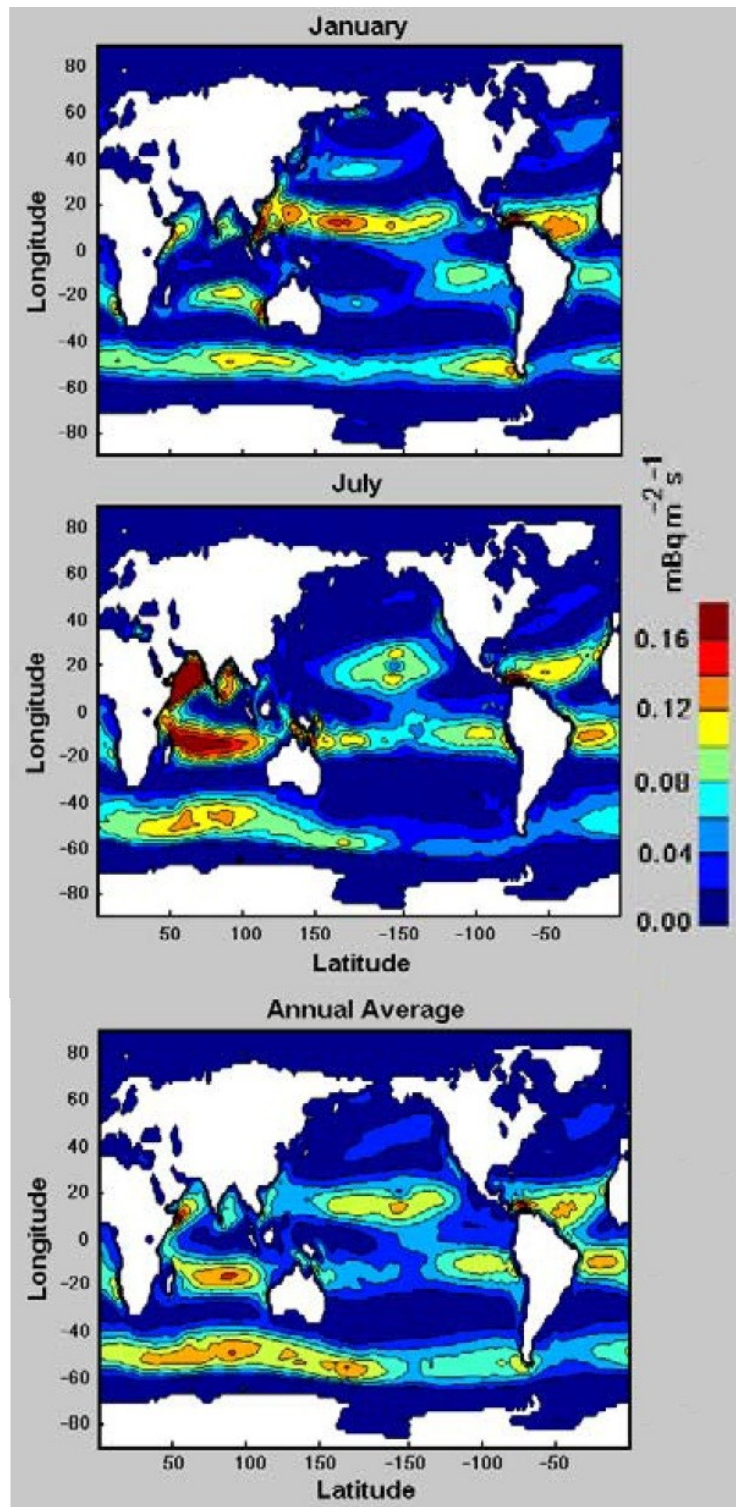


Figure 4.10: Modeled oceanic radon flux density for January (top) and July (bottom) modified from Schery and Huang (2004).

NSS-Calcium Concentration Weighted Trajectories
1996-2008

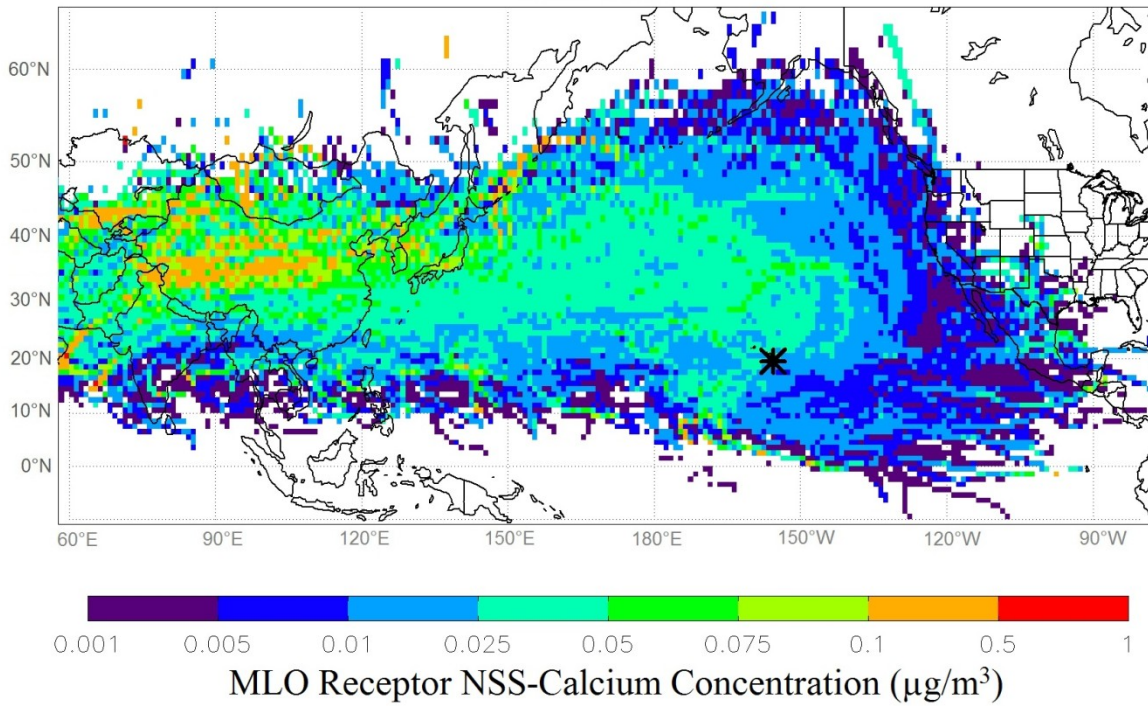


Figure 4.11: MLO NSS-calcium concentration weighted 10-day back trajectories for 1996-2008.

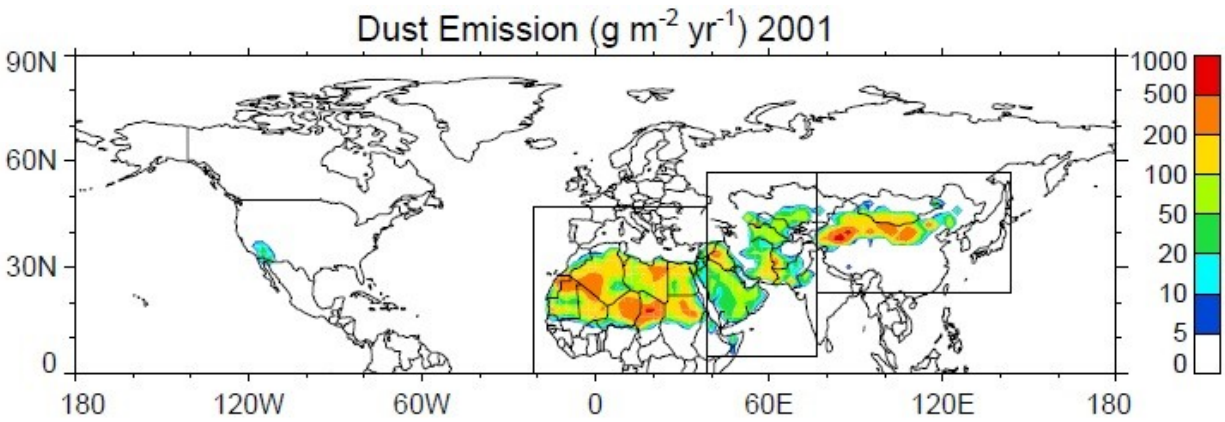


Figure 4.12: Annual dust emissions during 2001 used in the GOCART model from Chin et al. (2007).

Carbon Monoxide Concentration Weighted Trajectories
2005-2010

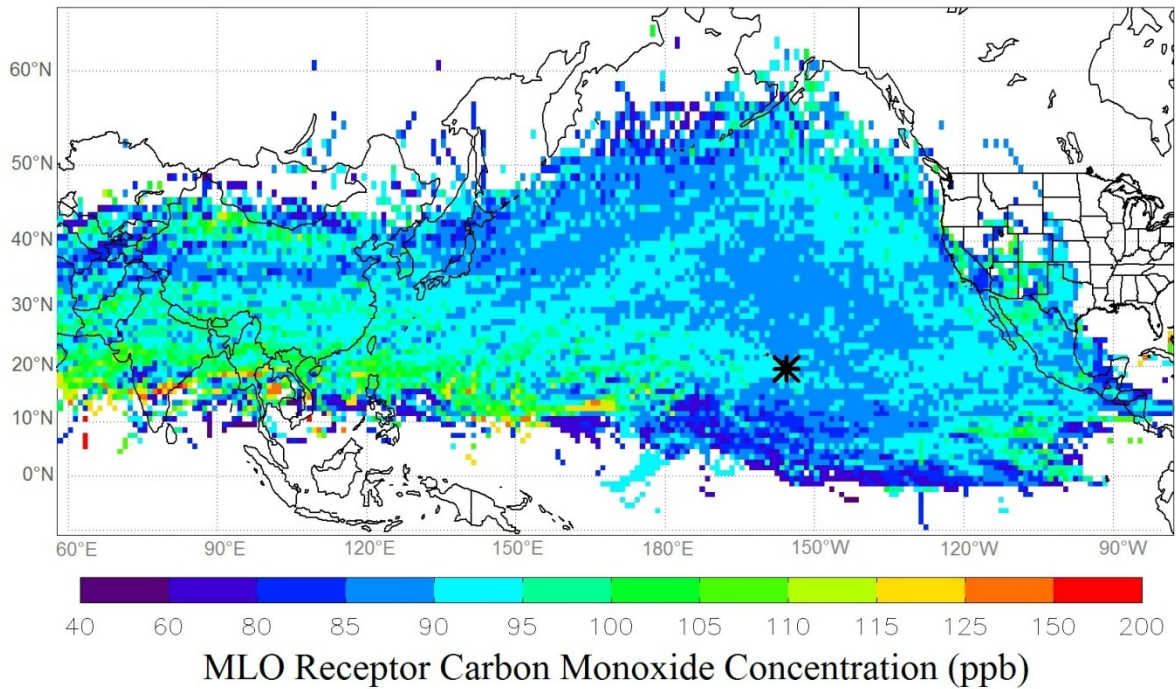


Figure 4.13: MLO carbon monoxide concentration weighted 10-day back trajectories for 2005-2010.

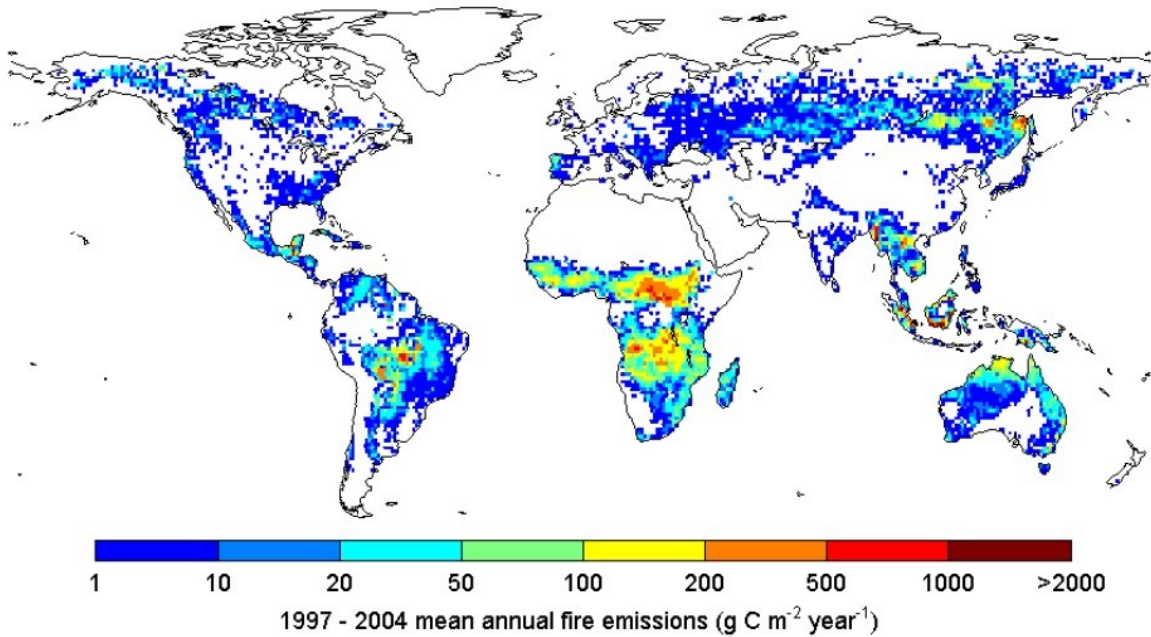


Figure 4.14: Annual mean biomass burning emissions during 1997-2004 from van der Werf et al. (2006).

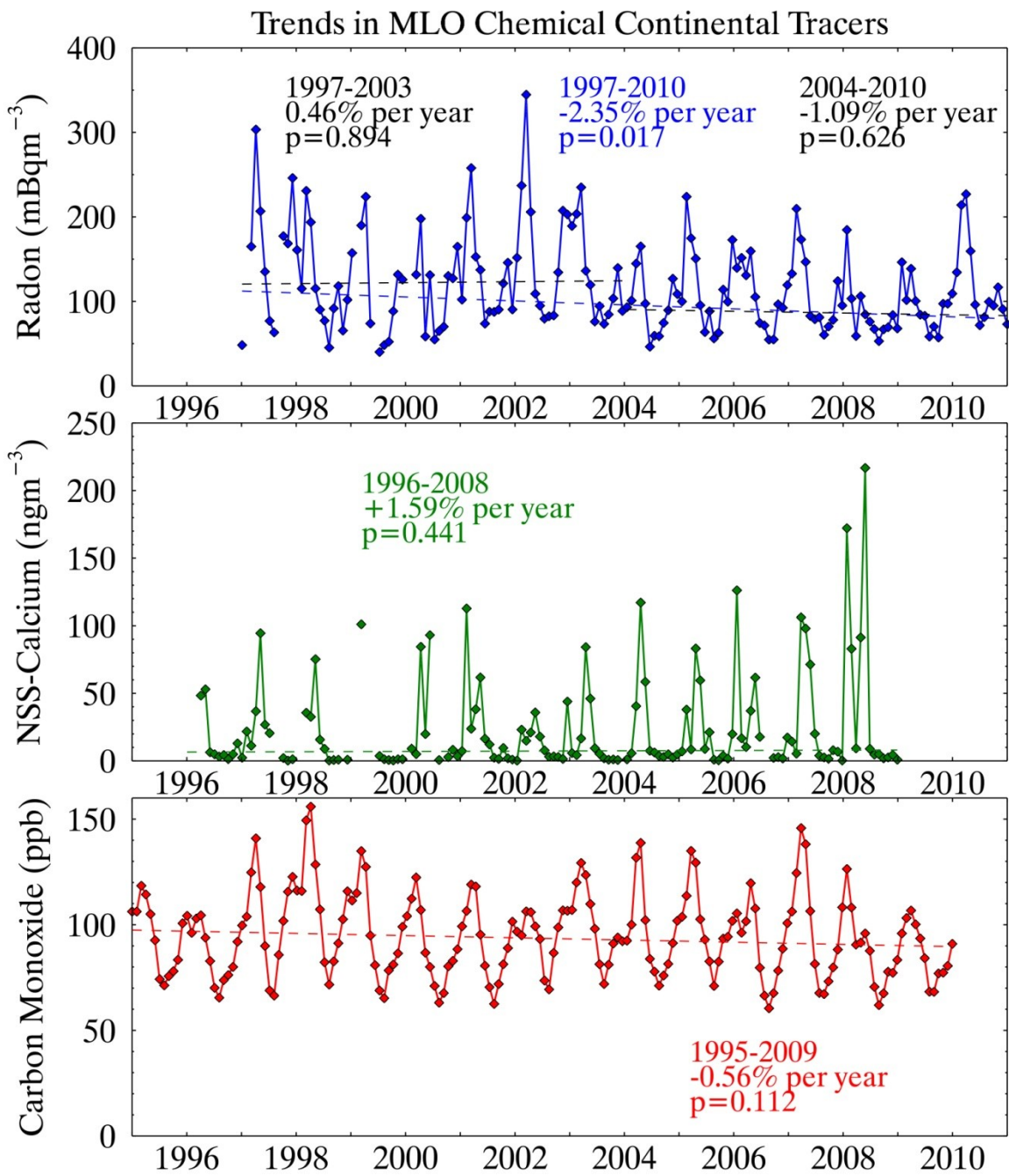


Figure 4.15: Trends in MLO chemical continental tracers: radon, NSS-calcium, and carbon monoxide. For radon a trend was calculated using all available data as well as two separate trends for the periods of 1997-2003 and 2004-2010 to determine whether the 1997-2010 patterns were likely a result of an instrumentation change in 2004.

Daily MLO Aerosol and Gas Concentrations (2005-2008)

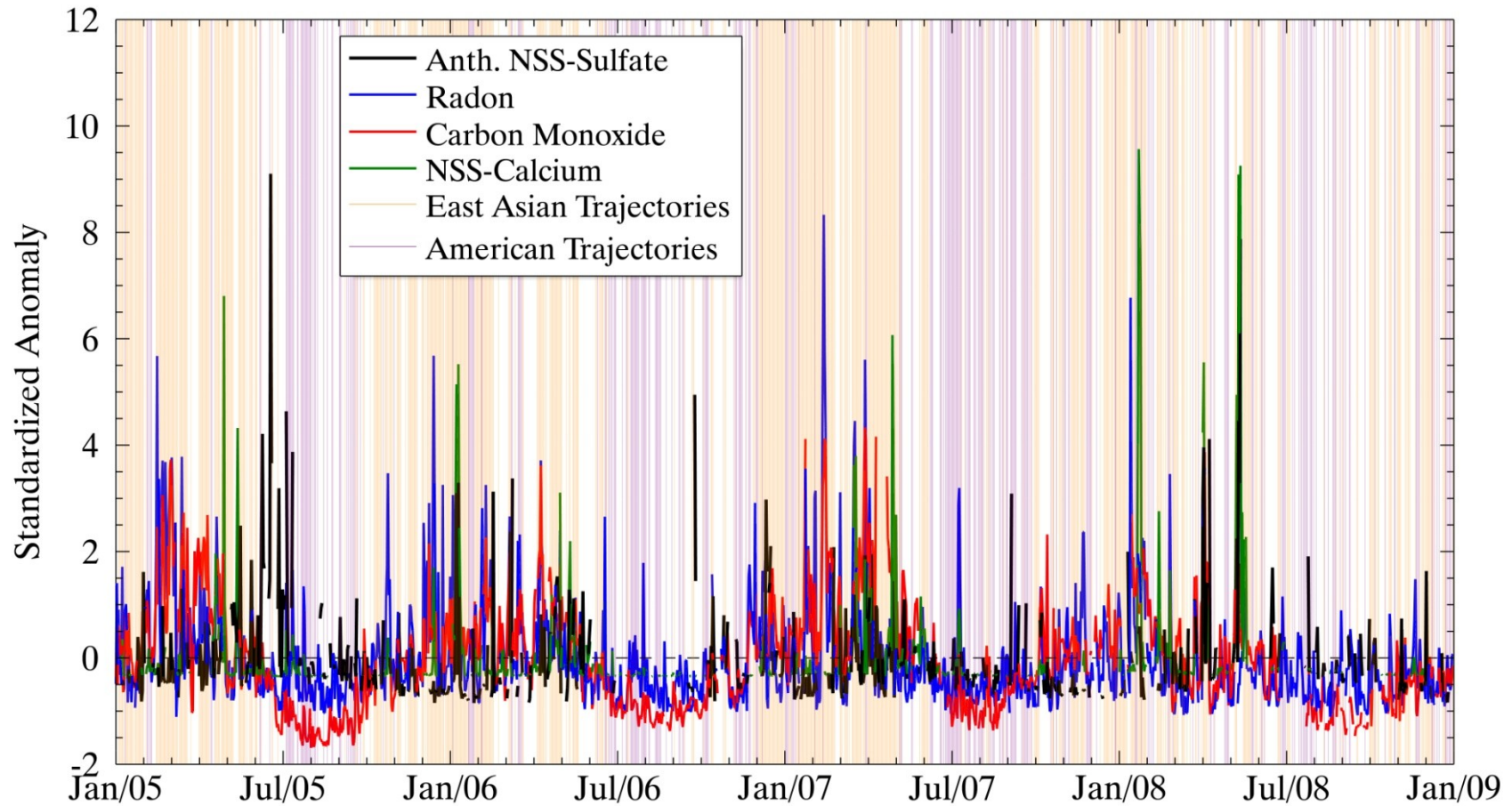


Figure 4.16: Standardized anomaly in daily concentrations of MLO sulfate aerosol and chemical continental tracers: NSS-calcium aerosol, radon gas, and carbon monoxide gas during 2005-2008.

4.2 Transport Controls on MLO Observations

4.2.1 Meteorology During Transport

Age weighted trajectories from 1995-2008, shown in Figure (4.17), were used to analyze transport speed to MLO. The age indicated by the color of each grid box represents the average amount of time required for air to be transported from that grid box to the MLO receptor. Near the MLO location, the direction of fastest transport extended to the east-northeast. Air masses arriving from this direction were more likely to be located further away geographically 2-5 days prior to arrival at MLO than air masses arriving from any other direction. However, this pattern changed at further distances for which the faster transport occurred to the north and west of MLO. In the midlatitude region extending from approximately 25°N-45°N, transport to MLO from the west typically occurred at a faster speed than transport along the same latitude range from the east. Transport from the Asian continent to MLO required approximately the same amount of time (6-10 days) as transport from the American continent, despite the fact that the Asian continent is located further from MLO as discussed in Section (4.1.2). The time required for MLO back trajectories to pass over China found in this study is consistent with results from Perry et al. (1999).

The combination of these two transport patterns demonstrates that the fastest long distance pathway frequently existed from eastern Asia across the Pacific Ocean and then curved anticyclonically to approach MLO from the northeast. Along this transport pathway, air masses passed over portions of Japan and central China during transport to MLO on average 6-7 days before arriving at the receptor site. Along the transport pathway from the east, it often took 7-10 days to reach MLO after passing over the southwestern US or Mexico. Near MLO, trajectories

indicated that horizontal transport slowed down during the last 4-5 days of transport as air circulated around MLO during vertical subsidence before reaching the receptor site.

Figures (4.18) and (4.19) show trajectories weighted by atmospheric pressure and height above mean sea level, respectively, for 1995-2008. These results can be used to understand the approximate elevation of transport to MLO. Transport to MLO across the Pacific Ocean was found to typically occur at levels between 400 and 700mb, corresponding to elevations of 3-7km above sea level. A strong meridional gradient was observed in both trajectory pressure and height, with trajectories crossing the midlatitudes more frequently having occurred at high elevations and trajectories crossing the tropics more frequently having occurred at low elevations. The fact that trajectories passing over the equatorial Pacific Ocean originated from elevations lower than MLO further supports the conclusion that this oceanic region often served as a source for radon and MSA at MLO. On average, trajectories which were transported over the Himalayas and the Tibetan plateau were at a much lower atmospheric pressure level than trajectories which were transported over other portions of the continent. This is not surprising as the high elevation of the Tibetan plateau allows it to heat from incoming solar radiation more efficiently than the surrounding continent during the spring and summer, which generates large scale rising motion, upper level divergence, and thus low surface pressure (Ye and Wu, 1998).

Figure (4.20) shows relative humidity weighted trajectories using NCEP/NCAR Reanalysis model relative humidity at each trajectory location during 1995-2008. Recent updates to the HYSPLIT model included the addition of specific humidity (g/kg) as a meteorological output tool which may provide more applicable information about atmospheric water content, regardless of temperature or pressure, encountered by trajectories prior to arrival at MLO. Nevertheless, atmospheric relative humidity along HYSPLIT trajectories may provide

information about clouds encountered by air masses during transport prior to arrival at MLO, identifying regions where cloud processing is likely an important factor for secondary sulfate formation. The production of atmospheric oxidants, particularly the formation of OH from ozone photolysis is also a function of atmospheric water content. On average, high relative humidity conditions were encountered during transport across the northern Pacific Ocean, and during transport along the southeastern portion of the domain, off the coast of Central America. Very low relative humidity conditions were encountered during transport across arid regions of Asia and during transport in the region extending northeast from MLO towards the western United States. These regions correspond with the Aleutian low and Pacific high which are semi-permanent pressure systems that control convection and cloud cover in these locations.

Figure (4.21) shows precipitation weighted trajectories using NCEP/NCAR Reanalysis model surface precipitation rate at each trajectory location during 1995-2008. Precipitation reaching the surface may originate at levels below the trajectory location which presented complications when interpreting this information. Air masses that were transported below or through the precipitation prior to arrival at MLO would likely have been subject to enhanced rates of wet deposition. The precipitation pattern observed in Figure (4.21) supports the conclusions of Barth et al. (1999), who reported that precipitation was frequently higher during transport from East Asia as compared with transport from Mexico, which reduced the sulfate potential of SO₂ emitted from East Asia.

Figure (4.22) shows the solar radiation weighted trajectories using NCEP/NCAR Reanalysis model solar radiation flux reaching the surface below the trajectory location during 1995-2008. Solar radiation along the trajectory may provide some indication about the efficiency of photochemistry and the availability of oxidants for secondary aerosol formation and

also the presence of clouds. The pattern of solar radiation is clearly related to the Northern Hemisphere seasonal patterns with more direct solar radiation in the summer, when transport is dominated by trade winds, and more influence was observed at MLO from the North American continent, and less direct solar radiation during the winter, when trajectories more frequently originated from the west and MLO is more influenced by the East Asian Continent.

The seasonal cycles of each NCEP/NCAR meteorological parameter discussed above, as well as the transport time from the previously defined East Asian and American continental regions are shown in Figure (4.23). The seasonal cycles of each variable were calculated as explained in Section (2.7.1) and then normalized by the annual mean and standard deviation for comparison with other meteorological variables. The seasonal cycles of trajectory transport time for the East Asian and American source regions in general were opposite the seasonal cycles of the number of trajectories originating from each region because faster moving trajectories were more likely to pass through these regions within 10 days before arrival at MLO. Precipitation reaching the surface along the HYSPLIT trajectory locations was largest during the winter and early spring, likely due to transport through the region between 30° and 50° N which was indicated as a high precipitation region in Figure (4.21). The interaction between solar radiation and precipitation may indicate controls on formation and removal of aerosol species during transport to MLO as the time of year when solar radiation increased and precipitation decreased corresponded with the springtime peak in anthropogenic NSS-sulfate concentrations. A similar relationship was observed during the autumn, which corresponded with the timing of the secondary peak in NSS-sulfate. Trajectory relative humidity was highest during the early spring and late fall when transport through the high latitude impacted by the Aleutian Low was most common, and lowest during the summer when slow transport from the American continent,

through the region impacted by the Pacific High was most common. Trajectory pressure was typically lowest during the winter and highest during the summer, although anomalously low mean trajectory pressure was observed during April, which was likely related to frequent transport over the topography-driven low pressure which has been found to occur over the Tibetan plateau.

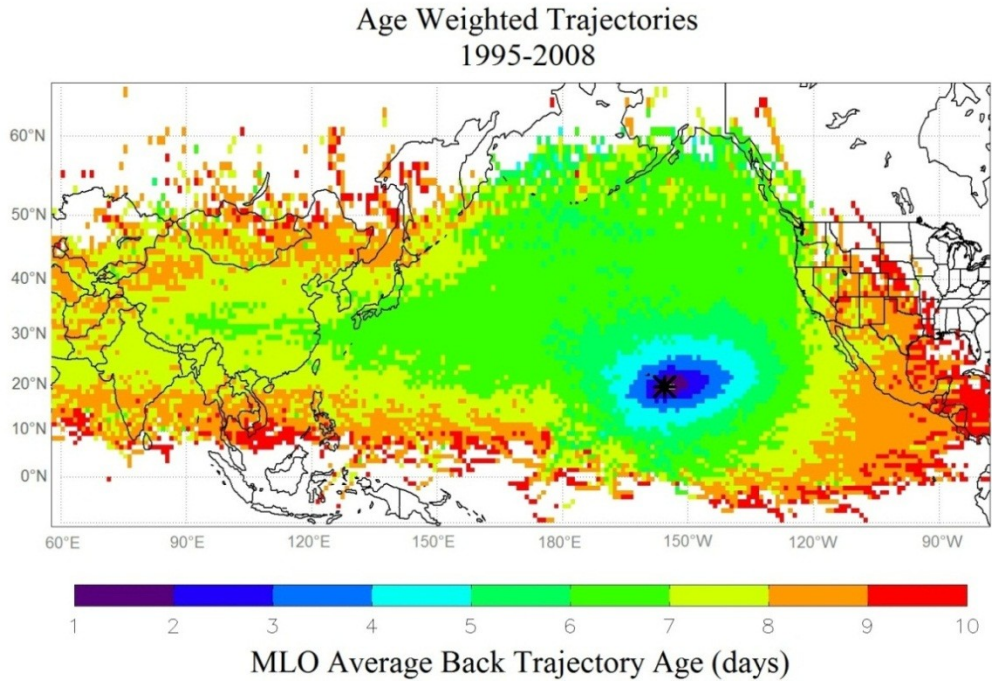


Figure 4.17: Age weighted HYSPLIT back trajectories from the MLO receptor site. Color represents the gridded average transport time to MLO.

Atmospheric Pressure Weighted Trajectories
1995-2008

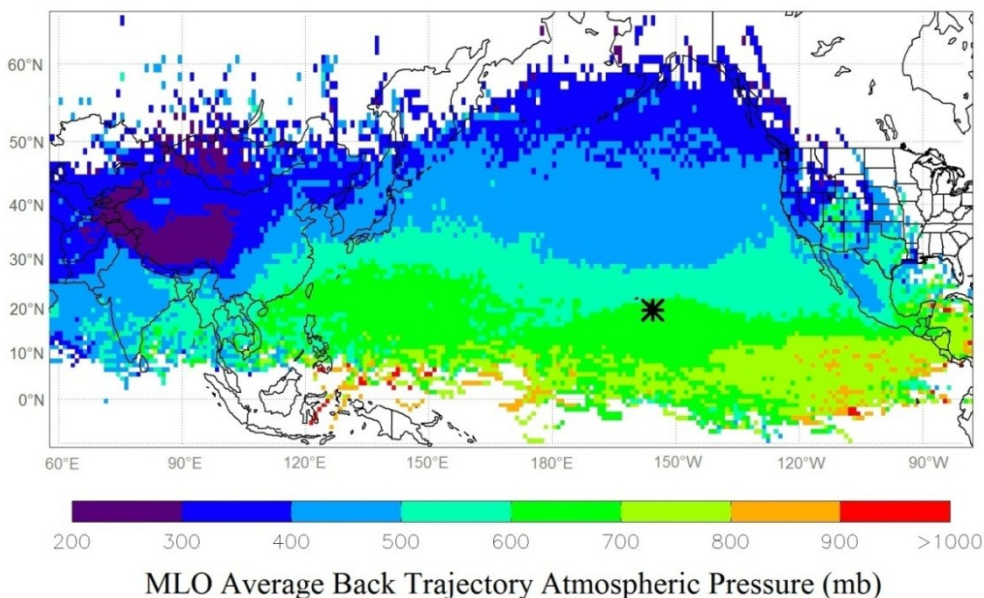


Figure 4.18: Pressure weighted HYSPLIT back trajectories from the MLO receptor site. Color represents the gridded average pressure level during transport to MLO.

Height Weighted Trajectories
1995-2008

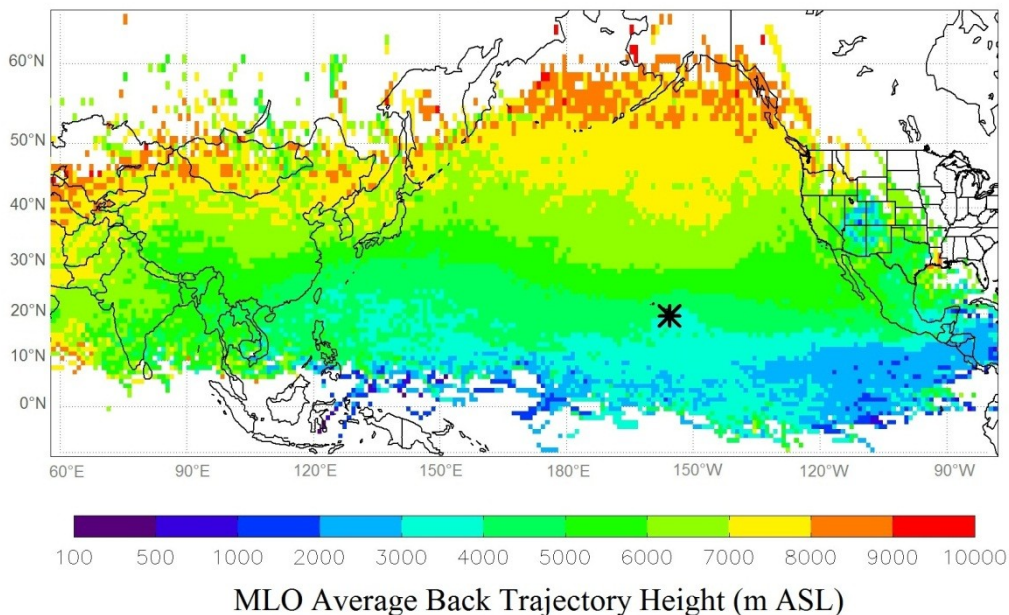


Figure 4.19: Height (above sea level) weighted trajectories from the MLO receptor site. Color represents the gridded average height during transport to MLO.

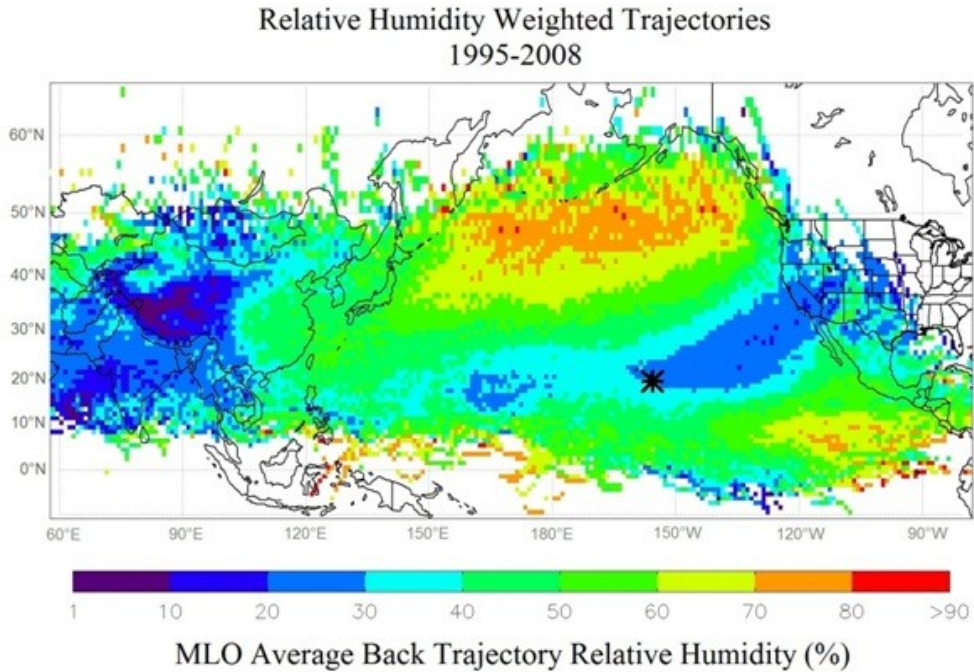


Figure 4.20: Relative humidity (RH) weighted HYSPLIT back trajectories from the MLO receptor site. Color represents the gridded average RH during transport to MLO.

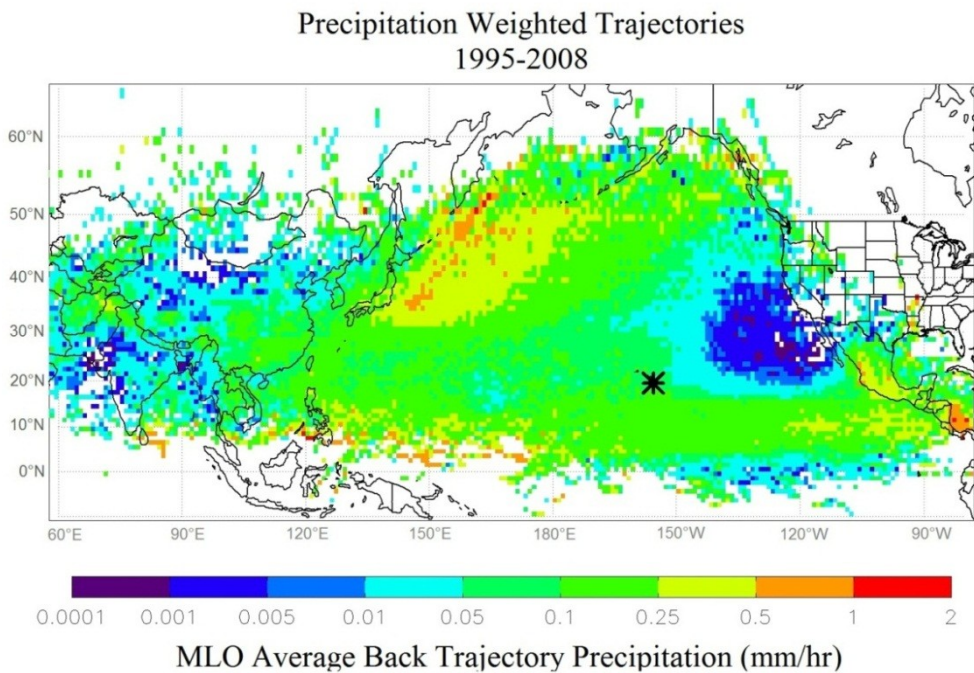


Figure 4.21: Precipitation weighted HYSPLIT back trajectories from the MLO receptor site. Color represents the gridded average surface precipitation beneath the air parcel position during transport to MLO.

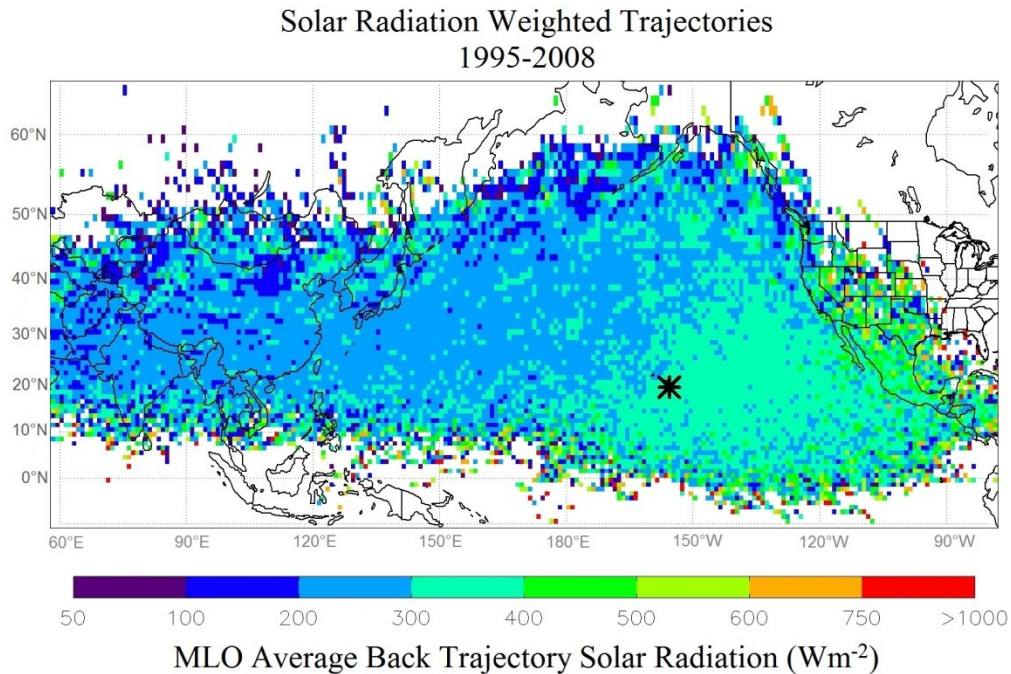


Figure 4.22: Solar radiation weighted HYSPLIT back trajectories from the MLO receptor site. Color represents the gridded average solar radiation reaching the surface beneath the air parcel position during transport to MLO.

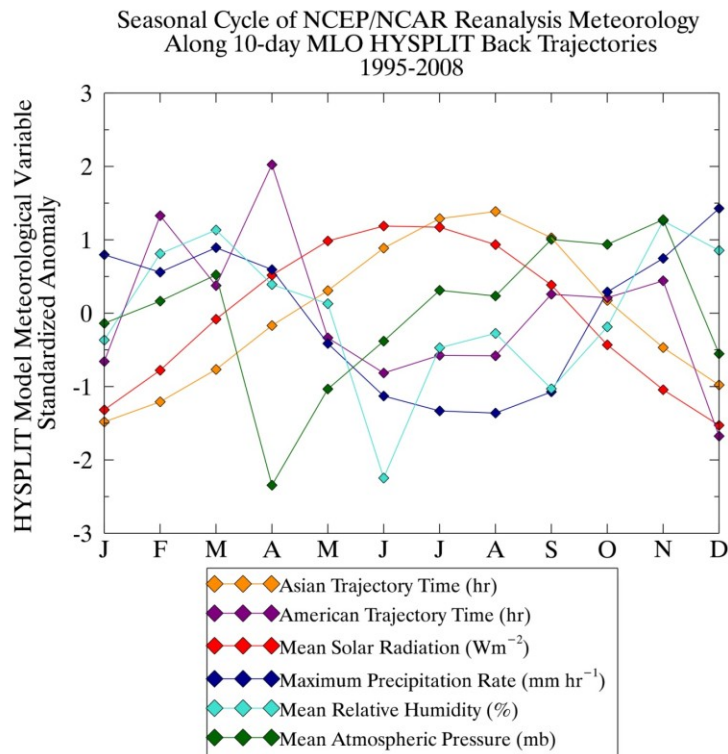


Figure 4.23: Seasonal cycle of NCEP/NCAR Reanalysis meteorological fields corresponding to HYSPLIT back trajectory locations. Each variable was normalized by the annual mean and standard deviation for intercomparison.

4.2.2 Circulation Patterns

We hypothesized that circulation changes in the Pacific Basin as indicated by the Multivariate ENSO Index (MEI) were likely responsible for a portion of the interannual variability observed in MLO anthropogenic NSS-sulfate and in the chemical continental tracer species. Figure (4.24) shows a timeline of MEI values which were explained in more detail in Section (2.4). During 1995-2008, MEI varied from positive to negative with an irregular multi-year cycle. This irregular interannual variability is illustrated in Figure (4.25) which shows the autocorrelation coefficient as a function of lag time for the MEI time series as well as similar autocorrelations for anthropogenic NSS-sulfate, carbon monoxide, NSS-calcium, and radon. A consistent seasonal cycle was present in each of the chemical species although the timing of the seasonal peaks did vary depending on the species, as discussed previously. Regardless of this variation, the seasonal datasets exhibited autocorrelation coefficient maxima at 12 month lag time intervals. This occurred because the datasets were positively correlated when offset by 12 months, when maximum concentrations during one year aligned with maximum concentrations during the following year, and negatively correlated when offset by 6 months, when peak concentrations of one year were compared with minimum concentrations of the same year. Secondary peaks in autocorrelation of anthropogenic NSS-sulfate were observed at mid-year intervals when autocorrelation of the other species was strongly negative because at these time intervals, the secondary autumn peak in the anthropogenic NSS-sulfate seasonal cycle was aligned with the primary springtime peak. In contrast to this pattern, MEI did not have high autocorrelation coefficients at each 12 month lag interval. The MEI autocorrelation pattern was lower in frequency, demonstrating the fact that MEI values were either anomalously high or low for varying periods of time typically lasting longer than 12 months.

The most notable feature of the MEI time series in Figure (4.24) was a period of large positive MEI anomalies during 1997-1998 associated with an El Niño event during this time. Carbon monoxide at MLO was similarly found to be anomalously high during the 1997-1998 El Niño event as shown in Figure (4.15). Elevated CO concentrations at MLO during this time were related to the anomalously high biomass burning activity in regions such as southeastern Asia and Central America as a result of regional drought conditions typical of this strong El Niño period (van der Werf et al., 2004). Although this relationship was clearly tied to El Niño/La Niña patterns, the increased carbon monoxide concentrations during 1997-1998 were related to changes in emissions as a result of dry conditions and severe wildfires, but not necessarily increased or decreased efficiency of transport due to circulation changes.

As discussed previously, Lintner et al. (2006) found that the relationship between ENSO phase and MLO concentrations of carbon dioxide was found to be seasonally dependent. To determine how ENSO circulation changes impacted the MLO chemical tracer species and anthropogenic NSS-sulfate during times of transport from the East Asia source region, the relationship between MEI and concentration was analyzed for correlation during only the 2-3 month time period of peak species concentration. As suggested by Wolter (2012), the MEI value for the earlier month in the sliding bi-monthly scale was used for comparison with other monthly values such as chemical concentration. In general, correlations between MEI and chemical concentration were not significant when the entire study period was included but stronger correlations existed when only the months representing the peak season of each species was included.

Interestingly, the correlation between MEI and species concentration during the relative season of maximum concentrations was found to be positive for gaseous species (radon and

carbon monoxide) but negative for aerosol species (NSS-calcium and anthropogenic NSS-sulfate) as shown in Figures (4.26) and (4.27). The positive correlations were stronger for radon and carbon monoxide than the negative correlations were for the aerosol species. Lintner et al. (2006) demonstrated a seasonally dependent relationship between circulation patterns characteristic of El Nino or La Nina conditions and circulation patterns characteristic of high or low carbon dioxide concentrations with an opposite relationship observed during summer than during winter, spring, or autumn. The peak in anthropogenic NSS-sulfate concentrations overlaps the spring and summer seasons (April, May, June) so a direct linear relationship between peak season sulfate concentrations and MEI may not be fully appropriate. These results seemed to indicate that circulation changes related to ENSO contributed to a portion of the variability at MLO but its influence, particularly in the particulate species, was complicated by variations in other controlling factors. The fact that the relationship between MEI and chemical concentrations at MLO was seasonally dependent suggested that this relationship may also exhibit interannual variability that would be difficult to easily detect.

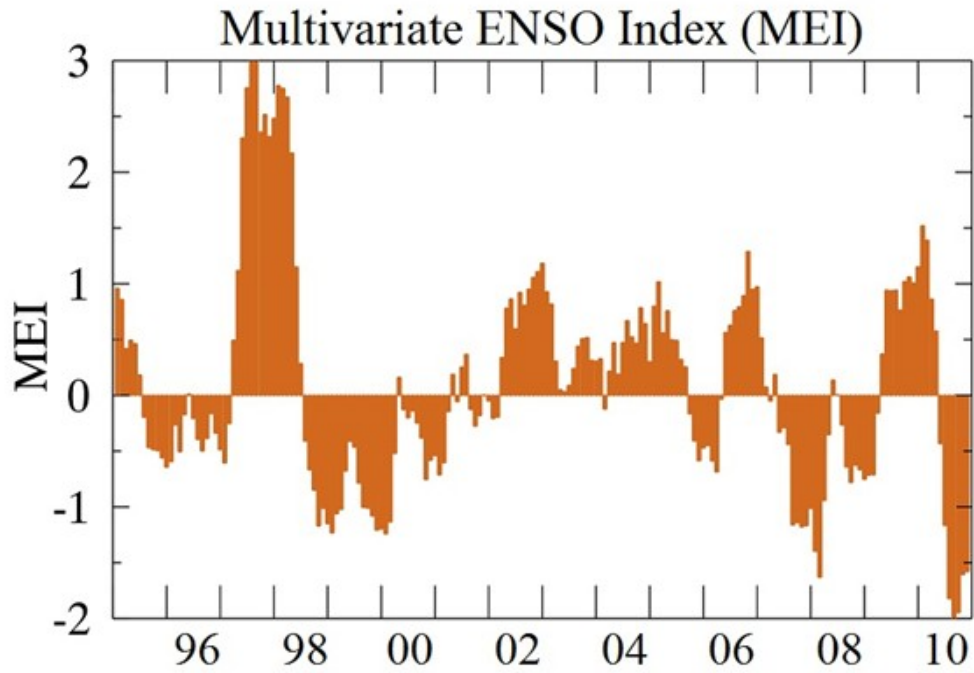


Figure 4.24: Multivariate ENSO Index (MEI) anomaly values for 1995-2008 (data from Wolter et al., 2012).

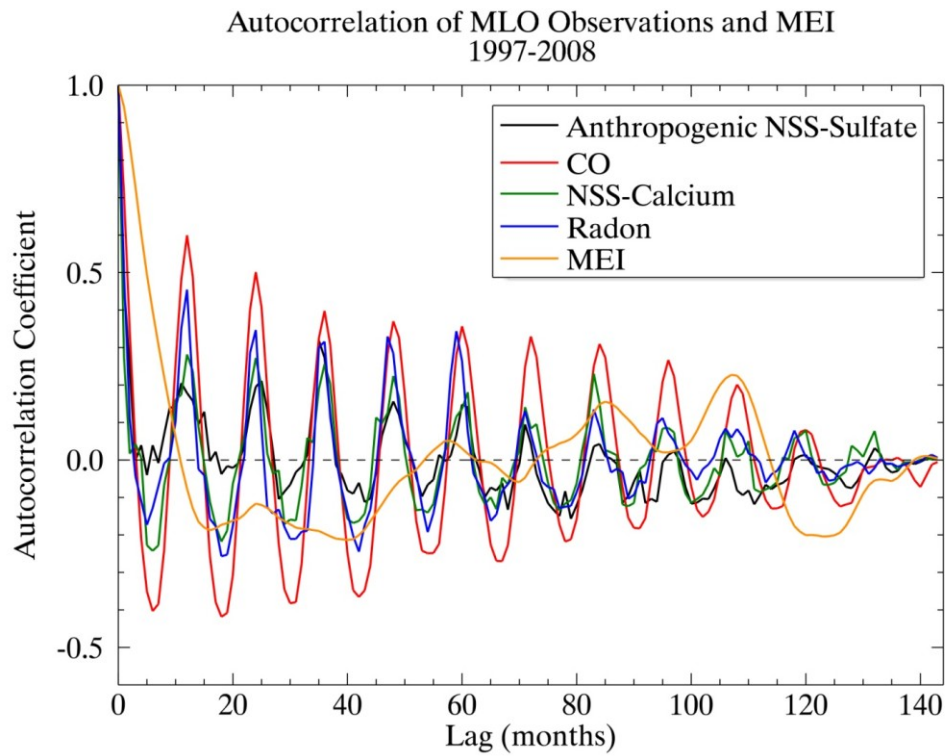


Figure 4.25: Autocorrelation of MLO chemical species and MEI beginning in January 1997.

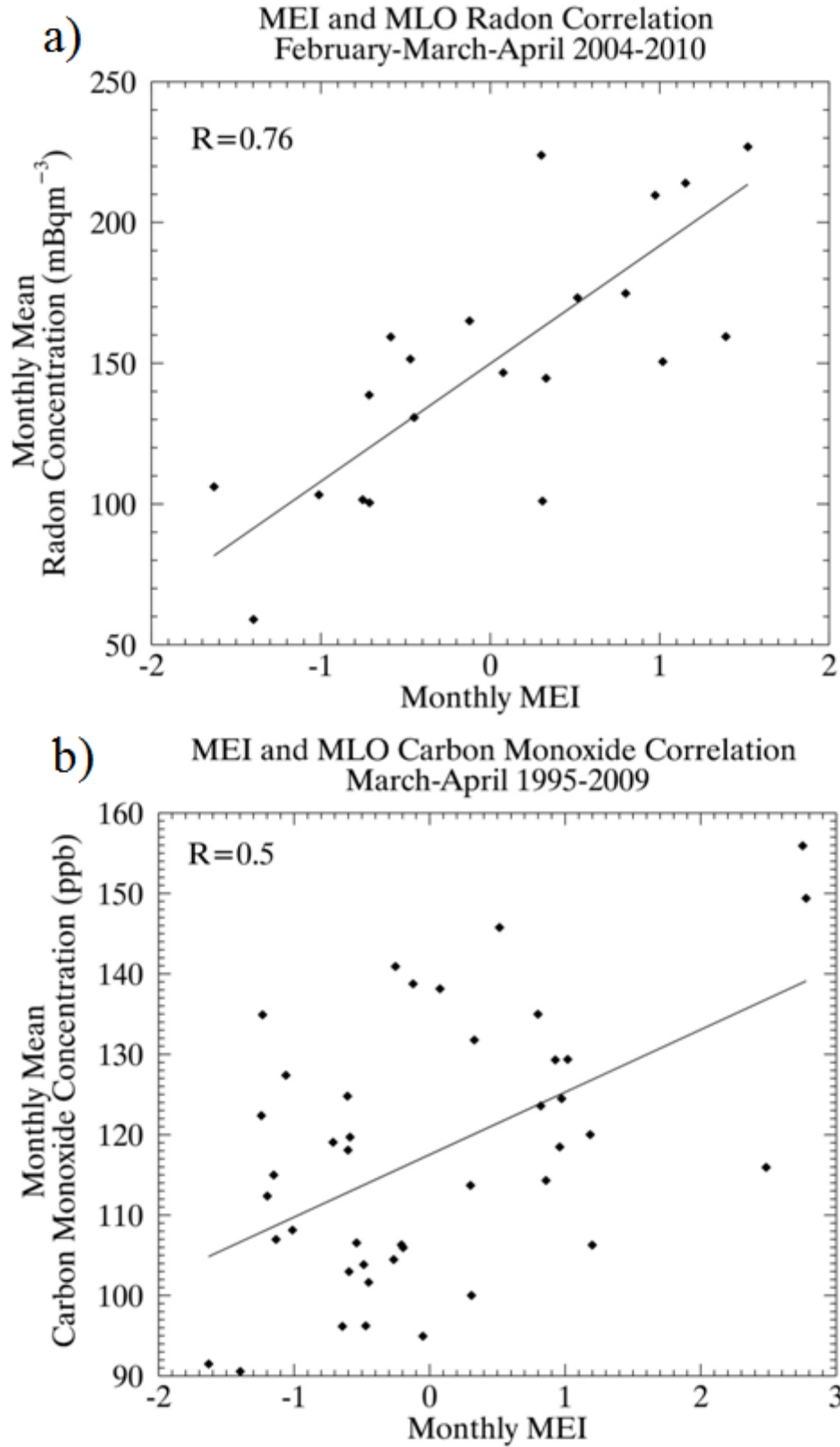


Figure 4.26: Correlation between MEI and peak season monthly concentrations of radon (a) and carbon monoxide (b).

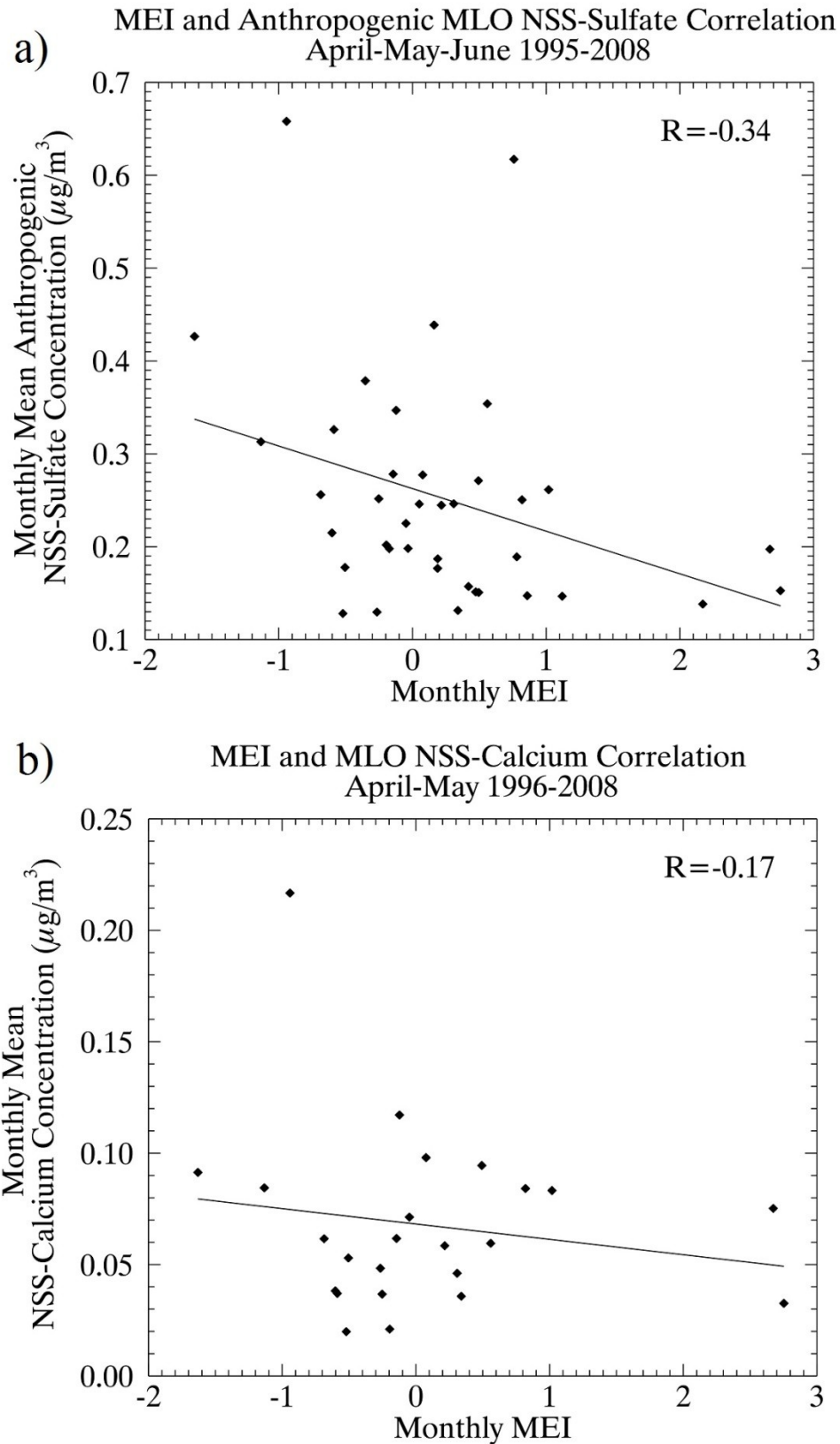


Figure 4.27: Correlation between MEI and peak season monthly concentrations of anthropogenic NSS-sulfate and NSS-calcium.

4.3 Multiple Linear Regression for Identifying Role of Transport

A multiple linear regression technique was applied to simultaneously analyze the contributions of different independent variables towards variability in concentrations of sulfate and selected continental tracers. The details of this method are described further in Section (2.7.3). Regression was first performed on the gaseous continental tracers radon and carbon monoxide using meteorological variables derived from HYSPLIT trajectory analysis and indices of circulation and transport discussed previously. The results of the continental tracer regression analysis were compared with regression of anthropogenic NSS-sulfate using the same regressors, and then additional meteorological variables as regressors which were likely to impact sulfate aerosol transport to MLO were also included. Finally, anthropogenic SO₂ emissions from East Asia and volcanic emissions from Kilauea, Hawaii were also included as regressors to determine what portion of the observed anthropogenic NSS-sulfate trend could be explained using the assumed East Asian anthropogenic SO₂ emissions trends published by Lu, Zhang, and Streets (2011).

Nine variables were selected to represent estimates of precursor emissions, production, transport, and removal of sulfate. Annual mean values were used for East Asian SO₂ emissions and Kilauea SO₂ emissions (Elias and Sutton, 2012) while monthly mean values were used for all other meteorological variables. Timelines of these independent variables used as regressors are shown in Figure (4.28). Selected subsets of these variables were used for regression of radon (1997-2008) and carbon monoxide (1995-2008). Regression of anthropogenic NSS-sulfate (1995-2008) was performed three times with different combinations of these variables to examine how results changed based on the application of additional information.

Correlations between all independent variables are shown in Table (4.2) with the labels corresponding to the letter associated with each variable in Figure (4.28). Reasonably strong correlations existed between trajectory speed and solar radiation, due to the fact that the solar radiation was strongest during the summer, when trajectory speed from East Asia was at a minimum and trajectory speed from America was at a maximum. Additionally, the seasonal cycles of solar radiation and precipitation were offset which resulted in negative correlations between these two variables. As discussed previously, it was hypothesized that the overlap between the seasonal cycles of these variables may be a contributing factor controlling the seasonal cycle of anthropogenic NSS-sulfate at MLO so meteorological variables were not excluded for being positively or negatively correlated. There were a select number of variable pairs which did exhibit a significant correlation although there was not a logical physical explanation behind this correlation (i.e. East Asian Emissions and Kilauea Volcano Emissions). Over half of the possible combinations of two independent variables exhibited very weak correlations which were not significant at the 90% confidence level.

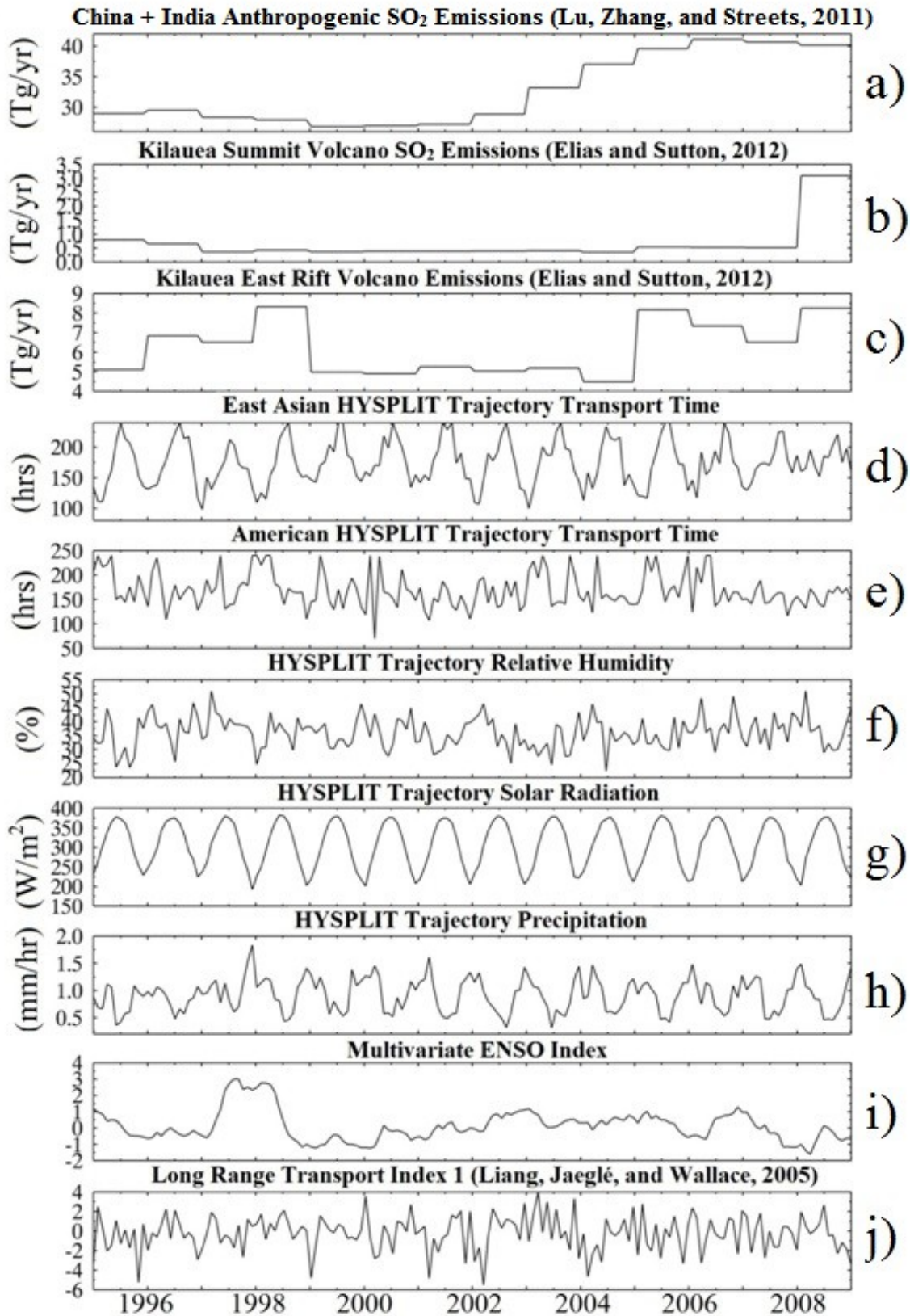


Figure 4.28: Timelines of all independent variables used for multiple linear regression.

Table 4.2: Correlations of monthly independent variables during 1995-2008. Variables are defined by letter in Figure (4.34).

Correlation Coefficients of Independent Variables Used for Multiple Linear Regression (1995-2008)										
	(a)	(b)	(c)	(d)	(e)	(f)	(g)	(h)	(i)	(j)
(a)	1	0.399	0.459	0.0168	-0.0101	0.0443	0.0166	-0.0353	-0.0557	-0.0352
(b)	0.399	1	0.459	0.0421	-0.0681	0.0276	0.00969	-0.0546	-0.247	-0.0269
(c)	0.459	0.459	1	-0.024	0.109	0.111	0.00993	0.00971	0.08	0.0509
(d)	0.0168	0.0421	-0.024	1	-0.204	-0.252	0.717	-0.674	-0.075	0.0753
(e)	-0.0101	-0.0681	0.109	-0.204	1	-0.0444	-0.0105	0.11	0.238	0.00943
(f)	0.0443	0.0276	0.111	-0.252	-0.0444	1	-0.232	0.403	-0.149	-0.167
(g)	0.0166	0.00969	0.00993	0.717	-0.0105	-0.232	1	-0.728	0.132	0.062
(h)	-0.0353	-0.0546	0.00971	-0.674	0.11	0.403	-0.728	1	-0.0479	-0.0682
(i)	-0.0557	-0.247	0.08	-0.075	0.238	-0.149	0.132	-0.0479	1	0.112
(j)	-0.0352	-0.0269	0.0509	0.0753	0.00943	-0.167	0.062	-0.0682	0.112	1

*Red values indicate a significant correlation at >90% confidence

4.3.1 Regression Analysis of Continental Tracers

To better understand the variables influencing anthropogenic NSS-sulfate aerosol at MLO, the continental tracers were first analyzed to determine the extent to which variations in transport efficiency could be explained using a select number of meteorological variables. The four variables selected for multiple linear regression of gaseous continental tracers radon and carbon monoxide are labeled (d), (e), (i), and (j) in Figure (4.28), representing HYSPLIT trajectory transport time from each continental source region as well as MEI and LRT1. It was hypothesized that the first two variables would explain a majority of the seasonal cycle in long distance transport to MLO while the second two variables would explain a portion of the interannual variability. The HYSPLIT trajectory transport time variables were defined as the amount of time in hours for a back trajectory to reach either the East Asian or American pre-defined regions as shown in Figure (4.4) in Section (4.1.1) so these variables are inversely proportional to transport speed. An additional categorical variable which is not shown in Figure (4.28) was included for the regression of radon only, intended to correct for an apparent shift in mean concentrations after the instrument replacement during 2003. This variable was defined to be equal to one for all months prior to January 2004 and zero for all months after January 2004.

The MLR results for radon during 1997-2008 are shown in Figure (4.29). Trajectory speed and the selected transport indices captured approximately 57% of radon variability during this time period. The seasonal cycle was well predicted, primarily from the strong agreement with trajectory transport speed from the East Asian region. Table (4.3) summarizes statistical significance and the predicted beta value with standard error for each regressor. East Asian HYSPLIT trajectory transport time and the instrument correction variables were found to be

statistically significant regressors while MEI and LRT1 were not significant at the 90% confidence level.

Although a majority of radon variability was predicted, the regression model performed particularly poorly during years with anomalously high late winter/early spring peaks in radon concentrations. Radon originating from either local island sources or surrounding oceanic regions may have contributed to the high concentrations during these time periods. Such sources would not be explained by long distance transport time or large scale circulation and transport phenomena captured by MEI and LRT1. As discussed in Section (4.1.2), radon concentrations were anomalously high during the early spring of 2002 although both carbon monoxide and NSS-calcium concentrations were anomalously low. The regression results predicted low radon concentrations during this year which further suggests that contamination or instrument error may be responsible for a portion of the high concentration observations made during this season.

The MLR results for carbon monoxide during 1995-2008 are shown in Figure (4.30). Trajectory speed and transport indices captured 64% of carbon monoxide variability during 1995-2008. Similar to the results for radon, the seasonal cycle was very well captured although the magnitude of certain late winter/early spring peak concentrations was error prone at times. In contrast, the relative magnitude of the summer minimum in carbon monoxide concentrations was well explained with the exception of anomalously low summer carbon monoxide concentrations during 1996, 2006, and 2008. Statistical significance and predicted beta values with standard error for each regressor are summarized in Table (4.4). The HYSPLIT trajectory transport time from East Asia was found to be a statistically significant regressor for carbon monoxide although unlike radon, the HYSPLIT trajectory transport time from the American continent was also statistically significant for carbon monoxide. Interestingly, the beta values for East Asian

transport time for both radon and carbon monoxide are positive, which implies that larger (and therefore slower) transport times corresponded to higher observed concentrations at MLO while the beta values for American HYSPLIT trajectory time were negative implying that faster transport from the American continent resulted in higher concentrations. We expected to see an inverse relationship between concentrations and transport time although as discussed before, the increased favorability of lofting and free tropospheric export from East Asia occurs during the spring, as trajectory speed slows down somewhat compared to the extremely fast transport during the winter. We hypothesized that this phenomenon would be captured in part by the LRT1 index although strong correlations didn't exist between LRT1 and either radon or carbon monoxide. The development of this index by Liang, Jaeglé, and Wallace (2005) is explained in more detail in Section (2.5). The regression results suggest that perhaps Asian outflow used to define this index was modeled at a more northern latitude band than is relevant for transport to MLO and the development of more MLO-specific long range transport indices would capture more of this variability.

Although MEI was not found to be a statistically significant regressor at the 90% confidence level for either species, it is possible that the relationship between MEI and radon/carbon monoxide was skewed by the anomalously high MEI event during 1997-1998 and that it would be more relevant during a period of years without such a strong El Nino event. As previously mentioned, the relationship between MEI and chemical concentrations at MLO also varied with season and regression results are unable to account for this variability if monthly time series are used that include all seasons over several years. Therefore, the linear assumptions made in this regression model may not be accurate for capturing transport variability related to ENSO.

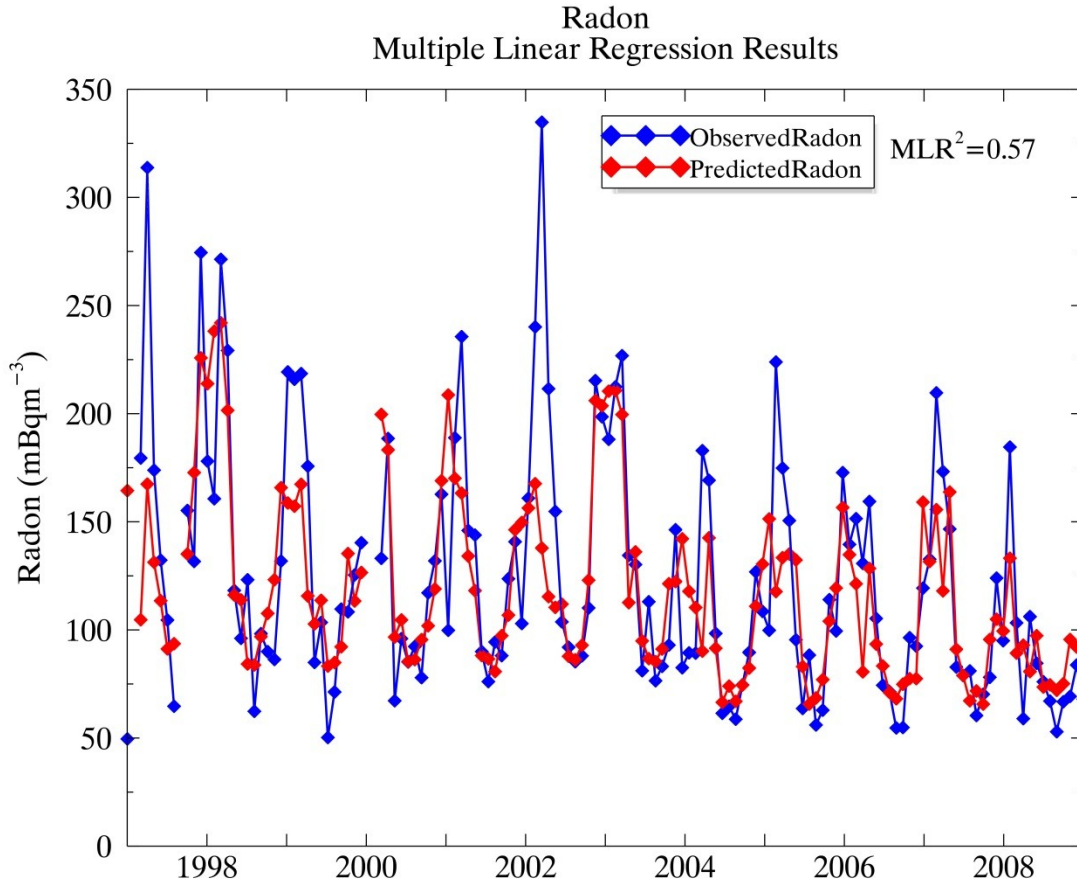


Figure 4.29: Multiple linear regression results for MLO radon concentrations during 1997-2010.

Table 4.3: Statistical significance and calculated β values with associated error for each independent variable used for regression of MLO radon.

MLO Radon MLR Results 1997-2008		
Regressor	Statistically Significant Regressor (>90%)	MLR Beta Value
East Asian HYSPLIT Trajectory Transport Time	Yes	1.00 +/- 0.117
American HYSPLIT Trajectory Transport Time	No	-0.125 +/- 0.184
Multivariate ENSO Index	No	0.0126 +/- 0.0259
Long Range Transport Index 1 (Liang, Jaeglé, and Wallace, 2005)	No	-0.00746 +/- 0.0138
Instrument Correction	Yes	0.243 +/- 0.0499

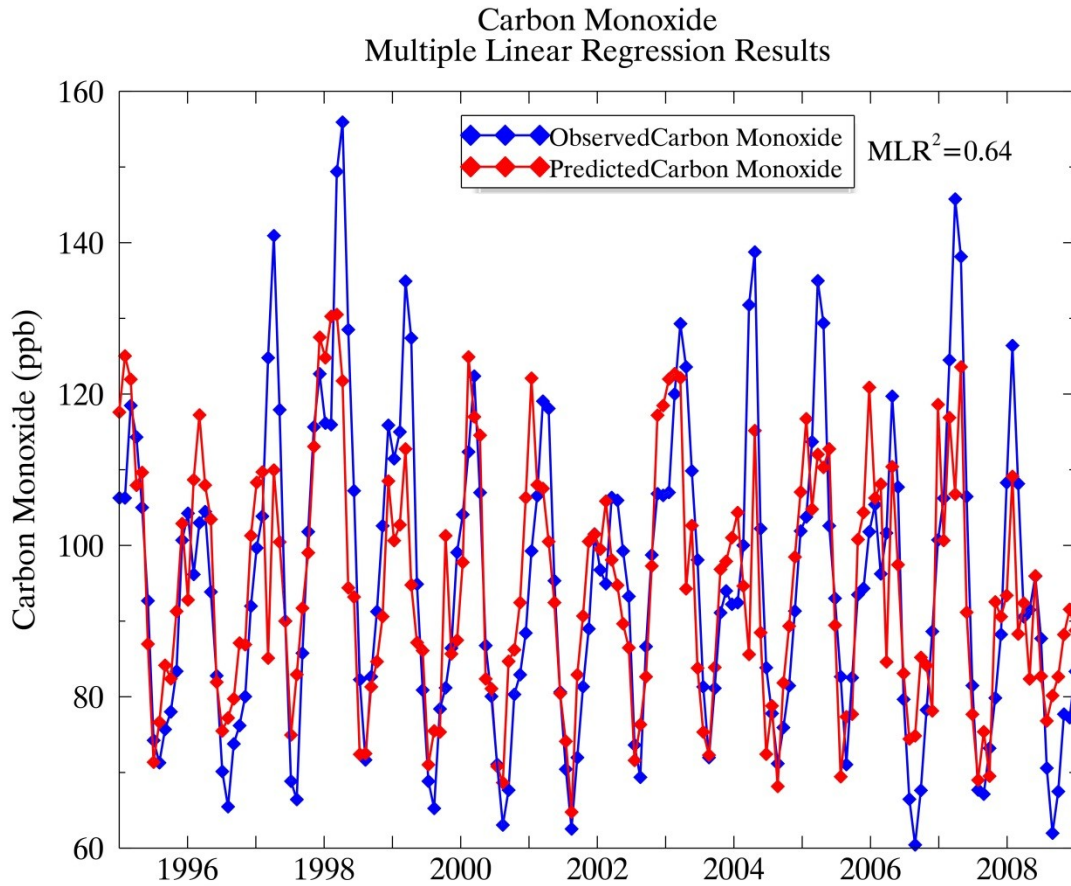


Figure 4.30: Multiple linear regression results for carbon monoxide concentrations during 1995-2008.

Table 4.4: Statistical significance and calculated β values with associated error for each independent variable used for regression of MLO carbon monoxide.

MLO Carbon Monoxide MLR Results 1995-2008		
Regressor	Statistically Significant Regressor (>90%)	MLR Beta Value
East Asian HYSPLIT Trajectory Transport Time	Yes	0.426 +/- 0.0477
American HYSPLIT Trajectory Transport Time	Yes	-0.367 +/- 0.0777
Multivariate ENSO Index	No	0.00575 +/- 0.0106
Long Range Transport Index 1 (Liang, Jaeglé, and Wallace, 2005)	No	0.00159 +/- 0.00553

4.3.2 Regression Analysis of Anthropogenic NSS-Sulfate

Regression for anthropogenic NSS-sulfate was initially performed using the same meteorological variables which were used for regression of radon and carbon monoxide. The results of this analysis were found to explain only 6% of anthropogenic NSS-sulfate variability as shown in Figure (4.31). This result indicates that although the selected meteorological parameters did explain a majority of the variability in radon and carbon monoxide, other factors are certainly driving the variability of anthropogenic NSS-sulfate concentrations at MLO during the study period.

As discussed in Section (4.2.1), it was hypothesized that a combination of influences from solar radiation, relative humidity, precipitation, and source region transport favorability controlled a majority of the seasonal cycle in anthropogenic NSS-sulfate. To test this hypothesis, three additional variables representing solar radiation, relative humidity, and precipitation along each HYSPLIT trajectory pathway were added as regressors to the previous four meteorological variables and the regression was repeated. The regression results with all six meteorological variables are shown in Figure (4.32). Using these regressors, approximately 34% of anthropogenic NSS-sulfate variability during 1995-2008 was captured. The anthropogenic NSS-sulfate seasonal cycle was well represented by considering solar radiation and precipitation, although very little of the observed trend was captured and no statistically significant trend was found in the predicted concentrations. These results suggest that variations in meteorology and transport, as represented by the variables considered in this study, cannot explain the increasing trend observed in anthropogenic NSS-sulfate during 1995-2008 which suggests that a combination of anthropogenic and natural emissions were likely driving the observed trend in sulfate aerosol at MLO.

The three additional regressors representing Kilauea volcanic east rift and summit SO₂ emissions and East Asian anthropogenic SO₂ emissions (Figure 4.3.3) were added to the previously applied meteorological variables and the anthropogenic NSS-sulfate regression was repeated. The results of this are shown in Figure (4.34). This regression model captured 46% of the observed variability in anthropogenic NSS-sulfate concentrations. However, this improved regression model frequently overestimated the seasonal minimum concentrations and underestimated the seasonal maximum concentrations. Statistical significance and beta values with standard error for each independent variable used for regression of anthropogenic NSS-sulfate are summarized in Table (4.5). Statistically significant regressors included East Asian emissions, East Asian transport time, HYSPLIT trajectory solar radiation, and HYSPLIT trajectory precipitation.

The linear trend in predicted anthropogenic NSS-sulfate concentrations using this statistical model was found to be 5.6 ng/m³ per year. This underestimation in predicted anthropogenic NSS-sulfate trend could be a result of one or more of the following:

- Underestimation of East Asian or volcanic emissions during this time period, particularly during 2008
- Influence of additional emissions sources such as biomass burning, additional volcanic influence, or shipping activity which were not included in this study
- Influence of transport variability which is not accounted for by the selected meteorological parameters
- Statistical errors associated with the simplified multiple linear regression technique

Although the inclusion of East Asian and Kilauea Volcanic emissions did result in a predicted increasing anthropogenic NSS-sulfate trend, this does not necessarily confirm that the

increase in anthropogenic NSS-sulfate at MLO was caused by the trend in East Asian emissions. The East Asian SO₂ emissions variable was the only independent variable that exhibited a statistically significant increasing trend, and therefore the model predicted sulfate using this variable also exhibited an increasing trend. Additionally, although a linear trend in East Asian SO₂ emissions was calculated, as shown in Figure (4.33), emissions from this region were highly non-linear throughout the study period and any error in estimation of annual emissions averages would introduce error into the prediction of an associated anthropogenic NSS-sulfate trend as well. Regardless of the important caveats associated with this regression method, the results do support the conclusion that the observed increasing anthropogenic NSS-sulfate trend of 7.3 ng/m³ per year cannot reasonably be explained by variations in meteorology alone, but is likely attributable to a combination of volcanic and anthropogenic emissions sources.

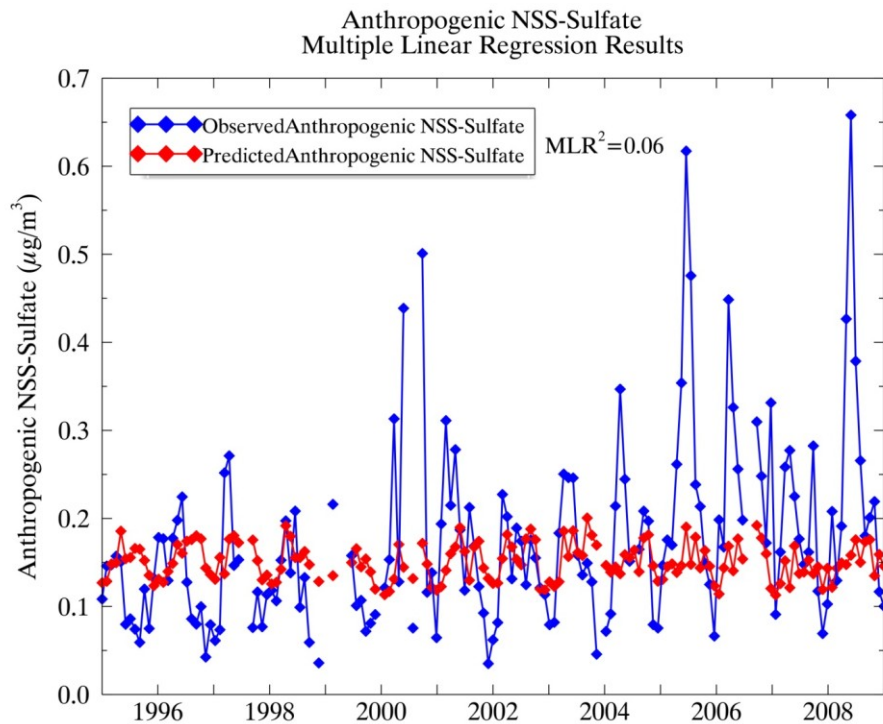


Figure 4.31: Multiple linear regression results for anthropogenic NSS-sulfate during 1995-2008 using selected meteorological regressors (d), (e), (i), and (j) as defined in Figure (4.28).

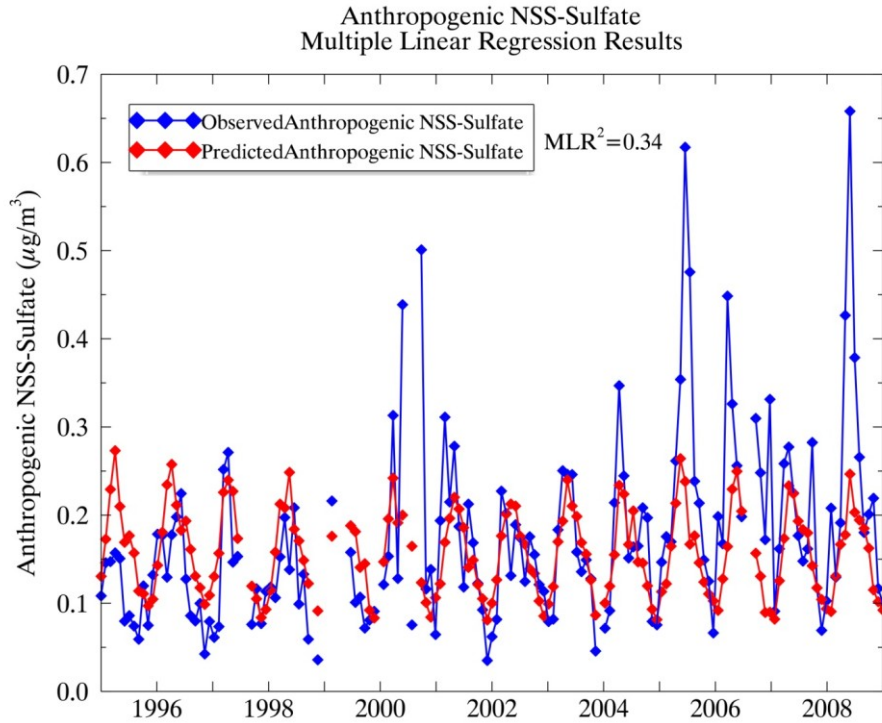


Figure 4.32: Multiple linear regression results for anthropogenic NSS-sulfate during 1995-2008 using selected meteorological regressors (d), (e), (i), (j), (g), and (h) as defined in Figure (4.28).

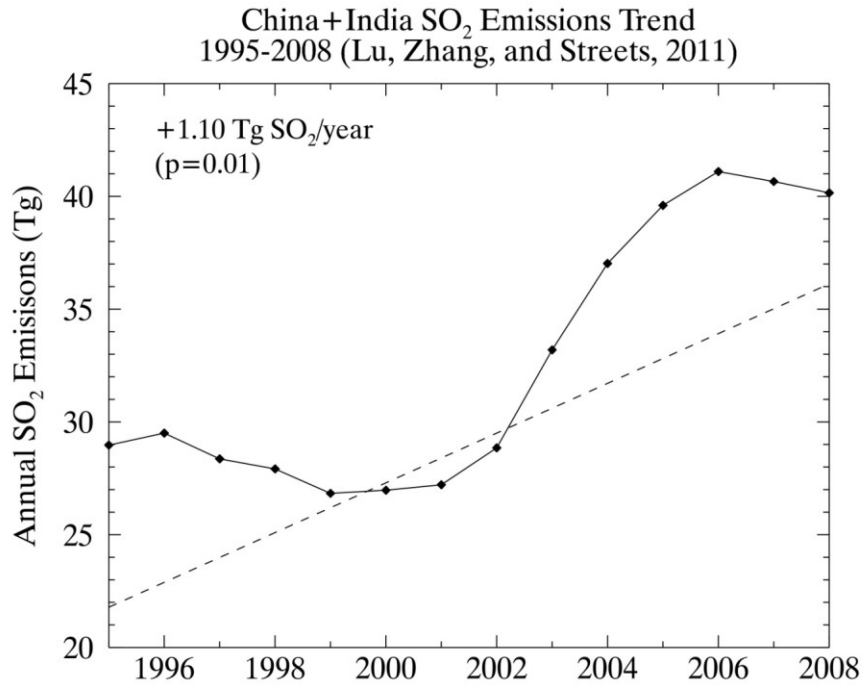


Figure 4.33: Annual combined SO₂ emissions and average trend during 1995-2008 for China and India from Lu, Zhang, and Streets (2011).

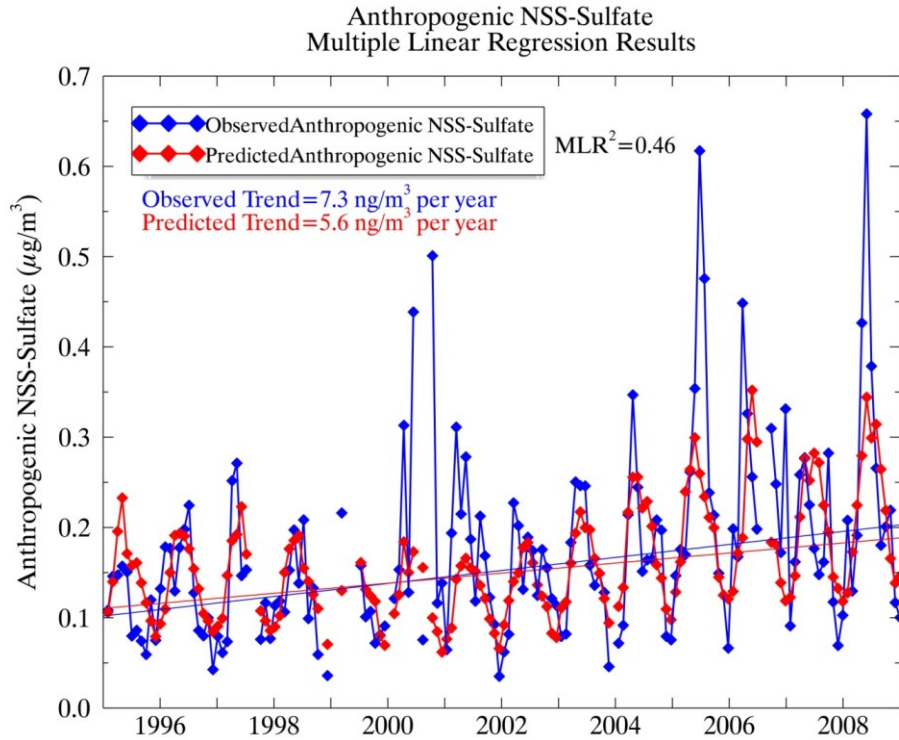


Figure 4.34: Multiple linear regression of anthropogenic NSS-sulfate using all variables shown in Figure (4.28) as regressors. Their trends for observed monthly mean data and predicted monthly data are shown in blue and red respectively.

Table 4.5: Statistical significance and calculated β values with associated error for each independent variable used for regression of MLO radon.

MLO Anthropogenic NSS-Sulfate MLR Results 1995-2008		
Regressor	Statistically Significant Regressor (>90%)	MLR Beta Value
China + India SO ₂ Emissions (<i>Lu, Zhang, and Streets, 2011</i>)	yes	0.0344 +/- 0.00706
Kilauea Summit Volcano SO ₂ Emissions (<i>Elias and Sutton, 2012</i>)	no	0.0506 +/- 0.0588
Kilauea East Rift Volcano SO ₂ Emissions (<i>Elias and Sutton, 2012</i>)	no	0.00402 +/- 0.0314
East Asian HYSPLIT Trajectory Transport Time	yes	-0.00226 +/- 0.00147
American HYSPLIT Trajectory Transport Time	no	0.000791 +/- 0.00102
HYSPLIT Trajectory Relative Humidity	no	-0.00335 +/- 0.00684
HYSPLIT Trajectory Solar Radiation	yes	0.00752 +/- 0.00101
HYSPLIT Trajectory Precipitation	yes	0.388 +/- 0.178
Multivariate ENSO Index	no	-0.0143 +/- 0.0441
Long Range Transport Index 1 (<i>Liang, Jaeglé, and Wallace, 2005</i>)	no	-0.00356 +/- 0.0197

5. Conclusions and Suggestions for Future Work

5.1 What are the anthropogenic and natural components of MLO sulfate aerosol?

Sulfate aerosol observed at MLO during 1995-2008 was determined to be predominately of anthropogenic origin (83.2%) with small but non-negligible contributions of biogenic DMS-derived (15.3%) and sea-salt sulfate (1.79%) sources. Additional work on quantifying the branching ratio of DMS to MSA and NSS-sulfate would provide a more accurate estimate than was used in this study to quantify the biogenic component of sulfate aerosol at MLO. The strict criteria applied to sulfate aerosol observations should be revisited to determine whether valid free-tropospheric observations were improperly omitted from analysis to provide an even more complete dataset for future studies. Hourly radon data could be applied as a relevant indicator of local contamination at MLO for this purpose.

Sulfate aerosol of volcanic origin has the potential to impact MLO despite the fact that data were specifically screened to remove local volcanic influence. Kilauea Volcano emissions were not found to be a statistically significant regressor for anthropogenic NSS-sulfate although this result did not eliminate the possibility that Kilauea emissions and anthropogenic NSS-sulfate exhibited a non linear relationship, with influence detected during the spring 2008 eruption only. The application of a more comprehensive volcanic emissions database would provide more insight into the impacts of long-range volcanic influence at MLO, particularly from volcanic eruptions which occurred in Asia or Alaska during the study period. Application of the long-term gridded volcanic emissions inventories A2-MAP and A2-ACCMIP, discussed by Diehl et al. (2012), would likely reveal relevant SO₂ emissions sources of anthropogenic or volcanic origin which were not identified in this study.

5.2 Can we identify long distance continental influence at MLO?

Mauna Loa Observatory experienced seasonally dependent periods of influence from both the Asian and North American continents during 1995-2008. Indications of long distance continental influence were evident in anthropogenic NSS-sulfate, radon, carbon monoxide, NSS-calcium, and HYSPLIT trajectory modeling although pros and cons associated with each method of tracing long distance influence were identified and discussed. Natural (radon and NSS-sulfate) and anthropogenic (CO, anthropogenic NSS-sulfate) components of the continental signal were interrelated but exhibited differences in seasonal peaks and variability. East Asian influence at MLO was most clearly observed during late winter and early spring while American influence was more evident during summer. Trends in continental tracers and HYSPLIT trajectory origin suggested that the magnitude of springtime East Asian influence at MLO was decreasing during 1995-2008 despite increasing trends in anthropogenic NSS-sulfate during the same time period. It was found that anthropogenic SO₂ emissions from both the Asian and American continents contributed to the observed sulfate aerosol at MLO with differing meteorological patterns controlling secondary production and transport efficiency from each region. Comparison of the observations at MLO during this long term study period with modeling results of radon and carbon monoxide at MLO would provide more information about factors driving the seasonal and interannual variability of long distance continental influence at MLO. Additionally, a finer resolution meteorological dataset for trajectory modeling would provide more accurate results particularly if applied to a receptor location which is in closer proximity to multiple pollution sources of interest.

5.3 What are the meteorological controls on transport to MLO?

The typical seasonal maxima in anthropogenic NSS-sulfate were found to correspond to overlapping seasonal cycles of solar radiation and precipitation across the regions of frequent transport. Regression results revealed that each of these variables was statistically significant as a regressor for anthropogenic NSS-sulfate. Nevertheless, indicators of this type of meteorological variability that are more applicable to transport in the free troposphere would be more reliable for understanding long range transport to a high elevation site like MLO. Additional application of the deposition and dispersion capabilities in HYSPLIT would also increase understanding of meteorological influences on production, transport, and loss of both SO₂ and sulfate aerosol.

Chemical continental tracer concentrations (radon and carbon monoxide) were found to be correlated with indicators of the El Niño-Southern Oscillation (ENSO). Anomalously high late winter and early spring radon and carbon monoxide concentrations at MLO typically corresponded to anomalously high MEI values, which suggested that continental transport may be more favorable during El Niño conditions than during La Niña Conditions. However, springtime anthropogenic-NSS sulfate and NSS-calcium concentrations were negatively correlated with corresponding springtime MEI values, which suggest that there may be additional meteorological factors related to El Niño and La Niña conditions which impact aerosol species differently than gaseous species during transport to MLO. The multivariate ENSO index was selected for this study to represent circulation changes relevant for transport to MLO. However, another climate index may be a more appropriate representation of the phenomena controlling transport from continental source regions to MLO. Two additional

options for climate indices are shown in Figure (5.1) in comparison with the MEI and future work will explore correlations between these indices and MLO observations.

Finally, it was hypothesized that the long range transport index developed by Liang et al. (2005) would indicate favorable times for export out of the East Asian source region which would then be detected as higher concentrations of both natural and anthropogenic species at MLO. This variable was not found to be a statistically significant regressor for any of the species tested using MLR. The development of new MLO-specific convective lifting and long range transport indices using a technique similar to that applied by Liang et al. (2005), combining chemical and meteorological data, would be useful for understanding transport variability at MLO.

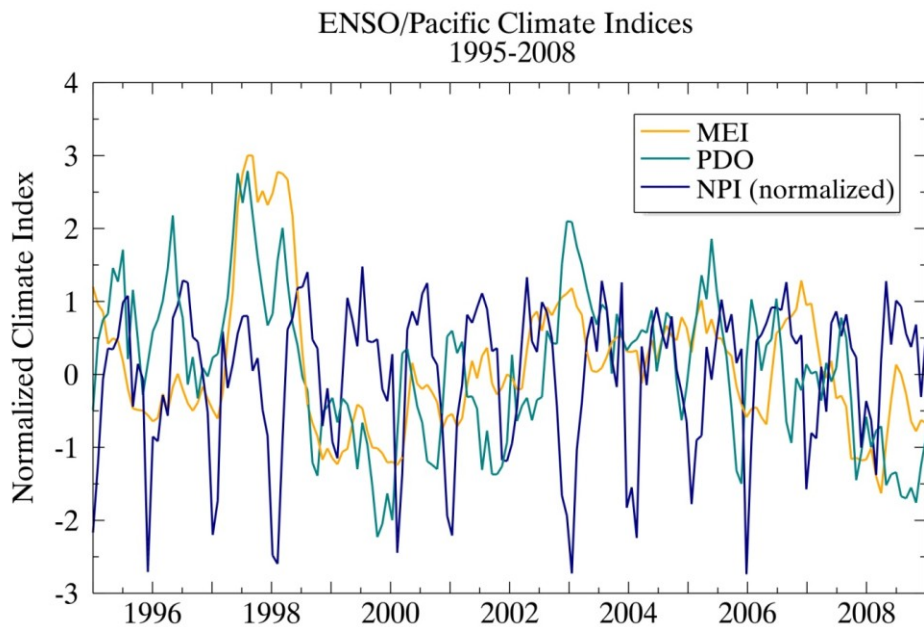


Figure 5.1: Time series of the Multivariate ENSO Index, Pacific Decadal Oscillation, and North Pacific Index.

5.4 Can observed sulfate trends be attributed to anthropogenic emission trends?

The application of a multiple linear regression technique has demonstrated the potential to simultaneously investigate impacts of meteorology, transport efficiency, and emissions on chemical concentrations using a computationally simple method although the relevance of the model results are dependent on careful selection of variables on the basis that they are expected to exhibit realistic physical relationships. Monthly mean anthropogenic NSS-sulfate concentrations were increasing at MLO during 1995-2008 at a rate of 4.8% (7.3 ng m^{-3}) per year. Increasing trends were statistically significant for both monthly mean and median concentrations during springtime (March-April-May) and early autumn (August-September-October) corresponding with the two seasonal peaks in concentrations.

Multiple linear regression was used as a tool to quantify contributions of meteorology and anthropogenic emissions to sulfate concentrations under highly simplified conditions that only account for meteorological controls on transport as determined by HYSPLIT trajectory modeling or transport indices, and trends in SO_2 emissions from China, India, and Kilauea Volcano. The regression technique was able to capture the seasonal variability and increasing trend of anthropogenic NSS-sulfate although several anomalously high springtime peak concentrations were not well explained by the selected regressors. If any portion of the springtime concentration peaks which were not well captured by the regression model are actually related to variations in anthropogenic emissions from East Asia, then the resulting anthropogenic NSS-sulfate trend associated with East Asian anthropogenic SO_2 emissions is likely an underestimate. The inclusion of more detailed anthropogenic emissions inventories than used in this study, such as those previously mentioned from Diehl et al. (2012), would likely improve these regression results. The Diehl et al. (2012) inventories also specifically include

anthropogenic shipping emissions which have been implicated as a large contributor to global SO₂ emissions in recent years by Klimont et al. (2013).

Additional work on sulfate aerosol trends at MLO may involve more robust comparison with other satellite datasets or model results. An example of such comparisons is shown in Figure (5.2) which shows that MLO observed concentrations generally overlapped with the Navy Aerosol Analysis and Prediction System (NAAPS) model total sulfate at the location of MLO during 2006-2008. Interestingly, a substantial increase in sulfate aerosol was predicted by NAAPS during 2011 and 2012 which further motivates continued long-term sulfate aerosol measurements at the MLO site for comparisons with future anthropogenic SO₂ emissions trends.

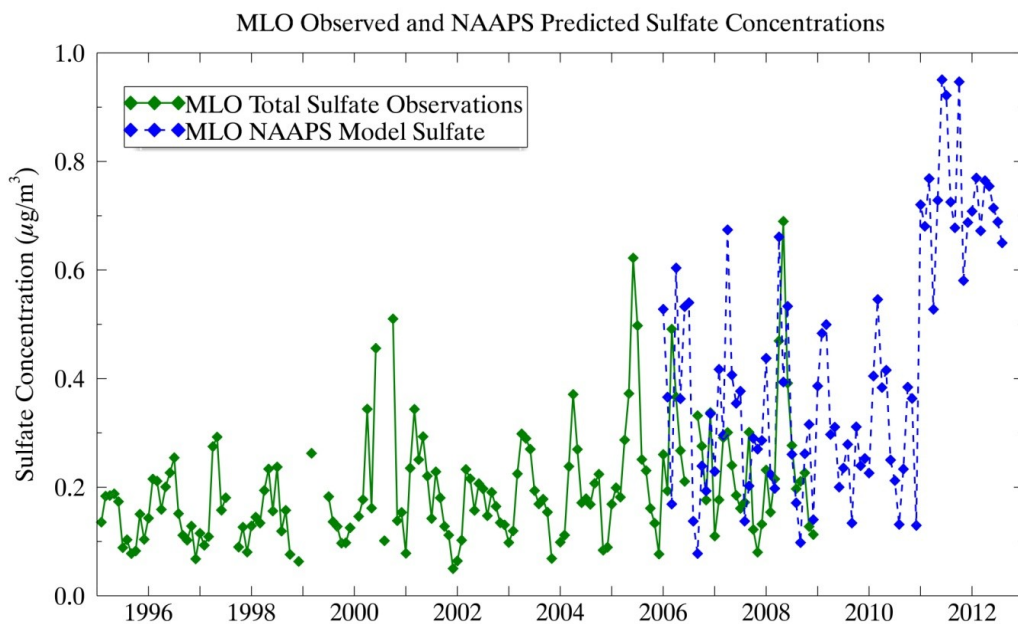


Figure 5.2: Comparison between anthropogenic NSS-sulfate observations at MLO used in this study and NAAPS model total sulfate aerosol at the corresponding latitude and longitude of MLO.

Despite the limitations present in this study, we were successfully able to identify a statistically significant increasing trend in sulfate aerosol at MLO which had not been reported

previously. We demonstrated the applicability of a regression technique for quantifying the effects of natural and anthropogenic emissions changes on sulfate aerosol observations at MLO after accounting for variations in transport. This work also represents one of the first studies to investigate the influence of circulation changes related to ENSO on transport of anthropogenic sulfate aerosol to MLO. The broad scope of this study have allowed us to present many different opportunities for future research which can be expanded upon to better understand long range pollution transport and trends in anthropogenic aerosols.

REFERENCES

- Akimoto, H., 2003: Global Air Quality and Pollution. *Science*, **302**, 1716-1719.
- Andreae, M.O., H. Berresheim, T.W. Andreae, M.A. Kritz, T.S. Bates, and J.T. Merrill, 1988: Vertical Distribution of Dimethylsulfide, Sulfur Dioxide, Aerosol Ions, and Radon over the Northeast Pacific Ocean. *Jour. Atmos. Chem.*, **6**, 149-173.
- Andreae, M.O., and P.J. Crutzen, 1997: Atmospheric Aerosols: Biogeochemical Sources and Role in Atmospheric Chemistry. *Science*, **276**, 1052-1058.
- Andres, R.J. and A.D. Kasgnoc, 1998: A time-averaged inventory of subaerial volcanic sulfur emissions. *J. Geophys. Res.* **103 (D19)**, 25251-25261.
- Ashbaugh, L.L., W.C. Malm, and W.Z. Sadeh, 1985: A residence time probability analysis of sulfur concentrations at Grand Canyon National Park. *Atmos. Environ.*, **19 (8)**, 1263-1270.
- Ayers, G.P. and J.M. Cainey, 2007: The CLAW hypothesis: a review of the major developments. *Environ. Chem*, **4**, 366-374.
- Barth, M.C., and A.T. Church, 1999: Regional and global distributions and lifetimes of sulfate aerosols from Mexico City and southeast China. *J. Geophys. Res.*, **104 (D23)**, 30231-30239.
- Bates, T.S., B.K. Lamb, A. Guenther, J. Dignon, and R.E. Stoiber, 1992: Sulfur Emissions to the Atmosphere from Natural Sources. *Jour. Atmos. Chem.*, **14**, 315-337.
- Benkovitz, C.M., S.E. Schwartz, M.P. Jensen, and M.A. Miller, 2006: Attribution of Modeled Atmospheric Sulfate and SO₂ in the Northern Hemisphere for June-July 1997. *Atmos. Chem. Phys*, **6**, 4023-4059.
- Berglen, T.F., T.K. Berntsen, I.S.A. Isaksen, J.K. Sundet, 2004: A global model of the coupled sulfur/oxidant chemistry in the troposphere: The sulfur cycle, *J. Geophys. Res.*, **109 (D19)**, D19310.
- Bian, H., M. Chin, S.R. Kawa, H. Yu, T. Diehl, and T. Kucsera, 2010: Multiscale carbon monoxide and aerosol correlations from satellite measurements and the GOCART model: Implication for emissions and atmospheric evolution. *J. Geophys. Res.* **115**, D07302.
- Bjerkenes, J., 1969: Atmospheric teleconnections from the equatorial Pacific. *Mon. Weather Rev.*, **97 (3)**, 163-172.
- Buermann, W., B.R. Lintner, C.D. Koven, A. Angert, J.E. Pinzon, C.J. Tucker, and I.Y. Fung, 2007: The changing carbon cycle at Mauna Loa Observatory. *PNAS*, **104 (11)**, 4249-4254.

- Castebrunet, H., P. Martinerie, C. Genthon, and E. Cosme, 2009: A three-dimensional model study of methanesulphonic acid to non sea salt sulfate ratio at mid and high-southern latitudes, *Atmos. Chem. Phys.*, **9**, 9449-9469.
- Charlson, R.J., J.E. Lovelock, M.O. Andrea, S.G. Warren, 1987: Oceanic phytoplankton, atmospheric sulphur, cloud albedo, and climate. *Nature*, **326 (16)**, 655-661.
- Chin, M., R. B. Rood, S. Lin, J. Muller, and A.M. Thompson. 2000: Atmospheric sulfur cycle simulated in the global model GOCART: Model description and global properties. *J. Geophys. Res.*, **105 (D20)**, 24671-24687.
- Chin, M., A. Chu, R. Levy, L. Remer, Y. Kaufman, B. Holben, T. Eck, P. Ginoux, and Q. Gao 2004: Aerosol distribution in the Northern Hemisphere during ACE-Asia: Results from global model, satellite observations, and Sun photometer measurements. *J. Geophys. Res.*, **109**, D23S90
- Chin, M., T. Diehl, P. Ginoux, and W. Malm, 2007: Intercontinental transport of pollution and dust aerosols: implications for regional air quality. *Atmos. Chem. Phys.*, **7**, 5501-5517.
- Diehl, T., A. Heil, M. Chin, X. Pan, D. Streets, M. Schultz, and S. Kinne, 2012: Anthropogenic, biomass burning, and volcanic emissions of black carbon, organic carbon, and SO₂ from 1980 to 2010 for hindcast model experiments. *Atmos. Chem. Phys. Discuss.*, **12**, 24895-24954.
- DOE, 1994: Handbook of methods for the analysis of the various parameters of the carbon dioxide system in sea water; version 2, Chapter 5, A.G Dickson and C. Goyet, eds., ORNL/CDIAC-74. [<http://cdiac.esd.ornl.gov/ftp/cdiac74/chapter5.pdf>].
- Draxler, R.R., and G.D. Hess, 1999: An overview of the HYSPLIT_4 modelling system for trajectories, dispersion, and deposition. *Australian Meteorological Magazine*, **47**, 295-308.
- Draxler, R.R. and Rolph, G.D., 2012. HYSPLIT (HYbrid Single-Particle Lagrangian Integrated Trajectory) Model access via NOAA ARL READY PC Version (<http://ready.arl.noaa.gov/HYSPLIT.php>). NOAA Air Resources Laboratory, Silver Spring, MD.
- Elias, T., Sutton A. J., Stokes, J.B., Casadevall, T.J., 1998: Sulfur dioxide emission rates of Kilauea Volcano, Hawaii, 1979-1997. U.S. Geological Survey Open-File Report 98-462.
- Elias, T. and A.J. Sutton, 2002: Sulfur dioxide emission rates of Kilauea Volcano, Hawaii, 1998-2001. U.S. Geological Survey Open-File Report 02-460.
- Elias, T. and A.J. Sutton, 2007: Sulfur dioxide emission rates of Kilauea Volcano, Hawaii, 2002-2006. U.S. Geological Survey Open-File Report 2007-1114.

- Elias, T. and A.J. Sutton, 2012: Sulfur dioxide emission rates of Kilauea Volcano, Hawaii, 2007-2010. U.S. Geological Survey Open-File Report 2012-1107.
- Faloona, I., 2009: Sulfur processing in the marine atmospheric boundary layer: A review and critical assessment of modeling uncertainties. *Atmos. Environ.*, **43(18)**, 2841-2854.
- Gondwe, M., M. Krol, W. Gieskes, W. Klaassen, and H. de Baar, 2003: The contribution of ocean-leaving DMS to the global atmospheric burdens of DMS, MSA, SO₂, and NSS SO₄⁼. *Global Biogeochem. Cy.*, **17(2)**, 1056.
- Hand, J.L., K.A. Gebhart, B.A. Schichtel, and W.C. Malm, 2012a: Increasing trends in wintertime particulate sulfate and nitrate ion concentrations in the Great Plains of the United States (2000-2010). *Atmos. Environ.*, **55**, 107-110.
- Hand, J.L., B.A. Schichtel, W.C. Malm, and M.L. Pitchford, 2012b: Particulate sulfate ion concentration and SO₂ emission trends in the United States from the early 1990s through 2010. *Atmos. Chem. Phys.*, **12**, 10353-10365.
- Heald, C.L et al., 2003: Asian outflow and trans-Pacific transport of carbon monoxide and ozone pollution: An integrated satellite, aircraft, and model perspective, *J. Geophys. Res.*, **108 (D24)**, 4804.
- Hirsch, R.M, J.R Slack, and R.A. Smith, 1982: Techniques of Trend Analysis for Monthly Water Quality Data. *Water Resour. Res.***18(1)**, 1007-121.
- Hopke, P.K., 2003: Recent developments in receptor modeling. *J. Chemometr.*, **17 (15)**, 255-265.
- Hsu, Y., T.M. Holsen, and P.K. Hopke, 2003: Comparison of hybrid receptor models to locate PCB sources in Chicago. *Atmos. Environ.*, **37**, 545-562
- Hsu, N.C., R. Gautam, A.M. Sayer, C. Bettenhausen, C. Li, M.J. Jeong, S.C. Tsay, and B.N. Holben, 2012: Global and regional trends of aerosol optical depth over land and ocean using SeaWiFS measurements from 1997-2010. *Atmos. Chem. Phys.*, **12**, 8037-8053.
- Huebert, B.J. et al., 2001: Long-term measurements of free-tropospheric sulfate at Mauna Loa: Comparison with global model simulations. *J. Geophys. Res.*, **106 (D6)**, 5479-5492.
- Itahashi, S., I. Uno, K. Yumimoto, H. Irie, K. Osada, K. Ogata, H. Fukushima, Z. Wang, and T. Ohara, 2012: Interannual variation in the fine-mode MODIS aerosol optical depth and its relationship to the changes in sulfur dioxide emissions in China between 2000 and 2010. *Atmos. Chem. Phys.*, **12**, 2631-2640.
- Jacobson, 2002: *Atmospheric Pollution: History, Science, and Regulation*. Cambridge University Press, 399 pp.

- Jaffe, D., T. Anerson, D. Covert, R. Kotchenruther, B. Trost, J. Danielson, W. Simpson, T. Berntsen, S. Karlsdottir, D. Blake, J. Harris, G. Carmichael, and I. Uno, 1999: Transport of Asian Air Pollution to North America. *Geophys. Res. Lett.*, **26 (6)**, 711-714.
- Kalnay et al., 1996: The NCEP/NCAR 40-year reanalysis project, *Bull. Amer. Meteor. Soc.*, **77**, 437-470.
- Khoder, M.I., 2002: Atmospheric conversion of sulfur dioxide to particulate sulfate and nitrogen dioxide to particulate nitrate and gaseous nitric acid in an urban area, *Chemosphere*, **49 (6)**, 675-684.
- Keeling, C.D., R.B. Bacastow, A.E. Bainbridge, C.A. Ekdahl Jr., P.R. Guenther, L.S. Waterman, J.F.S. Chin, 1976: Atmospheric carbon dioxide variations at Mauna Loa Observatory, Hawaii, *Tellus*, **28 (6)**, 538-551.
- Klimont, Z., S.J. Smith, and J. Cofala, 2013: The last decade of global anthropogenic sulfur dioxide: 2000-2011 emissions. *Environ. Res. Lett.*, **8**, 6pp.
- Kloster, S., J. Feichter, E. Maier-Reimer, K.D. Six, P. Stier, and P. Wetzel, 2006: DMS cycle in the marine ocean-atmosphere system – a global model study. *Biogeosciences*, **3**, 29-51.
- Knoll, G.F., 2010: *Radiation Detection and Measurement*. Wiley, 829 pp.
- Korhonen, H., K.S. Carslaw, D.V. Spacklent, G.W. Mann, and M.T. Woodhouse, 2008: Influence of oceanic dimethylsulfide emissions on cloud condensation nuclei concentrations and seasonality over the remote Southern Hemisphere oceans: A global model study, *J. Geophys. Res.*, **113**, D15204.
- Li, L., Z.M. Chen, Y.H. Zhang, T. Zhu, J.L. Li, and J. Ding, 2006: Kinetics and mechanism of heterogeneous oxidation of sulfur dioxide by ozone on surface of calcium carbonate. *Atmos. Chem. Phys. Discuss.*, **6**, 579-613.
- Liang, Q., L. Jaegle, D.A. Jaffe, P. Weiss-Penzias, A. Heckman, and J.A. Snow, 2004: Long-range transport of Asian pollution to the northeast Pacific: Seasonal variations and transport pathways of carbon monoxide. *J. Geophys. Res.*, **109**, D23S07.
- Liang, Q., L. Jaegle, and J.M. Wallace, 2005: Meteorological indices for Asian outflow and transpacific transport on daily to interannual timescales. *J. Geophys. Res.*, **110**, D13104.
- Likens, G.E., T.J. Bulter, and D.C. Buso, 2001: Long- and short-term changes in sulfate deposition: Effects of the 1990 Clean Air Act Amendments. *Biogeochemistry*, **52**, 1-11.
- Lintner, B.R., W. Buermann, C.D. Koven, and I.Y. Fung, 2006: Seasonal circulation and Mauna Loa CO₂ variability. *J. Geophys. Res.*, **111**, D13104, doi:10.1029/2005JD006535.

- Liu, H., D.J. Jacob, I. Bey, R.M. Yantosca, B.N. Duncanc, and G.W. Sachse, 2003: Transport pathways for Asian pollution outflow over the Pacific: Interannual and seasonal variations. *J. Geophys. Res.*, **108**, 8786.
- Liu, J., D.L. Mauzerall, L.W. Horowitz, 2008: Source-receptor relationships between East Asian sulfur dioxide emissions and Northern Hemisphere sulfate concentrations. *Atmos. Chem. Phys. Disc.*, **8 (2)**, 5537-5561.
- Longo, B.M., A. Grunder, R. Chuan, A. Rossignol, 2005: SO₂ and fine aerosol dispersion from the Kilauea plume, Kau district, Hawaii, USA. *Geology*, **33 (3)**, 217-220.
- Lu, Z., D. G. Streets, Q. Zhang, S. Wang, G. R. Carmichael, Y. F. Cheng, C. Wei, M. Chin, T. Diehl, and Q. Tan, 2010: Sulfur dioxide emissions in China and sulfur trends in East Asia since 2000. *Atmos. Chem. Phys.*, **10**, 6311-6331.
- Lu, Z., Q. Zhang, and D.G. Streets, 2011: Sulfur dioxide and primary carbonaceous aerosol emissions in China and India, 1996-2010. *Atmos. Chem. Phys.*, **11**, 9839-9864.
- Luria, M., J. F. Boatman, J. Harris, J. Ray, T. Straube, J. Chin, R. L. Gunter, G. Herbert, T. M. Gerlach, and C. C. Van Valin, 1992: Atmospheric Sulfur Dioxide at Mauna Loa, Hawaii. *J. Geophys. Res.*, **97 (D5)**, 6011-6022.
- Lynch, J.A., V.C. Bowercox, J.W. Grimm, 2000: Changes in sulfate deposition in eastern USA following implementation of Phase I of Title IV of the Clean Air Act Amendments of 1990. *Atmos. Environ.*, **11**, 1665-1680.
- Ma, X., K. von Salzen, and J. Li, 2008: Modelling sea salt aerosol and its direct and indirect effects on climate. *Atmos. Chem. Phys.*, **8**, 1311-1327.
- Meehl, G. A., and Coauthors, 2007: Global climate projections. *Climate Change 2007: The Physical Science Basis*, S. Solomon et al., Eds., Cambridge University Press, 747-845.
- Merrill, J.T., M. Uematsu, R. Bleck, 1989: Meteorological analysis of long range transport of mineral aerosols over the North Pacific, *J. Geophys. Res.*, **94 (D6)**, 8584-8598.
- NASA Earth Observatory, 2008: New Activity on Kilauea. [<http://earthobservatory.nasa.gov/NaturalHazards/view.php?id=19711>].
- Nau, R.F., cited 2013: Testing the assumptions of linear regression. [people.duke.edu/~rnau/testing.htm].
- NIST/SEMATECH, cited 2013: e-Handbook of Statistical Methods, [<http://www.itl.nist.gov/div898/handbook/>]

- NOAA, Air Resources Laboratory, 2012: HYSPLIT Model Research, A Complete Modeling System for Simulating Dispersion of Harmful Atmospheric Material, 2 pp.
- Novelli, P.C., L.P. Steele, and P.P. Tans, 1992: Mixing Ratios of Carbon Monoxide in the Troposphere, *J. Geophys. Res.*, **97(D18)**, 20731-20750.
- Ohara, T., H. Akimoto, J. Kurokawa, N. Horii, K. Yamaji, X. Yan, and T. Hayasaka, 2007: An Asian emission inventory of anthropogenic emission sources for the period 1980-2020. *Atmo. Chem. Phys.*, **7**, 4419-4444.
- Perry, K.D., T.A. Cahill, R.C. Schnell, and J.M. Harris, 1999: Long-range transport of anthropogenic aerosols to the National Oceanic and Atmospheric Administration baseline station at Mauna Loa Observatory, Hawaii. *J. Geophys. Res.*, **104 (D15)**, 18521-18533.
- Prospero, J.M., D.L. Savoie, R. Arimoto, 2003: Long-term record of nss-sulfate and nitrate in aerosols on Midway Island, 1981-2000: Evidence of increased (now decreasing?) anthropogenic emissions from Asia. *J. Geophys. Res.*, **108 (D1)**, 4019.
- Quinn, P.K. and T.S. Bates, 2011: The case against climate regulation via oceanic phytoplankton sulphur emissions, *Nature*, **480**, 51-56.
- Reid, J.S., H.H. Jonsson, M.H. Smith, and A. Smirnov, 2001: Evolution of the vertical profile and flux of large sea-salt particles in a coastal zone. *J. Geophys. Res.*, **106 (D11)**, 12039-12053.
- Rinsland, C.P., A. Goldman, F.J. Murcray, T.M. Stephen, N.S. Pougatchev, J. Fishman, S.J. David, R.D. Blatherwick, P.C. Novellil, N.B. Jones, and B.J. Connor, 1999: Infrared solar spectroscopic measurements of free tropospheric CO, C₂H₆, and HCN above Mauna Loa Hawaii: Seasonal variations and evidence for enhanced emissions from the Southeast Asian Tropical fires of 1997-1998. *J. Geophys. Res.*, **104 (D15)**, 18667-18680.
- Sanderson, M., T. Schroeder, D. Nullet, T. Giambelluca, S. Price, P. Ekern, 1993: *Prevailing Trade Winds Weather and Climate in Hawai'i*. University of Hawaii Press. 126pp.
- Saltzman, E.S., D.L. Savoie, J.M. Prospero, and R.G. Zika, 1986: Methanesulfonic Acid and Non-Sea-Salt Sulfate in Pacific Air: Regional and Seasonal Variations, *J. Atmos. Chem.*, **4**, 227-240.
- Savoie, D.L., J.M. Prospero, R. Arimoto, and R. A. Duce, 1994: Non-sea-salt sulfate and methanesulfonate at American Samoa. *J. Geophys. Res.*, **99 (D2)**, 3587-3596.
- Saxena, P. and C. Seigneur, On the oxidation of SO₂ to sulfate in atmospheric aerosols. *Atmos. Environ.*, **21 (4)**, 807-812.
- Schery, S.D. and S. Huang, 2004: An estimate of the global distribution of radon emissions from the ocean, *Geophys. Res. Lett.*, **31**, L19104.

- Sen, P.K, 1968: Estimates of the regression coefficient based on Kendall's tau statistic. *J. Am. Stat. Assoc.*, **63**, 1379-1389.
- Siebert L, Simkin T (2002-). *Volcanoes of the World: an Illustrated Catalog of Holocene Volcanoes and their Eruptions*. Smithsonian Institution, Global Volcanism Program Digital Information Series, GVP-3, [<http://www.volcano.si.edu/world/>].
- Smith, S.J., H. Pitcher, and T.M.L. Wigley, 2001: Global and regional anthropogenic sulfur dioxide emissions. *Global Planet. Change*, **29**, 99-119
- Smith, S.J., J. van Aardenne, Z. Klimont, R. J. Andres, A. Volke, and S. Delgado Arias, 2011: Anthropogenic sulfur dioxide emissions: 1850-2005. *Atmos. Chem. Phys.*, **11**, 1101-1116.
- Sofiev, M., J. Soares, M. Prank, G. de Leeuw, and J. Kukkonen, 2011: A regional-to-global model of emission and transport of sea salt particles in the atmosphere, *J. Geophys. Res.*, **116**, D21302.
- Stenchikov, G.L., I. Kirchner, A. Robock, H.F. Graf, J.C. Antuna, R.G. Grainger, A. Lambert, and L. Thomason, 1998: Radiative forcing from the 1991 Mount Pinatubo volcanic eruption. *J. Geophys. Res.*, **103 (12)**, 13837-13857.
- Stern, D.I., 2006: Reversal of the trend in global anthropogenic sulfur emissions. *Global Environ. Change*, **16 (2)**, 207-220.
- Streets, D.G., N. Y. Tsai, H. Akimoto, K. Oka, 2000: Sulfur dioxide emissions in Asia in the period 1985-1997. *Atmos. Environ.*, **34**, 4413-4424.
- Su, S., B. Li, S. Cui, and S. Tao, 2011: Sulfur Dioxide Emissions from Combustion in China: From 1990 to 2007. *Environ. Sci. Technol.* **45**, 8403-8410.
- Tai, A.P.K., L.J. Mickley, and D.J. Jacob, 2010: Correlations between fine particulate matter (PM_{2.5}) and meteorological variables in the United States: Implications for the sensitivity of PM_{2.5} to climate change. *Atmos. Environ.*, **44 (32)**, 3976-3984.
- Tanaksa, T.Y. and M. Chiba, 2006: A numerical study of the contributions of dust source regions to the global dust budget. *Global Planet Change*, **52**, 88-104.
- Theil, H., 1950: A rank-invariant method of linear and polynomial regression analysis. I, II, III. *Nederl. Akad. Wetensch. Proc.*, **53**, 386-392, 521-525, 1397-1412.
- Trenberth, K.E. and A. Dai, 2007: Effects of Mount Pinatubo volcanic eruption on the hydrological cycle as an analog of geoengineering. *Geophys. Res. Lett.*, **34 (15)**, L15702.
- United States Environmental Protection Agency, cited 2012: Sulfur Dioxide. [<http://www.epa.gov/airquality/sulfurdioxide/>].

- University of Hawaii at Manoa School of Ocean and Earth Science and Technology, cited 2012: Chemical composition of seawater; Salinity and the major constituents. [http://www.soest.hawaii.edu/oceanography/courses/OCN623/Spring2012/Salinity2012web.pdf]
- VanCuren, R.A., T.A. Cahill, 2002: Asian aerosols in North America: Frequency and concentration of fine dust. *J. Geophys. Res.*, **107 (D24)**, 4804.
- van der Werf, G.R., J.T. Randerson, G.J. Collatz, L. Giglio, P.S. Kasibhatla, A.F. Arellano Jr., S.C. Olsen, and E.S. Kasischke, 2004: Continental-Scale Partitioning of Fire Emissions During the 1997 to 2001 El Niño/La Niña Period. *Science*, **303 (5654)**, 73-76.
- van der Werf, G.R., J.T. Randerson, L. Giglio, G.J. Collatz, P.S. Kasibhatla, and A.F. Arellano Jr., 2006: Interannual variability of global biomass burning emissions from 1997 to 2004. *Atmos. Chem. Phys. Discuss.*, **6**, 3175-3226.
- Wallace, J.M. and P.V. Hobbs, 2006: *Atmospheric Science: An Introductory Survey*. 2nd Ed. Academic Press, 483pp.
- Wilkening, M.H. and W.E. Clements, 1975: Radon 222 from the ocean surface. *J. Geophys. Res.*, **80 (27)**, 3828-3830.
- Wilks, D.S., 2006: *Statistical Methods in the Atmospheric Sciences*. 2nd Ed. Elsevier, 627 pp.
- Weiss-Penzias, P., D. A., Jaffe, P. Swartzendruber, J.B. Dennison, D. Chand, W. Hafner, and E. Prestbo, 2006: Observations of Asian air pollution in the free troposphere at Mount Bachelor Observatory during the spring of 2004. *J. Geophys. Res.*, **111**, D10304.
- Whittlestone S. and Zahorowski, W., 1998: Baseline radon detectors for shipboard use: Development and deployment in the First Aerosol Characterisation experiment (ACE 1). *J. Geophys. Res.*, **103**, 16743-16751.
- Wolter, K., cited 2012 : Multivariate ENSO Index (MEI). (<http://www.esrl.noaa.gov/psd/enso/mei/>)
- Ye, D. and G. Wu, 1998: The Role of The Heat Source of the Tibetan Plateau in the General Circulation. *Meteorol. Atmos. Phys.*, **67**, 181-198.
- Yienger, J.J., M. Galanter, T.A. Holloway, M.J. Phadnis, S.K. Guttikunda, G.R. Carmichael, W.J. Moxim, and H. Levy II, 2000: The episodic nature of air pollution transport from Asia to North America, *J. Geophys. Res.*, **105 (D22)**, 26931-26945.
- Zahorowski, W. et al., 2005: Radon-222 in boundary layer and free tropospheric continental outflow events at three Ace-Asia sites. *Tellus B*, **57 (2)**, 124-140.

Zhang, D. and Y. Iwasaka, 1999: Nitrate and sulfate in individual Asian dust-storm particles in Beijing, China in spring of 1995 and 1996. *Atmos. Environ.*, **33**, 3123-3223.

APPENDIX A

The following timelines show daily concentrations of anthropogenic NSS-sulfate, radon, carbon monoxide, and NSS-calcium and occurrence of continental trajectory origin for each year during 2005-2008. The timeline for all years combined is included and discussed further in Section (4.1.2). The timelines for each year provide more detail of concentration variability on a daily timescale and allow for detailed interannual comparisons.

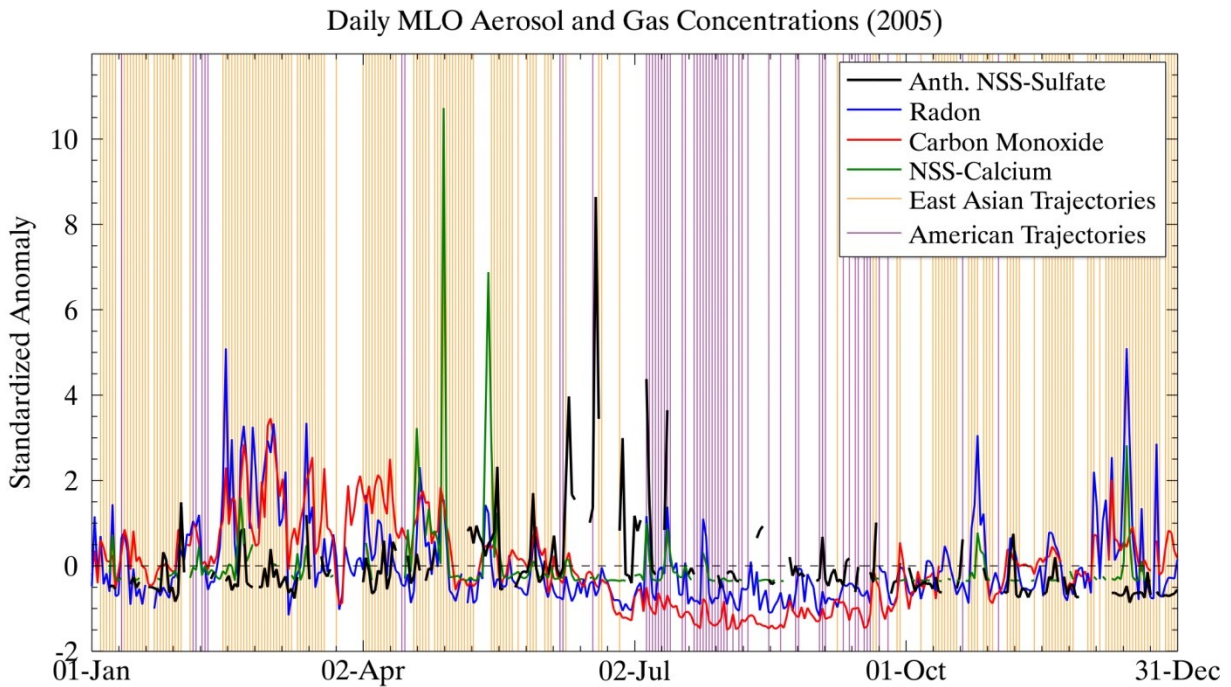


Figure A.1: Daily MLO concentrations and trajectory origin during 2005.

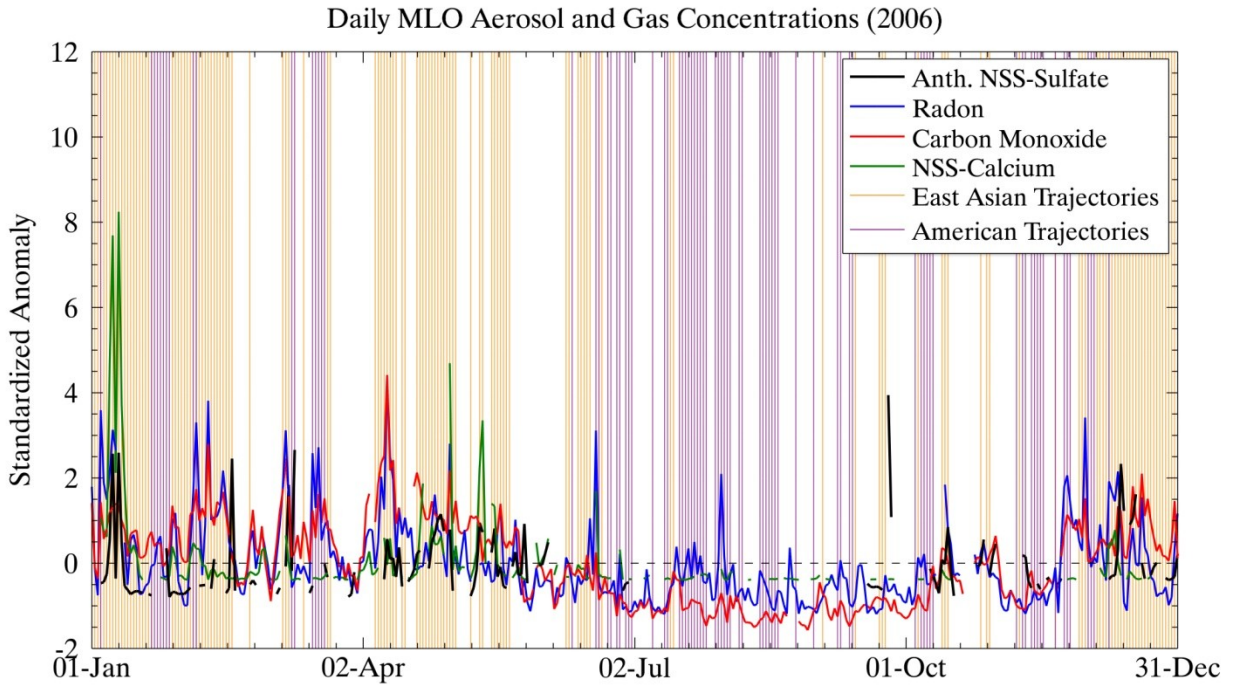


Figure A.2: Daily MLO concentrations and trajectory origin during 2006.

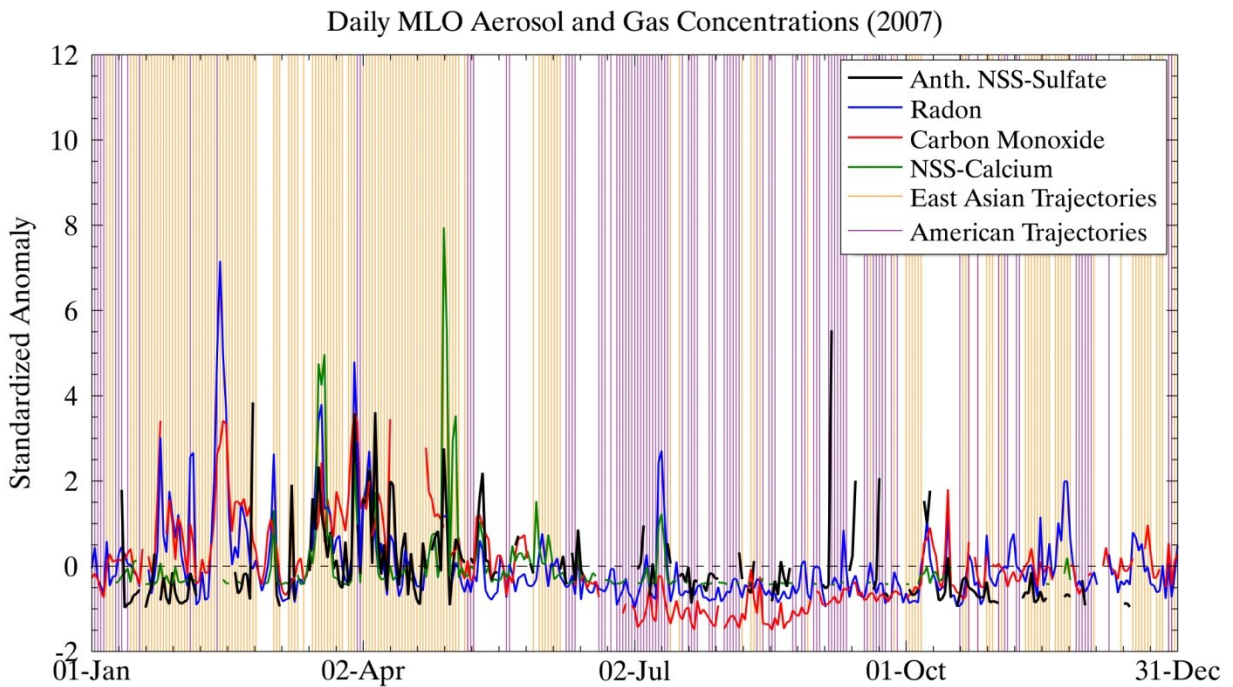


Figure A.3: Daily MLO concentrations and trajectory origin during 2007.

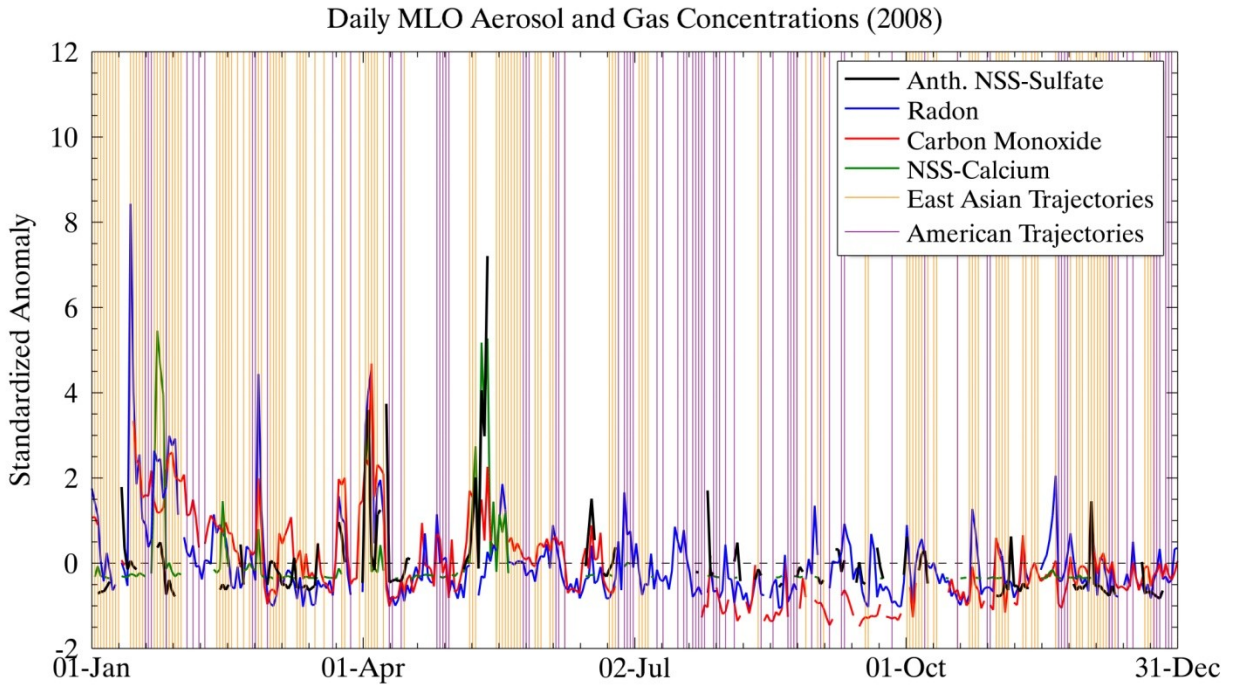


Figure A.4: Daily MLO concentrations and trajectory origin during 2008.

APPENDIX B

The following plots were used as graphical tests of regression results to determine whether assumptions of normality, linearity independence, and homoscedasticity were reasonable. Results for radon, carbon monoxide, and anthropogenic NSS-sulfate are included. Regression results are discussed further in Section (4.3) and details about the assumptions tested using these figure are discussed in Section (2.7.3)

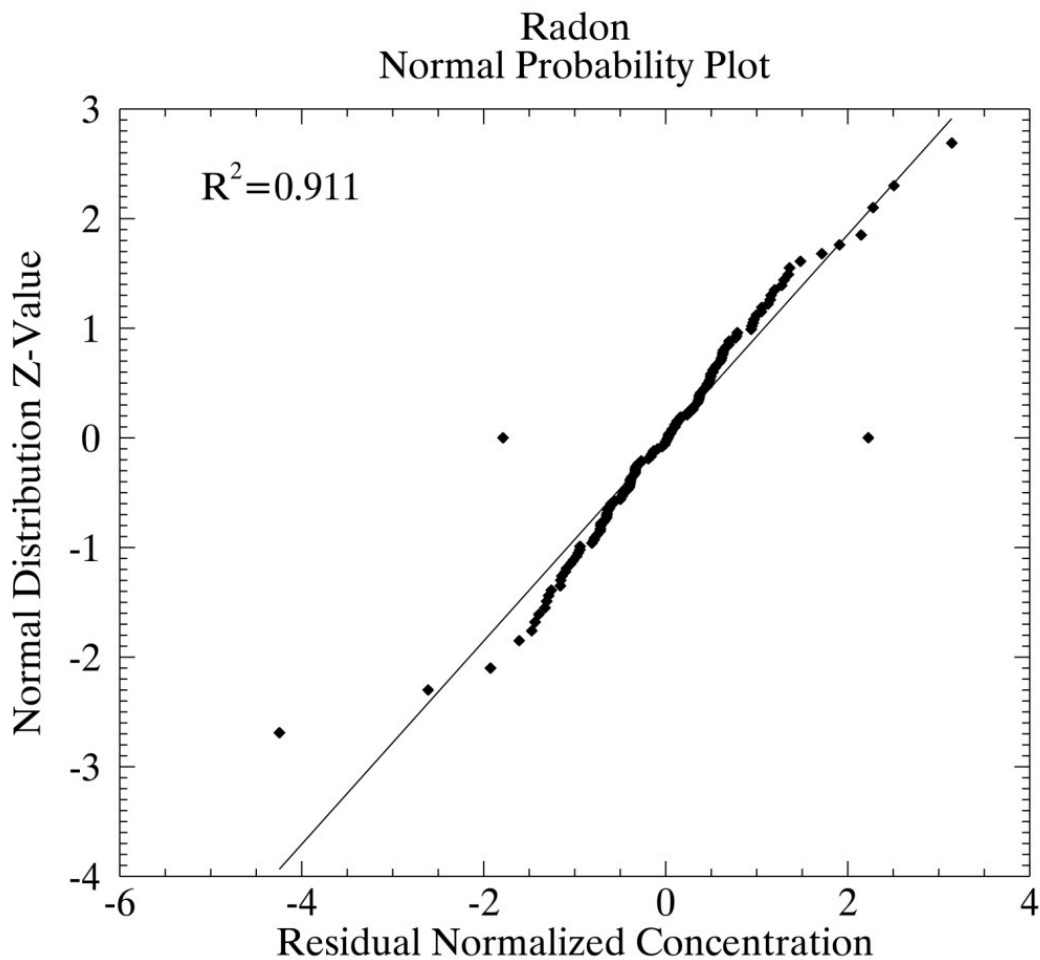


Figure B.1: Normal probability plot to test for normality of radon residuals

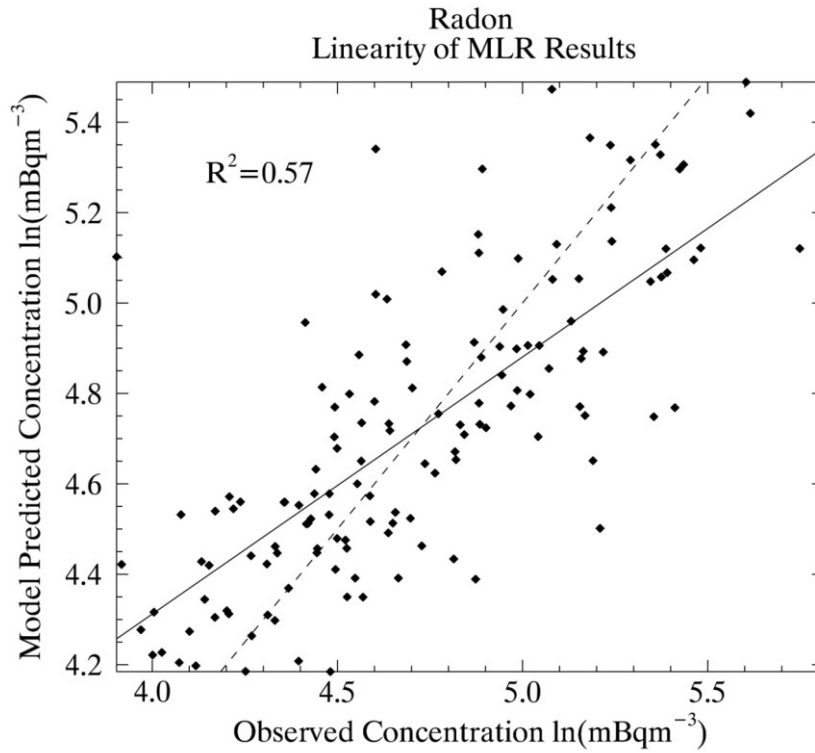


Figure B.2: Test for linearity of radon residuals.

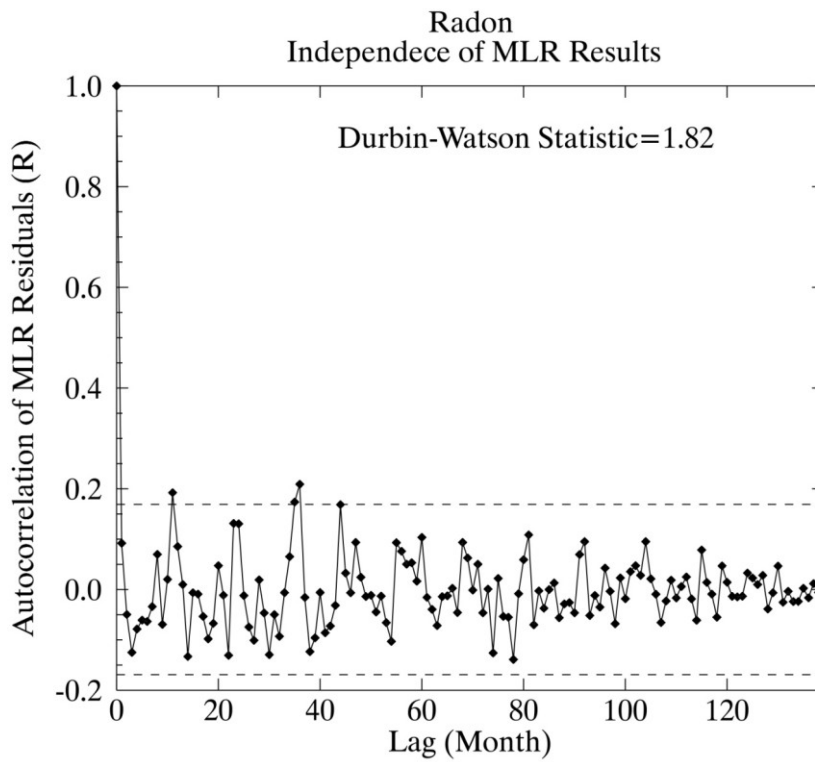


Figure B.3: Test for independence of radon residuals.

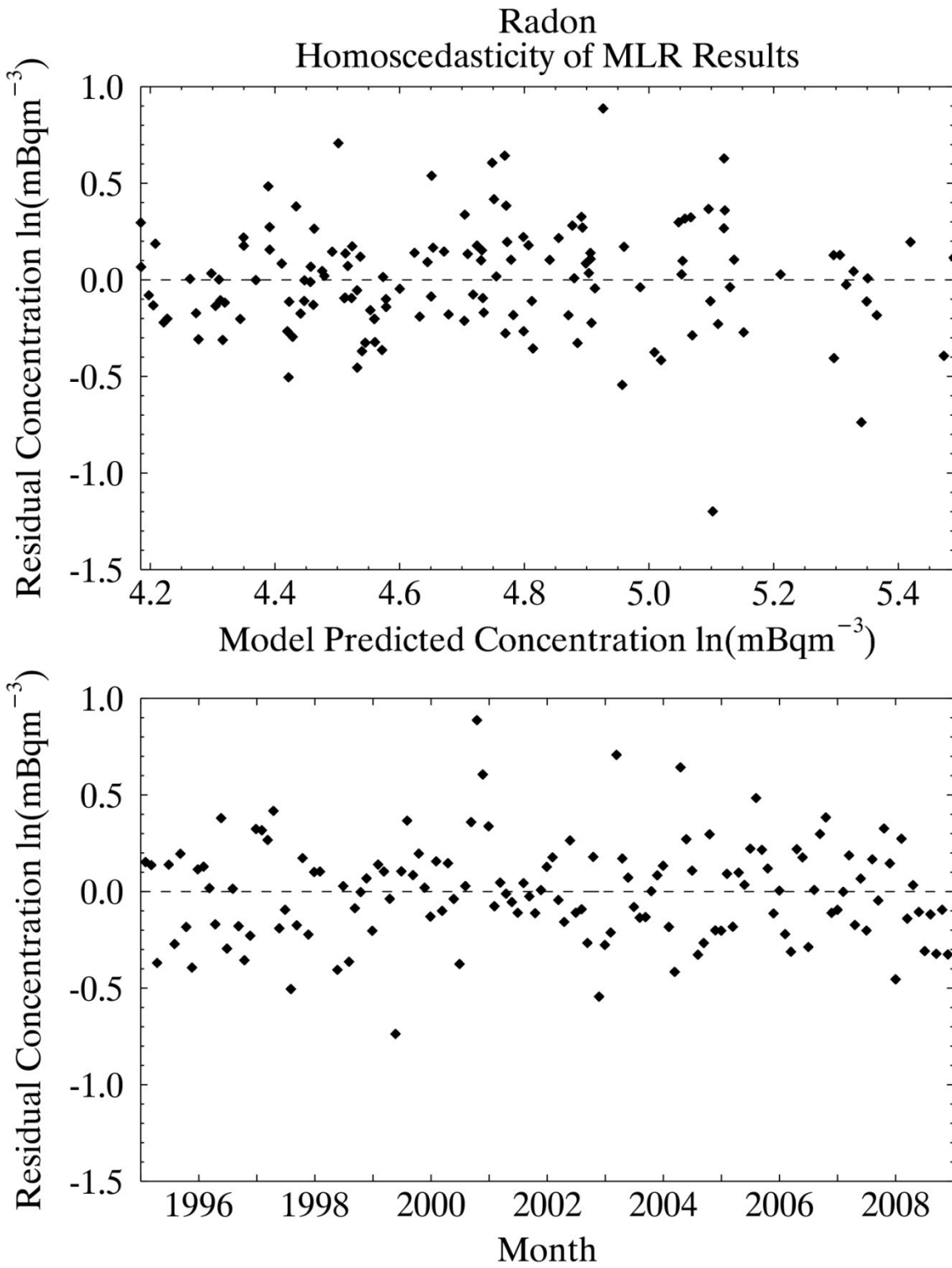


Figure B.4: Test for homoscedasticity of radon residuals.

Carbon Monoxide
Normal Probability Plot

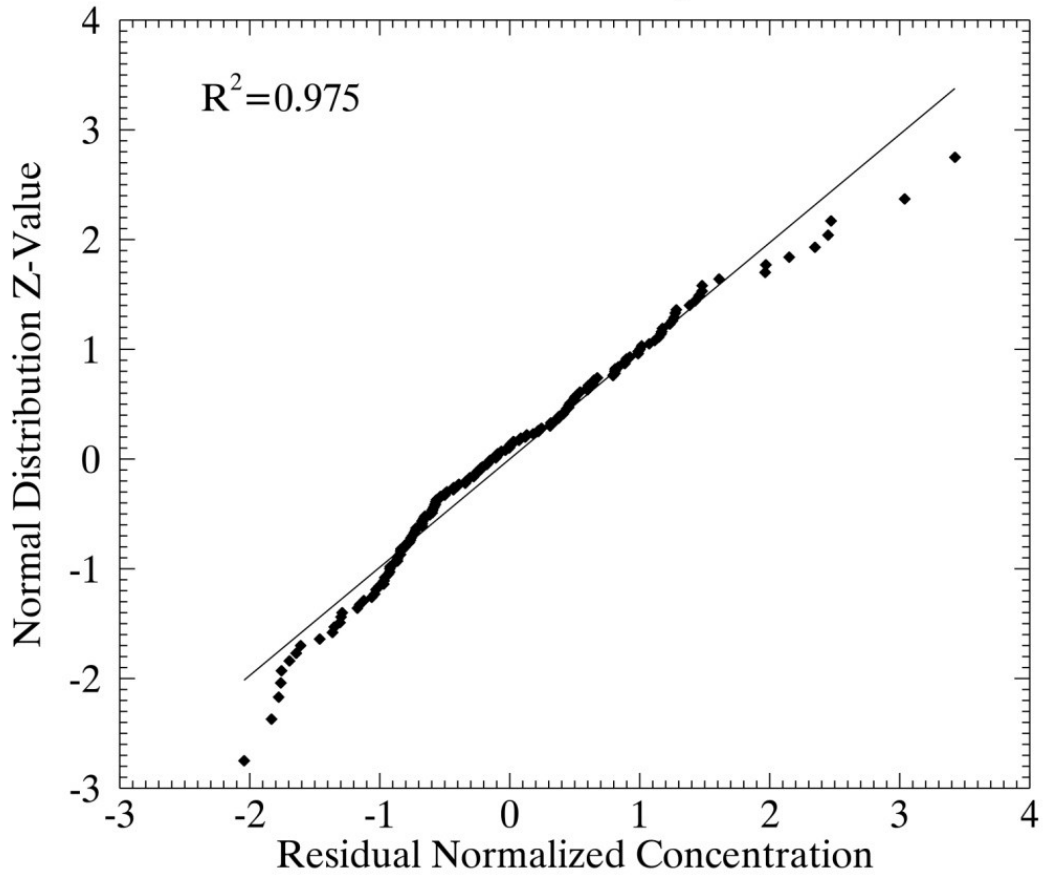


Figure B.5: Normal probability plot to test for normality of carbon monoxide residuals.

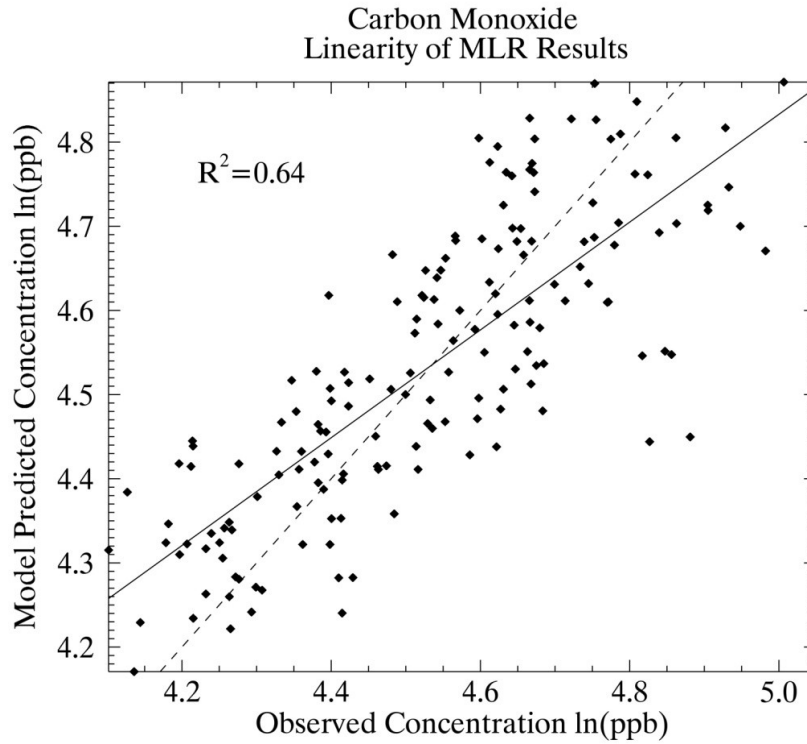


Figure B.6: Test for linearity of carbon monoxide residuals.

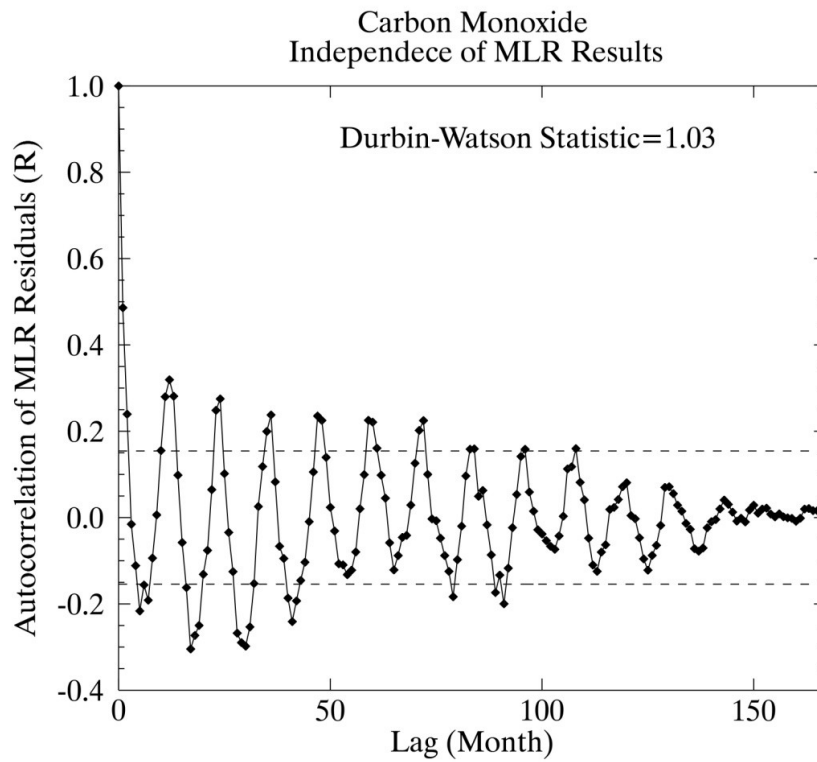


Figure B.7: Test for independence of carbon monoxide residuals.

Carbon Monoxide
Homoscedasticity of MLR Results

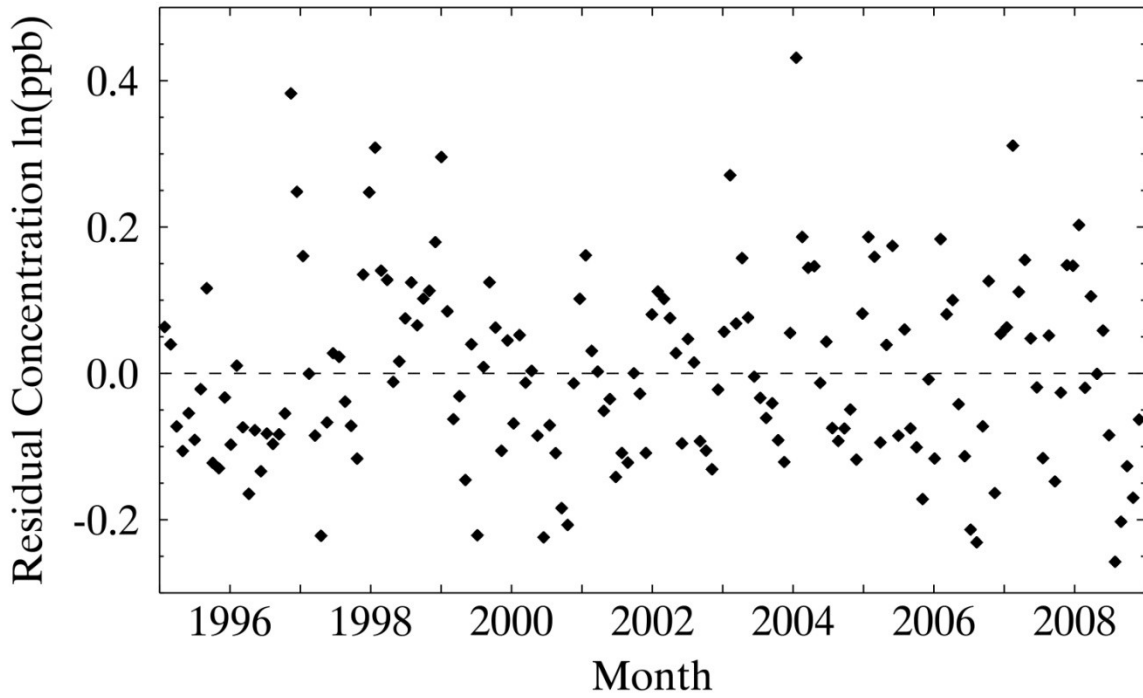
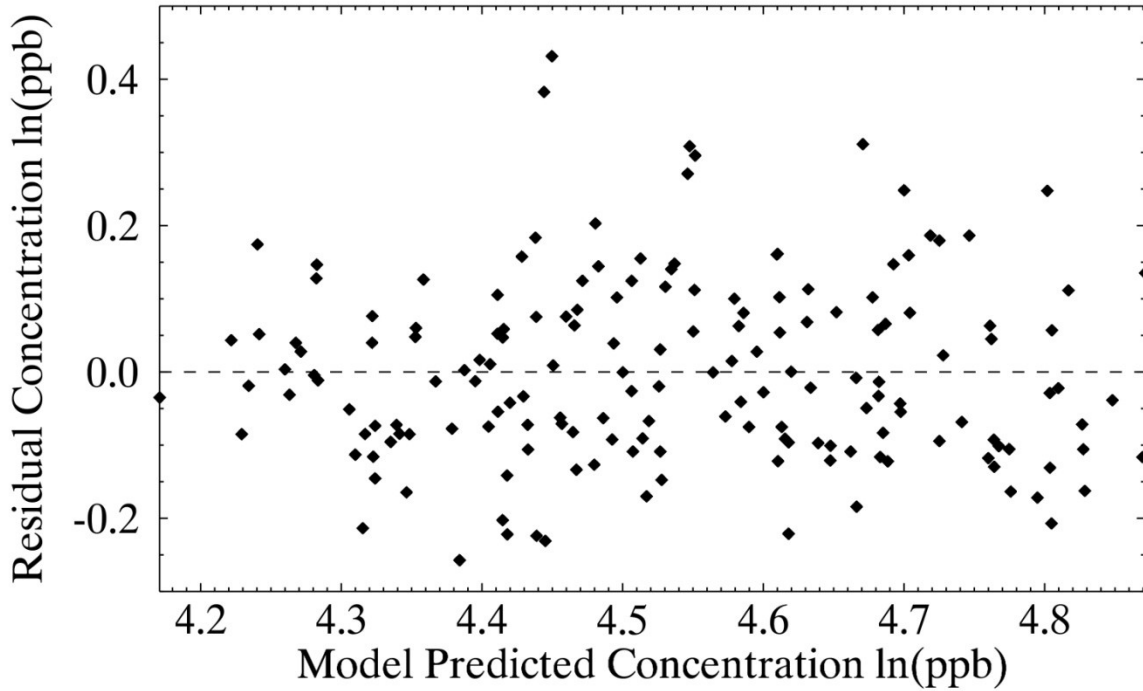


Figure B.8: Test for homoscedasticity of carbon monoxide residuals.

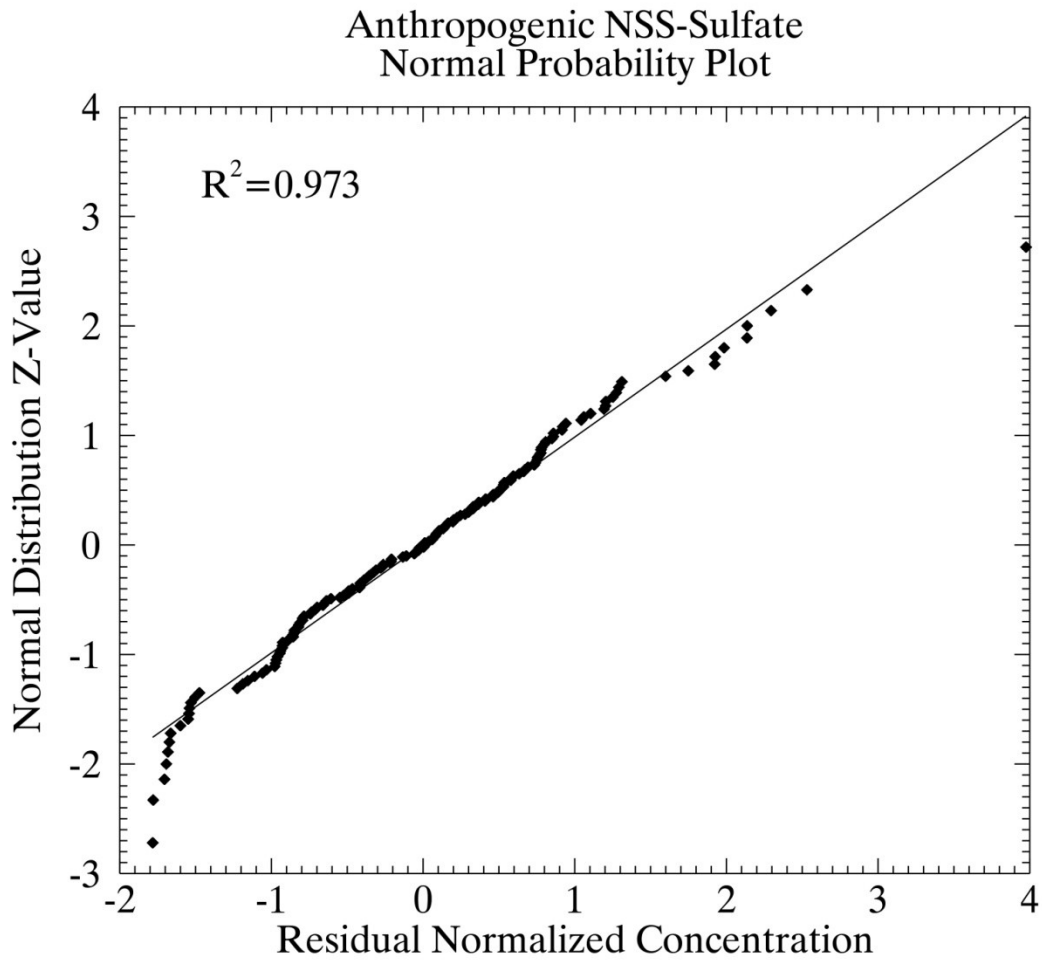


Figure B.9: Normal probability plot to test for normality of anthropogenic NSS-sulfate residuals.

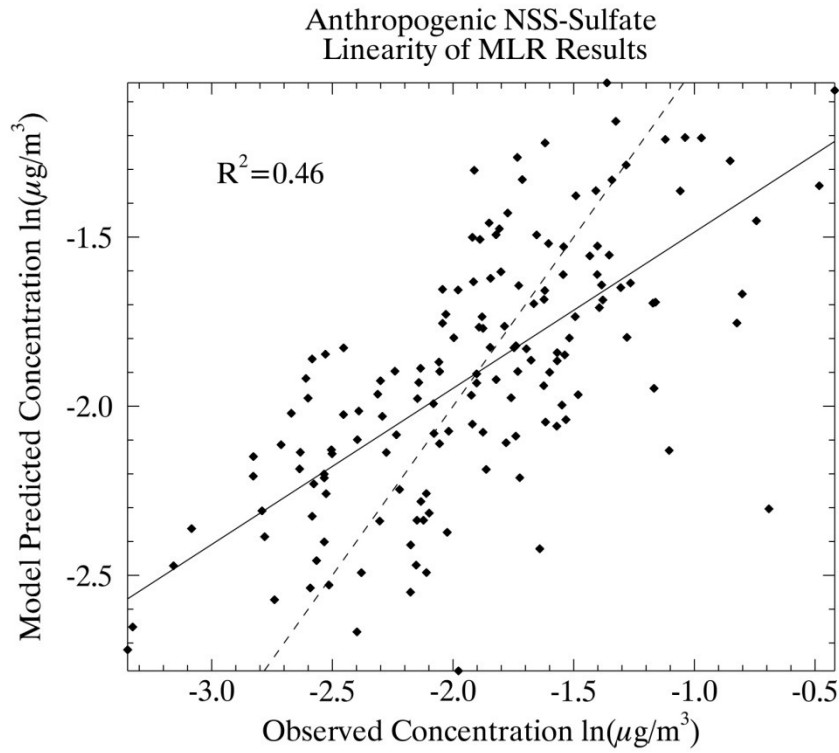


Figure B.10: Test for linearity of anthropogenic NSS-sulfate residuals.

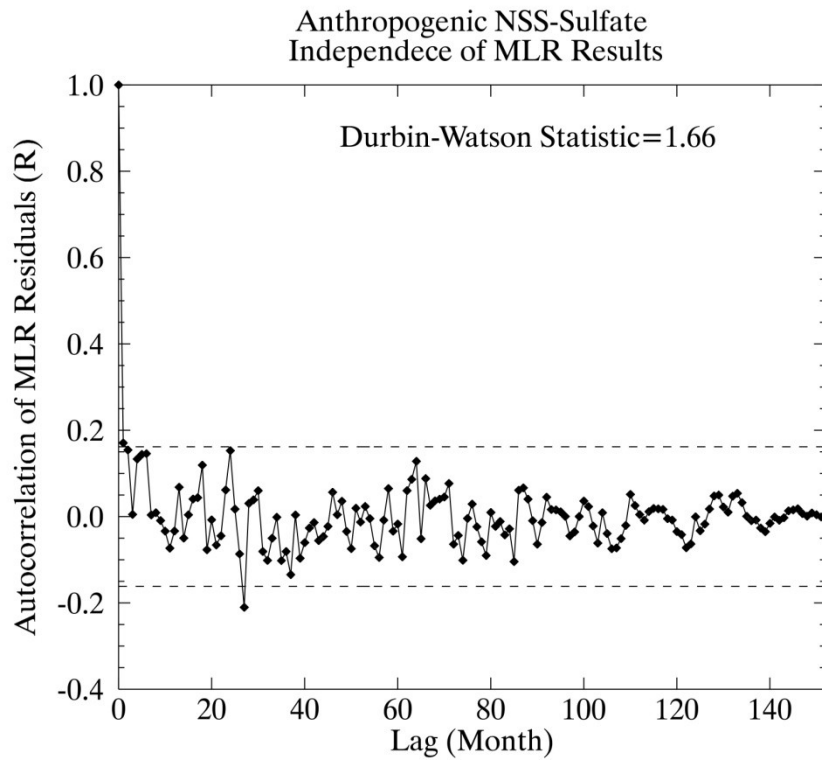


Figure B.11: Test for independence of anthropogenic NSS-sulfate residuals.

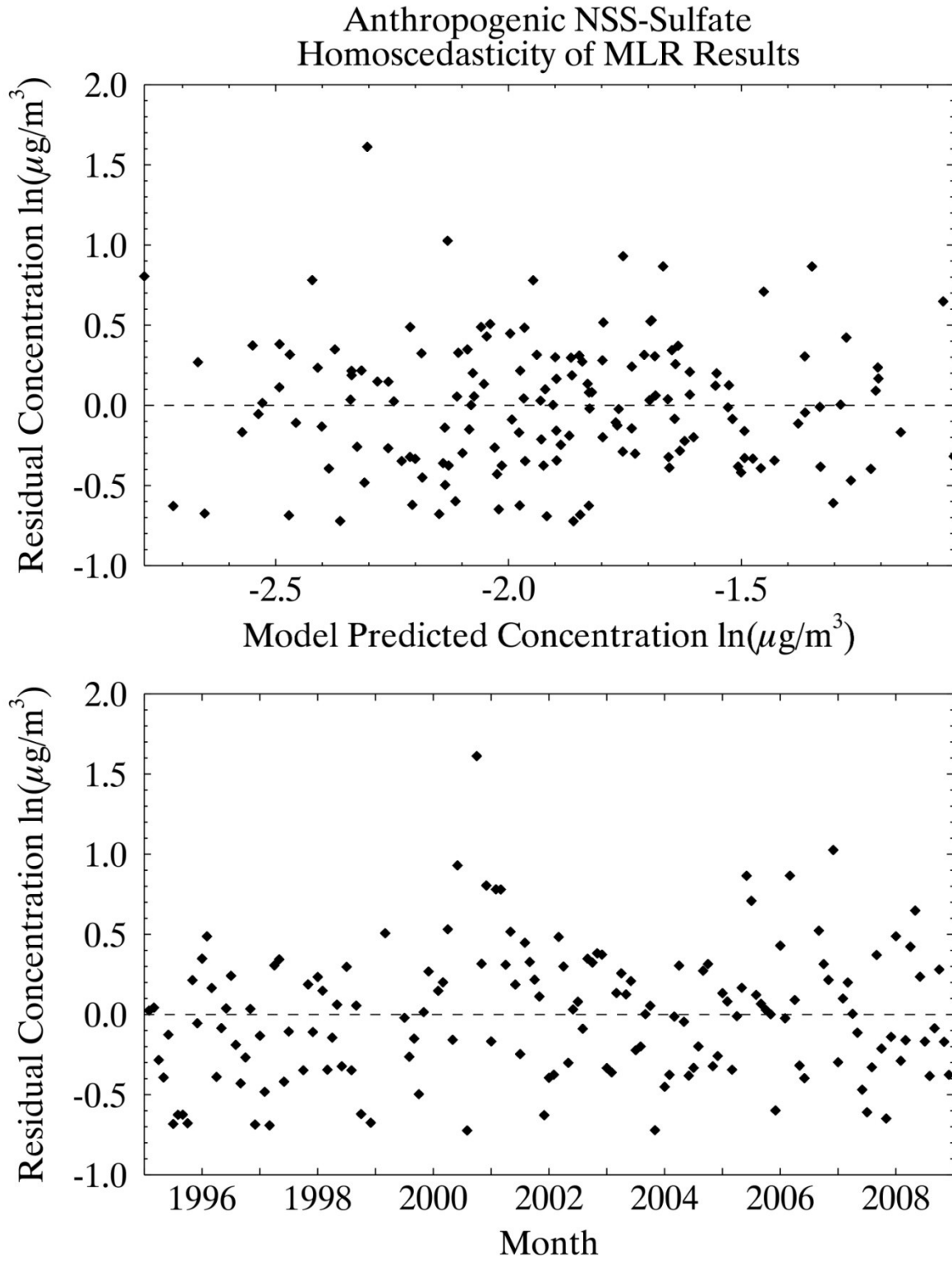


Figure B.12: Test for homoscedasticity of anthropogenic NSS-sulfate residuals.